

# Numerical Simulation of Fracture Propagation Based on Finite Element Method and Peridynamics



Swansea University  
Prifysgol Abertawe

**Yanan Sun**

Department of Civil Engineering  
Swansea University

This dissertation is submitted for the degree of  
*Doctor of Philosophy*

January 2022



I would like to dedicate this thesis to my loving parents ...

## Declaration

### DECLARATION

This work has not previously been accepted in substance for any degree and is not being concurrently submitted in candidature for any degree.

Signed .....  ..... (candidate)

Date .....2022/01/05.....

### STATEMENT 1

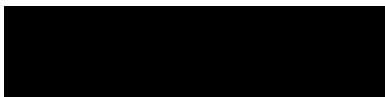
This thesis is the result of my own investigations, except where otherwise stated. Other sources are acknowledged by footnotes giving explicit references. A bibliography is appended.

Signed .....  ..... (candidate)

Date .....2022/01/05.....

### STATEMENT 2

I hereby give consent for my thesis, if accepted, to be available for photocopying and for inter-library loans **after expiry of a bar on access approved by the Swansea University**.

Signed .....  ..... (candidate)

Date .....2022/01/05.....

## Acknowledgements

First of all, I would like to express my deepest gratitude and appreciation to my supervisors, Professor Michael G Edwards, and Professor Chenfeng Li. In the past four years, they have given me sincere guidance, encouragement and support. Michael G Edwards is always open to discussions and new ideas. His rich experience and profound knowledge have broadened my research ideas. His rigorous academic attitude and detailed feedback have encouraged me and made me make progress in all aspects. In addition, he is very considerate and cares about my physical and mental health during the lockdown due to the COVID-19 epidemic. He advised me to do more exercise, and I am very grateful to him for giving me the advice, which helps me build a regular daily routine and balances my life and research during the epidemic. I would also like to thank my second supervisor, Prof. Chenfeng Li, who has created a valuable learning environment to do the research in the best possible way. In his team, I can get opinions and suggestions from different majors and fields. In addition, he has helped me in finding my research goals. Whenever I meet difficulties in my research, he always gives constructive opinions and criticism to help me solve the problem and make progress. My sincere thanks also go to both two professors for providing me with many opportunities to attend conferences to broaden my academic horizons. I will always be grateful. I am and will always be thankful for having the opportunity to work with my two supervisors.

Next, I would like to thank my colleagues and my friends. Completing this work would have been more difficult if I did not have the support from them. Dr Bin Chen, thank you very much for always being there with your helpful guidance and emotional support. Our horizon widening discussions and cooperation in work have always contributed to the quality of this thesis. Dr Jinlong Fu, thank you very much for your valuable suggestions and great food during the lockdown. Dr Tao Ni, thank you for your help and inspiration for the development of the hybrid FEM and PD model. And my housemate Dr Han Wang, thank you for every moment we have spent together. Thanks to Dr Sizeng You, Dr Tongming Qu, Dr Yawei Xie, Dr Tingting Zhao, Dr Dunhui Xiao and all the other friends for your precious friendship and constant support.

Last but not least, my most sincere thanks to my precious family, my father and mother, and my husband, Dr Guoyin. No words can express my gratitude and the deepest love I have for you. Thank you very much for supporting me and always being there for me.

## Abstract

Hydraulic fracturing has attracted a tremendous amount of attention due to its abundant applications, such as magma-driven dykes, fracturing of oil and gas reservoirs, heat production from geothermal reservoirs, ice melt, and fault reactivation in mining. Therefore, the development of fracture propagation models is of great significance to provide more effective technical tools for the dynamic simulation of fracture formation and propagation. Hydraulic fracturing involves a complex process due to the strong coupling between the fluid and solid rock. The finite element method (FEM) is a traditional method for solving the fracture propagation problem. FEM has the advantage of being robust and flexible. However, special treatment is required when dealing with complex fracture problems such as fracture intersection and branching because of discontinuities across fracture surfaces. Instead of seeking to approximate partial differential equations in a conventional framework, the peridynamic approach (PD) uses spatial integral equations that overcome the limitations of defining partial derivatives at discontinuities, which makes it quite suitable for solving complex fracture problems. Therefore, it is of great importance to combine the advantages of both FEM and PD to develop a more robust and flexible fracture propagation model. The main contribution of the thesis is to study fracture propagation problems in fully saturated porous media based on both FEM and PD. Three fracture models based on FEM, PD, hybrid FEM and PD are developed to simulate and explore more “realistic” fracture propagation processes. The main research work of the thesis contains the following four parts.

First, comprehensive reviews of the fracture propagation literature, crack branching and PD theory are given. The fracture propagation review includes a review of the fracture propagation process, fracture models and various numerical methods for predicting fracture propagation. The review of crack branching provides a state-of-the-art review of crack branching, including experimental observations, physics, fracture models and associated numerical methods. The latest advances and existing issues of crack branching are discussed. The review of PD theory provides a review of theoretical aspects of PD and related applications of PD in different fields, especially in the field of fracture mechanics. The challenges and new prospects for the development of PD are discussed.

Then, a fully implicit, FEM-based fracture model using zero thickness cohesive interface elements is developed. The rock formation is considered as a fully saturated porous medium. The fracture surface is deemed to be permeable, the fracturing fluid is treated as an incompressible Newtonian fluid, and the cohesive zone model is employed for the fracture propagation criterion. After verifying the model, the stepwise phenomenon, which has been observed in the field and experiments and reported recently in the numerical modelling literature, is investigated with the model.

Then, an explicit PD approach for simulating fracture propagation in saturated porous media is developed. A staggered method is adopted to solve the coupled system. The solid deformation equation is solved for the displacement field, and the fluid flow equation is solved for the pressure field with PD. After verification via benchmark examples, including a 1D consolidation problem and a 2D fluid-filled crack propagation problem, a series of tests are conducted to study the fracture propagation phenomena in porous media, including the crack branching phenomenon and the stepwise phenomenon. Effects of pore pressure in

fracture propagation branching are investigated, and the stepwise phenomenon is successfully reproduced. All the examples presented demonstrate the capability of the approach in solving fracture propagation problems in saturated porous media.

Finally, a fully coupled hybrid FEM-PD approach for simulating fracture propagation in saturated porous media is presented. Considering the ability of PD in solving discontinuous problems, the area where cracks can potentially occur is discretised by PD and the crack-free area is discretised by FEM. The solid deformation and fracture propagation are captured by PD and FEM, while the fluid flow in both the reservoir and fracture is simulated with FEM. The whole process is solved in a monolithic way with an implicit scheme. The approach demonstrates the capability of modelling complex dynamic crack propagation via benchmark examples. The branching phenomenon is then investigated with the proposed approach. In conclusion, complex crack patterns are prone to form with faster loading rate, more brittle and impermeable media, and with lower energy release rate.





# Table of contents

<b>List of figures</b>	<b>13</b>
<b>List of tables</b>	<b>19</b>
<b>1 Introduction</b>	<b>21</b>
1.1 Background and motivation . . . . .	21
1.2 Outline of the thesis . . . . .	22
<b>2 literature review</b>	<b>25</b>
2.1 Review of fracture propagation . . . . .	25
2.1.1 Introduction . . . . .	25
2.1.2 Hydraulic fracture physical processes . . . . .	26
2.1.3 Development of fracture propagation models . . . . .	31
2.1.4 Development of numerical methods in fracture propagation . . . . .	36
2.1.5 Summary and Prospective Work . . . . .	45
2.2 Review of crack branching phenomenon . . . . .	46
2.2.1 Introduction . . . . .	46
2.2.2 Experimental Observations of Crack Branching . . . . .	48
2.2.3 Physics of Crack Branching . . . . .	52
2.2.4 Crack models and numerical methods . . . . .	60
2.2.5 Summary and Prospective Work . . . . .	88
2.3 Review of peridynamics . . . . .	89
2.3.1 Introduction . . . . .	89
2.3.2 Theoretical aspects of peridynamics . . . . .	91
2.3.3 Numerical implementation . . . . .	98
2.3.4 Applications of peridynamics . . . . .	104
2.3.5 Summary and Prospective Work . . . . .	109

<b>3</b>	<b>A finite element model for hydraulic fracturing in porous media</b>	<b>111</b>
3.1	Introduction . . . . .	111
3.2	Governing equations . . . . .	115
3.2.1	Deformation of porous formation . . . . .	115
3.2.2	Fluid flow in porous media . . . . .	116
3.2.3	Fluid flow in the fracture . . . . .	117
3.2.4	Fracture propagation criteria . . . . .	117
3.3	Numerical implementation . . . . .	118
3.3.1	Discretisation for the governing equations . . . . .	119
3.3.2	Solution details . . . . .	121
3.4	Model Verification . . . . .	122
3.4.1	Dynamic solution verification . . . . .	122
3.4.2	Cohesive zone verification . . . . .	123
3.4.3	KGD model . . . . .	125
3.5	Discussions . . . . .	127
3.6	Investigation of stepwise fracture propagation . . . . .	129
3.6.1	Young's modulus and Poisson's ratio . . . . .	129
3.6.2	Biot coefficient and Biot modulus . . . . .	131
3.6.3	Porosity and permeability . . . . .	131
3.6.4	Fracture energy . . . . .	132
3.6.5	Viscosity and injection flow rate . . . . .	133
3.7	Conclusions . . . . .	133
<b>4</b>	<b>A peridynamic approach for modelling hydraulic fracturing in porous media</b>	<b>135</b>
4.1	Introduction . . . . .	135
4.2	Mathematical models for hydraulic fracturing . . . . .	139
4.2.1	Governing equations for deformation of porous media . . . . .	139
4.2.2	Governing equations for fluid flow in porous media and in the fracture	141
4.2.3	Propagation criterion . . . . .	143
4.3	Numerical implementation . . . . .	144
4.3.1	Space discretisation . . . . .	144
4.3.2	Time integration . . . . .	144
4.4	Verification of the model . . . . .	145
4.4.1	1D porous media bar . . . . .	145
4.4.2	2D fluid-filled crack problem . . . . .	147
4.5	Application . . . . .	151
4.5.1	Study of crack branching . . . . .	152

---

4.5.2	Study of the stepwise phenomenon . . . . .	156
4.6	Conclusions . . . . .	160
<b>5</b>	<b>A hybrid FEM and PD approach for modelling hydraulic fracturing in porous media</b>	<b>161</b>
5.1	Introduction . . . . .	161
5.2	Mathematical models for hydraulic fracturing . . . . .	164
5.2.1	Deformation of a porous formation . . . . .	165
5.2.2	Fluid flow in porous media and in the fracture . . . . .	166
5.2.3	Failure criterion . . . . .	167
5.3	Numerical implementation . . . . .	169
5.3.1	FEM spatial discretisation of the governing equations . . . . .	169
5.3.2	PD spatial discretisation of the governing equations . . . . .	170
5.3.3	Coupling strategy . . . . .	172
5.3.4	Solution strategy . . . . .	174
5.4	Model verification . . . . .	178
5.4.1	Static problem without failure . . . . .	178
5.4.2	Static problem with failure . . . . .	180
5.4.3	Dynamic problem without failure . . . . .	183
5.4.4	Dynamic problem with failure . . . . .	184
5.4.5	Dynamic problem with failure and pressure field . . . . .	186
5.5	Dynamic branching study . . . . .	191
5.5.1	Effect of flux rate . . . . .	193
5.5.2	Effect of Young's modulus . . . . .	194
5.5.3	Effect of porosity and permeability . . . . .	196
5.5.4	Effect of viscosity . . . . .	196
5.5.5	Effect of energy release rate . . . . .	199
5.6	Conclusions . . . . .	199
<b>6</b>	<b>Conclusions and outlook</b>	<b>201</b>
6.1	Conclusions . . . . .	201
6.2	Outlook . . . . .	205
	<b>References</b>	<b>207</b>



# List of figures

1.1	Leading countries in natural gas and oil production in 2014 and 2017, adopted from [234]. . . . .	21
1.2	A schematic illustration of hydraulic fracturing technology. . . . .	22
2.1	Three fracture loading modes. . . . .	28
2.2	Different forms of the traction-separation law. . . . .	29
2.3	Schematic of (a) PKN model and (b) plane strain assumption on vertical section. . . . .	31
2.4	Schematic of (a) KGD model and (b) plane strain assumption on horizontal section. . . . .	32
2.5	Schematic of the radial model. . . . .	33
2.6	Two types of P3D model: (a) the cell-based model and (b) the lumped elliptical model. . . . .	34
2.7	Planar 3D (PL3D) model based on (a) moving mesh system and (b) fixed mesh system. . . . .	35
2.8	Crack branching photographs from experimental results. . . . .	47
2.9	Yoffe's crack branching model [467]. . . . .	52
2.10	Ravi-Chandar's micro crack model [352]. . . . .	53
2.11	Typical 'mirror', 'mist' and 'hackle' regions are identified in Homalite-100 [351]. . . . .	53

2.12	Three aspects of the evolution of the branching instability as the crack propagates from left to right [385]. (a) The velocity of the crack is a smooth function of time when $v < v_c$ , the crack velocity starts to oscillate when $v \sim v_c$ , the oscillation amplitudes increase when $v > v_c$ . (b) The fracture surface is smooth when $v < v_c$ , small regions of different texture are distributed along the surface when $v \sim v_c$ , these regions coalesce, forming a periodic pattern with wavelength on the order of 1 mm when $v > v_c$ . (c) A single crack is observed when $v < v_c$ , micro-branches appear when $v \sim v_c$ , and increase in length when $v > v_c$ . . . . .	55
2.13	Crack models and numerical methods. . . . .	61
2.14	A schematic illustration of crack branching with remeshing models based on FEM. . . . .	63
2.15	A schematic illustration of crack branching with element deletion models . . . . .	64
2.16	A numerical example of crack branching with element deletion models. [127] . . . . .	64
2.17	A schematic illustration of crack branching with CPMs. . . . .	66
2.18	A 3D example of crack branching with CPMs [328]. . . . .	66
2.19	Traction-separation laws for intrinsic (left) and extrinsic (right) CZMs. . . . .	67
2.20	A 2D example of crack branching with CZM [481]. . . . .	70
2.21	A 3D example of crack branching with CZM [33]. . . . .	70
2.22	A 2D example of crack branching with PFM [112]. . . . .	73
2.23	A 3D example of crack branching with PFMs, showing isosurfaces of phase field at $\phi = 0.3$ [207]. . . . .	73
2.24	A numerical example of crack branching with nonlocal models [446]. . . . .	75
2.25	A numerical example of damage for crack branching with XFEM [35]. . . . .	80
2.26	A schematic illustration of crack branching with BEM. . . . .	81
2.27	A 2D example of crack branching with MMs [489]. . . . .	84
2.28	A 3D example of crack branching with MMs [53]. . . . .	84
2.29	A 2D example of crack branching with PD [49]. . . . .	86
2.30	A 3D example of crack branching with PD [63]. . . . .	86
2.31	A schematic illustration of crack branching with DEM. . . . .	87
2.32	A numerical example of crack branching with DEM [178]. . . . .	87
2.33	Number of citations of [394] per year versus year from 2000 till present. . . . .	90
2.34	Schematic diagram of different PD models. . . . .	91
2.35	Schematic of bond kinematics. . . . .	96
2.36	Schematic of local damage. . . . .	97
2.37	Crack propagation path in a 2D solid media. . . . .	98

---

2.38	Spatial discretisation. . . . .	99
2.39	Graphical descriptions for the $m$ -convergence and $\delta$ -convergence. . . . .	103
3.1	Fracture propagation in porous media. . . . .	115
3.2	Cohesive traction on the fracture surface. . . . .	119
3.3	The traction-separation law. . . . .	119
3.4	A case to illustrate the FE mesh with cohesive elements. . . . .	122
3.5	The basic geometry of 1D column model. . . . .	123
3.6	The pressure history at different nodes. . . . .	124
3.7	Cohesive zone verification. . . . .	124
3.8	The basic geometry of the KGD model. . . . .	125
3.9	The KGD model verification. . . . .	127
3.10	Fracture length versus time. . . . .	128
3.11	Stepwise phenomenon with different Young's moduli. . . . .	130
3.12	The stepwise phenomenon with different Poisson's ratios. . . . .	130
3.13	Stepwise phenomenon with different Biot coefficients. . . . .	131
3.14	Stepwise phenomenon with different Biot moduli. . . . .	131
3.15	Stepwise phenomenon with different permeability. . . . .	132
3.16	Stepwise phenomenon with different porosity. . . . .	132
3.17	Stepwise phenomenon with different fracture energy. . . . .	132
3.18	Stepwise phenomenon with different viscosity. . . . .	133
3.19	Stepwise phenomenon with different injection rate. . . . .	133
4.1	Interaction of a material point with its neighbouring points. . . . .	140
4.2	The flow chart for the simulation process. . . . .	146
4.3	The basic geometry of the poroelastic bar. . . . .	146
4.4	The comparison of analytical and numerical solution along the bar. . . . .	148
4.5	The basic geometry of the fluid-filled crack problem model. . . . .	148
4.6	Horizontal and vertical displacement at $t = 0.01$ s (deformed configuration with a magnification of $10^4$ ). . . . .	150
4.7	Comparison of pressure distribution at $t = 0.01$ s (deformed configuration with a magnification of $10^4$ and pressure unit: Pa). . . . .	150
4.8	Pressure distribution with crack prorogation at different times (deformed configuration with a magnification of $10^4$ and pressure unit: Pa). . . . .	151
4.9	Description of the crack propagation problem. . . . .	153
4.10	Crack pattern under the condition that stress applied on boundaries. . . . .	154
4.11	Description of the crack propagation problem. . . . .	154

4.12	Crack pattern under the condition that stress applied on crack surfaces. . . .	154
4.13	The comparison of crack branching between brittle media and porous media under two loading conditions: (a) crack pattern in brittle media under the first loading condition; (b) crack pattern in brittle media under the second loading condition; (c) crack pattern in porous media under the first loading condition; (d) crack pattern in porous media under the second loading condition; (e) pore pressure distribution in porous media under the first loading condition; (f) pore pressure distribution in porous media under the second loading condition. . . . .	155
4.14	Mechanical loading sample. . . . .	157
4.15	Crack tip advancement under mechanical loading condition. . . . .	158
4.16	Comparison of crack tip advancement under mechanical loading. . . . .	158
4.17	Hydraulic loading sample. . . . .	159
4.18	Crack tip advancement under hydraulic loading condition. . . . .	159
4.19	Comparison of crack tip advancement under hydraulic loading. . . . .	159
5.1	Crack formed by broken bonds ( $\delta = 2\Delta x$ ). . . . .	168
5.2	Illustration of FEM and PD sub-domain. . . . .	173
5.3	Flowchart for solving the static failure problem with the FEM-PD approach. . . . .	175
5.4	Flowchart for solving the dynamic failure problem with the FEM-PD approach. . . . .	177
5.5	Geometry and discretisation of 1D bar model. . . . .	178
5.6	The comparison of displacement under the first loading condition. . . . .	179
5.7	The comparison of displacement under the second loading condition. . . . .	179
5.8	Geometry and discretisation of 2D solid deformation model. . . . .	179
5.9	The relative error of horizontal displacement u. . . . .	180
5.10	The relative error of vertical displacement v. . . . .	180
5.11	Geometry and discretisation of a double cantilever beam crack model. . . . .	181
5.12	Crack development history with time varying from (a) to (d). . . . .	181
5.13	Geometry and discretisation of a diagonally loaded square plate crack model. . . . .	182
5.14	Crack paths with time varying (a) initial crack and (b) final crack. . . . .	182
5.15	Experimental result of a diagonally loaded square plate crack model. . . . .	182
5.16	Geometry and discretisation of a 2D plane stress model subjected to an external load. . . . .	183
5.17	The comparison of horizontal displacement at point A with FEM and PD-FEM. . . . .	184
5.18	The comparison of vertical displacement at point A with FEM and PD-FEM. . . . .	184
5.19	Geometry and discretisation of a three-point bending model. . . . .	185



---

5.20	crack development history with time varying (a) $t = 400 \mu s$ , (b) $t = 500 \mu s$ , (c) $t = 650 \mu s$ and (d) $t = 850 \mu s$ . . . . .	185
5.21	The basic geometry of 1D porous media bar model. . . . .	186
5.22	The comparison of analytical and numerical solution along the bar. . . . .	187
5.23	Geometry and discretisation of a KGD model. . . . .	188
5.24	Verification of the KGD model. . . . .	190
5.25	Pore pressure and fracture pressure distribution with time varying (unit: Pa). . . . .	190
5.26	Geometry and discretisation of fracture interaction model. . . . .	191
5.27	Fracture path evolution with time varying. . . . .	192
5.28	Pore pressure and fracture pressure distribution with time varying (unit: Pa). . . . .	192
5.29	Crack patterns under different flux rate. . . . .	194
5.30	The variation of pressure under different flux rate. . . . .	194
5.31	Crack patterns under different Young's modulus. . . . .	195
5.32	The variation of pressure under different Young's modulus. . . . .	195
5.33	Crack patterns under different porosity. . . . .	197
5.34	Crack patterns under different permeability. . . . .	197
5.35	The variation of pressure under different porosity. . . . .	198
5.36	The variation of pressure under different permeability. . . . .	198
5.37	Crack patterns under different viscosity. . . . .	198
5.38	The variation of pressure under different viscosity. . . . .	198
5.39	Crack patterns under different energy release rate. . . . .	199
5.40	The variation of pressure under different energy release rate. . . . .	200



# List of tables

2.1	Experimental techniques for crack branching. . . . .	51
2.2	Advantages and limitations of different crack models for crack branching. . . . .	62
2.3	Numerical methods for crack branching simulation. . . . .	76
2.4	Algorithm of the numerical implementation for the dynamic PD model with an explicit scheme. . . . .	100
2.5	Algorithm of the numerical implementation for the quasi-static PD model with an implicit scheme. . . . .	102
2.6	PD applications for different problems. . . . .	104
3.1	Material properties for the poroelastic column. . . . .	123
3.2	Rock properties and fluid properties used in KGD simulation . . . . .	126
3.3	Key variables influencing the stepwise phenomenon. . . . .	130
4.1	Material properties for the poroelastic column. . . . .	147
4.2	Material properties for the 2D fluid filled crack problem. . . . .	149
4.3	Material properties for the crack branching problem. . . . .	153
4.4	Material properties for two loading cases. . . . .	157
5.1	Rules for the application of boundary conditions for peridynamics. . . . .	173
5.2	Parameters for 1D bar model. . . . .	178
5.3	Parameters for 2D plane stress square model. . . . .	179
5.4	Parameters for a double cantilever beam crack model. . . . .	180
5.5	Parameters for a diagonally loaded square plate crack model. . . . .	181
5.6	Parameters for 2D plane stress crack model. . . . .	183
5.7	Parameters for a three-point bending model. . . . .	185
5.8	Material properties for the poroelastic column. . . . .	187
5.9	Rock properties, fluid properties and loading conditions used in KGD simulation. . . . .	189
5.10	Comparison between the previous conclusions and our conclusions. . . . .	193



# Chapter 1

## Introduction

### 1.1 Background and motivation

Fracture propagation and hydraulic fracturing have received a great deal of attention due to their importance in engineering applications, including shale gas recovery stimulation of reservoirs, magma-driven dykes, caving and fault reaction in mining etc. [22, 123, 198]. One of applications is shale gas reservoir stimulation, which has attracted extensive investigation due to the vast potential of unconventional oil and gas resources. As an essential technique for the exploitation of low-permeability oil and gas resources, hydraulic fracturing has an essential impact on the economic development of oil and gas. The United States is leading the world in natural gas and oil production by unlocking the enormous oil and natural gas resources in tight-rock formations with hydraulic fracturing [234], see Fig. 1.1.

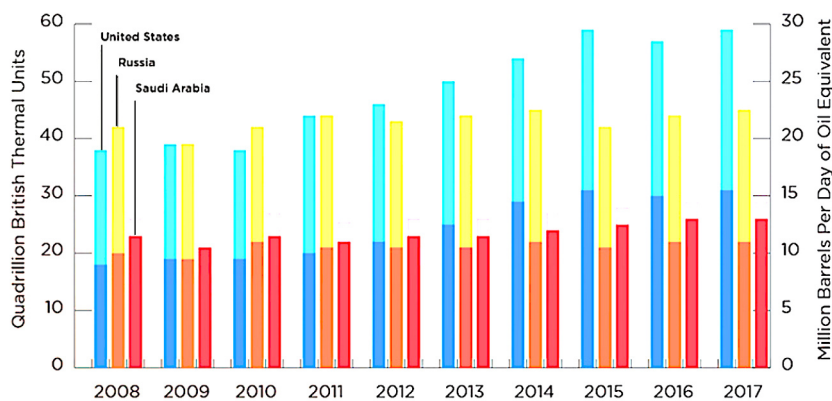


Fig. 1.1 Leading countries in natural gas and oil production in 2014 and 2017, adopted from [234].

In the development and production of oil and gas fields, the main goal of hydraulic fracturing is to use the injection of fluid at high pressure to create fractures in the impermeable formation to provide channels for oil and gas, thereby increasing the extraction of petroleum and natural gas. Fig. 1.2 shows a schematic illustration of hydraulic fracturing technology. According to seismic observations, the interaction between hydraulic fractures with existing natural fractures in shale gas reservoirs can produce complex fracture networks that affect production. However, traditional fracture models are often limited to a fracture with simple geometry. They encounter difficulties, such as crack tip singularity modelling, the need for external propagation criteria and the requirement for defining the crack surfaces in dealing with complex fracture development patterns. Therefore, it is of great importance to develop fracture models for tackling complex fracture patterns, such as the interaction between natural fractures and hydraulic fractures, fracture bifurcation, and fracture networks.

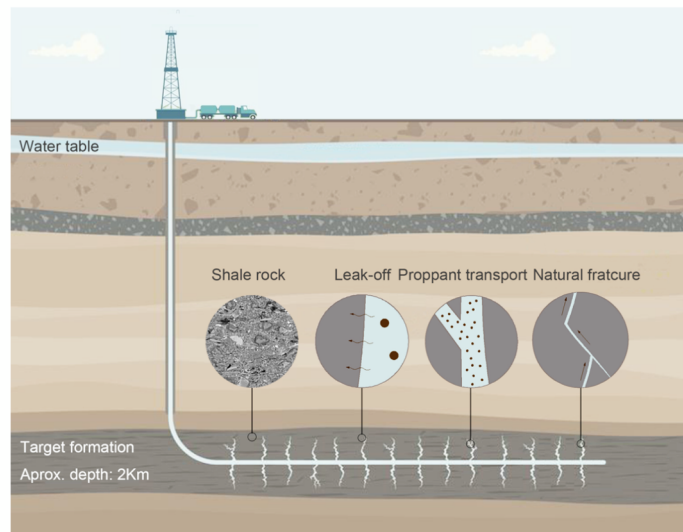


Fig. 1.2 A schematic illustration of hydraulic fracturing technology.

## 1.2 Outline of the thesis

The main focus of this PhD thesis is to develop a fracture propagation model that can simulate more “realistic” fracture propagation processes to explore the specific mechanism behind fractures. The thesis is composed of six chapters, and the following chapters of the thesis are as follows.

In Chapter 2, fracture propagation, crack branching and peridynamics (PD) theory are reviewed. The fracture propagation review provides a review of the fracture propagation

process, fracture models and various numerical methods in fracture propagation. Then, we give a state-of-the-art review of crack branching, including experimental observations, physics, fracture models and associated numerical methods. Key features, advantages and limitations of fracture models and numerical methods are highlighted, and the future research directions of crack branching modelling are discussed. The review of PD provides a summary of the theoretical aspects of PD and related applications of PD in different fields, especially in the area of fracture mechanics. The challenges and new prospects for the development of PD are discussed.

In Chapter 3, a fully implicit, FEM-based fracture propagation model is developed using zero thickness cohesive interface elements. The rock formation is considered a fully saturated porous medium so that both pore pressure and leak-off are taken into consideration. The nonlinearity of the crack tip is addressed with the cohesive zone model. It is demonstrated that the developed model is capable of simulating fracture propagation in porous media accurately with strong coupling between the rock formation and the fracturing fluid. After verification of the model, the stepwise phenomenon, which has been observed in the field and experiments and reported recently in the numerical modelling literature, is investigated with the model.

In Chapter 4, an explicit PD approach for simulating fracture propagation in saturated porous media is developed. A staggered method is adopted to solve the coupled system. The solid deformation equation is solved for the displacement field, and the fluid flow equation is solved for the pressure field with PD. After approach verification via benchmark examples, including a 1D consolidation problem and 2D fluid-filled crack propagation problems, a series of tests related to fracture propagation phenomenon are performed, including the crack branching phenomenon and the stepwise phenomenon in porous media. The effect of pore pressure in fracture branching is investigated, and the stepwise phenomenon is successfully reproduced.

In Chapter 5, a hybrid FEM and PD approach for modelling fracture propagation in porous media is presented, which combines the advantages of both the FEM and the PD method. Considering the ability of PD in solving discontinuous problems, the area where cracks can potentially occur is discretised by PD and the crack-free area is discretised by FEM. The solid deformation and fracture propagation are captured by PD and FEM, while the fluid flow in both the reservoir and fracture is simulated with FEM. The whole process is solved in a monolithic way with an implicit scheme. The approach presented demonstrates the capability of modelling complex dynamic crack propagation via benchmark examples, including a 1D consolidation problem, a 2D KGD problem [151, 215] and a fracture interaction problem.

The effects of different factors on the branching phenomenon were investigated using the approach.

Finally, in Chapter 6, the overall conclusions and prospective work of the thesis are presented.



# Chapter 2

## literature review

### 2.1 Review of fracture propagation

#### 2.1.1 Introduction

Fracture propagation has attracted a tremendous amount of attention from researchers in the oil and gas industry and the department of mechanics [231]. Numerous fracturing models have been developed to improve the fracturing treatment design or understand some specific mechanisms such as screen-out and near-wellbore tortuosity. The 1950-1980 period saw the development of a series of classic hydraulic fracturing models, including the KGD model, the PKN model, the pseudo 3D (P3D) model, and the planar 3D (PL3D) model. Until now, the P3D model and PL3D model are still playing vital roles in commonly used commercial software for hydraulic fracturing design. With the increasing attention on fracture propagation in recent decades, diverse numerical methods, including the finite element method (FEM), extended finite element method (XFEM), boundary element method (BEM), phase field method (PFM), and discrete element method (DEM), have also been applied.

The purpose of this section is to provide an extensive review of fracture propagation modelling in the application of reservoir stimulation on three aspects: (1) physical processes in hydraulic fracturing; (2) the development of fracture propagation models; (3) the development of various numerical methods in fracture propagation. The rest of the section is organised as follows. The physical processes involved in hydraulic fracturing is introduced in § 2.1.2. The historical development of fracture propagation models over the past decades is reviewed in § 2.1.3. In § 2.1.4, the development of diverse numerical methods in fracture propagation is highlighted. § 2.1.5 provides a summary of work in the current stage and points out the challenges and necessary work in the future.

### 2.1.2 Hydraulic fracture physical processes

Hydraulic fracturing can be defined as the process by which a fracture is created due to hydraulic loading applied by fluid inside the fracture [1]. It is a complex process because the structure field, stress field and pressure field keep changing during fracture propagation due to the strong coupling between the solid and fluid. The physical processes involved in hydraulic fracturing include deformation of rocks, the fluid flow within the fracture, fracture propagation and the poroelastic effect.

#### Deformation of rocks

The deformation of rocks in hydraulic fracturing is mainly caused by the pressure of the fluid in the fracture. The fluid pressure as well as the in-situ stress can be applied as boundary conditions when solving the deformation equation. The linear elastic theory is commonly used for the constitutive relation of the solid rock [1, 231], and the elastoplastic theory [306] and damage theory [391] are also adopted.

In a 2D hydraulic fracturing model in linear elastic homogeneous rock materials, fluid is injected into the fracture and the fluid pressure  $p_f$  acting on the fracture surface causes deformation. The linear elastic theory is adopted to establish the relationship between fracture width  $w$  and fluid pressure  $p_f$ , and the constitutive model is expressed as:

$$\boldsymbol{\sigma} = \mathbf{C} : \boldsymbol{\varepsilon} \quad (2.1)$$

where  $\boldsymbol{\sigma}$ ,  $\boldsymbol{\varepsilon}$  and  $\mathbf{C}$  denote the stress, strain and elastic tensor determined by Poisson's ratio  $\nu$  and Young's modulus  $E$  respectively.

The equilibrium equation is expressed as:

$$\nabla \cdot \boldsymbol{\sigma} + \rho \mathbf{g} - \rho \ddot{\mathbf{u}} = 0 \quad (2.2)$$

where  $\boldsymbol{\sigma}$  is the Cauchy stress,  $\mathbf{g}$  the gravity acceleration, and  $\ddot{\mathbf{u}}$  the acceleration of the solid phase. The fracture width  $w$  is computed by the displacement difference between the upper and lower surfaces of the fracture.

#### Fluid flow in the fracture

The fluid flow in the fracture is usually described by fluid flow lubrication theory, which applies if one dimension of the space occupied by the fluid is much smaller than the other dimensions. In hydraulic fracturing, the fluid in the fracture width direction is much smaller than the directions of height and length. Poiseuille's law [30] is adopted to describe the

relationship between fluid flow velocity, fracture width and pressure spatial gradient:

$$q = -\frac{w^3}{12\mu} \frac{\partial p_f}{\partial x} \quad (2.3)$$

where  $q$  is the flow rate,  $w$  the fracture width,  $\mu$  the viscosity of the fracturing fluid,  $p_f$  the fluid pressure and  $x$  the local coordinate.

The continuity equation with leak-off considered is expressed as:

$$\frac{\partial w}{\partial t} + \frac{\partial q}{\partial x} + q_l = 0 \quad (2.4)$$

where  $q_l$  is the leak-off flow rate.

If the rock is impermeable, the leak-off term can be ignored. By substituting fluid flow equation Eq. (2.3) into the fluid continuity equation Eq. (2.4), the global continuity equation of the fluid flow in the fracture can be obtained:

$$\frac{\partial w}{\partial t} - \frac{\partial}{\partial x} \left( \frac{w^3}{12\mu} \frac{\partial p}{\partial x} \right) = 0 \quad (2.5)$$

The analysis can be conducted based on the assumption that there is no fluid lag. Then the fluid is completely filled with fractures, and the fracture tip and the fluid front are perfectly aligned [373, 150]. It can also be based on the assumption that there exists a fluid lag, and the fluid front is lagging behind the fracture tip [149, 193].

### Fracture propagation

Fluid pressure in the fracture causes deformation of rocks, resulting in the initiation and propagation of the fracture. Various theories have been used to predict fracture propagation, among which the linear elastic fracture mechanics (LEFM) theory and the cohesive zone model (CZM) are commonly used. The CZM considers the nonlinear effect near the fracture tip while LEFM doesn't.

In LEFM, the criterion for fracture propagation is usually given either by the conventional energy approach or by the stress intensity approach [390]. In the energy approach, the energy release rate  $G$  defined as the energy dissipated during the fracture per unit process of a newly created fracture surface area [310] is used. When the energy release rate is greater than a critical energy release rate, the fracture propagates:

$$G > G_c \quad (2.6)$$

where  $G_c$  is the critical energy release rate related to material properties.

In the stress intensity approach, the stress intensity factor is employed for quantifying the conditions of stress at the crack tip [95]. A fracture propagates when the stress intensity factor  $K$  at the tip exceeds the fracture toughness  $K_{IC}$  (critical stress intensity factor):

$$K > K_{IC} \quad (2.7)$$

In linear elastic materials, the energy release rate can be computed from stress intensity factors directly.

$$G = \frac{K_I^2}{E'} + \frac{K_{II}^2}{E'} + \frac{K_{III}^2}{2\mu_s} \quad (2.8)$$

where  $\mu_s$  is the shear modulus,  $E'$  is related to Young's modulus  $E$  and Poisson's ratio  $\nu$ , which can be expressed as:

$$E' = \begin{cases} E, & \text{(plane stress)} \\ \frac{E}{1-\nu^2}, & \text{(plane strain)} \end{cases} \quad (2.9)$$

$K_I$ ,  $K_{II}$ , and  $K_{III}$  are the stress intensity factors under loading mode Mode-I, Mode-II, and Mode-III, respectively. The loading mode Mode-I, Mode-II, and Mode-III represent the opening, in-plane sliding and out-of-plane shearing modes for fractures, respectively, see Fig. 2.1.

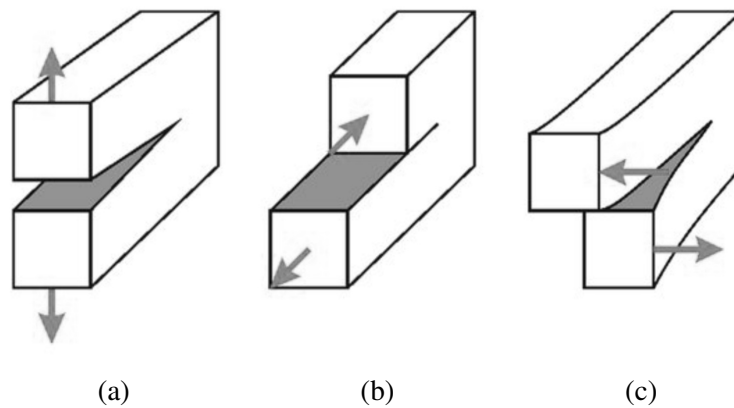


Fig. 2.1 Three fracture loading modes.

When considering the nonlinear effect zone ahead of the fracture tip, the LFEM can not be applied, and the CZM is usually adopted. The CZM assumes a process zone ahead of

the real fracture tip. In the process zone, the crack propagation is directly related to the parameters in the cohesive traction-separation law. The traction-separation law defines the relationship between the crack width (distance between the crack surfaces) and the cohesive traction in the process zone. The crack surfaces begin to separate (initiate) when the cohesive strength is reached. When the separation reaches a critical value and the traction decreases to zero, total failure occurs (the crack surfaces fully separate).

There are many types of traction-separation laws. For example, the exponential form [27], the polynomial form [275], the bi-linear form [155] and the linear form [303], as shown in Fig.2.2. The absorbed energy  $G$  during the fracture process can be obtained by calculating the area under the traction-separation curve. If the Griffith energy balance is applied, then the absorbed energy  $G$  is equal to the critical fracture energy  $G_c$ . Following this rule, the parameters (the cohesive strength and maximum fracture opening) in the cohesive traction-separation law can be set.

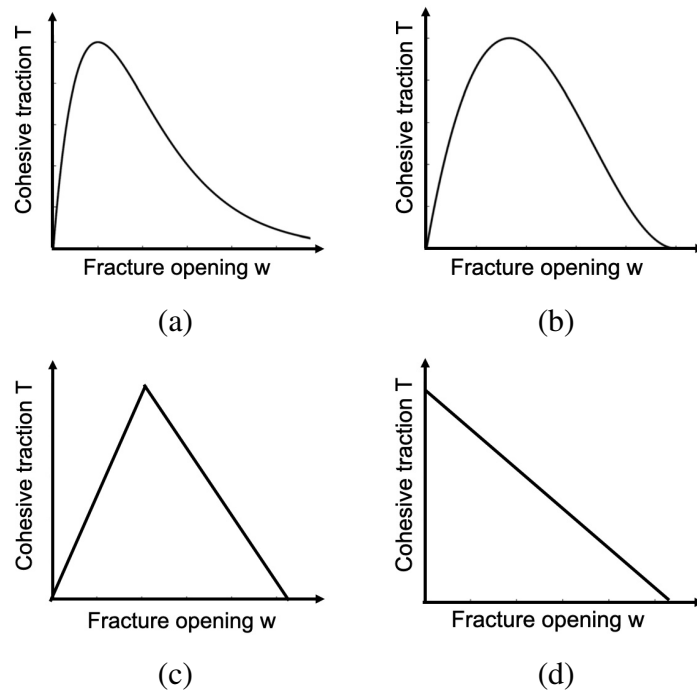


Fig. 2.2 Different forms of the traction-separation law.

### Poroelastic effect

The porous medium is composed of a solid skeleton containing pores and fluid/gas filling in the pores. Because of the special structure, the mechanical behaviour of porous media belongs to multifield problems. In porous media, the deformation of a solid skeleton affects the flow

of the pore fluid. Likewise, the flow of the pore fluid alters the solid skeleton deformation. Therefore, the deformation of the porous medium is caused by both the effective stress and the fluid pressure. To make the equilibrium equation Eq. (2.2) in § 2.1.2 applicable to porous media, the total stress tensor  $\boldsymbol{\sigma}$  is represented with the effective stress tensor  $\boldsymbol{\sigma}'$  and pore pressure  $p$  [421]:

$$\sigma_{ij} = \sigma'_{ij} - I_{ij}\alpha p \quad (2.10)$$

where  $I_{ij}$  is the identity tensor, and  $\alpha$  is the Biot coefficient. The Biot coefficient  $\alpha$  denotes the ratio of the fluid volume gained (or lost) in a material element to the volume change of that element, and it equals 1 for incompressible solids. Note that Eq. (2.10) corresponds to the sign convention that compressive pore pressure is positive which is widely used in soil mechanics.

The continuity equation for the fluid flow in porous media is [51]:

$$\frac{\partial \zeta}{\partial t} + \nabla \cdot \mathbf{q} = 0 \quad (2.11)$$

where  $\zeta$  is the variation of fluid volume per unit volume of the porous material, and  $\mathbf{q}$  denotes the flux. Described by Darcy's law, the flux  $\mathbf{q}$  can be expressed as:

$$\mathbf{q} = -\frac{\mathbf{k}_w}{\mu} \cdot \nabla p \quad (2.12)$$

where  $\mu$  is the fluid viscosity, and  $\mathbf{k}_w$  the permeability tensor.

The constitutive equation for the pore fluid is

$$p = Q(\zeta - \alpha \varepsilon_b) \quad (2.13)$$

where  $Q$  is the Biot modulus, and  $\varepsilon_b$  the bulk volumetric strain.

The above equations can be combined by substitution and elimination as:

$$\alpha \nabla \cdot \dot{\mathbf{u}} + \frac{1}{Q} \dot{p} + \nabla \cdot \mathbf{q} = 0 \quad (2.14)$$

where  $\dot{\mathbf{u}}$  denotes the velocity of the solid phase and  $\frac{1}{Q}$  the compressibility coefficient. The first term can be seen as a source term driving pressure distribution and the flux. The compressibility coefficient  $\frac{1}{Q}$  is defined as:

$$\frac{1}{Q} = \frac{\alpha - n}{K_s} + \frac{n}{K_w} \quad (2.15)$$

where  $n$  is the porosity,  $K_s$  and  $K_w$  are the bulk module of the solid and fluid phases, respectively.

### 2.1.3 Development of fracture propagation models

The accuracy of the fracture propagation model is essential to the fracture propagation simulation and production. An excellent fracture propagation model can provide a deeper understanding of fracture propagation mechanisms. In recent decades, a variety of fracture propagation computational models has been developed. In this subsection, several classic hydraulic fracturing models, including the PKN model, the KGD model, the radial model, the Pseudo 3D model and the Planar 3D model, are reviewed.

#### PKN model

The pioneering work for the PKN model can be found in [313], where the so-called PK model was developed. Then, the PK model was extended to the PKN model in [288] by including the effects of storage and leak-off. It is a classic hydraulic fracturing model with a long fracturing length, limited but constant fracture height and small fracture width, see Fig. 2.3.

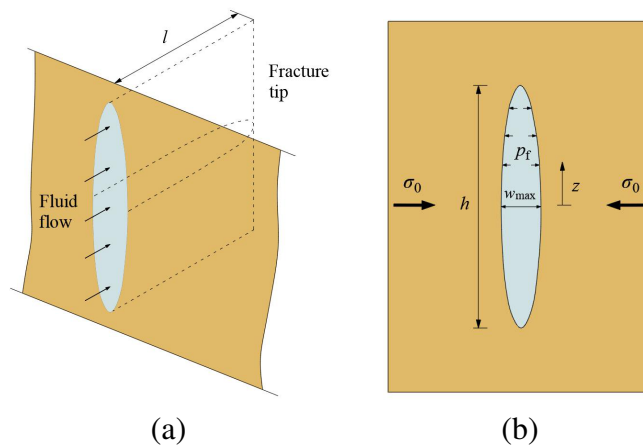


Fig. 2.3 Schematic of (a) PKN model and (b) plane strain assumption on vertical section.

To simplify the problem, some assumptions are made: (1) the rock is a uniform linear elastic medium; (2) the fracture height is assumed to be constant; (3) the fluid is Newtonian fluid, which flows along the direction of the fracture length and is one-dimensional flow; (4) the net pressure is zero at the tip; (5) the fracture length is long compared to the fracture width and fracture height. The width at any vertical section is restricted to be elliptical and is

computed based on a plane strain assumption [288]:

$$w = \frac{(1 - \nu)}{G} \sqrt{(h^2 - 4z^2)} (p_f - \sigma_0) \quad (2.16)$$

where  $G$  is the shear modulus,  $\nu$  the Poisson's ratio,  $h$  the fracture height,  $p_f$  the fluid pressure,  $\sigma_0$  the confining stress, and  $p_f - \sigma_0$  the net fluid pressure. The net fluid pressure is constant in the  $z$ -direction but is different along fracture propagation direction.

In [404], the PKN model was improved by considering the relationship between fracture height and fluid pressure, which extends its application to layered reservoirs. In [110], the PKN model was developed by considering the poroelastic effect. Later in [428], the model extended its application for non-Newtonian fluid.

### KGD model

The KGD model was first developed in [215] and [151]. It is a classic hydraulic fracturing model under plane strain assumption where the fracture width is constant in the direction of the fracture height, as shown in Fig. 2.4.

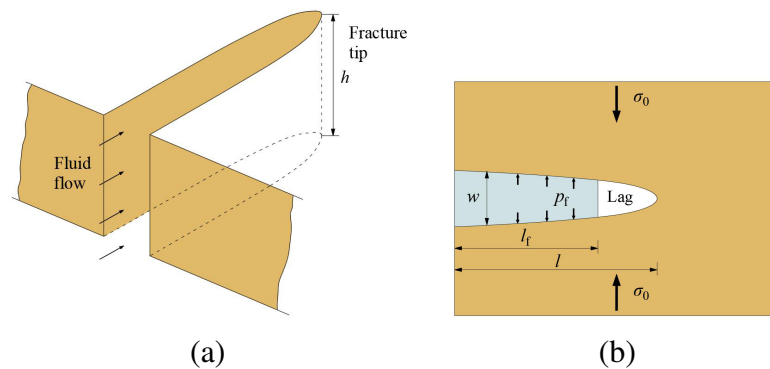


Fig. 2.4 Schematic of (a) KGD model and (b) plane strain assumption on horizontal section.

Similar to the PKN model, the KGD model also has the following assumptions: (1) the rock is a uniform linear elastic medium; (2) the height of the fracture is assumed to be constant; (3) the fluid is Newtonian fluid, which flows along the direction of the fracture length and is one-dimensional flow; (4) the net pressure is zero at the tip. The difference between the KGD model and the PKN model lies in that: (1) the vertical section is a rectangle for the KGD model, while in the PKN model, the vertical section is an ellipse. Thus, the fracture width remains constant along the direction of the fracture height in the KGD model; (2) in the KGD model, the fracture pressure decreases with the increase of the fracture length while in the PKN model, the fracture pressure increases with the increase of the fracture



length [86]; (3) in the KGD model, the plane strain assumption is on horizontal section while in the PKN model, the plane strain assumption is on vertical section. Therefore, the KGD model is more applicable for fractures in the early stage with a small fracture length, while the PKN model is applicable for fracture in the middle or late stage with a considerable fracture length. This thesis uses KGD model for verification with the following reason. The thesis focuses on the study of fracture propagation mechanisms. The KGD plane strain assumption is on horizontal section. Poroelastic effect and cohesive zone can be straightforwardly added to the model. However, in PKN model, the plane strain assumption is on vertical section and the fracture propagates out of the plane with a constant height. Additional assumptions are required to model the fracture propagation, which makes the whole process complicated. This is not consistent with our goal of studying two-dimensional fracture propagation mechanisms without making more assumptions.

The relationship between fracture width and net pressure  $p_n$  can be expressed as [148]:

$$w = \frac{1}{E'} \int_0^l G\left(\frac{x}{l}, \frac{s}{l}\right) (p_f - \sigma_0) ds \quad (2.17)$$

where  $p_f - \sigma_0$  is the net pressure  $p_n$ ,  $E' = E/(1 - \nu^2)$  the plane strain modulus,  $l$  half length of the fracture, and  $G$  the integral kernel.

The KGD model was further extended in [102], where it can be applied to the non-Newtonian fluid. Moreover, the fracture toughness was introduced into the model to solve the problem of crack tip propagation in [317]. Later, the KGD model was further developed in [69] by making some corrections in the governing equations or solution methods to make the model more rigorous.

### Radial model

The radial model was proposed in [151]. When the minimum principal stress is applied, the formation tends to form a penny-shaped hydraulic fracture perpendicular to the direction of the wellbore, as shown in Fig. 2.5.

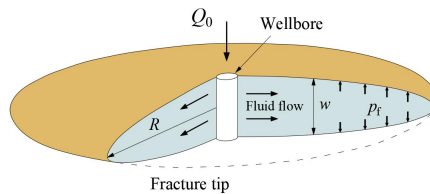


Fig. 2.5 Schematic of the radial model.

The elasticity equation relating the fracture width to the fluid-pressure can be expressed as [373]:

$$w = \frac{8R}{\pi E'} \int_{r/R}^1 \frac{\xi}{\sqrt{\xi^2 - (r/R)^2}} \int_0^1 \frac{xp}{\sqrt{1-x^2}} dx d\xi \quad (2.18)$$

where  $x$  is the position,  $R$  the radius of the model, and  $\xi$  the ratio of the position  $r$  to the radius  $R$ .

The development of the radial model and its solutions can be found in a series of studies [8, 373, 118]. In [8], explicit time-dependent solutions for the crack geometry and fluid pressure associated with Newtonian and non-Newtonian fracturing fluids were derived. In [373], asymptotic solutions of the propagation of a penny-shaped hydraulic fracture in an impermeable elastic rock were presented. In [118], the solution of the propagation of a penny-shaped hydraulic fracture was further developed by considering the effect of fracture toughness, fluid viscosity and leak-off.

### Pseudo 3D (P3D) model

The Pseudo 3D (P3D) model was developed on the PKN model [90]. Compared with the 2D PKN model, it removes the limitations of the unchanged fracture height. The P3D model can be roughly divided into two types [231]: (1) the cell-based models, where the fracture has been divided into several self-similar cells along horizontal direction [146, 404]; (2) the lumped elliptical model, where a fracture can be assumed as consisted of two half ellipses joined at their centres in the fracture propagation direction [90], as shown in Fig 2.6.

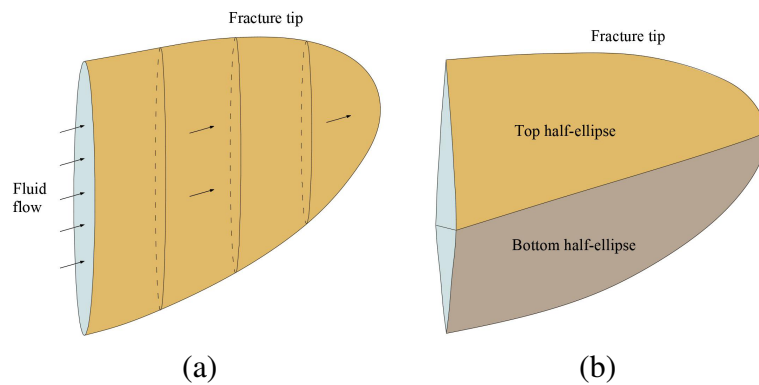


Fig. 2.6 Two types of P3D model: (a) the cell-based model and (b) the lumped elliptical model.

Compared with 2D models, the P3D model can predict fracture propagation in multiple layers and the evolution of fracture width, height along the direction of fracture length. In [302], a 3D model was developed to investigate the effect of variations of stress and

rock properties on fracture height. In addition, the LEFM theory was introduced as the fracture propagation criterion on each vertical plane. In [339], a P3D model allowing fracture initiation in multiple layers with different mechanical and fluid flow properties was developed to study the effects of mechanical and fluid flow properties on fracture dimension and proppant transport. In [2], the model for a hydraulic fracture with equilibrium height growth across two symmetric stress barriers was analysed, and the scaling of the controlling equations shows that the solution highly depends on the fracture toughness and leak-off coefficient. In [343], a detailed discussion about the development of 2D models (the PKN model and the KGD model) and the P3D model was given and a P3D-C model incorporating the Carter solution of material balance was proposed, which proves to be a promising tool for hydraulic fracture design optimisation.

### Planar 3D (PL3D) model

The P3D model cannot simulate fracturing with arbitrary shapes. Therefore, planar 3D (PL3D) models have been developed [7, 406]. PL3D models simulating the coupled fracture propagation and fluid flow can be based on moving triangular mesh or fixed rectangular mesh [231], as shown in Fig. 2.7.

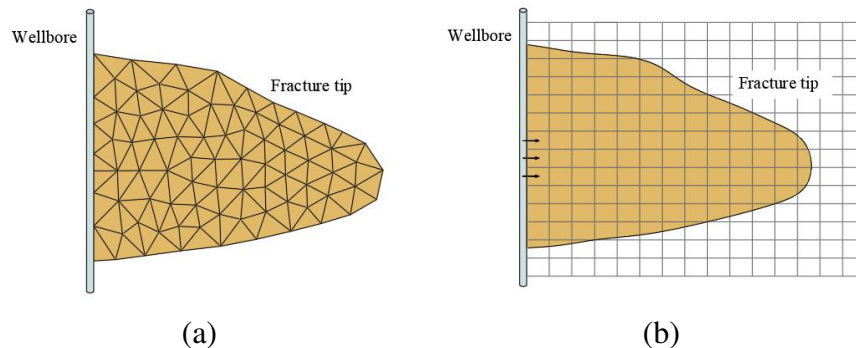


Fig. 2.7 Planar 3D (PL3D) model based on (a) moving mesh system and (b) fixed mesh system.

The first PL3D model based on moving mesh was developed in [91] with the assumption that the fracture driven by a fluid propagates in an infinite, homogeneous, isotropic, elastic solid rock with in-situ stresses that vary with depth. Later, in [92], multiple fluids, proppant transport, and thermal effects were considered in the improved model. In [93], the model was further developed by considering the poroelastic effects in the rock. Later, the leak-off effect and proppant transport have been considered and been added into the model [222, 9, 301]. The first PL3D model based on a fixed mesh was developed in [29]. Later, in [393], a

more flexible PL3D model based on a displacement discontinuity method was presented, in which the mesh composed of rectangular elements is fixed, and a special fracture tip tracking strategy that allows a tip element to be partially fractured is utilised. The model proves to be able to model complex planar fracture propagation problems in multi-layer elasticity materials. In [1], the fixed mesh PL3D model was further developed by adding the effects of leak-off and proppant transport and employing the volume of fluid (VOF) method to track the crack tip. Compared with a moving mesh, a fixed mesh avoids interpolation errors and remeshing difficulties. However, the fracture tip in a fixed mesh approach can not be captured as accurately as in the moving mesh approach.

Compared with 2D models and the P3D model, the flexibility of the PL3D model is better. The PL3D model can be applied to more complex situations, such as the case where the layer confinement stress varies non-monotonously with depth[1]. In addition, since more factors influencing hydraulic fracturing are considered, the accuracy of the PL3D model is also better than the 2D models and the P3D model. However, the computational cost is also increased.

Instead of solving the deformation field based on domain discretisation and the constitutive model, these models solve the elastic equation relating the fracture width to fluid pressure directly. Both the numerical computation cost and the mesh updating process are reduced in this case. For example, 2D or even 3D fracture geometry is solved in the PKN, KGD and radial model using a 1D mesh, while 3D geometry of hydraulic fracture is solved on a 2D mesh in the PL3D model. 1D fluid flow is assumed in the PKN and the P3D model while 2D fluid flow is for the PL3D model. The solution method can be analytical or numerical. One limitation of these models is that the fracture is restricted to propagate along a straight line or planar plane. In addition, the effect of natural fractures is ignored to simulate hydraulic fracturing in more complex scenarios in terms of fracture mode and material properties. Diverse numerical methods have been applied to develop more advanced hydraulic fracturing models, which are discussed in detail in § 2.1.4.

#### **2.1.4 Development of numerical methods in fracture propagation**

Though a variety of fracture propagation models have been developed to investigate the fracture propagation process, the study of fracture propagation still faces many challenges. For example, the existing fracture models can not model fracture propagation in complex patterns or geological conditions. Therefore, the numerical method becomes another essential tool for the study of fracture propagation. Various numerical methods have been developed and applied to fracture propagation, and the corresponding physical mechanisms are investigated.

In this subsection, the development of various numerical methods in fracture propagation has been reviewed. The commonly used methods for fracture propagation include the finite element method (FEM), the extended finite element method (XFEM), the boundary element method (BEM), the phase-field method (PFM) and the discrete element method (DEM). We note that this subsection focuses more on the development and application of the methods. A further detailed description of the essential characteristics of these methods and implementation procedures can be found in § 2.2.4. Finally, the advantages and shortcomings of these numerical methods are discussed, and the most promising methods are highlighted.

### **The finite element method (FEM)**

As a robust and flexible approach, the finite element method (FEM) has been applied to a wide range of hydraulic fracturing problems [77]. In [301], an adaptive finite element model was developed for describing the fracture propagation with proppant transport. The LEFM is utilised as a fracture propagation criterion, and the proppant distribution is obtained by solving governing equations of fluid and elasticity. In [193], a finite-element-based algorithm was proposed to simulate hydraulic fractures in an impermeable elastic medium, and the fracture tip and the fluid front are tracked separately. Based on this, a 2D hydraulic fracturing model was developed in [77] to perform comprehensive parametric studies on the evolution of fluid lag. The geology conditions in the above models are relatively simple and the poroelastic effect is not considered. When considering the conditions where “real” hydraulic fracturing occurs, pore pressure in the formation and the nonlinear behaviour (plasticity) in the front of a pre-existent crack needs to be added [32].

By taking into account the poroelastic effects, the biot theory [39] is introduced to describe the interaction between the porous skeleton deformation and the pore pressure diffusion in the porous medium. Moreover, the cohesive zone model with cohesive interface elements is introduced to represent nonlinear processes in the vicinity of the crack tip. The first successful application of cohesive elements in 2D hydraulic fracturing in porous media can be traced back to the early 1990s [51], where the FEM is used for rock deformation, and a finite difference method is used for fluid flow along the fracture. Zero-thickness interface elements are employed to represent the nonlinear behaviour of the crack tip, which makes the fracture length a natural outcome of the solution of the equation system. In [305], the influence of plasticity in hydraulic fracturing was investigated with a combined finite difference–finite element model, which is developed with the lubrication theory for fluid flow and the Mohr-Coulomb flow theory of plasticity for deformation. Introducing the transversal conductivity for double-node zero-thickness elements, a fully coupled FEM-based hydro-mechanical model established via staggered and fully coupled approaches was presented in [383]. In

terms of the strong coupling between the deformation and fluid flow within the fracture, the coupled hydro-mechanical fracture behaviour in 2D dimensions was modelled in [162] with triple-node zero-thickness interface elements considering the anisotropic description of the flow propagation in the fracture. With the double-nodded interface elements and an adaptive mesh refinement approach, a quasi-static hydraulic fracturing model in porous media was established in [381]. Later, the model was developed to 3D dimension in [379]. As the crack tip advances, the mesh updates continuously by an efficient mesh generator based on Delaunay tessellation. With the same strategy, the hydraulic fracturing model in porous media was extended from quasi-static conditions to dynamic conditions in [380, 213]. The interaction between crack tip velocity and fluid flow velocity in the fracture was highlighted, and the effects of inertia on hydraulic fracturing were investigated. In [278], a pre-processing tool to insert cohesive interface elements into the finite element mesh was developed to simulate the hydraulic fracturing process. Details on the computational aspects of hydraulic fracture modelling such as mesh generation, execution time, convergence and numerical integration issues are discussed.

Since the implementation of cohesive zone elements is relatively straightforward in commercial or open-source FE packages, software Abaqus and codeAster, are also employed for investigating the hydraulic fracturing process in porous media. A model was developed with Abaqus in [370] to simulate the fluid-driven fracture propagation under plane strain conditions. Six-node cohesive elements are employed to model the fluid flow in the fracture, and the effects of the cohesive zone on fluid-driven fracture are investigated. Later, with the same model, the main parameters that affect the hydraulic fracture propagation are investigated in a poroelastic medium [371], and in a poroelasto-plastic medium [372]. In [82], a fluid pressure cohesive zone finite element model was developed with Abaqus to investigate the effect of cohesive material parameters and fluid viscosity on the hydraulic fracture behaviour. In [70], a zero-thick cohesive element was proposed and implemented into the hydraulic fracturing model with the open-source software Code Aster. With the model, the influence of the fluid viscosity and rock formation permeability on hydraulic fracturing is investigated.

Although the adaptive FEM has the advantage of being capable of capturing the crack tip front accurately, the mesh needs to be dense enough to avoid the stress singularity at the crack tip [70]. Another shortcoming of the adaptive FEM is that it is not applicable in modelling complex fracture patterns or geometry, especially in 3D. The cohesive zone model is introduced to overcome the shortcomings. The advantages of the cohesive zone model are multifold: (1) the cohesive zone describes the fracture propagation behaviour more realistically and avoids the singularity at the crack tip; (2) with straightforward implementation into

the finite element mesh, it avoids remeshing problems; (3) it is capable of modelling complex crack patterns since the crack propagation can be a natural outcome of the solution [199]; (4) the fluid diffusion in the porous medium and its coupled mechanical response can be better described with ad-hoc interface elements [70]. In summary, both the adaptive FEM and the cohesive zone model are robust and stable in simulating hydraulic fracturing. Compared with the adaptive FEM, the cohesive zone model is more suitable for modelling large-scale and complex hydraulic fracturing problems.

### **The extended finite element method (XFEM)**

The extended finite element method (XFEM) was developed in [34, 264]. The core idea of XFEM is to use the enriched shape function with discontinuous features to represent the discontinuity in the element [488], which allows the crack to propagate on any surface within one element instead of along element boundaries. It overcomes the remeshing and mesh dependency issues met in FEM and CZM.

The earliest work about the application of XFEM in hydraulic fracturing could be tracked to [223] and [358]. In [223], an XFEM hydraulic fracturing model was developed by introducing special tip functions encapsulating tip asymptotics encountered in hydraulic fractures. In [358], the governing equations of XFEM for hydraulic fracture modelling were derived based on the virtual work principle and considering water pressure on the crack surface. The accuracy of the presented XFEM hydraulic fracturing model is verified, and the advantages of XFEM in modelling hydraulic fracturing are given.

The LEFM is adopted as propagation criterion in [157, 158, 99, 107] to model hydraulic fracturing in an elastic medium with XFEM. In [157], two novel XFEM-based schemes were proposed to couple the equations governing hydraulic fracture propagation, which proves the capability of coping with various tip behaviours and propagation regimes encountered in hydraulic fracturing modelling. In [158], a novel implicit level set algorithm was employed to resolve the singular free boundary problem for hydraulic fracture propagation without a fluid lag. In [99], with an energy-based criterion, an XFEM complex hydraulic fracturing model was established to investigate the influence of in-situ stresses, rock toughness, natural-fracture cement strength and natural fractures orientations on the hydraulic fracturing patterns. The model was later extended from 2D to 3D in [107] to investigate the interactions between a hydraulic fracture and a pre-existent fracture. It is found that the energy release rate has an important effect on the hydraulic fracturing propagation process.

Instead of using LEFM, the CZM implemented with interface elements is employed in [440, 267, 214, 432]. In [440], lower-dimensional interface elements were developed to represent discontinuities, and local enrichment approximations for a discontinuous displacement

was adopted. With the modified XFEM, the method demonstrates its ability in dealing with multiple fractures and hydraulic fracturing problems. A fully coupled numerical model was developed in [267] combining both CZM and XFEM. Later, the model was extended to model the dynamic mixed-mode crack propagation in saturated porous media in [214], in which two alternative computational algorithms, namely the partitioned solution algorithm and the time-dependent constant pressure algorithm, are employed to compute the forces exerted on the fracture surfaces by fluid pressure. Instead of simulating the fluid inside and outside the fracture separately, a novel hydraulic fracturing model based on XFEM was presented in [435], where the fluid is simulated in a unified framework by considering the fracture as a special porous medium. Under the unified framework, the model demonstrates its ability in modelling the fluid flow in the complex fracture network. In [465], a novel XFEM method was proposed to simulate the nonlinear hydro-mechanical process in crossing fractures with a new junction enrichment function for the discontinuous of pressure across the T-shaped fracture. With the method, the fracture interaction phenomenon is investigated. In [311], a 3D numerical model of hydraulic fracture propagation was developed, which enables a full coupling between fluid and solid rocks based on an improved XFEM enrichment technique. The ability of the model in simulating complex non-planar fracture geometries and multiple fracture intersections are demonstrated.

In summary, compared with FEM, XFEM circumvents the difficulties of remeshing at each calculation time step and allows to simulate hydraulic fractures in complex geometries. However, when dealing with multiple fractures or fracture intersections, special enrichment needs to be developed to account for the discontinuous at junctions and the computational cost increases.

### **The boundary element method (BEM)**

The BEM is designed for solving boundary value or initial value problems and formulated in terms of boundary integral equations [243]. Compared with FEM, BEM has the following advantages: (1) discretisation is only required at boundaries of the domain, which reduces the computational cost; (2) the commonly used fracture propagation criterion, namely the stress intensity factor in LEFM, can be easily computed with BEM.

As a kind of BEM formulation designed for solving the issue of the coincidence of crack nodes [265], the displacement discontinuity method (DDM) is the most commonly used formulation of BEM in hydraulic fracturing. In [116], a general DDM was presented to deal with the problems with curved and straight-line cracks. With this method, crack reorientation in hydraulic fracturing was simulated, and the effect of fault on crack reorientation was investigated. A 2D DDM-based model that can separately track the crack tip and the fluid



front was developed. Later, the model was employed to study the effects of frictional behaviour and re-initiation from flaws on fracture growth in [478]. In [479], an investigation of fluid-driven fracture growth in naturally fractured reservoirs with simple network geometries based on DDM was conducted. In [290] and [291], a numerical model based on DDM has been developed to investigate the mechanical interaction between the hydraulic fracture and preexisting natural fractures. Though hundreds of fracture tips can be simulated simultaneously, the pressure distribution resulting from the fluid flow along the fracture network has not been solved and a simplified constant pressure boundary condition has been used for all fracture segments. A novel fracture-propagation model that does not require constant pressure boundary condition was developed in [452], where multiple-hydraulic-fracture propagation from a horizontal wellbore is modelled. The DDM is used for deformation, while the lubrication theory is used for fluid flow. The physics-based complex fracture network is then imported into reservoir models to conduct production. Later, the model was extended to 3D in [453] to investigate the effects of perforation-cluster spacing, differential stress, and the geometry of various natural fractures on fracture complexity.

Several fully 3D models of hydraulic fracturing have been developed with BEM [72, 430, 365, 462]. As one of the most commonly used models, HYFRANC3D, based on the 3D fracture analysis code (FRANC3D) and developed by the Cornell fracture group [72], is capable of modelling multiple, arbitrary, non-planar 3D fractures patterns. The maximum circumferential tensile stress and minimum strain energy density criterion are employed as propagation criteria. The lubrication theory is used for governing the fluid flow inside the fracture. The Carter leak-off model is adopted for leak-off (fluid seepage), and the poroelastic effect is neglected. The HYFRANC3D is used to study the non-planar propagation of a single hydraulic fracture and the interaction between closely spaced but disjoint hydraulic fractures [342, 117, 183]. The other BEM-based fully 3D models include the model developed by [430] and [462] based on DDM, and the model developed by [365] and [73] based on symmetric Galerkin boundary element method (SGBEM). Based on DDM, three different components, including stress/displacement analysis, fluid-flow analysis and the propagation criterion, were described, and two parallel penny-shaped hydraulic fractures were simulated in [430]. In [462], a three-dimensional simulator of the fracturing process was developed to model multiple fracture propagation from different wellbore cases. Based on SGBEM, a single hydraulic fracture from an inclined wellbore under varying in-situ stresses with different layers was investigated in [365] and the simultaneous growth of non-planar hydraulic fractures and the stress shadows from hydraulic fractures created were investigated in [73].

The BEM offers clear advantages: the stress field in the vicinity of the crack tip can be accurately calculated, and the computational efficiency can be greatly increased due to the reduction of the dimension. Nevertheless, for hydraulic fracturing problems with advanced constitutive models such as elastoplasticity, more efforts for the discretisation and more computational cost are required [360].

### **The phase field method (PFM)**

Based on the principle of minimum total potential energy, the phase field method (PFM) solves a fracture problem as an energy minimisation problem, which turns the intact material into a broken material smoothly instead of treating cracks as strong discontinuities. The PFM overcomes difficulties in modelling complex crack problems in three dimensions since the fracture shape is controlled by the variable, and the fracture propagation is obtained through the solution of the differential equation [485].

Because no special treatment is required in fracture propagation criteria, the PFM enjoys great popularity in the study of hydraulic fracturing. To the best of the author's knowledge, the first PFM-based hydraulic fracturing model is developed by Boudin et al. [58]. The model is capable of simulating hydraulic fracturing in a linear elastic impermeable material. The pressure along the fracture surface is assumed to be uniform, and the propagation regime is toughness-dominated. Later, the model was extended from brittle media to porous media in [468]. Mikelic and his co-workers made essential contributions [258, 256, 226]. In [258, 256], a phase field model for a fluid-driven fracture in a poroelastic medium was developed where the pressure field is determined simultaneously with the displacement. The phase-field variable is used as an indicator function to combine reservoir and fracture pressure. The reservoir heterogeneity is considered, and the intersection between hydraulic fracture and natural fractures in porous media is successfully modelled. Later, in [226], the model was extended to a proppant-filled fracture model by incorporating a power-law fluid and proppant transport. A formulation for the robust numerical treatment of a four-field system for coupling displacements, phase-field, pressure and proppant concentration is proposed. Miehe and his collaborators have also made contributions to hydraulic fracturing with PFM [255, 253]. In [255], a formulation incorporating alternative crack driving forces and a concept for a Poiseuille-type fluid flow with an evolving anisotropic permeability tensor were proposed. A modelling framework for the analysis of hydraulic fracture in porous media was demonstrated by a benchmark simulation of 3D hydraulic fracturing propagation with existing natural fractures. The model was further developed in [253], a macroscopic framework for a continuum phase field modelling of fracture propagation is proposed, which provides a rigorous geometric approach for a diffusive fracture modelling based on the

introduction of a constitutive balance equation for a regularised crack surface and its modular linkage to a Darcy–Biot-type bulk response of hydro-poroelasticity. The performance of the formulation is demonstrated by simultaneous propagation of 3D multiple hydraulic fractures.

Modelling hydraulic fracturing based on PFM is a quite hot topic since PFM has the following advantages: (1) remeshing is not required with the fracture propagation, which makes it suitable for 3D modelling of complex crack patterns; (2) external propagation criteria are not required since fracture propagation is a natural outcome of the solution of the equation, which makes it easier to simulate intersections between the hydraulic fracture and natural fractures; (3) the heterogeneity is easy to be introduced into the solution scheme. However, the advantages of PFM do not come without a cost, at least for the current PFM models. The computational cost of PFM simulation is high, especially when a relatively sharp interface is to be captured. Very fine mesh and small time steps are essential for validation with semi-analytical analytical solutions.

### **The discrete element method (DEM)**

Albeit originally developed in [98] for the modelling of jointed structures and granular materials, the discrete element method (DEM) has also been used in the modelling of fracturing and fragmentation, where the discontinuities are the natural outcome of the deformation process and control the mechanical behaviour. As a discontinuum method, the DEM treats a material medium as an assembly of distinct particles. The motion of particles is governed by Newton's laws, and forces between particles are calculated according to the small overlap between them. A variety of numerical software based on DEM has been developed, among which the UDEC, 3DEC and PFC2D are popular software for hydraulic fracturing.

The UDEC stands for Universal Distinct Element Code (UDEC), and 3DEC is the 3D version. In [480], UDEC was employed to investigate the effects of hydraulic fracture patterns and far-field stress conditions for different wellbore pressures, which obtains a better understanding of wellbore instability. In [273], the effects of in-situ stress, rock strength parameters, rock mass major discontinuities on the fracturing process were investigated with UDEC. The results show that the in-situ stress, rock strength parameters, and rock mass major discontinuities have a strong influence on hydraulic fracturing. In [172], a three-dimensional hydraulic fracturing model in intact rock with 3DEC was presented. The effects of in-situ stress and rock properties on hydraulic fracturing are investigated. Compared with rock properties, the in-situ stresses have more influence on hydraulic fracturing. In [272], the simulation of hydraulic fracture propagation in a naturally fractured rock mass was conducted with 3DEC. Critical factors that control the interaction between hydraulic

fracture and natural fractures are summarised, including the natural fracture network, the mechanical properties, the in-situ stress and the operational parameters like injection rate, fluid viscosity, and injected volume.

The PFC stands for Particle Flow Code, which has also been used in hydraulic fracturing simulation but restricted in 2D models currently. PFC differs from UDEC and 3DEC in three aspects: (1) the discrete elements (disk in 2D and sphere in 3D) are forced to be rigid while the blocks in UDEC or 3DEC can be either deformable or rigid; (2) interaction between discrete elements is easier to be implemented in PFC compared with UDEC or 3DEC, which makes the PFC more efficient; (3) the extent of displacement is essentially not limited in PFC [436]. In [12], the acoustic emissions results obtained from a further developed PFC2D hydraulic fracture model was compared with the experimental results. It is found that the hydraulically induced fracture in the granite sample is predominantly caused by tensile failure, and the shear cracks recorded in the experiment were due to slip on natural fractures. Later, the interaction between hydraulic fracture and a preexisting fracture presented by weakened normal and shear bonds was investigated with a similar model in [482]. In [476], an explicitly coupled hydro-geomechanical model in two-dimensional Particle Flow Code (PFC2D) was employed to investigate the effects of different parameters on the interaction between hydraulic fractures and natural fractures. It is found that under higher intersection angle, higher in-situ differential stress states, higher fracturing fluid injection rate and fluid viscosity conditions, the hydraulic fracture becomes less likely to be arrested by the natural fracture. In [240], the mechanism of hydraulic fracture behaviour in a heterogeneous reservoir under the stress perturbation was analysed with an improved PFC2D model. It is found that both the stress wave frequency and situ stress ratios have a non-negligible influence on the hydraulic fracturing process.

In some problems, DEM can be combined with FEM, where DEM is used to model the interaction between different solid regions produced by fracturing and FEM is used to analyse deformation of each solid region based on the specific constitutive model. Using the combined FEM and DEM method, a commercial software called ELFEN is developed [362]. It presents a real transition from a continuous medium to a solid with discrete fractures by dynamically inserting cracks into the model with adaptive remeshing. In [322], the propagation of hydraulic fracture in 2D intact or naturally fractured reservoir was simulated with ELFEN. In [445], Leak-off was added and propagation of hydraulic fracture in 2D naturally fractured reservoir with two sets of natural fractures was simulated. The capacity of ELFEN in modelling hydraulic fracturing in complicated conditions was further demonstrated in [323], where nonplanar propagation of single hydraulic fracture and interaction between hydraulic fractures were simulated in 3D rock mass. In addition, proppant transport, flowback

and clean-up of fracture region and gas production have been added into ELFEN, which makes it an integration of hydraulic fracturing simulator and reservoir simulator.

Compared with the continuum methods, DEM considering hydraulic fracturing from a more microscopic perspective. The advantages of DEM in hydraulic fracturing are: (1) the remeshing problem with the fracture propagation process is circumvented; (2) no additional fracture criteria are needed, and fracture behaviour like fracture initiation, propagation, branching and intersection are the natural outcome of the solution of equation system; (3) it is suitable to study the hydraulic fracturing in heterogeneous materials and fracture networks. However, its limitations are obvious: a large scale simulation of hydraulic fracturing leads to high computational cost, which is easily influenced by many factors, such as particle numbers, particle shapes and contact force models [201].

### 2.1.5 Summary and Prospective Work

This section provides an overview of fracture propagation, including the hydraulic fracture physical process, the development of fracture propagation models, and various numerical methods. In terms of the hydraulic fracture process, three basic processes are included: (1) the mechanical deformation; (2) the fluid flow within the fracture; and (3) the fracture propagation. In addition to the three basic ones, the poroelastic effect is also considered. The historical development of several classic hydraulic fracturing models, including the PKN model, the KGD model, the radial model, the P3D model and the PL3D model, are introduced. Compared with 2D models and the P3D model, both the flexibility and the accuracy of the PL3D model are improved, which in turn also increases the computational cost.

More importantly, various numerical methods applied in fracture propagation are reviewed, and their advantages and limitations are highlighted. The FEM has flexibility and universal applicability in dealing with fracture propagation problems under various conditions but encounters challenges with remeshing, crack tip singularity and calculation cost for multiple fractures. The XFEM is independent of mesh, but special enrichment needs to be developed to account for the discontinuous at junctions when dealing with multiple fractures or fracture intersections. The BEM has an advantage in computational efficiency due to its relatively easy implementation of mesh updating. At the same time, it is not suitable for modelling heterogeneous formation properties and complex constitutive models (e.g. elastoplasticity). The PFM is easy to be implemented in 3D space and heterogeneous materials, and remeshing is avoided when dealing with the complex intersection of fractures. However, it has an expensive computational cost when a fine mesh is required for accuracy. DEM does not need a specific propagation criterion for modelling, and remeshing is not required with

fracture propagation. It is suitable to study fracture propagation in heterogeneous materials or fracture networks. However, a drawback of DEM is that the computational cost is influenced by many factors, resulting in difficulty in the determination of reasonable particle size and parameters.

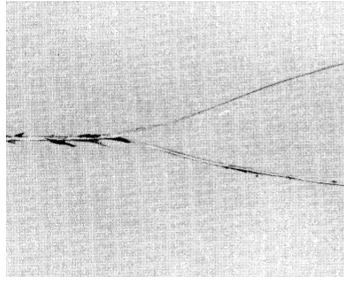
Despite a bunch of references and noteworthy contributions, the theoretical and numerical aspects for fracture propagation are yet to be investigated, including but not limited to the following: (1) The physical mechanism behind fracture propagation, especially in heterogeneous material or fracture networks. The effects of different parameters from the rock formation and the fluid properties on fracture propagation still need to be further explored. (2) How to simulate the fracturing more realistically. Compared with real fracture propagation problems, the current models solve the complex fracture geometry with relatively simple geological conditions. The capability of simulating complex three-dimensional fractures in reservoir scale needs to be improved to better define the petroleum industry's completion design and injection schedule. (3) Numerical approaches need to be developed to increase the robustness and computational efficiency of the model.

## **2.2 Review of crack branching phenomenon**

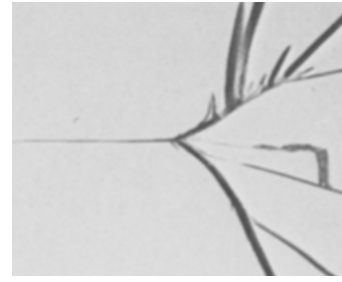
### **2.2.1 Introduction**

Crack branching is encountered in many practical engineering problems, and is particularly common in brittle materials and metal alloys with stress corrosion cracking [206, 287]. As shown in Fig. 2.8, crack branching can occur symmetrically or asymmetrically. The study of crack branching phenomena, including branching mechanisms, branching criteria, experimental measurement and numerical simulation, is of great significance for robust and reliable prediction of crack propagation. A good understanding of the initiation and propagation of cracks inside structural materials is important for preventing catastrophic failure of engineering components and for developing new materials.

The theory of straight line crack expansion is basically mature, with the help of three main types of investigation techniques, namely experimental, analytical and numerical techniques. The mechanism for crack propagation is examined using the simple energy balance theory: the crack occurs when the energy available for crack growth is sufficient to overcome the resistance of the material [16]. In linear elastic fracture mechanics, the propagation criteria of a single steady crack are mainly based on the concept of stress intensity factor or energy release rate. While in nonlinear fracture mechanics, the  $J$ -integral is often applied, which can be viewed as a nonlinear stress intensity parameter or energy release rate. However, the



(a) Symmetrical crack branching [347].



(b) Asymmetrical crack branching [352].

Fig. 2.8 Crack branching photographs from experimental results.

mechanism for crack branching is more complex and still in exploration. The propagation velocity was thought to be a determining factor in crack branching: when the crack velocity exceeds the critical value, the stress field in front of the crack tip changes and branching occurs. However, it was later found that experimentally observed crack velocities at crack branches were much smaller than the theoretical ones [347], consequently, other mechanisms were considered, including instability caused by interactions between microcracks and the existence of micro-scale variations in the symmetries, criteria based on the stress intensity factor and energy release rate. If near-tip instabilities are suppressed, then supersonic cracks are also possible [165]. While many studies on the crack branching phenomenon have been performed both experimentally and theoretically, a uniform theory that accounts for dynamic crack propagation instability and crack branching remains an open question.

In addition to the experimental and analytical techniques, numerical simulations are also employed to study crack branching. Various crack models and numerical methods have been proposed to simulate crack initiation and propagation including crack branching and intersection with reasonable computational cost, and both crack propagation velocity and branching angles have been correctly predicted. With the development of numerical techniques, the modelling of complex crack propagation processes has become more accurate and robust, while the mechanism of crack branching has been further understood. Dependent on how cracks are represented, the crack models essentially divide into two categories: discrete crack models and smeared crack models. Popular discrete crack models usually represent the fracture topology explicitly, which include remeshing, element deletion, cracking particles, enrichment and cohesive zone models. Smeared crack models average the crack over a certain width without explicit tracking of fracture surfaces, and they include phase field, nonlocal, gradient and viscous models. Based on whether spatial derivatives are employed in the controlling equation, the main numerical methods for crack branching can also be summarized in two categories: the continuum methods and discontinuum methods. The continuum methods model the domain as a continuous body and use partial differential equations

with spatial derivatives to describe the underlying physics. They include the finite element method (FEM), the extended finite element method (XFEM), the boundary element method (BEM), and the meshfree methods (MMs). Spatial derivatives are avoided in discontinuum methods. The peridynamic method (PD) and the discrete element method (DEM) are two commonly used discontinuum methods. We note that each numerical method has its own advantages and disadvantages, and no consensus has been reached for the general numerical simulation standard of crack branching.

While dynamic crack propagation has been investigated in the literature [142, 349], there has been little effort to systematically examine crack branching. Therefore, the aim of this section is to summarize the research on crack branching and lead to an improved understanding of branching mechanisms and the study direction in the future. The structure of the section is arranged as follows. The experimental results on crack branching are summarized in § 2.2.2. Based on the experimental results as well as the theoretical derivations, the physics of crack branching is provided in § 2.2.3, which includes § 2.2.3 describing the causes of crack branching and § 2.2.3 describing commonly used branching criteria. § 2.2.4 summarises and compares different crack models and numerical methods for crack branching. Finally, § 2.2.5 summarises the existing findings related to crack branching, highlights some of the most demanding outstanding questions, and indicates potential directions for future research.

## 2.2.2 Experimental Observations of Crack Branching

A number of experimental studies on dynamic crack propagation have been carried out to provide qualitative observations and quantitative data for the explanation of crack branching phenomena. In this subsection, the important experimental results are reviewed in chronological order and wherever applicable these experiments are summarized: (1) from the observation and measurement techniques, for example, the high speed photography and electronic timer; (2) from the experimental material, which includes inorganic glass, Plexiglas, Holmalite-100; (3) with respect to loading conditions such as dynamic loading and quasi-static loading; (4) from the research objectives, including the conditions under which crack branching occurs (crack tip speed, stress intensity factor and its rate) and how crack propagation proceeds after branching (e.g. the branching angle).

Pioneering work was performed in [374] on observing crack branching in inorganic glasses with a multiple spark camera technique. We note that the crack speed remains at a constant value when crack bifurcation occurs. A significant decrease of crack speed only occurs when hackle marks appear as a result of surface energy increase. The number of crack branches greatly increases when increasing loading stress. Crack surface undulation



was predicted by imposing stress waves with ultrasonic transducers and the crack speed was measured in [211]. It is found that the limiting velocity is highly related to the composition of inorganic glass. The dynamic fracture toughness of Homalite-100 and crack propagation velocity variation with dynamic photoelasticity were determined in [220] and [100]. In [100], the equation describing the relationship between the number of branches, the arrest toughness and branching toughness based on the experiment data was further modified. The number of branches is in proportion to the ratio of branching toughness to arrest toughness. The dynamic crack propagation and branching problem was examined in Homalite-100 comprehensively using high speed photomicrography with the load triggered by an electrical pulse [350–353]. A series of important conclusions were obtained: (1) the stress intensity factor increases while crack velocity remains constant, and there exists a quantitative correlation between the stress intensity factor and the fracture surface roughness (mirror, mist and hackle); (2) from macroscopic examination of the fracture surface, it was found that crack dissipates excess energy supplied to the crack tip by creating a rough surface rather than by changing the velocity of crack propagation; (3) from microscopic observations of fracture surface roughness, it was found that crack branching is a natural evolution from a “cloud” of microcracks that accompany and lead the main crack; (4) The terminal velocity in Homalite-100 was found to be  $0.45c_R$ , about half of the Rayleigh wave speed  $c_R$ .

Following the work in [350–353], the micro-branch instabilities were investigated with a series of experiments performed on thin sheets of Plexiglas (PMMA) in [133, 134, 386, 385, 387]. An experimental system was designed in [133], where the resistance voltage increases as a crack progresses across a sample and cuts the conductive layer, the crack tip velocity is measured by detecting the voltage. By plotting the evolution of crack velocity during crack growth, the existence of dynamic instabilities in a brittle fracture is detected. It is found in [134] that once the crack velocity is greater than a critical value, dynamic instabilities occur and the amplitude of the oscillations depends linearly on the mean velocity of the crack. To explain the origin of instability, the presence of microscopic local crack branching was investigated as a possible source for instability in dynamic fractures occurring in thin sheets of brittle PMMA in [386]. The crack micro-branches are observed and measured optically and a connection between microscopic and macroscopic crack branching is established. Later, with the same experiment system, both the energy flux into the tip of a moving crack and the total surface area created via the microbranching instability were measured in [387]. It is found that a crack does not need to dissipate increasing amounts of energy by accelerating because it has another option of dissipating energy by creating an increased fracture surface, which provides an explanation for why the theoretical limiting velocity of a crack is never realized. Readers are referred to [135] for a comprehensive review of

the early work on the micro-branching instability. In recent years, under the help of brittle poly-acrylamide gel (an aqueous elastomer), which enables probing the fracture process in unprecedented detail by high-speed cameras, a number of important experiments have been carried out to study the dynamic fracture process [56, 57, 55, 244]. These experimental developments have been reviewed in [132] and it has been shown that (1) an intrinsic length scale, which is associated with nonlinear elastic deformation near the crack tip, plays an important role in dynamic instabilities; (2) dynamic instabilities include micro-branching instabilities and oscillatory instabilities. The micro-branching instability may be closely related to the oscillatory instability and it appears to be an intrinsically 3D instability instead of a 2D instability. Further discussions about the physics of crack branching can be found in § 2.2.3.

A necessary and sufficient condition for crack branching was proposed by [347] (see further discussions in § 2.2.3). The criteria was verified in [177] by using the 16-spark-gap camera to record the dynamic photoelastic patterns of curving and branching cracks in Homalite-100 specimens under biaxial loading conditions. Increasing the biaxial stress ratio of horizontal loading to vertical loading and the stress level increases both the curvature and the number of branching cracks. The modes of energy dissipation in dynamic crack propagation and branching process in Homalite-100 were investigated in [176] by using a potential drop technique and qualitative comparisons with PMMA were made. Fast-growing cracks before and after bifurcation were investigated in [418] by using high-speed holographic microscopy and obtained the crack branching velocity, branching angles, and energy release rate in Homalite 100 and Araldite B. In Homalite 100 the crack branching velocity is  $0.48C_R$  with an average branching angle of  $17 \pm 6^\circ$ , and in Araldite B the crack branching velocity is  $0.46C_R$  with an average branching angle of  $16 \pm 4^\circ$ . The energy release rate increases gradually and continuously across the bifurcation point both in Homalite 100 and in Araldite B and PMMA. It was observed in [270] that the branching patterns of PMMA single edge notched tensile specimens with scanning electron and optical microscopes and measured the crack propagation speed by electrical resistance methods. Each macroscopic branch is accompanied by many small cracks along its length with most crack branches being straight. The experimental results indicate that crack branching is a natural outcome of the growth and coalescence with microcracks. Both subsurface damage and the frequency of crack speed oscillations increase during the branching process. An example of using digital image correlation (DIC) to investigate the cracking process and branching mechanisms in lightly reinforced concrete beams was given in [129]. The DIC can visualise surface displacement by tracking the deformation of a random speckle pattern applied to the surface through digital images acquired at different instances of deformation [405]. Crack branching angles

and propagation path are found to be related to the beam height and ductility. Another technique, called digital gradient sensing (DGS), employs 2D DIC with an elasto-optic effect to directly quantify both crack-tip fields and crack speeds. Using this technique, the branching phenomenon was investigated in soda-lime glass in [416]. This study overcomes measurement challenges such as low fracture toughness and high crack propagation speed and proposed that the critical material length scale can be a criterion for crack branching. Compared with normal observation and measurement techniques, the DIC and DGS have advantages of lower cost and simpler operation.

The advantages and disadvantages of different observation and measurement techniques are summarised in Table 2.1. In order to better explore the mechanism of crack propagation and branching, current research on experimental methods is focused on both the improvement of experimental technologies to overcome existing shortcomings and the development of new experimental technologies. With respect to testing materials, most experiments have adopted inorganic glass, Plexiglas, and Homalite-100. The limiting velocity is studied in different materials and it is found that the limiting velocity is  $0.5 \sim 0.65c_R$  for glass,  $0.6 \sim 0.7c_R$  for PMMA and  $0.35 \sim 0.45c_R$  for Homalite-100 [42]. The branching angles are also investigated although they are easily influenced by the loading conditions, geometry and material properties. From a macroscopic viewpoint, the angle subtended by the new branch (immediately after branching) and the original crack plane typically lies between  $10^\circ$  and  $45^\circ$  [108]. For different materials, detailed experimental results on branching angles can be found in [135, 108, 221]. The branch shape and branch number are also influenced by the loading conditions, geometry and material properties. The increasing of loading stress may lead to the increasing of branch number of the cracks while the loading conditions, geometry and material properties may have an impact on the branching angle as well as the branch curvature, thus, the branching shape.

Table 2.1 Experimental techniques for crack branching.

	Techniques	Advantages	Disadvantages
High Speed Photography	(photoelasticity [100, 220], caustics [219], holographic microscopy [417, 418])	high temporal and spatial resolution	high cost
	(DIC [405], DGS [416])	high resolution, low cost, simple experimental setup	low measurement accuracy in stress concentrations (DIC)
Wallner Lines (stress wave fractography [192])		accurate measurement for crack speed	low spatial resolution
Electrical Resistance Methods [195, 270]		high spatial resolution	sensitive to the variation of film thickness

### 2.2.3 Physics of Crack Branching

#### Causes of Crack Branching

Many attempts have been made to explain the crack branching phenomenon. One of the classical theories is from [467]. On the assumption that the crack propagates along the direction normal to the maximum stress, when the velocity is lower than the critical velocity  $0.6c_S$ , where  $c_S$  is the shear wave speed, the crack propagation process remains at a steady state. When the crack velocity exceeds this critical value, the propagation process becomes unstable. The stress state at the crack tip will change, and the hoop stress in the vicinity of the crack tip will have a maximum angle of about  $60^\circ$  from the propagation direction, which may lead to crack branching, as shown in Fig. 2.9. By considering a crack growing from zero initial length at a uniform velocity rather than staying constant length, Yoffe's analytical model was further improved in [61]. It is reaffirmed that crack branching occurs if the velocity exceeds  $0.6c_S$ . The aforementioned studies suggest that the crack propagation become unstable and cracks are more likely to start branching when the velocity exceeds a critical value. This mechanism is corresponding to the "velocity criterion", see details in § 2.2.3. Though this mechanism is not sufficient to explain the branching phenomenon, the velocity criterion resulting from it is often employed in numerical simulation due to its simplicity.

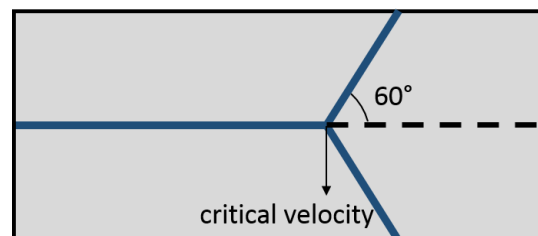


Fig. 2.9 Yoffe's crack branching model [467].

An alternate attempt to explain crack branching is via the viewpoint of energy. By assuming the energy inputting into the crack and the energy required to create new branch surfaces is balanced, it is argued in [124] that the crack tip velocity should at least be  $0.5c_R$  to allow the energy at the crack tip to be sufficient enough to create new surfaces for crack branches, where  $c_R$  is the Rayleigh wave speed. However, according to the experimental observations, the crack velocity does not change significantly before and after crack branching [352]. An explanation to that is given in [147], which proposed a more definitive analytic model called the wavy-crack model, where two velocities are defined: the macroscopic crack velocity  $v_a$  and the microscopic local velocity  $v_c$ . If the crack speed is above  $0.5c_R$ , the crack

propagates along a wavy path and the energy absorbed into the crack is used to increase  $v_c$  while  $v_a$  remains constant. This explains why the crack speed does not decrease much after branching.

Another possible explanation is given in [352], which suggested that there exist many microcracks in front of the main crack as shown in Fig. 2.10, and branching is a natural outcome of the growth and coalescence of the microcracks. In Homalite-100, a varying fracture surface roughness during branching, ‘mirror’, ‘mist’, and ‘hackle’, can be observed [351], see Fig. 2.11. The fracture processes that occur over a spatial domain comparable to the surface roughness dominate the dynamics of crack growth. Initially, a crack propagates with a mirror-like fracture surface. Then, because of the coalescence of microvoids or preexisting defects ahead of the crack, the crack surface may become rough and subsequently microcracks form. The microcracks within the fracture process zone interact with each other and form micro-branches, which results in the final crack branching.

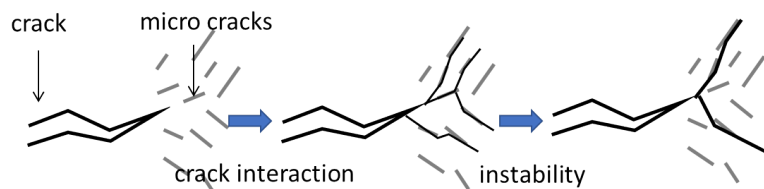


Fig. 2.10 Ravi-Chandar's micro crack model [352].

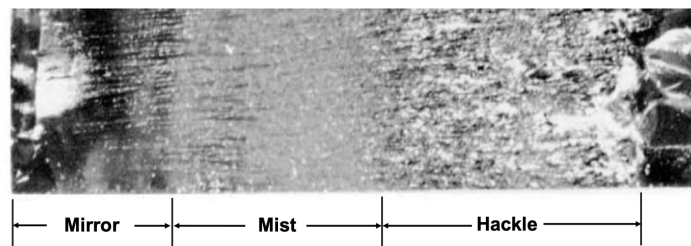


Fig. 2.11 Typical ‘mirror’, ‘mist’ and ‘hackle’ regions are identified in Homalite-100 [351].

Following the work of [350–353], micro-branches and their instability have been studied in great detail recently [134, 386, 385, 387, 135, 56, 57, 55, 244, 132, 245]. Using dynamic instabilities, these studies explain a number of long-standing problems in the dynamic fracture of amorphous including (1) velocity oscillations and limiting velocity, (2) fracture roughness, (3) the origin of the large increase in the energy dissipation of a crack with its velocity and (4) transition to crack branching. A detailed discussion about velocity oscillations and limiting is given in § 2.2.3. When the crack velocity exceeds the critical value (limiting

velocity), the velocity begins to oscillate rapidly [134]. A good correlation is demonstrated between the measured crack velocity and appearance of fracture roughness on the fracture surface [385]. The initial crack with a velocity lower than the critical crack velocity  $v_c$  corresponds to a mirror-like fracture surface. After achieving the critical crack velocity  $v_c$ , the velocity begins to oscillate. As the velocity increases, rib-like patterns observed on the fracture surface become more apparent. Microscopic branches have also been observed when the velocity exceeds the critical value, see Fig. 2.12. These characteristic features are independent of the brittle material due to the fact that in two extremely different classes of material (poly-acrylamide gel and soda-lime glass), identical characteristic behaviour is observed [245]. The origin of the large increase in the energy dissipation of a crack with its velocity can also be explained by the micro-branching instability [387]. When micro-branching instabilities occur, the energy dissipation of a crack increases because more surfaces are formed by the micro-branches. As the velocity of the crack increases, transition to crack branching occurs with the branches becoming longer and more numerous. Micro-branches can smoothly transform to macro-branches with similar characteristic features of crack branching exhibited between the micro-branches and macro-branches [386]. The onset of the micro-branching instability therefore provides a well-defined criterion for the process that eventually culminates in macroscopic crack branching. As the crack velocity increases larger than the critical velocity, the branch width increases and the surface roughness diverges. This transition may be a sufficient condition for macroscopic crack branching to occur [385]. The dynamic instabilities have been further studied with a series of theoretical analysis in [56] and with experiments in brittle gels in [244]. A weakly nonlinear theory of dynamic fracture has been introduced, which implies that the understanding of crack instabilities requires the introduction of new physical ingredients, e.g. length scales [56, 57, 55]. Intrinsic nonlinear scales in the near-tip region play a decisive role in dynamic crack instabilities. A comprehensive review of important experimental and theoretical work in dynamic crack instabilities was given in [132], which states that the micro-branching instability is an intrinsically 3D instability and to understand the dynamic instabilities, the framework of fracture mechanics should be extended to include 3D crack propagation.

Through theoretical analyses, the crack branching mechanisms including dynamic crack instability and 3D microbranching instability were systematically studied in [5, 3, 4, 210, 6]. Dynamic crack branching instability under general antiplane loading [3] and under general loading [4] are studied and the path and geometry of the branched crack are predicted. It is shown that after branching the in-plane elastic fields immediately exhibit self-similar properties, and the jump in the energy release rate is maximized. Under this assumption, the crack branching phenomenon, which is found to be energetically possible, may be seen as a

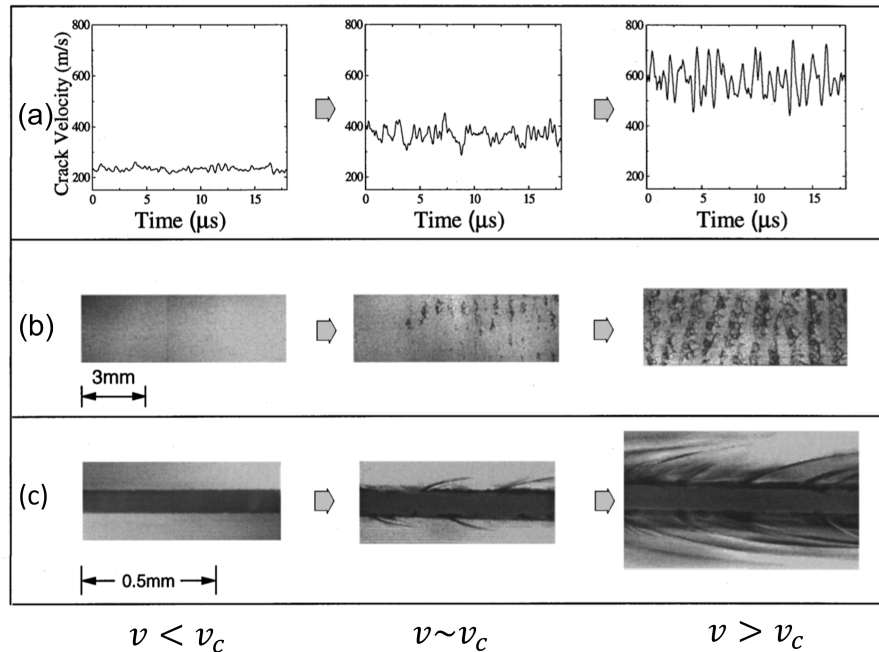


Fig. 2.12 Three aspects of the evolution of the branching instability as the crack propagates from left to right [385]. (a) The velocity of the crack is a smooth function of time when  $v < v_c$ , the crack velocity starts to oscillate when  $v \sim v_c$ , the oscillation amplitudes increase when  $v > v_c$ . (b) The fracture surface is smooth when  $v < v_c$ , small regions of different texture are distributed along the surface when  $v \sim v_c$ , these regions coalesce, forming a periodic pattern with wavelength on the order of 1 mm when  $v > v_c$ . (c) A single crack is observed when  $v < v_c$ , micro-branches appear when  $v \sim v_c$ , and increase in length when  $v > v_c$ .

dynamic instability in which a self-similar single crack propagation would lose its stability at some point dependent on crack velocity [210]. Later, in [6], the 3D out-of-plane nature of crack front waves (generated by both the interaction of a crack with a localized material inhomogeneity and the intrinsic formation of micro-branches [384]) and the microbranching instability with the Willis-Movchan 3D linear perturbation formalism were investigated. It is demonstrated that within a minimal linear elastic fracture mechanics scenario, the existence of an out-of-plane crack front instability is dependent on critical velocity, which may trigger a 3D microbranching instability, and its fractographic implications.

For materials like inorganic glasses, where microcracks cannot be found in front of the main crack, different mechanisms have been proposed. It is suggested in [192] that micro-scale variations lead to twisting and tilting of the stress vector near the crack tip, cause local instability to the dynamic properties of cracks, and are responsible for the increase of

crack surface roughness and crack branching. The surface roughening are explained in [384] and [50] from the interaction of the shear wave with the tip of the growing crack. The shear wave proves the existence of front waves in dynamic fractures. The front waves feature an out-of-plane component, which leaves marks on the fracture surfaces and causes surface roughness and crack shape perturbations [132].

Though crack branching in dynamic fractures has long been observed and investigated in various literatures, up to now, there has not been a universally agreed-on explanation for crack branching mechanisms. Based on the above work, the mechanisms of branching can be summarized as: (1) the increase of the velocity may cause unstable crack propagation, which causes crack branching; (2) the microvoids and microcracks may increase surface roughness and the growth and coalescence of microcracks which form micro-branches resulting in macro-branches with the energy absorbed in the crack relating to the limiting velocity; (3) the dynamic instability plays an important role. Cracks undergo an oscillatory instability controlled by small-scale, near crack-tip, elastic nonlinearity, and this oscillatory instability may trigger microbranching instability, which provides a well-defined criterion for the process that eventually culminates in macroscopic crack branching; (4) the crack front waves and the tilting and twisting of the stress vector at the crack front may cause local dynamic instability, increasing of crack surface roughness leading to crack branching.

### **Branching Criteria**

Crack branching criteria tend to be artificially formulated based on physical mechanisms to improve crack branching simulation. We divide the criteria into two types: external criteria and internal criteria. Here, “external” means that in the numerical simulation additional criteria are needed to determine how the crack branching occurs. The criteria required in a whole process for branching simulation include criteria for crack initiation, criteria for crack propagation, criteria for crack branching time and criteria for branching angles. A series of studies on criteria for dynamic crack initiation and crack propagation are summarized in dynamic fracture mechanics [142, 349]. The following discussion will focus on criteria for branching time and branching angles, instead of being exhaustive. In contrast to the “external”, “internal” means that no additional criteria are required, and any occurrence of branching is a natural outcome of the simulation.

**External criteria** To determine the branching time, three commonly used criteria are introduced, namely the velocity criterion, the stress intensity factor criterion, and the energy criterion.



**Velocity criterion** The velocity criterion suggests that once the crack tip velocity exceeds a critical value, branching occurs. Note that there exists two branch types, namely micro-branches and macro-branches, which are discussed separately here. Both theoretical and experimental approaches have been used to investigate the critical velocity of a fast moving crack.

An energy balance equation was given in [142], which considers a crack growing with a nonuniform speed under time-independent/dependent loading:

$$G^{dyn} \approx \left(1 - \frac{v}{c_R}\right) K_I^0(t, l(t), 0) = \gamma \quad (2.19)$$

where  $G^{dyn}$  is the dynamic energy release rate,  $v$  crack velocity,  $K_I^0(t, l(t), 0)$  the instantaneous stress intensity factor at time  $t$  for a stationary crack of length  $l(t)$  and  $\gamma$  the fracture energy. Based on Eq. (2.19), the fracture energy for a moving crack will vanish when the crack velocity  $v$  increases to the Rayleigh wave speed  $c_R$ . Therefore, from the elastodynamic fracture mechanics theory, the limiting velocity for crack propagation is no larger than the Rayleigh wave speed. However, from an experimental view, it is found that only cracks on the cleavage planes in crystalline materials grow at a rate close to Rayleigh wave velocity. For cracks in noncrystalline materials, the limiting velocity of the crack is significantly smaller than the theoretically predicted limiting crack velocity [349]. The reason behind this phenomenon can be explained by dynamic instabilities [134].

The critical velocity for micro-branches states that once the velocity exceeds the critical velocity  $v_c$ , the crack propagation becomes unstable with the occurrence of velocity oscillations, increase of surface roughness and microbranching [135]. The critical velocity for instability and micro-branches has been investigated with experimental approaches. It is found in [133, 134] that the critical velocity for crack propagation in PMMA is  $0.36c_R$ . It is observed that the critical velocity for crack propagation in Homalite is  $0.37c_R$  in [176] and [351]. The critical velocity for crack propagation is found to be  $0.42c_R$  in soda-lime glass in [160]. Based on the experimental observations above, the existence of a critical velocity for the instability of brittle fracture may be a universal aspect [134]. While micro-branches instability is seen as one of the reasons for crack branching, the transition from critical velocity criterion for micro-branches to critical velocity criterion for macro-branches is still unknown [135]. The critical velocity for macro-branches is used to determine when macro-branches develop. Theoretically, as discussed in § 2.2.3, various authors established models to analyse the critical velocity. The critical velocity is assumed to be  $0.6c_S$  in [467],  $0.5c_R$  in [124] and [147],  $0.52c_R$  in [4]. Experimentally, as discussed in § 2.2.2, the limiting velocity is  $0.5 \sim 0.65c_R$  for glass,  $0.6 \sim 0.7c_R$  for PMMA and  $0.35 \sim 0.45c_R$  for Homalite-100.

In addition, many experimental results show that the crack velocity does not change significantly after branching [352]. These limitations have challenged or weakened the velocity criterion for crack branching. However, due to its simplicity, the velocity criterion is widely used in numerical simulation for crack branching. For example, a branching model using FEM was proposed in [235], where branched elements are added to represent discontinuities if the crack tip velocity exceeds a given threshold. The influence of different critical velocities on branching was also investigated with the FEM-based model. With a similar model, the crack propagation path and branching characteristics were also successfully captured in [18]. An additional enrichment in XFEM was set up in [456] to describe crack branching and adopted Yoffe's criterion as branching time criterion. The crack branching occurs when the maximum normalized circumferential stress occurs in two symmetrical directions and at this moment the velocity is over  $0.74c_R$ . By comparing numerical and experimental results  $0.4c_R$  they concluded that the crack velocity error was due to the velocity criterion adopted.

**Stress intensity factor (SIF)** In elastodynamic fracture mechanics, the theoretical framework is fairly well established through a series of analyses of a dynamically propagating crack in an infinite body in [139–142]. Taking mode I crack as an example, the dynamic crack growth criterion is given as:

$$K_I^{dyn}(t, v) = K_{ID} \quad (2.20)$$

where  $K_I^{dyn}$  is the dynamic SIF,  $t$  the time, and  $K_{ID}$  the dynamic crack growth toughness. For the left-hand side of the Eq. (2.20), theoretically, the dynamic SIF is related to both the crack velocity and the instantaneous SIF of a stationary crack, which can be expressed as:

$$K_I^{dyn}(t, v) = k(v)K_I^0(t, l) \quad (2.21)$$

where  $k(v)$  is a function of crack velocity and  $K_I^0$  the instantaneous SIF of a stationary crack with length  $l$  at time  $t$ . Numerically, the dynamic SIF can be calculated through the  $J$ -integral or interaction integral. Unlike the calculation in quasi-static conditions, the numerical calculation of the  $J$ -integral or interaction integral is no longer path independent in dynamics. The reader is referred to the book [16] for more details. For the right-hand side of Eq. (2.20), the crack growth toughness  $K_{ID}$  can be determined experimentally, and the  $K$ - $v$  relationship is often employed. Experimentally, it was found that the dynamic SIF is related to crack velocity, however, the relationship is not unique, but an average can be obtained [100, 349].

By experimental investigations, it is indicated in [220] and [100] that branching occurs when the SIF reaches a critical value that is between two and three times the quasi-static fracture toughness of the material. It is suggested in [89] that the dynamic SIF should reach a critical value for branching to occur at terminal velocity. Based on previous theoretical and experimental studies on crack curving and crack branching, the following necessary and sufficient conditions for crack branching are proposed [347]:

$$\begin{aligned} K_I &\geq K_{Ib} \rightarrow \text{necessary condition} \\ r_0 &\leq r_c \rightarrow \text{sufficient condition} \end{aligned} \quad (2.22)$$

where  $K_{Ib}$  is the critical branching SIF, and  $r_c$  is the characteristic distance from the crack tip. With experimental observations, it was concluded in [349] that a crack will split into two or more branches if it reaches the critical stage identified by its SIF, and each branch will propagate with the same speed as the parent crack. The SIF criterion is applied to decide crack branching time when modelling crack propagation [217, 338]. Using the SIF-based fracture criterion, a crack model of crack kinking and branching on the rock-concrete interface of a gravity dam was developed in [217]. Using a time-domain BEM approach, the dynamic crack propagation was examined in [338], where a critical mode I SIF was used for the branching event and the maximum circumferential stress criterion was employed for determining the branching angle and each branch's growth rate.

**Energy criterion** The energy criterion is applicable to both linear and nonlinear fracture mechanics, e.g. the energy release rate  $G$  and the  $J$ -integral. The crack extension occurs when the energy available for crack growth is sufficient to overcome the resistance of the material [472].

The branching criterion theory was proposed in [124] based on the balance between the energy inputting into the crack and the energy required to create new branch surfaces. Based on this study, with the help of the Griffith's energy criterion and the principle of local symmetry, a series of analytical solutions for crack branching problems were presented [3, 4]. The energy criterion was assumed to be a necessary condition for a branching configuration, and the stress field in front of the crack tip, the branched shape and the dynamic branching instability were predicted and analysed. A dynamic  $J$ -integral was proposed in [419], where the energy flux per unit time into the crack tip was calculated. Once a given critical energy release rate is surpassed, the branch occurs and an implicit prediction for branching path is adopted. In [455], an energy-based fracture mode for the mode-I crack branching was presented, where branching toughness was proposed, the branching critical energy release

rate was derived and the branching angle was predicted. The criterion shows good agreement with the experimental observations reported in the literature.

**Criteria for branching angles** After the branching time is determined, the next step is to determine how the crack propagates with branching. The branching angle has been studied both experimentally and theoretically. Experimentally, as discussed in § 2.2.2, the angle subtended by the new branch (immediately after branching) and the original crack plane typically lies between  $10^\circ$  and  $45^\circ$ . Theoretically, the crack propagation direction can be predicted by the maximum circumferential stress theory, the minimum strain energy density factor theory, the principle of local symmetry and the maximum strain energy release rate theory [347]. A comprehensive review of earlier analytical research work on elastostatic and elastodynamic self-similar crack branching problems in homogeneous, isotropic and elastic brittle solids was given in [108]. Later, a series of analytical research work on elastodynamic crack kinking or branching problem were conducted in [5, 3, 4] and a more general solution was given. The branching angles and crack path are determined by calculating the elastodynamic stress field / the dynamic SIF associated with the propagation of anti-plane kinked or branched cracks under general antiplane loading [3] and arbitrary loading condition [4]. Later, the theory of dynamic crack branching in brittle materials was further summarized in [210]. With the theory, a systematic analysis of the branching problem is made and the critical velocity, the branching angle, the branching tip velocity, and the subsequent branch path described by a curvature parameter are successfully predicted.

**Internal criteria** Internal criteria are combined with numerical methods and embedded in the specific crack models, which leads to crack branching as a natural outcome of the simulation. A simple way to judge whether a model or a method contains internal criteria is to check whether branching angle criteria are required during simulation. If not, cracks are allowed to form freely in the simulation. Models and methods containing internal branching criteria include, but are not limited to, the cracking particles method, the peridynamics, the phase field model, the element deletion model, the cohesive zone model, the enrichment models and nonlocal models/gradient models/viscous models. More detailed information about all of these models and methods can be found in § 2.2.4.

## 2.2.4 Crack models and numerical methods

Crack models are used to describe how to represent the fracture, including the geometry and the stress concentration. Numerical methods are employed to solve equations, describe the bulk material behaviour, and capture the fracture propagation process. Different models can

be combined with each other and they can be integrated with multiple numerical methods. Likewise, different numerical methods can be combined to form hybrid methods, and they can also work with different fracture models, see Fig. 2.13. Smear crack models can account for the crack tip nonlinearity. While discrete fracture models integrated with notable methods such as finite element method, extended finite element method, boundary element method often do not account for crack tip nonlinearity unless the cohesive zone model is employed.

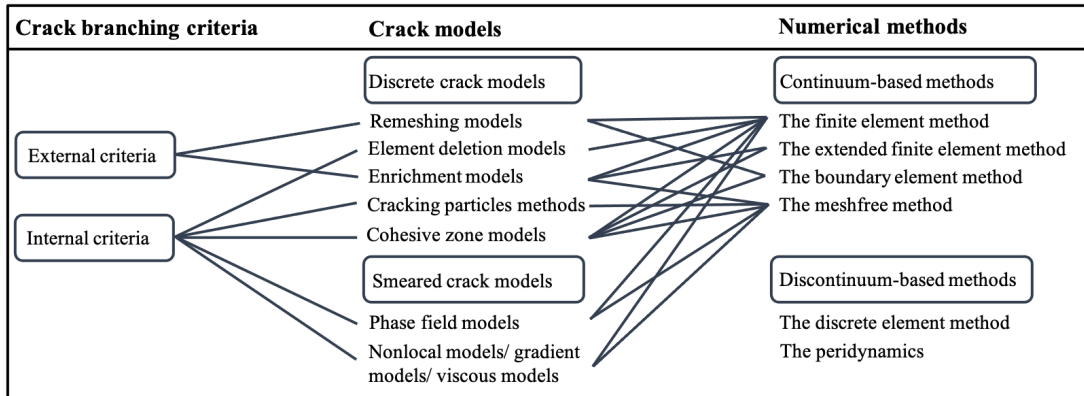


Fig. 2.13 Crack models and numerical methods.

### Crack models

Crack models are used to describe how to represent the crack, and they can be roughly divided into two categories: discrete crack models and smeared crack models. Based on how the crack is represented, the “discrete” means the crack topology is explicitly represented while the “smeared” means the crack is smeared over a certain width without explicit tracking of crack surfaces. Popular discrete crack models include remeshing, element deletion, cracking particles, and enrichment models. Popular smeared crack models include phase field, nonlocal, gradient and viscous models. We note that different from the models mentioned above which describe how to represent cracks, the cohesive zone model describes the nonlinear behaviour in the process zone ahead of the crack tip with a traction-separation law and it is essentially a discrete concept. Therefore, we describe the cohesive zone model as part of the discrete crack models. However, it can also be implemented in smeared context by distributing the work of separation or fracture energy over the width of an element [104]. See [105] for various smeared representations of cohesive-zone type behaviour. As a summary, Table 2.2 lists the advantages and limitations of different crack models, and their details are separately discussed in the following subsections.

### Discrete crack models

Table 2.2 Advantages and limitations of different crack models for crack branching.

Crack Models	Advantages	Limitations
Remeshing models [287, 419]	flexible in dealing with complex geometries and boundary conditions	awkward in dealing with complex three-dimensional geometries
Element deletion models [410, 304, 414]	easy implementation	special treatment is required to solve the mesh dependency
Enrichment models [34, 264, 334]	solve parts of difficulties associated with the mesh	rely on different types of enrichment adopted, see detail in § 2.2.4
Cracking particles methods [327, 328, 336]	suitable for complex crack patterns, straightforward implementation in 3D	special treatment is required to solve the “spurious cracking” problems and reduce the computational cost
Cohesive zone models [461, 66]	suitable for complex crack patterns, removes singularity in the crack tip	special treatment is required to solve the mesh dependency and bias
Phase field models [60, 54]	suitable for complex crack patterns, straightforward implementation in 3D	fine mesh is required to obtain more accurate results
Nonlocal models/gradient models/viscous models [31, 143]	solve the ill-posed boundary value problem, suitable for modelling failure caused by progressive damage	physical inconsistencies may appear, fine mesh is required to obtain more accurate results

**Remeshing models** As the crack propagates and branches, new discontinuities form across the crack, therefore, crack surfaces need to be redefined as boundaries and the mesh needs to be updated. Remeshing models update the crack surface with remeshing techniques, where an explicit representation of crack surfaces and a crack tracking algorithm are usually required. During the simulation process, external criteria including the crack initiation, propagation, branching time and angle criterion are employed, which increases the difficulty of computational simulation. The reasons are manifold: (1) until now, there is no universally agreed explanation for branching time and branching angles; (2) the formula to calculate the associated parameters under dynamic situation remains a challenge; (3) a remeshing rule including the selection of element type, mesh generation method, data transfer during remeshing is required for which computation efficiency needs to be considered.

The remeshing models can be combined with such numerical methods as FEM and BEM to simulate crack branching. A schematic illustration of crack branching with remeshing models based on FEM is shown in Fig. 2.14. Compared with remeshing models based on FEM, remeshing models based on BEM is much simpler due to the reduced dimensional features of BEM. Details will be explained in § 2.2.4. Both methods assume that the crack surface is generally determined by the separation between elements, which makes it difficult to capture crack surface roughness relating to dynamic brittle fracture. We note that another commonly used application of the remeshing models is its combination with cohesive zone models by actively inserting cohesive interface elements into the finite element mesh, which will be discussed separately later.

**Element deletion models** Element deletion models are often integrated with FEM, where the crack is represented by a set of deleted / deactivated elements, as shown in

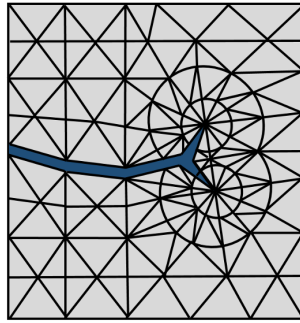


Fig. 2.14 A schematic illustration of crack branching with remeshing models based on FEM.

Fig. 2.15. There is no need for explicit representation of the crack's topology by remeshing. The deactivation of elements can be achieved through two approaches: (1) complete element deletion technique, in which deleted elements are replaced by rigid masses and (2) setting the stress of the deactivated elements to zero [325, 410]. The elements, which are deactivated or deleted, have no material resistance or stress for the rest of the simulation process [265].

However, unless the constitutive equation is properly scaled or adjusted, the released energy due to deleting an element depends on the element size, which can cause spurious mesh dependency and lead to high computational cost in dynamic crack simulations [205]. To reduce the spurious mesh dependency, the softening curve slope should be scaled so that fracture energy is independent of the element size [410]. The mesh dependency problem is also handled with variational formulations [304]. A method called "eigenerosion" was developed in [304], which is characterized by the restriction of element erosion in a binary sense: it can be equal to 0, if the element is eroded or 1 in case of fully elastic behaviour. The fracture propagation is then treated as failing elements when the elastic energy release is higher than the corresponding dissipated fracture energy. Compared with the original element deletion model, the eigenerosion, as an extension version, is more suitable for crack branching problems for its accuracy and convergence in complex crack simulations [410, 304, 414, 375].

In [410], the performance of the element deletion model for dynamic crack propagation in brittle materials was checked. It is found that the element deletion model gives a very irregular crack velocity and performs poorly for the accurate prediction of crack branching. To reduce the high computational cost caused by a relatively fine mesh during modelling, a dynamic adaptive eigenfracture scheme was presented in [127] by combining the eigenfracture scheme and the adaptive mesh refinement algorithm, which reduces the element size locally while improving the Griffith fracture convergence property. The ability of the dynamic adaptive eigenfracture scheme in predicting crack propagation was proved by numerical examples of crack branching, see Fig. 2.16. It is found that the crack pattern, the crack branching

velocity and crack instabilities in the simulation are in good agreement with the experimental observations.

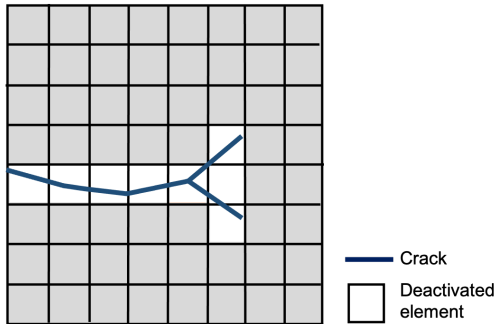


Fig. 2.15 A schematic illustration of crack branching with element deletion models

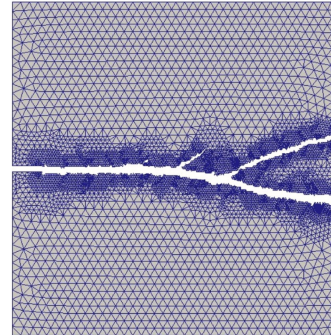


Fig. 2.16 A numerical example of crack branching with element deletion models. [127]

The element deletion model deletes elements that satisfy a certain criterion explicitly with no additional criteria used to determine the branching time and branching angles. However, special treatment is required to solve the mesh dependency problem [205]. The mesh needs to be fine enough to obtain accurate crack path prediction in dynamic crack simulations, which may in turn cause high computational cost. To the best of the author's knowledge, there is a limited number of papers studying the performance of the element deletion model in dynamic crack branching simulation [410, 414, 127], and no 3D examples are provided. Though its ability in modelling the crack pattern and the crack branching velocity has been demonstrated in 2D [127], further multiple crack braching tests and crack branching in 3D are yet to be demonstrated.

**Enrichment models** The enrichment models use the so-called “enrichment approaches” to account for the discontinuous displacement fields in the crack. The enrichment approach involves enriching a polynomial approximation space so that the crack can be modelled independently of the mesh. There are commonly two types of enrichment, namely, the intrinsic enrichment and the extrinsic enrichment. The intrinsic enrichment is to replace (at least some of) the shape functions in the polynomial approximation space with special shape functions. The number of shape functions and unknowns is unchanged during simulation. While the extrinsic enrichment can be achieved by adding special shape functions to the polynomial approximation space, where more shape functions and unknowns result in the approximation [144].

The enrichment model can be combined with XFEM or MMs. Important features about enrichment in XFEM are [144]: (1) the enrichment is extrinsic and realized by the partition



of unity (PU) concept; (2) the enrichment is local because only a subset of the nodes is enriched; (3) the enrichment is mesh-based, i.e. the PU is constructed using standard FE shape functions; (4) enrichments for arbitrary discontinuities in the function and their gradients are available. Compared with the enrichment in XFEM, the enrichment in MMs can be both intrinsic and extrinsic. The extrinsic enrichment can be further classified into an extrinsic moving least-square (MLS) enrichment and an extrinsic PU enrichment. The ability of the model to capture crack branching depends on the methods used in combination, further details will be given in § 2.2.4.

**Cracking particles methods** In the cracking particles method (CPM), the crack is modelled by a set of discrete cracks. As shown in Fig. 2.17, the discrete crack is restricted to lie on the particles. Since the crack is described by the set of cracked particles, no representation of the crack's topology is needed [327, 328, 336]. The method was first developed in [327]. In the model implemented with the cracking particles method, the displacement approximation is given by:

$$\mathbf{u}^h(\mathbf{x}) = \sum_{i \in N} \hat{N}_i(\mathbf{x}) \mathbf{u}_i + \sum_{i \in N_c} N_i(\mathbf{x}) S(f_i(\mathbf{x})) \mathbf{q}_i \quad (2.23)$$

where  $\mathbf{u}_i$  is the displacement vector,  $N$  the total set of nodes in the model,  $N_c$  the set of cracked nodes,  $\hat{N}_i$  the continuous shape functions,  $N_i$  the discontinuous shape functions,  $S(f_i(\mathbf{x}))$  the step function defined as 1 and  $-1$  on two sides of the crack, and  $\mathbf{q}_i$  the enrichment parameter. Therefore, the displacement jump across the crack can be obtained from Eq. (2.23):

$$[[\mathbf{u}]] = 2 \sum_{i \in N_c} N_i(\mathbf{x}) S(f_i(\mathbf{x})) \mathbf{q}_i \quad (2.24)$$

A discrete crack is introduced whenever a cracking criterion is met at a particle [327]. The cracking criteria differ with different material properties, e.g. loss of hyperbolicity is used for a rate independent material while loss of material stability is used for a rate dependent material [335]. The reader is referred to [334] for detailed description of commonly used cracking criteria.

The original model extended its application to three dimensional problems in [328], where the discontinuity consists of cylindrical planes centred at the particles. where a continuous crack is represented by a contiguous set of cracked particles. The sphere particles are separated by a crack plane that passes through the centre of the particle. The method proves its capability in large deformations and arbitrary nonlinear and rate-dependent materials with different examples. A crack branching example in 3D with CPM is given, see Fig. 2.18.

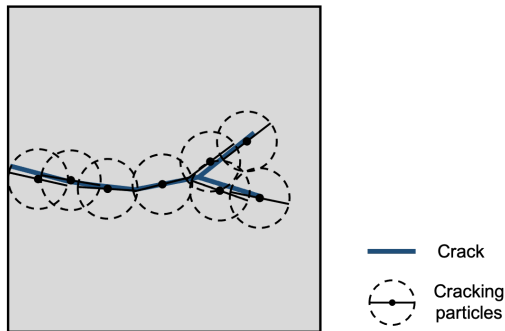


Fig. 2.17 A schematic illustration of crack branching with CPMs.

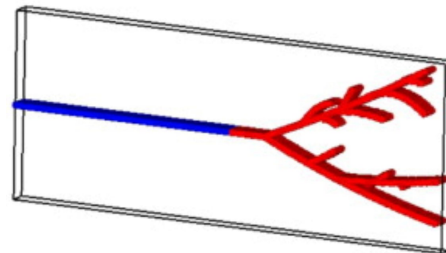


Fig. 2.18 A 3D example of crack branching with CPMs [328].

The crack front line is almost linear without capturing the fracture tunnelling feature. The reason may be the use of brittle materials while fracture tunnelling is often observed in ductile materials. Since the crack pattern along the out-of-plane direction is uniform, this example can be considered as a “2.5D” example. To further prove the ability of the method to simulate a real 3D problem, a non-planar crack growth example is given in [328], which is not shown here since this non-planar crack growth example doesn’t include the crack branching phenomenon. Later, the model was further developed in [336] to avoid the requirement of the enrichment. By splitting particles where the cracking criteria are met into two particles on opposite sides of the associated crack segments, the crack is modelled with no additional degrees of freedom being added in the formulation. By various benchmark examples, the model proves its capability in modelling complex crack patterns in statics and dynamics. Using the CPM, the instability in dynamic fracture was studied and the experimentally observed results, including the limiting velocity, microcrack branching and increase of energy dissipation, were reproduced in [333]. It is found that the existence of voids in the model has little effect on the occurrence of the microcrack branching. To solve the spurious cracking problems which appear in the original CPM [327], a CPM based on nodal integration with updated Lagrangian kernels was proposed in [460]. Crack branching examples are studied and the existence of limiting velocity (related to dynamic instabilities) observed in dynamic crack branching experiments is demonstrated with the simulation results.

In summary, the CPM is quite suitable for problems with complex crack patterns, especially crack branching. The CPM has the following advantages: (1) no representation of the crack’s topology and no crack path continuity are needed; (2) crack branching can happen automatically, no additional criteria are needed and dynamic instabilities related to micro-branches can be captured; (3) it is easily implementable in 3D; (4) no mesh orientation problem. On the limitation side, it is noted that: (1) due to the “discontinuous” representation of the crack surface, special techniques are required to solve the “spurious cracking”

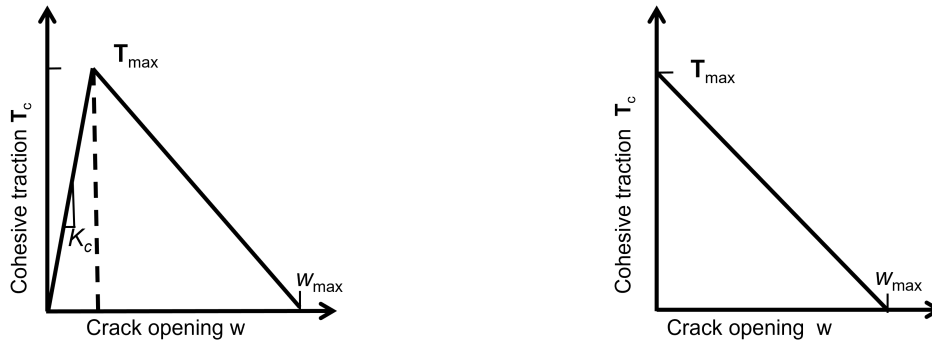


Fig. 2.19 Traction-separation laws for intrinsic (left) and extrinsic (right) CZMs.

problems; (2) since the crack path is approximated via a collection of cracking particles, a finer node distribution is required to increase the accuracy of the model, which may increase the computational cost.

**Cohesive zone models** The cohesive zone model (CZM) is developed to describe the nonlinear behaviour during material failure, and assumes a process zone ahead of the real fracture [121, 27], where a traction-separation law controls the variation of cohesive traction with the separation (width) of the crack. When maximum principal stress reaches the cohesive strength of the material  $T_{max}$ , the crack initiates. With the crack opening, the cohesive traction will decrease and once it has decreased to zero, the maximum crack opening  $w_{max}$  is obtained and complete separation is reached. There are many types of traction-separation laws, and a critical review on these laws and their physical/numerical properties was given in [308]. Depending on the characteristics of the traction-separation law, the CZMs can be divided into two groups: intrinsic and extrinsic CZMs, as shown in Fig. 2.19. In the intrinsic CZM, the cohesive traction first increases with the fracture opening at an initial stiffness  $K$ , while the extrinsic CZM does not have the initial stiffness.

The CZM is generally a concept to describe the nonlinear behaviour in the process zone and can be incorporated with different numerical methods and crack models [104]. For example, it can be employed by XFEM and the phase field model by introducing a length scale. For discrete cracks in a finite element context, cohesive interface elements (elements equipped with a traction-separation law) have been employed extensively. The simulation process of crack branch modelling with CZMs using cohesive interface elements is further discussed in the following paragraphs.

To model crack branching with the intrinsic CZM, the cohesive interface elements need to be assigned on all finite element surfaces before simulation and the displacement field is solved with the traction-separation law. During this process, remeshing is not required

and the crack is allowed to propagate along element boundaries. No additional criterion is needed for crack branching since the branching phenomenon emerges as a natural outcome of the initial-boundary value problem solution [461]. However, because the finite initial slope of the traction-separation law modifies the stiffness of the structure and alters the wave propagation, the intrinsic CZM has issues such as an artificial softening effect, loss of consistency, spuriously high crack velocity (the lift-off issue) (see [378] for a complete discussion about these issues). A remedy to reduce the effect of artificial compliance is to increase, if possible, the initial elastic slope of the traction-separation law, which results in severe stable time step restrictions and may even render the intrinsic approach unsuitable for explicit dynamic calculations, or in ill-conditioning of the tangent stiffness matrices in static or implicit dynamics analyses.

The process for modelling crack branching with the extrinsic CZM is slightly different from modelling with the intrinsic CZM. Instead of inserting all cohesive interface elements first, cohesive interface elements will be assigned adaptively when the criterion (the cohesive traction reaches the cohesive strength  $T_{max}$ ) is satisfied [66]. By doing so, it avoids the artificial softening effects, however, additional issues of the efficient parallelization of extrinsic cohesive interface elements with the change in mesh topology need to be addressed. In addition, the extrinsic CZM has the time discontinuity issue (the traction before and after insertion / activation of an interface element may not be continuous). This is because before cracking, the cohesive traction depends on the stress field within the neighbouring continuum elements while in a subsequent time step following cohesive element insertion, tractions rely on the cohesive law [378]. The time discontinuity leads to oscillatory behaviour, non-convergence in time and dependence on nonphysical regularization parameters [307]. To solve this, different approaches have been proposed to make sure the time continuity condition (the continuity of traction before and after insertion / activation of an interface element) is satisfied [307, 337, 366].

Both intrinsic CZMs and extrinsic CZMs have the problem of mesh dependency and bias since the cracks are only allowed to propagate along element facets. In [17], the macroscopic crack branching was modelled with the extrinsic approach and it is concluded that the occurrence of branching may be very sensitive to the mesh parameters. Due to the dependence on mesh, the crack paths predicted tend to be somewhat inaccurate. The problem can be remedied by using a finer mesh or special mesh operations. By investigating the different levels of mesh refinement for both structured and non-structured meshes, it is found in [10] that finer and unstructured mesh performs better than coarser and structured mesh in predicting the branching pattern observed experimentally. Special operations, such as nodal perturbation and edge-swap topological operation [312], splitting of polygonal finite

elements [227, 412], stress recovery and domain integral [85] are also proposed to reduce and remove mesh bias and dependency in CZMs where physical phenomena associated with dynamic crack branching are successfully captured.

Many successful applications can be found in modelling crack branching using CZMs. With the intrinsic CZM, the crack branching phenomenon was successfully modelled in [461]. The results show that the branching phenomenon has a close relationship with the applied loading and the dynamic crack velocity computed by the intrinsic CZM is in good agreement with experimental observations. By using extrinsic CZM and an advanced topological data structure representation, it is presented in [481] that the extrinsic cohesive modelling of dynamic fracture and emphasised the importance of adopting the extrinsic CZM for the simulation of multiple micro-branches where the results yield improved agreement with experiment compared to [261], which employs a potential-based intrinsic CZM for the same problem. As shown in Fig. 2.20, complex crack branching patterns including both multiple branches and micro-branches are predicted. After investigating the micro-branching process, the numerical results reveal that the increased energy input leads to increased crack surface roughness, longer micro-branches and higher crack speed. Adaptive mesh refinement and coarsening schemes for efficient computational simulation of dynamic cohesive fracture were proposed in [309]. The model successfully captures small branches which are observed experimentally before the crack branching and shows that the formation of micro-branches leads to a lower main crack velocity, which is closer to experimental observations. Though this work uses an advanced topology-based data structure to store the FE discretisation and realize parallelization, examples in three dimensions are not given due to the complexity of the implementation of the extrinsic approach. For more complex problems like dynamic fracture propagation in three dimensions, the hybrid discontinuous Galerkin and cohesive element method has been adopted [277]. The cohesive interface elements are assigned first on all element surfaces before simulation and are not allowed to open by a discontinuous Galerkin formulation. The model is then switched to the extrinsic cohesive crack model when a failure criterion is met. The method is capable of modelling large-scale dynamic crack propagation in three dimensions with powerful computers since it saves from the trouble of extensive updating of mesh information and avoids issues that intrinsic cohesive interface elements bring. A scalable 3D fracture and fragmentation algorithm based on the hybrid, discontinuous Galerkin, cohesive element method was presented in [337] and its ability in capturing complex patterns of cracks including branching were demonstrated. In [33], a fully-Discontinuous Galerkin formulation of nonlinear Kirchhoff–Love shells with CZMs was presented to perform thin body fracture simulations. Three-dimensional simulations including crack branching are given, see Fig. 2.21.

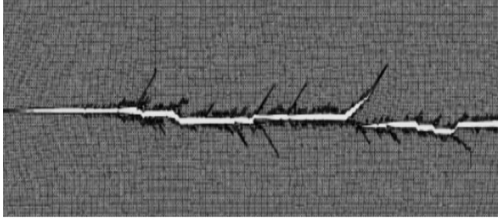


Fig. 2.20 A 2D example of crack branching with CZM [481].

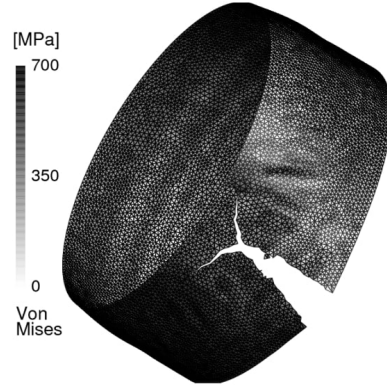


Fig. 2.21 A 3D example of crack branching with CZM [33].

In summary, the CZM is a good choice for the study of dynamic crack branching and can be combined with different models and methods to describe the nonlinear behaviour of the crack. With cohesive interface elements, it is easily incorporated into a finite element framework and has the ability of detecting crack initiation and capturing multiple branches and micro-branches. The mesh dependency problem it suffers can be solved by refining meshes or other special mesh operations, which in turn, may increase the computational cost and complexity of implementation procedure, especially in 3D. A promising approach to avoid these problems is the combination of the cohesive law and the discontinuous Galerkin formulation. Explanations about the approach and its application in dynamic fractures including branching can be found in [33, 277, 378, 337].

### Smearred crack models

**Phase field models** As a recently emerged model, the phase field model (PFM) smears the crack over a certain domain without tracking the crack surfaces. Based on the principle of minimum total potential energy, the PFM solves a fracture problem as an energy minimization problem. The energy functional for simulating crack propagation is first given in [138]:

$$E(\mathbf{u}, \Gamma) = \int_{\Omega} \Psi(\boldsymbol{\varepsilon}(\mathbf{u})) d\Omega + G_c \int_{\Gamma} d\Gamma \quad (2.25)$$

where  $\Omega$  is a domain describing a cracked solid,  $\Psi$  denotes the elastic energy density,  $\boldsymbol{\varepsilon}(\mathbf{u})$  is the strain field, and  $G_c$  is the fracture toughness, which yields an admissible crack set  $\Gamma \subset \Omega$ .  $\mathbf{u}$  is the displacement field and is discontinuous across  $\Gamma$ . Bourdin et al. [60] devised its

regularized formulation:

$$E_\varepsilon(\mathbf{u}, \varphi) = \int_{\Omega} f(\varphi) \Psi(\varepsilon(\mathbf{u})) d\Omega + G_c \int_{\Omega} \left( \frac{1}{4l_0} (1 - \varphi)^2 + l_0 |\nabla \varphi|^2 \right) d\Omega \quad (2.26)$$

where  $\varphi$  is damage-like crack phase-field parameter with 1 representing the unbroken part and 0 the totally broken part.  $f(\varphi)$  is the energetic degradation function to help prevent numerical difficulties where the material is broken (e.g.  $\varphi = 0$ ). The width of transition zone is controlled by the length scale  $l_0$ . When  $l_0$  is very small, the diffusive crack presented by the phase field would approximate a sharp crack solved in discrete crack approaches. With the help of Eq. (2.26), the scalar field (the phase field) turns the intact material into a broken material smoothly instead of treating cracks as strong discontinuities. This enables PFM to overcome difficulties in modelling complex crack problems in three dimensions with traditional numerical methods. Because the propagation of the crack is obtained through the solution of the differential equation, the PFM also avoids the need of extra criteria for crack propagation and additional work to track the fracture surface algorithmically [54].

The ability of PFM to simulate crack propagation and branching in two and three dimensions has been demonstrated [54, 180, 41, 450, 448, 281]. The quasi-static phase-field crack model was extended to a dynamic model in [54] and both 2D and 3D crack branching examples were used to show that the combination of the phase-field model and local refinement strategy is an effective method for simulating complex crack problems. In [180], a phase field model was established based on variational principle and its performance was demonstrated by means of representative 2D and 3D quasi-static and dynamic model problems including branching. In [41], the microbranching instability occurring in dynamic crack propagation was investigated with a 3D variational phase-field model. It is found that the microbranching process is a three-dimensional instability and the branching patterns are strongly influenced by phase-field internal length scale. To overcome the limitations of the strong dependence of crack branching patterns on internal length scale, a regularized phase field based cohesive model was introduced [450, 448, 281], which is insensitive to the length scale and capable of capturing multiple crack branching.

Compared with remeshing models which need the separation between the elements to describe the crack surface, PFMs are capable of modelling multiple branches, widening of damage zone (fracture roughness) and micro-branches. Regarding multiple branches, PFMs for simulating complex crack patterns were presented in [485] [484] and [355]. Multiple crack branches phenomenon is observed, which demonstrates the advantages of PFM in modelling complex crack propagation in rocks. Regarding micro-branches, it refers to the branch of which length is in order of length-scale of simulation [42]. Fig. 2.23 shows a

3D crack branching example with micro-branches based on PFM [41]. From the figure, a slightly curved crack front (the crack tunnelling feature) and slightly rough crack surfaces can be observed. Regarding the widening of the damage zone before branching, it can be seen as an increase in fracture surface roughness prior to branching and has been observed in experiments [347]. According to the branching mechanism proposed in [350–352], a widening damage process-zone appears before crack branching due to the increasing fracture roughness (mirror-mist-hackles transition). Then, after branching, as the crack branches go on propagating, the damage zone becomes “thinner”, indicating that the crack surfaces turn smooth again. If the energy provided is sufficiently high, the “widening-thinner process” is repeated, and secondary branches can be observed. Fig. 2.22 shows a 2D crack branching example, where the widening of the damage zone before branching and multiple branches are observed.

Given its strong ability in modelling crack branching without remeshing and external criteria, more authors choose to apply PFM for the study of the dynamic crack branching aiming at providing new analyses of the mechanisms behind this phenomenon. The crack velocity, the crack branching angle, the crack branching criterion, as well as the sensitivity of numerical simulation parameters to crack branching are studied.

In terms of the crack velocity, since the crack tip is not uniquely defined in PFM [180], a number of approaches are proposed to measure the crack tip position. In [54], the propagation velocity was calculated explicitly by finding the crack tip with a certain defined phase-field value. In [451], the crack speed was computed from using the slope of the line that best fits the three points, in a least square sense. And in [181], the velocity was obtained implicitly by using the crack surface velocity to represent the crack speed. All of the approaches are reasonable due to the definition of the crack tip position being physically implicit in PFM. Regarding the branching angle, similar conclusions are made in [451, 181] that with increasing loading amplitude or velocity, the crack branches earlier and the branching angle gets smaller. Various branching criteria have been examined. In [179], crack propagation in two dimensions was studied using PFM and it is found that the branching instability starts with a critical speed of  $0.48c_S$ , where  $c_S$  is the shear wave speed. In [451], the validity of the velocity branching criterion was denied by proving that crack speed at the moment of branching is very sensitive to the width of the sample with a 2D PFM model. Instead of crack velocity, the phase field velocity and the crack surface velocity was preferred in [181] as local and global indicators for branching. Through studying the limiting velocity, crack branching and velocity-toughening mechanisms with the PFM, it is proposed in [42] that the branching occurs when the local energy release rate exceeds twice the critical energy release rate. By quantifying the energy flux into the crack tip and fracture energy, it is confirmed in [423] that



the crack bifurcation obeys an energy criterion as it is observed that the crack bifurcation of PMMA always occurs with the energy flux into the crack tip exceeding a critical value. In [250], mesh convergence and length scale sensitivity in dynamic crack simulation with PFMs are systematically analysed. Quantitative evaluation of branching angles and crack tip velocity and comparison between PFM simulation results and experimental results are provided.

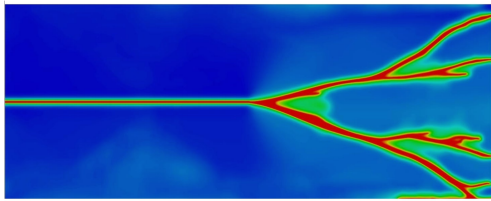


Fig. 2.22 A 2D example of crack branching with PFM [112].

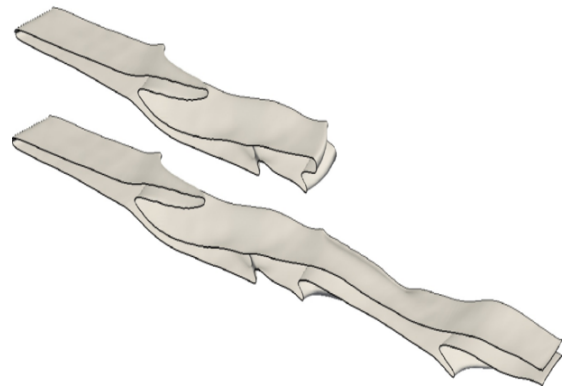


Fig. 2.23 A 3D example of crack branching with PFMs, showing isosurfaces of phase field at  $\phi = 0.3$  [207].

The crack branching phenomenon is very sensitive to numerical simulation parameters in PD. For example, the solution scheme is influential, e.g. the monolithic scheme and the staggered scheme may lead to different crack patterns [238] and different branching moment [483]. The mesh size is also a significant factor, e.g. multiple crack branches can only be captured by sufficiently refined meshes while a different mesh size may result in different branching time [180, 181, 451, 413, 483].

The sensitivity of the branching phenomenon to the mesh size leads to limitations of PFM. The computational cost will increase since the mesh needs to be fine enough for the phase field to represent the accurate position of the crack. However, PFM is a very promising model for crack branching studies with the following advantages: (1) no need for initial crack length settings and no external criteria for branching since the crack patterns can be automatically captured by solving the equation based on energy minimisation; (2) straightforward implementation in three dimensions; (3) capable of modelling multiple branches, widening of damage zone (fracture roughness) and micro-branches.

**Nonlocal models/ gradient models/ viscous models** When modelling failure caused by progressive distributed damage, the material exhibits strain-softening and the governing

differential equations may lose ellipticity, which renders the boundary value problem ill-posed and causes physically meaningless, mesh-dependent finite element results [202]. To solve these problems, non-local models, gradient models and viscous models are commonly employed. By introducing a characteristic length into the discretisation, these models “smear” the crack over a certain domain involving several elements and avoid representing the crack topology and crack tracking algorithms [325].

An integral-type nonlocal model is defined as a model in which the constitutive law at a point of a continuum involves weighted averages of a state variable over a certain neighbourhood of that point [31]. The integral formulation in the model allows the introduction of a characteristic length that qualifies the neighbourhood over which the parameters/calculated numbers get “smeared”. The gradient models can be constructed by including higher-order gradients directly in the damage loading function [208]. The higher-order gradients can be employed to smooth the non-uniformity or singularities in the strain field when regularisation of singularities or discontinuities is required. The viscosity models can be regarded as introducing higher order time derivatives and a length scale associated with the viscosity is employed, which also restore the well-posedness of the BVP or initial BVP [325]. Detailed explanations of these models are given in literature [31, 143, 325], here we mainly focus on the performance of these models in modelling and investigating dynamic crack branching.

Examples of the application of nonlocal models and gradient models to dynamic crack branching problems can be found in [446, 439]. With an integral-type nonlocal continuum damage model, simulations of dynamic crack branching in PMMA were conducted and the dynamic crack branching instabilities were studied in [446]. It is found that the selection of the rate-dependence damage law and the critical strain for damage initiation are necessary to predict crack patterns, crack tip velocities and dissipated energies accurately. A figure of crack branching with the integral-type nonlocal continuum damage model is shown in Fig. 2.24. We note that just like PFM, the nonlocal models are also capable of capturing the multiple branches, widening of damage zone (fracture roughness) and micro-branches. In [439], a localizing gradient damage model is proposed with micro inertia effect for modelling dynamic fracture propagation in quasi-brittle materials, which resolves the mesh sensitivity issue and spurious damage growth appeared in the conventional gradient damage models and shows good performance in reproducing crack patterns (from a straight crack, to sub-branching, and finally to macro branching), crack velocities, and fracture energies observed in the experiments.

The advantages of the nonlocal models, gradient models and viscous models are: (1) representation of the crack topology and crack tracking algorithms are avoided; (2) the issue of mesh dependency and additional criteria to control crack branching are avoided; (3) they

are capable of modelling crack surface roughness and micro-branches. Their limitations lie in that (1) physical inconsistencies may appear in the characterization of crack kinematics due to the wrong selection of related parameters, e.g. parameters for rate-dependence damage law; (2) computational cost may significantly increase due to the increase of mesh density to get a more accurate prediction of the crack.

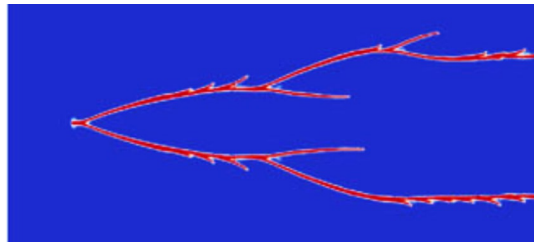


Fig. 2.24 A numerical example of crack branching with nonlocal models [446].

### Numerical methods

Numerical methods are employed to solve the equations of the bulk material. According to whether spatial derivatives are employed or not, the numerical methods can be further classified into continuum methods and discontinuum methods. The simulation of crack branching is a highly challenging problem due to its complexity. Until now, numerous methods have been applied to the modelling of crack branching with varying success. A superior method should have the following characteristics to better capture the phenomenon of crack branching:

- The ability of capturing different crack branching patterns, including macro crack bifurcation, micro-branches, a single crack with multiple branches and multiple cracks with branches.
- Good agreement with the experimental results and theoretical prediction in branching features, such as branching angles and the crack velocity.
- Relatively easy and robust implementation process with affordable computational cost.

Specifically from the view of crack branching, this subsection summarises and compares different numerical methods. For each method, the physical and mathematical principles are first introduced, followed by the explanation of crack branching simulation, after which historical and state-of-the-art applications in crack branching simulation are summarized with discussions of both advantages and limitations, see Table. 2.3. The emphasis differs in applications of different methods, for example, focusing more on verification (using various

branching examples to prove the superiority of the models built by the improved numerical methods) or focusing more on the analysis (analysing the mechanism behind the crack branching phenomenon with these models).

Table 2.3 Numerical methods for crack branching simulation.

Numerical Methods	Advantages	Limitations
FEM	flexible and robust	remeshing is required if the adaptive FEM-based model is used, which is difficult in 3D
XFEM	independent of mesh	needs special enrichment for junctions and branches
BEM	reduces dimensions	not well-suited for nonlinear problems
MMs	eliminate difficulties mesh-based methods brings	have boundary implementation, instability, numerical integration of the weak form, high computational cost issue
PD	avoids remeshing	has relatively high computational cost and difficulties in dealing with boundary conditions
DEM	well-suited when considering heterogeneity	limited in granular materials, awkward in predicting macroscopic properties and has relatively high computational cost

## The continuum methods

**The finite element method** The idea behind the finite element method (FEM) is to break the continuum into a number of simple geometric elements and estimate the characteristics of the continuous domain by assembling the discretised equations per node elementwise [320]. The method is suitable for modelling bulk materials. It has been applied to a wide range of crack problems [77] and can be combined with nearly any crack model due to its flexibility and robustness, see Fig. 2.13.

Depending on how the branching is simulated, a commonly used adaptive FEM-based model (FEM combined with remeshing models) is discussed. We note that the term “adaptive FEM-based model” here does not include the models based on both finite element method and cohesive elements, which are discussed in § 2.2.4. The simulation process of crack branching using the adaptive FEM-based model mainly includes the establishment and solution of the deformation equation, the selection of the propagation criterion, and the meshing strategy. By establishing and solving the deformation equation, the crack footprint can be obtained. Since the crack branching process is dynamic, the inertial force and the acceleration terms need to

be considered. Here the Newmark method [276] is used to solve the governing equations and the resulting system is given below:

$$(a_0\mathbf{M} + \mathbf{K})\{\mathbf{u}\}^{n+1} = \{\mathbf{F}\}^{n+1} + \mathbf{M}(a_0\{\mathbf{u}\}^n + a_2\{\dot{\mathbf{u}}\}^n + a_3\{\ddot{\mathbf{u}}\}^n) \quad (2.27)$$

$$\{\ddot{\mathbf{u}}\}^{n+1} = a_0(\{\mathbf{u}\}^{n+1} - \{\mathbf{u}\}^n) - a_2\{\dot{\mathbf{u}}\}^n - a_3\{\ddot{\mathbf{u}}\}^n \quad (2.28)$$

$$\{\dot{\mathbf{u}}\}^{n+1} = \{\dot{\mathbf{u}}\}^n + a_6\{\ddot{\mathbf{u}}\}^n + a_7\{\ddot{\mathbf{u}}\}^{n+1} \quad (2.29)$$

where  $\{\ddot{\mathbf{u}}\}$ ,  $\{\dot{\mathbf{u}}\}$ ,  $\{\mathbf{u}\}$ ,  $\{\mathbf{F}\}$  are the global vectors of nodal acceleration, nodal velocity, nodal displacement and nodal load, respectively; the superscript  $n$  represents time step,  $\mathbf{M}$  and  $\mathbf{K}$  are the mass matrix and the stiffness matrix, respectively. The coefficients  $a_0 - a_7$  are the parameters in the Newmark method [287].

The next step is to determine whether the crack will branch or not. The branching criterion for the adaptive FEM-based model can only be an external criterion, (see § 2.2.3) which increases the difficulty of the simulation. The time of branching, the branching angles and the branching speed need to be determined. Due to the singularity of the crack tip, determination of appropriate physical mechanisms and formula to calculate the associated parameters remains a challenge.

After obtaining the crack footprint, the mesh needs to be updated. It is possible to model one or two branches, but as more branches develop, remeshing becomes very complex. Both the singularity at the crack tip and the small angle between crack branches require a heavily refined mesh and may result in a large increase in computational cost.

To the best of the authors' knowledge, there do not appear to be many examples using the adaptive FEM-based model to simulate crack branching due to its implementation complexity. In [287], the dynamic crack branching phenomenon with a moving FEM (adaptive meshes) was modelled based on Delaunay triangulation and a switching method using the dynamic  $J$ -integral. The moving FEM has the advantage of exactly satisfying the boundary conditions in front of and behind the propagating crack tip dynamically. The switching method using the dynamic  $J$ -integral provides an accurate way of evaluating the dynamic  $J$ -integral regardless of crack path, which is especially applicable when the crack tips are very close to each other after branching. The generation of dynamic crack branching phenomenon in Homalite-911 is successfully modelled and the simulated results agree well with experiments [287]. However, only examples for a crack with two branches are presented and for more complicated crack branching patterns are not discussed. Using a further developed remeshing strategy, more complicated crack branching problems including multiple crack bifurcation were investigated [419]. A comparison between numerical and experimental results was provided but the calculation efficiency was not mentioned. We conclude that the adaptive FEM-based model

still faces challenges when dealing with crack branching as discussed above, especially in three dimensions.

**The extended finite element method** In order to solve mesh dependency problems, the extended finite element method (XFEM) was developed in [34, 264]. Similar to FEM, it is suitable for modelling bulk materials. To simulate crack propagation, XFEM uses the enriched shape function with discontinuous features to represent the discontinuity [488]. By doing so, the displacement discontinuity can be captured and the crack can propagate on any surface within one element instead of along element boundaries. Thus, remeshing and mesh dependency issues appearing in discontinuous problems with FEM can be overcome. However, the use of enrichment functions also brings the issue of incompatibility between accuracy of the solution and conditioning of the system matrix, especially when solving large 3-D problems. The condition numbers of the stiffness matrix can be worse if one utilizes enrichment functions, and thus it can affect the accuracy of the solution. Several studies have attempted addressing this issue [167, 166, 449].

Generally, there are two ways to enrich an approximation: intrinsic enrichment (enriching the basis vector) and extrinsic enrichment (enriching the approximation) [212]. The idea for intrinsic enrichment is to enhance the approximation space by building new basis functions which are derived from a specific problem into the standard approximation space. For instance, the asymptotic near tip displacement field can be built into the basis functions so that the singularities at the crack tip can be represented. For extrinsic enrichment, the enrichment functions are added to the standard approximation in specific zones, and as a result, the computational cost is reduced.

Though the characteristic of XFEM facilitates its application in modelling internal or external boundaries such as holes, inclusions, or cracks, the simulation process of crack branching with XFEM is not an easy task. First, appropriate enrichment schemes need to be considered for the element with the crack branch junctions and crack branches. Secondly, though the computational cost is less expensive without remeshing, the simulation process still requires external branching criteria, bringing issues such as the decision of reliable criteria and the calculation of related crack parameters. Thirdly, XFEM typically uses the level set method to track fractures, but as fracture branches increase the associated operation becomes increasingly complicated, especially in 3D cases. In the context of the crack branching problem, the displacement approximation  $\mathbf{u}^h$  with the partition of unity is

expressed as [103]:

$$\mathbf{u}^h(\mathbf{x}) = \sum_{i \in N} \mathbf{u}_i N_i + \sum_{j \in N^H} \mathbf{a}_j N_j H(\mathbf{x}) + \sum_{k \in N^{CT}} N_k \left( \sum_{\alpha=1}^4 \mathbf{b}_k^\alpha \Phi_\alpha \right) + \sum_{m \in N^J} \mathbf{c}_m N_m J(\mathbf{x}) \quad (2.30)$$

where  $\mathbf{u}_i$  is the vector,  $N_i$ ,  $N_j$ ,  $N_k$  and  $N_m$  are the standard finite element shape functions associated with node  $i$ ,  $j$ ,  $k$  and  $m$  respectively;  $\mathbf{a}_j$ ,  $\mathbf{b}_k^\alpha$  and  $\mathbf{c}_m$  represent the nodal enriched degrees of freedom associated with the Heaviside function  $H(\mathbf{x})$ , near tip asymptotic field function  $\Phi_\alpha$  and junction function  $J(\mathbf{x})$ , respectively;  $N$ ,  $N^H$ ,  $N^{CT}$  and  $N^J$  are the set of nodes to enrich for the crack, crack tip and junction.

Progress has been made on modelling the crack branching with XFEM. In [103] a methodology was developed to construct the enriched approximation based on the interaction of the discontinuous geometric features and calculated the SIF of static cracks with multiple branches. This can be used for static cracks, but the propagation of the dynamic crack branching process is not taken into consideration. To improve the modelling of dynamic crack propagation by XFEM, a new methodology was proposed in [35] for treating elements that contain crack tips, which allows the velocity field of the element containing the crack tip can change smoothly from a partially cut element to a fully cut element. The crack path and velocity can be determined directly by the loss of hyperbolicity criterion, which facilitates the modelling of dynamic crack growth problems, including crack branching. However, only a relatively simple bifurcation phenomenon is captured, while fracture roughness and micro-branches can not be captured, see Fig. 2.25. To seize the discontinuity around the junction of a branched crack, the enrich scheme of the element crossed by two separated cracks, the element embedded by a junction, and the way of constructing the diagonal mass matrix for the branched element were introduced in [456], with which the initial branching process of a moving crack (the main crack develops two branches) is successfully simulated. However, this method requires an increase in additional degrees of freedom. For more complex branching problems with increasing degrees of freedom in one element, an enhanced XFEM coupling the phantom node method [409, 80] was proposed and proved its robustness and accuracy in handling the complex branched crack problems.

In summary, the XFEM possesses the following advantages: (1) lower computational cost without the need of remeshing; (2) suitable for cracks with complex geometry or problems with geometric nonlinearities because of mesh independence. These advantages allow the XFEM to become a powerful and promising tool in the simulation of complex crack problems. However, the XFEM has imitations when dealing with multiple interacting and branched cracks and micro-branches, since the computational cost increases as the number of cracks grows and its formulation becomes increasingly complex. For branches or junctions, special

discontinuous displacement enrichment needs to be developed and external criteria for the injection of the enrichment are needed. Additionally, because of the lack of a reliable crack branching criterion, prediction of crack propagation and branching remains a challenge [325].

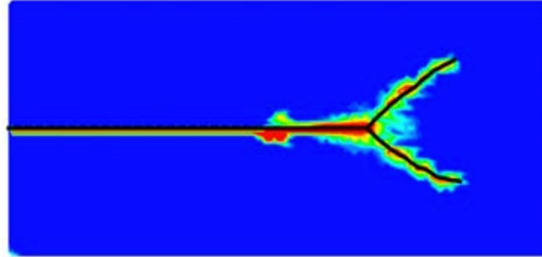


Fig. 2.25 A numerical example of damage for crack branching with XFEM [35].

**The boundary element method** The boundary element method (BEM) is also widely used in crack simulations due to its ability to automatically follow the propagation of the crack with limited remeshing and its inherent accuracy [14]. The BEM is designed for solving boundary value or initial value problems and formulated in terms of boundary integral equations [243]. Instead of discretising the whole domain into volume elements, the BEM only discretises the domain boundary for interpolation approximation. The basic process of modelling crack propagation with BEM is similar to FEM. However, remeshing is done by only adding the elements at end of the crack tip without changing the whole mesh.

The displacement integral equation at an interior point  $\mathbf{X}$  in the absence of a body force for linear elastic crack problems is given in [14]:

$$\mathbf{u}_i(\mathbf{X}) = \int_{\Gamma_S + \Gamma_n^+ + \Gamma_n^-} \mathbf{U}_{ij}(\mathbf{X}, \mathbf{x}) \cdot \mathbf{t}_j(\mathbf{x}) d\Gamma - \int_{\Gamma_S + \Gamma_n^+ + \Gamma_n^-} \mathbf{T}_{ij}(\mathbf{X}, \mathbf{x}) \cdot \mathbf{u}_j(\mathbf{x}) d\Gamma \quad (2.31)$$

where  $\Gamma_n^+$  and  $\Gamma_n^-$  represent the upper and lower crack surfaces, respectively,  $\Gamma_S$  the outer boundary,  $\mathbf{u}_j$  the boundary displacement,  $\mathbf{t}_j$  the traction,  $\mathbf{U}_{ij}$  the fundamental solutions for displacement, and  $\mathbf{T}_{ij}$  the traction. Fig. 2.26 shows a schematic illustration of crack branching simulated by BEM.

The difficulties of BEM for fracture problems reside in the coincidence of crack nodes, giving rise to a singular system of algebraic equations. Different techniques such as the sub-region boundary element method (SBEM), displacement discontinuity methods (DDM), dual-boundary element method (DBEM) and dual-reciprocity boundary element method have been developed to solve this problem [265]. Pioneering work modelling dynamic crack branching with BEM was presented in [382], where crack growth and branching criteria were combined and a time-domain boundary integral equation system is established. The



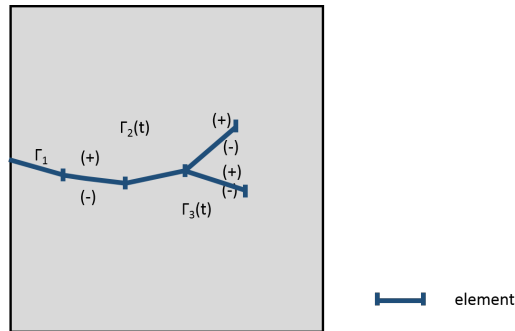


Fig. 2.26 A schematic illustration of crack branching with BEM.

crack propagation speed and the SIF were calculated, showing good agreement with the experimental observations. Since then, examples for BEM simulation of crack branching have been presented in the literature [346, 464, 367]. A complete set of piezoelectric Green's functions in closed form was introduced and a solution scheme based on the boundary integral equation method was developed in [346] to analyse plane cracks in piezoelectric solid. A double-branched crack model is used to verify this scheme. In [464], the crack-tip displacement discontinuity elements were placed at the corresponding crack tip on top of the constant displacement discontinuity elements that cover the entire crack surface. By using such elements and the SIF as a propagation criterion with a known branching angle, complex crack problems including a branched crack example are employed to demonstrate the efficiency and accuracy of the proposed method. In [367], the dual boundary element method (DBEM) was applied to the analysis of mixed-mode multiple-crack growth including branching cracks, where the SIF was evaluated via the  $J$  integral and the incremental analysis was used to define the direction and the extension of multiple interacting cracks. Other approaches focus on the study of the physical mechanisms behind the branching phenomenon. The fast running cracks branching under different bi-axial loading conditions was investigated in [338]. It is found that branching depends on the opening mode SIF, the crack velocity, and the orientation on the maximum circumferential stress in the vicinity of the crack tip. In [251], the crack branching process was modelled by using an indirect BEM specially developed to treat the kink points of propagating cracks in brittle solids and the mechanism of secondary crack initiation and propagation were studied. The results show that the formation of the wing crack and the secondary crack caused by the crack tip and the crack kink point may lead to a quasi-static crack bifurcation process. In [130], the BEM was applied to the analysis of the branched and intersecting cracks in statically and dynamically loaded plates. The influences of angles between branches of the crack and dimensions of the plate for the star-shaped crack on a dynamic SIF were analysed. In [392], a hydraulic fracture model with a three-dimensional displacement discontinuity method was developed and the interaction

between multiple cracks and branches was investigated. The heterogeneity of solid rocks is one reason for crack branches, which further results in a complex fracture network.

The BEM offers clear advantages. The stress field in the vicinity of the crack tip can be accurately calculated and the computational efficiency can be greatly increased due to the reduction of the dimension. Nevertheless, it still suffers from the inability to model crack propagation and branching autonomously as it needs external criteria. Besides, the application of BEM in nonlinear problems is limited, as it still requires that the fundamental solution is expressed in terms of Green's functions [325].

**The meshfree methods** When dealing with crack branching problems, the traditional FEM has the limitation of remeshing, which is time-consuming especially in 3D. The XFEM avoids the need of remeshing, however, it is awkward when dealing with multiple interacting and branched cracks, since the computational cost increases as the number of cracks grows and its formulation becomes increasingly complex. Meshfree methods (MMs) were devised with the objective of eliminating part of the difficulties associated with reliance on a mesh to construct the approximation [280], providing an advantage in dealing with crack growth problems.

In general, MMs refer to numerical techniques that do not require any predefined mesh information for domain discretisation, and they use a set of points scattered within the problem domain as well as on the boundaries of the domain to represent the problem domain and its boundaries [433]. MMs model the bulk material as a continuum. Modelling discontinuities in MMs can be classified into two types generally: methods based on the intrinsic and extrinsic enrichment and modification of the weight function [280]. The second type can be further classified into the visibility method, the diffraction method, the transparency method, and the "see through" and "continuous line" method [334]. Detailed descriptions of these MMs and their classifications, advantages, limitations, and computer implementation aspects can be found in [334, 325, 280, 239, 487, 191]. Here, we only give a brief introduction of some popular MMs including the smoothed particle hydrodynamics method (SPH), the element-free Galerkin method (EFGM) and reproducing kernel particle method (RKPM), and focus more on their ability of capturing crack branching.

The smoothed particle hydrodynamics method (SPH) is a pure Lagrangian, meshfree method, which was first developed to model hydrodynamic flows and then extended to solid mechanics [268, 232]. In SPH, the domain is discretised into particles and each particle interacts with its neighbour particles within its influence domain through a kernel function. Early work on studying crack formation with SPH can be found in [233, 348, 330, 331]. In most of the work, the SPH is based on Eulerian kernels and a crack can occur naturally

due to separating particles. By comparison with the traditional mesh-based methods, SPH avoids mesh dependence when dealing with cracks. However, it suffers from problems such as spurious instabilities, expensive computational cost and inaccurate crack path prediction [345, 280]. To solve these problems, Lagrangian kernels instead of Eulerian kernel functions are employed [329, 431]. However, Lagrangian kernels require specific strategies to deal with fractures since neighbour particles do not change during a simulation. A commonly used strategy is the visibility method, in which the displacement discontinuity is modelled by excluding the particles on the opposite side of the crack in the approximation of the displacement field under the assumption of an opaque crack boundary [334]. Recently, a strategy called “pseudo-spring” was developed in [74] to facilitate SPH to model crack propagation without any numerical artifact. The crack path can be tracked automatically by the broken pseudo-springs. Using the Pseudo-Spring smoothed particle hydrodynamics method (Pseudo-Spring SPH), the crack propagation and branching in 2D and 3D was simulated and effects of tensile loading amplitude on crack branching were studied in [194].

The element free Galerkin method (EFG), first developed in [36], is a method based on moving least-square (MLS) interpolants. The EFG requires only nodal data without the requirement of element connectivity. Compared with SPH, the EFG avoids the calculation of nodal volumes and obtains the gradient fields directly by taking the derivatives of the interpolants with respect to spatial variables, which increases the accuracy and stability [36]. This feature makes it quite suitable for static and dynamic crack problems. The extended element free Galerkin (XEFG) method was proposed in [326, 335] for modelling cohesive crack initiation, growth and junction in two and three-dimensional statics and dynamics. However, the closure of the crack along the front is ensured through near-tip enrichment, which leads to the difficult selection of near-tip enrichment fields in large strain or non-linear materials. To simulate crack propagation in non-linear solids including large deformations, an XEFG was proposed in [489], which closes the crack tip without near-tip enrichment. The entire crack is enriched by the sign function. The domain-decrease method is used to remove the branch enrichment from the discontinuous displacement field. The method is successfully applied to crack branching problems in 2D and the results agree well with the experiment results, see Fig. 2.27. Later, the method was extended to 3D by employing an extrinsic discontinuous enrichment and adding a Lagrange multiplier field along the crack front to close the crack in [53]. In this way, the computational cost was further decreased. The method proved to be capable of modelling initiation, branching, growth and coalescence of an arbitrary number of cracks in non-linear solids by different benchmark examples. Fig. 2.28 shows the branching example provided in [53], which is a “2.5D” example rather than a real 3D example. The ability of the method for simulation of real 3D crack growth is

demonstrated by another example of a circular-cylindrical chalk bar under torsion, which is not shown here since this example doesn't include the crack branching phenomenon.

To develop more accurate and efficient mesh-free interpolation functions, the reproducing kernel particle method (RKPM) was introduced as an improvement of the continuous SPH approximation in [241]. It maintains the advantages of SPH and gives more accurate results because of the addition of a correction function. In [161], the dynamic failure and fragmentation with a semi-Lagrangian RKPM were studied, which successfully alleviated mesh distortion difficulties associated with the Lagrangian FEM. In [218], a virtual internal bond model with RKPM was used to model the propagation of cohesive cracks. The capability of the model to predict the onset of crack path instabilities is demonstrated, simulations of crack tip instabilities and branching are conducted, and theoretical analysis of branching is given.

The MMs eliminate difficulties of mesh-based methods, such as mesh generation for complex 3D models, effect of distorted or low quality meshes on accuracy, adaptive remeshing resulting from dynamic problems. However, they still suffer from implementation of boundary conditions, high computational cost, instability and inconsistency problems. In addition, when modelling crack branching, crack surfaces representation and crack tracking algorithms are usually required, which introduces additional challenges associated with the numerical integration of the weak form through tracking complex crack geometry, especially for tracking complex 3D crack geometry.

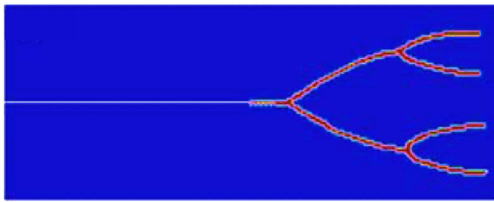


Fig. 2.27 A 2D example of crack branching with MMs [489].

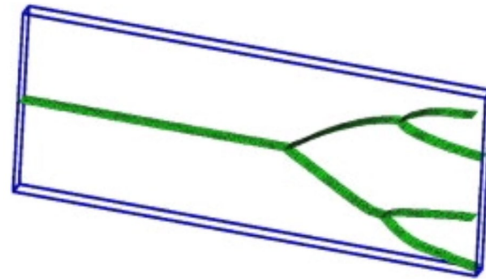


Fig. 2.28 A 3D example of crack branching with MMs [53].

### The discontinuum methods

**The peridynamics** As a promising tool for crack problems, peridynamics (PD) is a new continuum mechanics formulation originally developed in 2000 [394]. Detailed description of PD can be found in § 2.3. In the following paragraphs, applications of PD for crack branching are discussed from three perspectives.

First, by employing or improving the PD, demonstration of capturing complex crack patterns with crack branching and multiple crack branches examples is given. In [356], the dual-horizon PD formulation was proposed, which naturally includes varying horizon sizes and completely solves the “ghost force” issue [357, 332]. In [486], the extended non-ordinary state-based PD was proposed, where the stress-based failure criteria are implemented. The breakage of bonds is determined by the mean stresses between the interacting material points rather than the stretch of bonds. An adaptive refinement algorithms for 2D peridynamic grids was employed in [115] and as a consequence, computational resources are efficiently employed. All of the PD methods above select crack branching examples to prove their capability.

Secondly, after demonstrating the ability of capturing complex crack patterns, the PD is applied to capture various branching phenomena, including crack surface roughening, successive branching, micro-branches and multiple branches. Then numerical results from PD are compared with numerical results from other methods or results from experiments and theories. It is found in [169] that before branching the damage zone becomes thicker through PD simulation, which is similar to the roughening before branching observed in the experiments. Later, it is found that the PD model captures experimentally observed successive branching events and secondary cracking [170]. PD simulation demonstrating capture of small branches in a glass plate before the crack splits into two main branches is presented in [10]. As loading increases, multiple branches are observed in soda-lime glass under stress on boundaries [49], see Fig. 2.29. The widening of damage zone before branching can also be observed in the figure. With a 3D PD model, a local crack front bifurcation growing into a micro-branch was simulated [63], which quickly arrests or grows further into macro-branches. Distinct features on the crack surface due to the localized bifurcations and micro-branches are also captured with the model, known as “mirror”, “mist” and “hackle” fracture surfaces in experimental observations [351], see Fig. 2.30.

Thirdly, through the observation of various phenomena, influencing factors and the mechanisms of crack branching are discussed and analysed. It is summarized in [169] that reflecting stress waves from the boundaries have a strong influence on the shape and structure of the crack paths in dynamic fractures. Later, it is explained in [47] that why in the simulation of [169] the propagation velocity of a dynamic crack is influenced by the horizon size. This is because the crack propagation velocity, crack branching angles and branching time are independent of the horizon size only in the condition that the fracture process does not interact with the stress waves. The branching moment and velocity are found to be very sensitive to the micro-modulus function in [84] as the branching velocity after the first branching moment can slightly increase or decrease or stay constant under

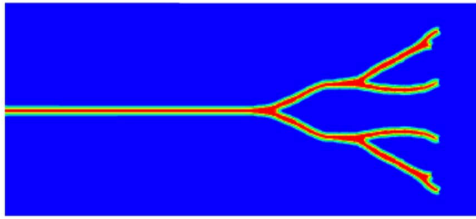


Fig. 2.29 A 2D example of crack branching with PD [49].

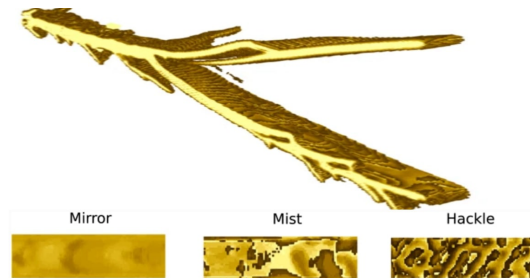


Fig. 2.30 A 3D example of crack branching with PD [63].

various micro-modulus functions. Through PD simulations under various conditions, In [49], it is proposed that stress waves pile up around the crack tip and lead to “migration” of damage sufficiently large, thus the material in front of the original crack tip becomes relaxed and the crack branching ensues. In [63], the influence of PD horizon, dimensionality and specimen size on dynamic fracture with PD analysis were investigated. It is found that all of these factors have an influence on the crack branching patterns.

Generally speaking, the PD has been observed to perform well in modelling branching problems by circumventing difficulties in remeshing and the requirement of an additional branching criterion. In addition, it has the ability of modelling multiple branches, widening of damage zone (fracture roughness) and micro-branches. However, more research is required to improve existing PD methods for better computational efficiency compared with traditional methods such as FEM. In addition, as a nonlocal method, the implementation of boundary conditions needs to be considered.

**The discrete element method** Originally developed in [98], the discrete element method (DEM) has been used in the modelling of jointed structures and granular materials. DEM models the bulk material as a discontinuum and can be applied in modelling of fracturing and fragmentation, where the discontinuities are the natural outcome of the deformation process [201]. As a discontinuum method, the DEM treats a material medium as an assembly of distinct particles, the motion of particles is governed by Newton’s laws, and forces between particles are calculated according to the small overlap between them. In DEM crack simulation, when the maximum stress exceeds the tensile or shear strength,

cracks initiate and propagate [265]:

$$\begin{aligned} F_n &= k_n u_n \\ \Delta F_s &= k_s \Delta u_s \\ \frac{|F_s|}{A} &\leq c_d + \frac{F_n \tan \beta}{A} \end{aligned} \quad (2.32)$$

where  $F_n$  is the normal force,  $A$  the area,  $k_n$  the normal stiffness,  $u_n$  the normal displacement,  $\Delta F_s$  the change in shear force,  $k_s$  the shear stiffness,  $\Delta u_s$  the incremental shear displacement,  $c_d$  the cohesion, and  $\beta$  the joint friction angle. An example of fracture simulation using the DEM is given in Fig. 2.31.

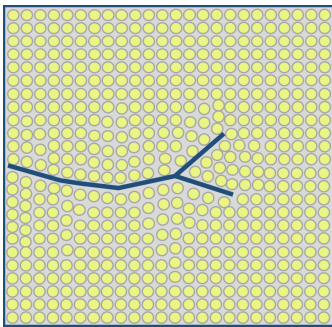


Fig. 2.31 A schematic illustration of crack branching with DEM.

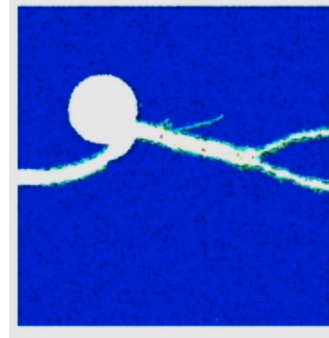


Fig. 2.32 A numerical example of crack branching with DEM [178].

DEMs can be classified with various criteria, e.g. the type of contact between bodies, the representation of deformability of solid bodies, the methodology for detection and revision of contacts, and the solution procedure for the equation of motion [236]. Though solution procedure for modelling crack propagation with DEM is different with different deformability of solid bodies (the explicit and implicit one), some steps are indispensable [201]: (1) identification of the unit (rock blocks, material particles, mechanical parts or fracture systems) system topology; (2) formulation and solution of equation of motion of the individual units; (3) the detection and updating of varying contacts (or connectivity) between the units as the consequences of their motions and deformations. The DEM differs from other methods based on continuum mechanics e.g. FEM in that the contacts between units are varying with time and deformation while remaining fixed in other methods. The DEM is most successful in modelling granular materials. Applications in modelling continuum materials are being explored, but have various limitations.

Due to the unique nature of DEM, it can model crack branching with taking into account heterogeneities [225]. Some examples of using DEM to study the crack branching in

heterogeneous materials are listed below. Taking into account the effect of local heterogeneity around the crack tip, crack branching in a vitreous biopolymer material is modelled in [178] with DEM, see Fig. 2.32. A hole is set in the material to investigate the influence of the position of the hole on crack branching patterns. The results showed that DEM is more sensitive to stress heterogeneities and has better agreement with experimental results than FEM. In [182], fracture branching with a grain-based modelling approach was studied. It is found that complex fracture patterns are governed by material heterogeneity and model discretisation. In [87], the DEM was used to model microcracks initiation and propagation in different crystal structures, and it is found that the crack branching pattern varies with different notch inclination angles: the larger the notch inclination angle is, the more branching occurs.

While DEM can be applied in the crack branching simulation in heterogeneous materials, the method has limitations: (1) it is not well suited to model complex material behaviour reliably and its application is mostly limited to granular materials; (2) it is awkward in predicting a variety of macroscopic properties (e.g. elastic stiffness, strength, critical energy release rate for uni-, bi- and tri-axial loading, etc.); (3) it usually has high computational cost, which is easily influenced by many factors, such as particle numbers, particle shapes and contact force models [201].

### **2.2.5 Summary and Prospective Work**

This section presents an overview of crack branching, including experimental observations, physics, crack models and associated numerical methods for simulation of crack branching problems. In terms of experimental observations, high speed photography is the most commonly used technique to be combined with photoelasticity, caustics, digital image correlation, digital gradient sensing to study the crack branching. The current focus is on (1) how to combine and improve upon existing shortcomings with the combination of technology development; (2) how to simplify the operations and reduce operating costs while ensuring high temporal and spatial resolution. Supported by experimental research, physics of branching including the causes of crack branching and branching criteria have been investigated and summarized. One explanation suggests that branching occurs once the crack velocity exceeds a critical value (related to the wave speed). Another explanation assumes branching is a natural outcome of the growth of microcracks near the crack tip and energy absorbed by the crack is related to the limiting velocity. Dynamic instabilities, which are related to critical velocity, fracture roughness and micro-branches, are also shown to be a strong mechanism for crack branching and are investigated. In addition, the crack front waves and the tilting and twisting of the stress vector at the crack front are responsible for



the crack branching. Corresponding to these potential causes of crack branching, different branching criteria have been proposed, including external and internal criteria. The crack models and numerical methods for crack branching have been developed and continuously improved according to various crack branching criteria, which are further applied to simulate crack branching, to shed light on the mechanisms behind branching. These models and methods are reviewed in this section with respect to their strengths and limitations.

Several outstanding issues and challenges are identified and need to be resolved for reliable crack branching prediction, these include the limitation of experimental techniques for the observation and measurements of physical parameters in front of the crack tip; current analytical techniques and existing branching criteria are not sufficient to define the mechanisms driving crack branching and associated dynamic instabilities; the limitations of various crack models and numerical methods proposed for simulating complex fracture propagation processes. Moreover, the study of the branching problem is further complicated by considerations such as heterogeneity of the material, softening behaviour and large fracture networks in which multiple length scale cracks develop.

## **2.3 Review of peridynamics**

### **2.3.1 Introduction**

In classical continuum mechanics, an object is assumed to be a continuum. However, when the displacement field of the object is discontinuous (e.g. material with cracks), the displacement derivative is not defined at the discontinuities. Therefore, difficulties arise when trying to solve discontinuous problems with classical continuum mechanics. Peridynamics (PD) is a new continuum mechanics theory established by Silling [394] in 2000. By replacing the partial differential equation with the integral equation, PD avoids the singularity and combines continuous and discontinuous descriptions. In PD, the continuum is subdivided into material points occupying the volume of space. The core of the PD theory is that the behaviour of each material point depends on how it interacts with other material points around it (inside its horizon). Since the deformation process depends on the interaction between material points, PD can simulate the crack initiation, propagation, bifurcation and intersection with a simple failure criterion defining the interaction force between material points. This feature makes it a promising tool for crack propagation problems. As shown in Fig. 2.33, PD, as a newly developed theory, has attracted more and more attention and application.

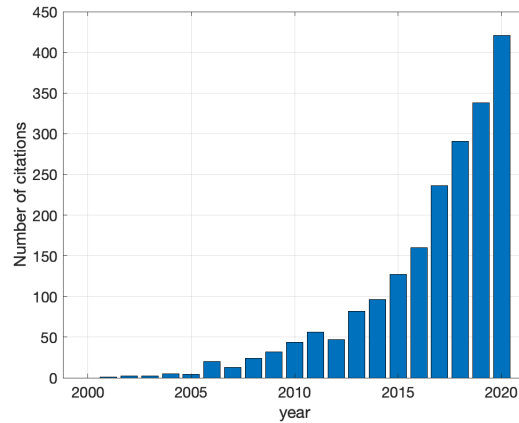


Fig. 2.33 Number of citations of [394] per year versus year from 2000 till present.

In recent years, the development of PD theory has become more and more mature. From the beginning, it is only applicable in the modelling of linear elastic materials [402, 247, 403, 395]. Later, it is successfully applied to the modelling of non-linear elastic materials [401], plastic materials [263], viscous elastic materials [262] and viscoplastic materials [137].

There are two types of theoretical models for PD [247]: bond-based PD and state-based PD. The bond-based assume that any pair of particles interact only through a central potential that is independent of all other local conditions [247]. The interaction force between two material points is equal in magnitude, opposite in directions, and parallel to the line between two material points. This assumption results in that the Poisson's ratio is limited to  $1/4$  (plane strain) or  $1/3$  (plane stress) for an isotropic, linear, microelastic material. To remove the restrictions for the Poisson ratio, the state-based theory was proposed by Silling et al. [402] in 2007. In state-based PD, the interaction between two material points depends on the bond between the two points and on the deformation of all the other bonds in the horizon. Furthermore, it can be further divided into ordinary state-based PD and non-ordinary state-based PD. In ordinary state-based PD, the interaction force between two material points is not equal in magnitude, opposite in directions and still being parallel to the line between two material points, while in non-ordinary state-based PD, the interaction force between two material points is not equal in magnitude, and not being parallel to the line between two material points. Differences between the bond-based PD, ordinary state-based PD and non-ordinary PD can be seen in Fig. 2.34. Different from the bond-based PD, the state-based PD is not only limited to linear elastic materials. Regular plasticity descriptions can be implemented as a constitutive description. In [248], the ordinary state-based peridynamic constitutive relations for plastic deformation based on von Mises yield criteria is presented. In [438], an extended non-ordinary state-based PD was proposed, where the maximum tensile

stress criterion is applied to determine the tensile failure of the bond between interacting particles and Mohr-Coulomb failure criterion is employed to define the shear failure of the bond between interacting particles. Additionally, compared to bond-based and ordinary state-based PD, the non-ordinary state-based PD has the advantages in the aspect of modelling general non-linear anisotropic materials. In bond-based PD and ordinary state-based PD, anisotropic materials are usually modelled as different isotropic materials (for instance, fibre and matrix of a composite laminate), where the stiffness of the bond depends on its orientation. In the non-ordinary state-based PD formulation, the material properties for each particle can be defined using the material constitutive matrix, rather than being defined through the bond stiffness between adjacent particles [175]. In this way, more general anisotropic materials are modelled.

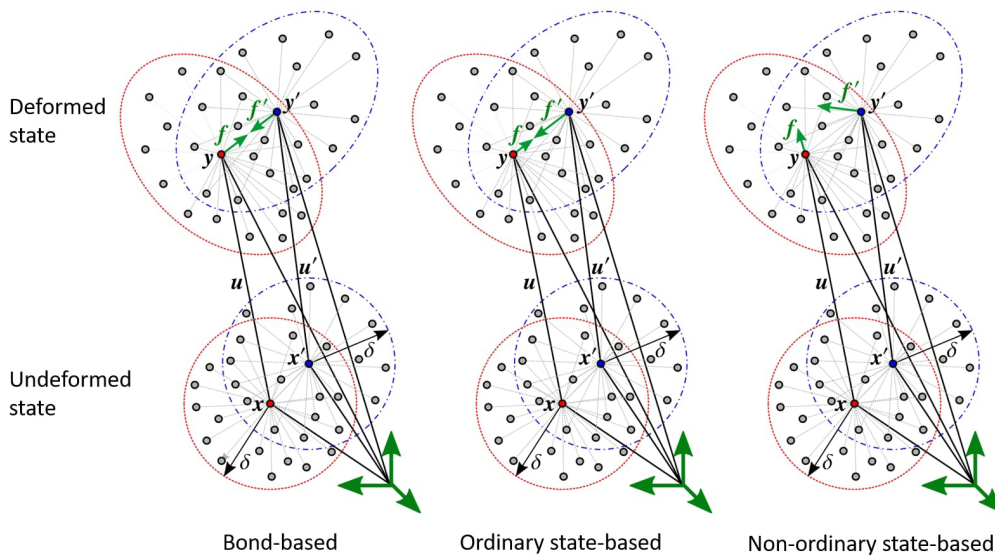


Fig. 2.34 Schematic diagram of different PD models.

The main purpose of this section is to describe PD theory and review the related applications of PD in different fields, especially in the field of fracture mechanics. The challenges and new prospects for the development of PD are also discussed.

### 2.3.2 Theoretical aspects of peridynamics

#### Bond-based PD

In the PD theory, it is assumed that each one of the material points  $\mathbf{x}$  interacts with the other material points  $\mathbf{x}'$  inside a horizon  $H_{\mathbf{x}}$ , and the interactions vanish when out of the horizon.

All the points inside the horizon of point  $\mathbf{x}$  is defined as

$$H_{\mathbf{x}} = \mathbf{x}' \in \Omega, |\mathbf{x}' - \mathbf{x}| < \delta \quad (2.33)$$

in which  $\delta$  is the horizon size (radius of the horizon).

As derived by Silling [394], the PD equation of motion at a reference position of  $\mathbf{x}$  and time  $t$  in an elastic material can be given as

$$\rho(\mathbf{x})\ddot{\mathbf{u}}(\mathbf{x}, t) = \int_{H_{\mathbf{x}}} \mathbf{f}(\mathbf{x}' - \mathbf{x}, \mathbf{u}' - \mathbf{u}) dV_{\mathbf{x}'} + \mathbf{b}(\mathbf{x}, t) \quad (2.34)$$

in which  $\rho$  is the mass density,  $\ddot{\mathbf{u}}$  the acceleration,  $\mathbf{u}$  the displacement vector field,  $\mathbf{b}$  the prescribed body-force density field,  $dV_{\mathbf{x}'}$  the differential volume of the  $\mathbf{x}'$ ,  $\mathbf{f}$  the force vector between two material points  $\mathbf{x}'$  and  $\mathbf{x}$ . Eq. (2.33) is valid at discontinuities. This is because the divergence of the stress tensor in the partial differential equation in classical continuum mechanics is replaced by the integral of the force density over the whole neighbourhood. Thereby, the interaction  $\mathbf{f}$  contains all constitutive properties of the material. For linear-elastic materials,  $\mathbf{f}$  can be expressed as

$$\mathbf{f}(\mathbf{x}' - \mathbf{x}, \mathbf{u}' - \mathbf{u}) = \lambda cs \frac{\mathbf{y}' - \mathbf{y}}{|\mathbf{y}' - \mathbf{y}|} \quad (2.35)$$

where  $\mathbf{y}$  represents the position of the material point in the deformed configuration and  $\mathbf{y} = \mathbf{x} + \mathbf{u}$ .  $\lambda$  is a scalar to describe the bond state: broken or not, which means the interaction disappears or not.  $c$  is the bond-constant, which can be represented with the material constants of classical continuum mechanics. For an isotropic material, it can be expressed as [247]:

$$c = \frac{2E}{A\delta^2} \quad (1D) \quad (2.36a)$$

$$c = \begin{cases} \frac{9E}{\pi h \delta^3} & (2D, \text{plane stress}) \\ \frac{48E}{5\pi h \delta^3} & (2D, \text{plane strain}) \end{cases} \quad (2.36b)$$

$$c = \frac{12E}{\pi \delta^4} \quad (3D) \quad (2.36c)$$

in which  $E$  is the Young's modulus of the solid skeleton,  $A$  is the cross-sectional area, and  $h$  is thickness.  $s$  is the stretch between the material points representing the relative elongation of the bond.

### State-based PD

In state-based PD theory, the “state” is used to replace the “tensor” in the classical elastic theory. Because tensors can only provide a continuous (smooth) spatial mapping, such as deformation gradient tensor, the PD theory requires a space mapping that takes into account both continuous (smooth) and discontinuous (non-smooth). Therefore, the “state” is defined as a mapping from vector space to tensor set [402], which is an array that stores information about a parameter of PD bonds associated with a particular material point [197].

The generalized state-based PD equation of motion can be expressed as:

$$\rho(\mathbf{x})\ddot{\mathbf{u}}(\mathbf{x},t) = \int_{H_{\mathbf{x}}} \{ \underline{\mathbf{T}}(\mathbf{x},t) \langle \mathbf{x}' - \mathbf{x} \rangle - \underline{\mathbf{T}}(\mathbf{x}',t) \langle \mathbf{x} - \mathbf{x}' \rangle \} dV_{\mathbf{x}'} + \mathbf{b}(\mathbf{x},t) \quad (2.37)$$

where  $\underline{\mathbf{T}} \langle \cdot \rangle$  is the force state.

### Ordinary state-based PD

In the ordinary state-based PD formulation, the PD forces between two material points are not equal in magnitude and in opposite directions, but their directions are parallel to the line between two material points. For linear elastic materials, the force state is given by:

$$\underline{\mathbf{T}}(\mathbf{x},t) \langle \mathbf{x}' - \mathbf{x} \rangle = \left( \frac{2ad\delta}{|\mathbf{x}' - \mathbf{x}|} \theta(\mathbf{x},t) + b\delta_s \right) \frac{\mathbf{y}' - \mathbf{y}}{|\mathbf{y}' - \mathbf{y}|} \quad (2.38)$$

where  $a$ ,  $b$ ,  $d$  are PD parameters and can be obtained by comparing the PD theory and classical mechanics theory. First, assume a body subjected to the simple loading conditions of isotropic expansion and simple shear. Then the strain energy density resulting from the PD theory and classical mechanics theory is compared to each other under the same loading conditions to obtain the corresponding parameters  $a$ ,  $b$ ,  $d$  in different dimensions, which can be defined as follows [247]:

$$\begin{aligned} a = 0, b = \frac{E}{2A\delta^3}, d = \frac{1}{2A\delta^2} \quad (1D) \\ a = \frac{1}{2}(\kappa - 2\mu_s), b = \frac{6\mu_s}{\pi h\delta^4}, d = \frac{2}{\pi h\delta^3} \quad (2D) \\ a = \frac{1}{2}\left(\kappa - \frac{5}{3}\mu_s\right), b = \frac{15\mu_s}{2\pi\delta^5}, d = \frac{9}{4\pi\delta^4} \quad (3D) \end{aligned} \quad (2.39)$$

where  $\kappa$  and  $\mu_s$  are the bulk modulus and shear modulus, respectively.  $\theta$  in Eq. (2.38) is the dilatation term, which is defined as:

$$\theta = \int_{H_x} d\delta_s \Lambda dV_{\mathbf{x}'} \quad (2.40)$$

$\Lambda$  is the PD auxiliary parameter, which is defined as:

$$\Lambda = \frac{(\mathbf{y}' - \mathbf{y}) \cdot (\mathbf{x}' - \mathbf{x})}{|\mathbf{y}' - \mathbf{y}| \cdot |\mathbf{x}' - \mathbf{x}|} \quad (2.41)$$

### Non-ordinary state based PD

The non-ordinary state based PD disregards the assumption in ordinary state based PD that the direction of PD forces between two material points should be parallel to the line between the two points. The force density vector  $\underline{\mathbf{T}}(\mathbf{x}, t) \langle \mathbf{x}' - \mathbf{x} \rangle$  can be related to the traditional stress as:

$$\underline{\mathbf{T}}(\mathbf{x}, t) \langle \mathbf{x}' - \mathbf{x} \rangle = \underline{\omega} \langle \mathbf{x}' - \mathbf{x} \rangle \mathbf{P} \mathbf{K}^{-1} \langle \mathbf{x}' - \mathbf{x} \rangle \quad (2.42)$$

where  $\underline{\omega}$  is the influence function that defines the strength of interactions.  $\mathbf{P}$  is the first Piola-Kirchhoff stress tensor [88], which can be obtained from Cauchy stress:

$$\mathbf{P} = \det(\mathbf{F}) \boldsymbol{\sigma} \mathbf{F}^{-T} \quad (2.43)$$

with  $\mathbf{F}$  being the nonlocal deformation gradient, which is defined as:

$$\mathbf{F} = \frac{\int_{H_x} \underline{\omega} \langle \mathbf{x}' - \mathbf{x} \rangle (\underline{\mathbf{Y}} \langle \mathbf{x}' - \mathbf{x} \rangle \otimes \underline{\mathbf{X}} \langle \mathbf{x}' - \mathbf{x} \rangle) dV_{\mathbf{x}'}}{\mathbf{K}} \quad (2.44)$$

$\mathbf{K}$  is the nonlocal shape tensor, which is defined as:

$$\mathbf{K} = \int_{H_x} \underline{\omega} \langle \mathbf{x}' - \mathbf{x} \rangle (\underline{\mathbf{X}} \langle \mathbf{x}' - \mathbf{x} \rangle \otimes \underline{\mathbf{X}} \langle \mathbf{x}' - \mathbf{x} \rangle) dV_{\mathbf{x}'} \quad (2.45)$$

In Eq. (2.44) and Eq. (2.45),  $\underline{\mathbf{X}}$  represents the position state which contains the relative position of  $\mathbf{x}'$  and  $\mathbf{x}$ , and  $\underline{\mathbf{Y}}$  represents the deformation state containing the relative position of  $\mathbf{x}'$  and  $\mathbf{x}$  in the deformed configuration.  $\otimes$  is the dyadic product operator.

### Damage predication

In classical continuum mechanics, an additional criterion is required in every time step to judge whether the crack propagates and in which direction it grows. However, in PD, only

one criterion is needed to decide when the bond breaks. The bond refers to the long-range interaction between pairs of points. When a bond is broken, the interaction between the pairs of material points disappears. The bond break is a process that cannot be recovered over time, and a series of bond breaks indicate the damage of the material. Two kinds of failure criteria are commonly used in the PD to decide when a bond has to be broken [299]: critical strain (critical bond stretch) criteria and critical energy criteria.

**Critical strain (critical bond stretch) criteria** Critical strain (critical bond stretch) criteria [400] are related to the stretch of the bond  $s$ . The bond breaks when its stretch  $s$  exceeds the critical stretch  $s_c$ . The stretch of the bond  $s$  is written as [394]:

$$s = \frac{|\mathbf{y}' - \mathbf{y}| - |\mathbf{x}' - \mathbf{x}|}{|\mathbf{x}' - \mathbf{x}|} \quad (2.46)$$

The critical stretch  $s_c$  can be determined by the energy release rate  $G_c$ . The relationship between  $s_c$  and  $G_c$  is defined as [247, 286, 471]:

$$s_c = \sqrt{\frac{4\pi G_c}{9E\delta}} \quad (2D, \text{plane stress}) \quad (2.47a)$$

$$s_c = \sqrt{\frac{5\pi G_c}{12E\delta}} \quad (2D, \text{plane strain}) \quad (2.47b)$$

$$s_c = \sqrt{\frac{5G_c}{6E\delta}} \quad (3D) \quad (2.47c)$$

In order to add the critical strain criterion to the numerical simulation,  $\lambda$  is introduced in Eq. (2.35) as a scalar to describe the bond state: broken or not.  $\lambda$  equals 1 when the bond is intact, and  $\lambda$  equals 0 when the bond is broken.

$$\lambda = \begin{cases} 0 & (s \geq s_c) \\ 1 & (s < s_c) \end{cases} \quad (2.48)$$

When the bond is broken, the interactions on the bond disappear, then the additional load is added onto the intact bonds, which may cause a series of bonds to break. The break of the bond is a process that cannot be recovered. The time taken by the bond break is determined by the material geometry and loading conditions. When a series of bonds break, the damage occurs, and the discontinuous space formed by these broken bonds becomes a macroscopic crack.

**Critical energy criteria** The critical bond stretch criterion is commonly used for dealing with mode I fracture in homogeneous [170, 389] and heterogeneous materials [156]. However, it is not suitable for simulating the fracture observed in elasto/visco-plastic materials, which involves the deviatoric deformation [114]. In order to overcome the disadvantage of critical bond stretch criteria, a criterion based on the energy was proposed in [137] for elasto/visco-plastic materials.

In the critical energy criterion, instead of depending on the stress or strain criteria, the failure criterion of a bond is derived from the amount of energy density stored in the bond. The total energy density stored in a bond,  $w_\xi$ , is obtained by the integration of the dot product of the force density vector and the relative displacement vector, see Eq. (2.49):

$$w_\xi = \int_0^{\eta(t_{final})} \{ \underline{\mathbf{T}}(\mathbf{x}, t) \langle \mathbf{x}' - \mathbf{x} \rangle - \underline{\mathbf{T}}(\mathbf{x}', t) \langle \mathbf{x} - \mathbf{x}' \rangle \} \cdot d\boldsymbol{\eta} \quad (2.49)$$

where  $\boldsymbol{\eta}$  is the relative displacement between two points  $\mathbf{x}$  and  $\mathbf{x}'$ , as shown in Fig. 2.35.  $\eta(t_{final})$  is a function of time, which represents the final scalar value of displacement. The equation represents the work density done on a bond is the dual force density integrated over the displacement. The idea is borrowed from that the work done to a body is the force acting on it integrated over the displacement of the body.

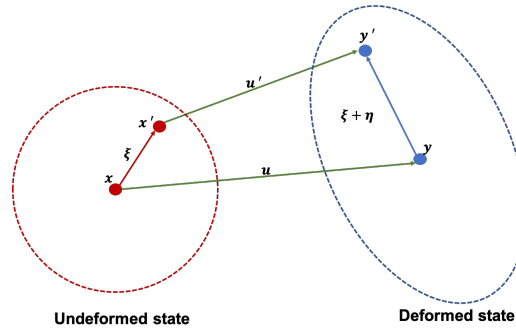


Fig. 2.35 Schematic of bond kinematics.

When the total energy density stored in a bond  $w_\xi$  is greater than the critical energy density  $w_c$ , the bond breaks. By summing up the energy critical energy densities  $w_c$  through integration and equating it to the energy release rate [137, 298], the relationship between  $w_c$  and energy release rate  $G_c$  can be obtained as follows:

$$w_c = \frac{9G_c}{4\delta^3} \quad (2D) \quad (2.50a)$$

$$w_c = \frac{4G_c}{\pi\delta^4} \quad (3D) \quad (2.50b)$$



To implement the bond-break criterion into numerical simulation, the influence function  $\underline{\omega}$  in Eq. (2.42) is used to describe the bond state: broken or not. When the bond is intact, it equals 1. When the bond is broken, it equals to zero. Therefore, the failure criterion can be expressed mathematically as:

$$\underline{\omega} = \begin{cases} 0 & (w_{\xi} \geq w_c) \\ 1 & (w_{\xi} < w_c) \end{cases} \quad (2.51)$$

**Local damage** To describe the crack path, a scalar  $\phi$  called damage parameter is used. It represents the local damage of point  $\mathbf{x}$ , which is defined as the ratio of the sum of the volumes bound to the family nodes connected by the broken bonds to the sum of the volumes of all the family nodes in the original horizon:

$$\phi(\mathbf{x}, t) = 1 - \frac{\int_H \chi dV_{\mathbf{x}'}}{\int_H dV_{\mathbf{x}'}} \quad 0 \leq \phi \leq 1 \quad (2.52)$$

where  $\chi$  is a time-dependent damage parameter. In the critical bond stretch criteria,  $\chi$  can be replaced by the influence function  $\lambda$ . In critical energy criteria,  $\chi$  can be replaced by the influence function  $\underline{\omega}$ .

Let us consider a point  $\mathbf{x}$  is close to a crack surface in a PD model. If there is no crack surface, the bonds are all intact and the value of  $\phi(\mathbf{x}, t)$  is zero. If crack surfaces exist, since failure occurs, bonds crossing the crack surface are all broken. As shown in Fig. 2.35, half of the bonds connected to the point  $\mathbf{x}$  are broken, leading to a local damage value  $\phi(\mathbf{x}, t)=0.5$ .

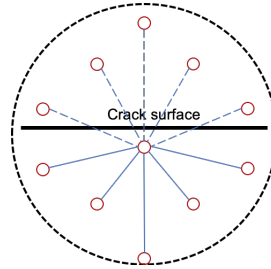


Fig. 2.36 Schematic of local damage.

Thereby, the value of the damage parameter  $\phi(\mathbf{x}, t)$  is between  $0 \sim 1$ . 0 represents no failure at the point  $\mathbf{x}$  while 1 represents total failure because all the bonds connected to the point are broken. The crack path can be indicated by plotting the damage parameter in global, as shown in Fig. 2.37.

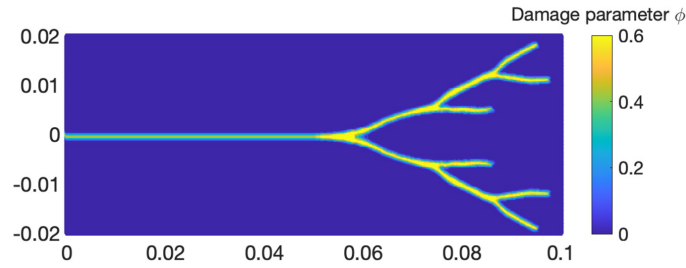


Fig. 2.37 Crack propagation path in a 2D solid media.

### 2.3.3 Numerical implementation

#### Spatial discretisation

There are two common approaches for spatial discretisation in PD: the meshless scheme [400] and the finite element discretisation [491].

The finite element discretisation for the bond-based PD model is proposed in [491]. For state-based PD, a morphing method is developed to couple classical continuum mechanics with state-based PD [173]. It is possible to apply traditional finite element discretisation in PD models in continuous problems. However, when modelling discontinuous problems, e.g. crack problems, finite element discretisation with PD models becomes nearly impossible. Because in the traditional FEM discretisation, nodes and edges are shared between adjacent elements, which prevents the possibility of separation between elements. In 2011, Chen and Gunzburger [81] pioneered the application of discontinuous Galerkin elements to PD models to solve discontinuity problems. It is proposed that discontinuous Galerkin elements are required if finite element discretisation is employed to simulate crack growth with PD models. In [424], a non-conforming discontinuous Galerkin finite-element scheme for nonlocal variational problems associated with some linear nonlocal diffusion and nonlocal PD operators was proposed. In [354], a 3D bond-based PD model was established with the discontinuous Galerkin finite element method for dynamic brittle failure analysis.

Compared with finite element discretisation, the meshless scheme is more straightforward [247]. In [400], the meshless scheme was first proposed, and detailed numerical implementation was given. Let us consider a domain  $\mathcal{B}$ . The domain can be seen as a composition of nodes associated with a specific volume, as shown in Fig. 2.38. Since there are no elements or other geometrical connections between the nodes, the method is meshfree. The spatial integration is implemented by the summation of the volumes of material points around the point  $\mathbf{x}_i$  within its horizon  $\mathcal{H}_{x_i}$ . For simplicity, let us consider the peridynamic equation of

motion in an elastic material in bond-based PD. The discretised form of the Eq. (2.34) of motion for node  $\mathbf{x}_i$  can be expressed as:

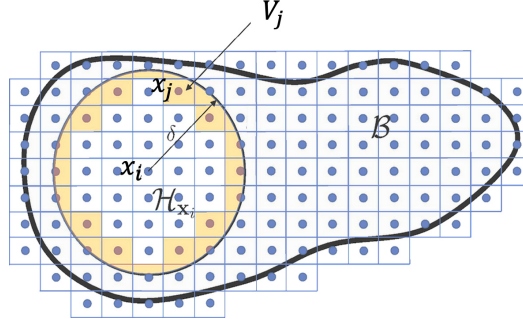


Fig. 2.38 Spatial discretisation.

$$\rho \ddot{\mathbf{u}}_i = \sum_{j=1}^{N_{\mathbf{x}_i}} \mathbf{f}_{ij}(\mathbf{x}_j - \mathbf{x}_i, \mathbf{u}_j - \mathbf{u}_i) V_j + \mathbf{b}_i \quad (2.53)$$

where  $N_{\mathbf{x}_i}$  is the number of points inside the horizon  $H_{\mathbf{x}_i}$  of material point  $\mathbf{x}_i$  and  $V_j$  the volume of material point  $\mathbf{x}_j$ .

### Time integration

The time integration scheme for PD falls into two broad categories: the explicit and implicit schemes. The explicit scheme is appropriate for simulating failure problems involving large deformations as well as dynamic problems where inertial effects play an important role [237]. However, it is conditionally stable, which means the time step is required to be small enough to satisfy the stable condition. Compared to the explicit one, the implicit scheme is unconditionally stable. Thereby, a larger time step is allowed. Besides, it is appropriate for static and quasi-static problems. However, one disadvantage for the implicit scheme is that it requires the calculation of tangent stiffness matrix when solving nonlinear problems, and the matrix needs to be updated when the failure occurs, which renders the problems of a high computational cost [237]. A detailed description of the explicit scheme for dynamics problems and the implicit scheme for static problems is given below. The explicit forward strategies and backward difference strategies are used for the explicit scheme, and the Newton iteration is used for the implicit scheme. We note that these strategies are just selected here for simplicity of explanation. Other numerical strategies can be found in [228].

**The explicit scheme** Generally, the explicit scheme calculates the state of a system at a later time based on the state of the system at the current time. Eq. (2.53) can be written in the

following form:

$$\rho \ddot{\mathbf{u}}_i^n = \sum_{j=1}^{N_{x_i}} \mathbf{f}_{ij}^n (\mathbf{x}_j - \mathbf{x}_i, \mathbf{u}_j^n - \mathbf{u}_i^n) V_j + \mathbf{b}_i^n \quad (2.54)$$

where  $n$  is the time step number. According to Eq. (2.54) and the initial value of  $\mathbf{u}^n$ ,  $\mathbf{b}_i^n$ , the PD force  $\mathbf{f}_{ij}^n$  is calculated and the acceleration field  $\ddot{\mathbf{u}}^n$  at time step  $n$  can be obtained. Then, the velocity field  $\dot{\mathbf{u}}^{n+1}$  at next time step  $n+1$  can be obtained by explicit forward Euler with the known displacement field  $\mathbf{u}^n$  and acceleration field  $\ddot{\mathbf{u}}^n$  at the time  $n$ .

$$\dot{\mathbf{u}}^{n+1} = \dot{\mathbf{u}}^n + \Delta t \ddot{\mathbf{u}}^n \quad (2.55)$$

After obtaining the velocity field  $\dot{\mathbf{u}}^{n+1}$  at time step  $n+1$ , the displacement field  $\mathbf{u}^{n+1}$  at time step  $n+1$  can be obtained by backward difference approximation:

$$\mathbf{u}^{n+1} = \mathbf{u}^n + \Delta t \dot{\mathbf{u}}^{n+1} \quad (2.56)$$

An algorithm is given in Table 2.4 to show the numerical implementation for the dynamic PD model with an explicit scheme.

Table 2.4 Algorithm of the numerical implementation for the dynamic PD model with an explicit scheme.

---

**Initial conditions and boundary conditions**

**Spatial discretisation**

**Repeat**

**For each node i do**

**For each node j inside the horizon of node i do**

- ▷ compute the interactions between node i and node j
- ▷ compute the stretch  $s$  of the bond between node i and node j
- ▷ check the bond stretch  $s$  against the critical value  $s_c$

**if  $s \geq s_c$ , then**

- ▷ break the bond

**end if**

**End for**

- ▷ compute the total interaction forces acting on node i
- ▷ compute the acceleration  $\ddot{\mathbf{u}}$  for node i
- ▷ compute the displacement  $\mathbf{u}$  for node i

**End for**

$t = t + \Delta t$

**Until** the time  $t$  exceeds the total time  $t_{total}$

---

**The implicit scheme** The implicit scheme calculates the state of a system at a later time with both the state of the system at the current time and the system's state at a later time. Compared with explicit schemes, implicit schemes allow for a large time step and are suitable for static and quasi-static problems [237]. An example of the application of an implicit scheme for quasi-static problems is presented to highlight the most salient aspects of implicit methods for PD. With failure occurs, the problem is nonlinear. Thereby, Newton iteration is employed. Regardless of the inertial term, Eq. (2.53) can be written in the following form:

$$\sum_{j=1}^{N_{x_i}} \mathbf{f}_{ij}(\mathbf{x}_j - \mathbf{x}_i, \mathbf{u}_j - \mathbf{u}_i) V_j + \mathbf{b}_i = 0 \quad (2.57)$$

By multiplying  $V_i$  to Eq. (2.57), the following equation can be obtained:

$$\sum_{j=1}^{N_{x_i}} \mathbf{f}_{ij}(\mathbf{u}_j - \mathbf{u}_i, \mathbf{x}_j - \mathbf{x}_i) V_j V_i + \mathbf{b}_i V_i = 0 \quad (2.58)$$

Eq. (2.58) can be expressed in a matrix form:

$$\mathbf{K}\mathbf{u} = \mathbf{F} \quad (2.59)$$

where  $\mathbf{K}$  is the stiffness matrix, by employing Newton iteration, the following equation system can be obtained:

$$\mathbf{u}^{n+1} = \mathbf{u}^n - \frac{\mathbf{R}}{\mathbf{K}} \quad (2.60)$$

where  $\mathbf{R}$  is the residual, and can be expressed as:

$$\mathbf{R} = \mathbf{K}\mathbf{u}^{n+1} - \mathbf{F}^{n+1} \quad (2.61)$$

By applying Newton iteration to minimise the residual until the convergence criterion is met, the displacement field  $\mathbf{u}^{n+1}$  at next time step  $n + 1$  can be obtained.

An algorithm is given in Table 2.5 to show the numerical implementation for the quasi-static PD model with an implicit scheme.

### Numerical stability

Since the explicit scheme is conditionally stable, its time step should be smaller enough to satisfy the stability condition. Two common approaches are employed in PD to determine the

Table 2.5 Algorithm of the numerical implementation for the quasi-static PD model with an implicit scheme.

---

**Initial conditions and boundary conditions**  
**Spatial discretisation**  
**Repeat**  
 ▷ update the load step and time step  
 ▷ assign an initial guess to the trial displacement  $\mathbf{u}_{trial}$   
   **Repeat**  
   ▷ update the stiffness matrix  $\mathbf{K}$   
   ▷ evaluate the residual  $\mathbf{R}$   
   ▷ compute the displacement  $\mathbf{u}$   
   ▷ check the bond stretch  $s$  against the critical value  $s_c$   
   **if**  $s \geq s_c$ , **then**  
   ▷ break the bond  
   **end if**  
**Until** the convergence criterion is met  
**Until** the time  $t$  exceeds the total time  $t_{total}$

---

critical time step. The first approach is derived by Silling in [400], which is given as follows:

$$\Delta t_{crit} = \sqrt{\frac{2\rho}{\sum_{j=1}^{N_{x_i}} V_j C_{ij}}} \quad (2.62)$$

where  $\rho$  is the density,  $C_{ij}$  the micro modulus between the material point  $\mathbf{x}_i$  and the material point  $\mathbf{x}_j$ . After looping over all material points in the material, the minimum value will be taken as the critical time step. Though derived for the 1D problem, the criterion can be applied in any number of dimensions by setting  $C_{ij} = |\mathbf{C}(x_j - x_i)|$  [400]. However, this criterion is only for linear problems. For nonlinear problems, a “safety factor” less than one is required to make sure the stability conditions are satisfied [247].

The second approach to determine the critical time step is the Courant-Friedrichs-Lewy (CFL) approach [96].

$$\Delta t_{crit} = \frac{h_c}{c_w} \quad (2.63)$$

where  $h_c$  and  $c_w$  are the characteristic length and the wave speed, respectively. If  $h_c$  equals grid spacing, then the evaluation of the critical time step will be very conservative. This is because the CFL condition is commonly applied in finite element methods, where the node interacts only with the nodes next to it. However, PD is a nonlocal theory in which nodes

interacts with each other within a horizon. Therefore, the selection of the size of  $h_c$  plays an important role in determining the criterion.

### Numerical convergence

Compared with finite element analysis, the convergence in PD is more complex, in which two parameters play important roles: the horizon size  $\delta$  and the grid spacing  $\Delta x$  [247]. The relationship between the two parameters can be expressed as follows:

$$m = \frac{\delta}{\Delta x} \quad (2.64)$$

where  $m$  is the ratio between the horizon size  $\delta$  and grid spacing  $\Delta x$ . It is of great importance to determine the relationship between these parameters to balance accuracy and computational cost. Two types of convergence are introduced in [169], which are  $m$ -convergence and  $\delta$ -convergence, as shown in Fig. 2.39.

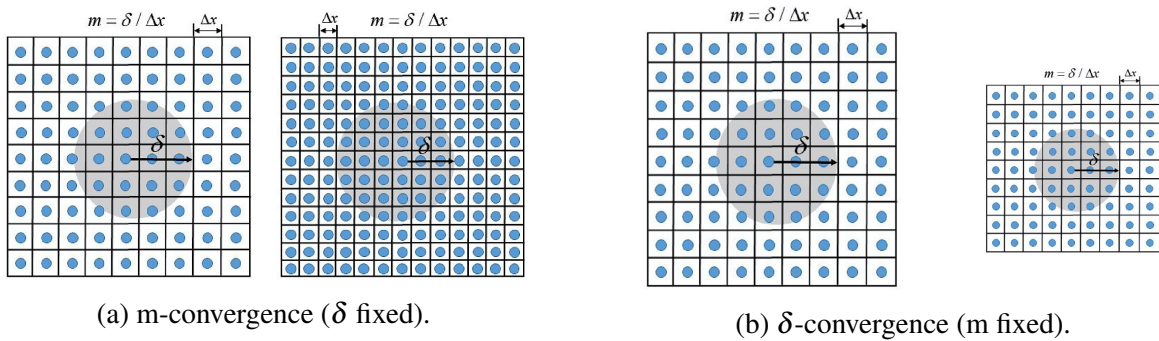


Fig. 2.39 Graphical descriptions for the  $m$ -convergence and  $\delta$ -convergence.

- In the  $m$ -convergence,  $\delta$  is fixed while  $m \rightarrow \infty$ .
- In the  $\delta$ -convergence,  $m$  is fixed while  $\delta$  decreases or  $m$  increases at a slower rate than  $\delta$  decreases.

For  $m$ -convergence, with  $\delta$  being fixed, the smaller  $\Delta x$  is, the bigger  $m$  is. When  $m \rightarrow \infty$ , the numerical peridynamic approximation converges to the exact non-local peridynamic solution for the given  $\delta$  [169]. A series of studies have been conducted on the selection of  $m$ . It is found that  $m = 3$  is most commonly used [247]. By setting  $m = 3$  and  $\delta = 3\Delta x$ , both the accuracy and the computational efficiency can be achieved. Examples of PD models with  $\delta = 3\Delta x$  can be found in different materials, such as micro brittle isotropic materials [396, 111] and composite laminates [186].  $m = 3$  and  $\delta = 3\Delta x$  are also applicable for a

variety of phenomena, such as crack prediction [400], crack branching [247], contact and impact prediction [46]. Besides  $m = 3$ , larger values for  $m$  are also selected for different cases. With  $m$  increasing, more neighbour points will be added to compute the PD interaction forces, and more information will be obtained.  $m = 4$  is utilized in [169, 49] for crack branching phenomenon in isotropic materials and for fluid flow phenomenon in porous media in [196].  $m = 5$  is chosen in [184, 185] for dynamic crack propagation and branching phenomenon in an-isotropic materials (unidirectional fiber-reinforced composites).

For  $\delta$ -convergence, with  $m$  fixed and  $\delta \rightarrow 0$ , the numerical peridynamic approximation converges to an approximation of the classical solution [169]. With smaller  $\Delta x$ , more accurate results can be achieved. However, it does not mean that the smaller  $\Delta x$ , the better. The selection of horizon size  $\delta$  is of the same importance. In [400], it is found that the selection of the horizon size should be dependent on the characteristic length dimensions of the material. In [369], it is proposed that the horizon size should be chosen to be capable of capturing the main characteristics of the damage evolution processes, independent of the discretisation size. A similar conclusion is obtained in [136], where it is said that the horizon size  $\delta$  should be at least as large as the size of the plastic process zone near the crack tip to capture physical mechanisms.

### 2.3.4 Applications of peridynamics

As a fast-developing method, PD theory has been applied to various problems in different fields, including, but not limited to, material failure, impact, multifield, multiscale, and wave dispersion problems, as shown in Table 2.6. We note that these applications are not mutually exclusive, e.g. the hydraulic fracturing process, which couples the deformation of rocks and fluid flow together, belongs to both material failure problems and multifield problems. Table 2.6 provides a rough classification and focused more to prove the capability of PD in simulation of physical problems and analysis of physical mechanisms.

Table 2.6 PD applications for different problems.

<b>Applications</b>	<b>Further classification</b>
Material failure problems	Damage; Fracture; Fatigue
Impact problems	High velocity impact; Low velocity impact
Multifield problems	Thermal-mechanics; Porelasticity; Electro-migration; Hygro-thermo-mechanics
Multiscale problems	Multiple scales of time; Multiple scales of space ranging from nanoscale to macroscale
Wave dispersion problems	Linear elastic materials; Non-linear materials



### **Material failure problems**

For material failure problems, the damage investigation has been conducted with the PD model in different materials, such as composite materials [469] and layered heterogeneous materials [204]. In addition, various damage phenomena and specific physical mechanisms have been reproduced and investigated with PD models. In [363], a PD model for simulating corrosion damage and crack propagation under the synergy of chemical corrosion and mechanical loading was established, which can predict corrosion pitting, nucleation, and crack propagation. In [106], a PD framework for the modelling of hydrogen adsorbed stress corrosion cracking was presented, which accounts for inter-granular crack propagation due to the flow of hydrogen along grain boundaries of the material. It is found that the PD model can predict the structural damage both qualitatively and quantitatively [197].

The PD model is also utilised in fracture mechanics to shed insights into understanding the mechanisms of fracture development. The fracture growth is modelled in different materials, such as concrete [153], rock [332], metals [447], ceramic [437], and polymers [364], and different fracture phenomena are investigated. In [271], a 3D simulation of the fracture process with PD in a heterogeneous medium was presented, and the factors that affect the fracture propagation were analysed. In [169, 49] the physical mechanisms behind dynamic crack branching in brittle materials were investigated with a PD model. In [171], with a PD model, the complex fracturing responses of a single flaw under compression were investigated, and effects of the flaw inclination angle and mechanisms behind the wing crack propagation were discussed.

For the fatigue fracture, a PD model enables the simulation of three phases of fatigue failure: fracture initiation, fatigue growth, and final failure [398]. A PD approach for predicting the fatigue failure of materials due to cyclic loading was presented in [292]. The crack growth phase of fatigue life rather than initiation was analysed. With a robust PD model, simulation of fatigue cracking in homogeneous and in composite materials was conducted in [475]. The numerical simulation results agree well with the experimental results. In [187], a PD model was applied in predicting the damage initiation and growth in fibre reinforced composites under cyclic loading. With the model, the strength of the materials reduces with the number of cyclic loading increases and the damage patterns observed in experiments are reproduced.

### **Impact problems**

The impact problems have been investigated with different impact velocities in various materials. For homogeneous materials, the impact of a rigid sphere against a homogeneous

brittle glass was simulated with a PD model in [399], which proves the ability of the peridynamic model to reproduce large deformation and fragmentation. In [216], a new response function including thermal loading and an efficient numerical algorithm for PD equation solutions were proposed for the progressive failure prediction in homogeneous materials. In [46], the impact of a high-velocity projectile against a multi-layered glass system was simulated with a PD model, which captures many damage morphologies observed in the experiments and uncovers a time-evolution of damage and the dynamic interaction between propagating cracks and interfaces. In [459], a PD model was utilised to simulate the detailed delamination and matrix damage process in composite laminates under the low-velocity impact, and the failure analysis was conducted. PD models are also utilized in [20], which predicted damage in laminates subjected to low-velocity impact, and the results agree well with the experimental results. In [168], an extended ghost inter-layer model for simulating laminated structures with multi-body interactions was proposed and verified for simulating the fracturing behaviour of laminated glass under high-velocity impact. As a supplement, numerical simulation of the damage of composite laminates subjected to impact under different velocities was conducted in [415, 454]. The whole process from low-velocity collision to high-velocity penetration appearing in composite laminate or concrete is analysed.

### **Multifield problems**

In addition to deformation fields, PD can be applied in other fields, such as thermal diffusion, moisture diffusion, electric potential distribution [44]. These fields can be coupled with the deformation fields, making PD a promising tool for coupling problems of different fields in the presence of discontinuities. The coupling problems include thermal-mechanics, hygro-thermo-mechanics, poroelasticity, and electro-migration problems.

For thermal-mechanics problems, a PD formulation for one-dimensional transient heat conduction was proposed in [43], and later the formulation was extended to crack problems in multiple dimensions in [46]. Based on [46], a PD fully coupled formulation for one-dimensional thermal-mechanics was developed in [11]. And this formulation was extended to multiple dimensions in [294] and thermally heterogeneous materials, e.g. fiber-reinforced composites in [295]. In [295], the derivation of ordinary state-based PD heat conduction equation was presented, and a detailed numerical implementation process was given. With the PD thermal diffusion model, the effect of temperature changes in the vicinity of the crack tip due to dynamic loading was captured, and the temperature rise at the crack tips when a crack propagates was predicted in [15].

Based on thermal-mechanics problems, another factor affecting the deformation field, the moisture diffusion, is incorporated in the PD formulation, resulting in the hygro-thermo-mechanics problems. The hygro-thermo-mechanics problems include both the effects of temperature and moisture on the deformation field. A PD formulation that couples moisture, temperature, vapour pressure, and the deformation field was presented in [297], which enables failure mechanisms analysis as well as the damage prediction in materials or layered material systems such as the electronic packages.

For poroelasticity problems, in [426], a new formulation for incorporating the effects of pore pressure in PD was presented to simulate the deformation of porous media, and the proposed formulation is applied to modelling the consolidation of fluid-saturated rocks. Later, in [209], a state-based PD formulation of pressure-driven convective fluid transport in heterogeneous porous media was developed, and the model proves to be capable of capturing arbitrary flow discontinuities/heterogeneities. Following the above work, a hydraulic fracturing model, which couples a state-based PD formulation of porous flow and the existing PD solid formulation together, was developed to simulate fluid-driven fractures in an arbitrary heterogeneous poroelastic medium in [300]. Later, the model was utilised to simulate complex natural fracture networks and investigate the interactions between hydraulic fractures and natural fractures [299]. A 3D linear visco-elastic PD model, which is applicable to hydraulic fracturing initiation and propagation in a heterogeneous porous medium, was employed to investigate the interaction between induced fractures and existing fractures [271]. Considering the analogy between poroelasticity and thermo-elasticity, a new fully coupled poroelasticity PD formulation was presented in [296] to analyse sophisticated poroelasticity problems, e.g. fluid-filled rock fractures.

Electro-migration concerns the coupling of deformation, heat transfer, electrical potential distribution and charge flow, and vacancy diffusion [44]. The electric potential and charge flow cause Joule heating, which in turn causes a thermal field and thermal deformation. Due to electro-migration, thermal migration and stress migration, the atomic flux diverges, and material degradation occurs [242]. In [154], a PD framework, which is capable of modelling four coupled physical processes: mechanical deformation, heat transfer, electrical potential distribution, and vacancy diffusion, was presented and utilised to analyse electro-migration and thermo-mechanical crack formation. Similarly, in [293], the PD framework coupling the four physical processes was also presented and applied to model the electro-migration phenomenon. The PD results agree well with FEM results, which proves the ability of PD in predicting failure in interconnects due to electro-migration.

### **Multiscale problems**

There exists a wide range of phenomena and processes whose characterisation requires simultaneous and consistent modelling at multiple spatial and temporal scales [197]. For example, fracture propagation is a common multiscale phenomenon, which can operate across both spatial and temporal scales [44]. In addition, for phenomena that occur in complex materials such as bio-materials, crystalline materials, polymers, and composite materials, multiscale modelling is required [197]. Three successful multiscale applications of PD related to fracture problems were reviewed in [19], including fracture and failure of composites, nanofiber networks, and polycrystal fracture, which demonstrates that the PD has a compelling advantage in multiscale modelling with length scales ranging from nanoscale to macroscale. As one of the early applications in multiscale modelling with PD, an adaptive refinement for one dimension was introduced in [48]. And later in [45], adaptive refinement algorithms for the bond-based PD model for solving statics problems in two dimensions were proposed. The coupling of molecular dynamics (MD) and PD is often employed to solve multiscale problems. In [425], a multiscale model coupling molecular dynamics and PD was proposed, which has three dynamic equations at three different scales, namely microscale, mesoscale, and macroscale. The transition from the microscale to the macroscale is made by employing the adaptive multiscale element, which is capable of passing information from different scales. In [344], a multiscale modelling framework was established between PD and atomistic models. A smaller length scale PD model is seamlessly linked with the atomistic model, and the displacement field is captured in the atomistic region. The finite element method (FEM) and PD are also coupled for the multiscale problems. In [457], a multiscale implementation based on adaptive mesh refinement for the nonlocal PD model was developed. An adaptive strategy is used to detect the discontinuous area and make seamless transitions between the multiscale grid. The PD grid is utilised in the area where cracks are likely to occur, while relatively larger finite element grid is utilised in the area where cracks do not occur. Similar transitions and coupling strategies between FEM and PD can be found in [284, 444]. In addition to the multiscale models (MD and PD models, FEM and PD models), there are other multiscale PD models. Readers are referred to [13] for a detailed discussion.

### **Wave dispersion problems**

In addition to the applications mentioned above, PD has also been applied in wave dispersion problems since the formulation of PD has the following characteristics: if there exist long-range forces, elastic wave dispersion occurs, and the horizon size will have an effect on the amount of dispersion [197]. The wave propagation is investigated with PD in linear elastic

materials and nonlinear materials. Moreover, different approaches have been proposed to reduce the wave dispersion in PD [442, 443].

Numerical dispersion in bond-based PD models has been addressed in [441], and the effect of the nonlocal PD forces on the dynamic response of a one-dimensional linear micro-elastic bar was studied. Later, the wave dispersion and propagation in state-based PD models in linear elastic solids were investigated [64]. A mathematical study of nonlinear PD wave equations was presented in [37]. Then, the propagation of large amplitude, non-dispersive, solitary waves in a nonlinear solid was investigated with PD in [397]. A detailed review of PD modelling of wave dispersion problems can be found in [197], where examples of PD simulation in other types of materials, such as the granular materials, layered composite, graphene, are given.

### 2.3.5 Summary and Prospective Work

As a relatively new theory proposed in 2000, PD has attracted increasing attention for application in fracture problems due to its intrinsic advantages in dealing with discontinuities. This section has completed two aspects of work. First, it gives an overall picture of PD theory, including the basic concepts, classification of PD, damage prediction and numerical implementation. Second, a summary of the application of PD in different fields, including, but not limited to, material failure, impact, multifield, multiscale, and wave dispersion problems.

The advantages of PD are multiple: (1) PD combines continuous and discontinuous descriptions and allows the crack growth to be captured without additional crack propagation criteria; (2) for multiscale problems, it can be used to study large deformation and impact/failure problems on the macro-scale and kinetics of phase transformations and damage/failure problems on the micro-scale; (3) it is applicable in multifield problems: the coupling formulations involving PD have been developed for the analysis of thermal, chemical, diffusion, electrical and porous flow problems [197]; (4) it is straightforwardly implemented in any spatial dimension.

Disadvantages have also been found in PD: (1) the computational cost is high since there exists a large number of interactions between the nodes; (2) the boundary conditions can be challenging to implement since PD is a nonlocal approach, and erroneous behaviour may be observed at boundaries; (3) wave dispersion occurs due to the existence of long-range (nonlocal) forces, leading to a distortion of the wave speed and crack propagation speed, which is not beneficial for failure analysis.

Despite these shortcomings, PD is still a competitive tool for fracture and damage analysis due to its unique characteristics of dealing with discontinuities straightforwardly. In addition,

with further improvement of the theory and technology, the above shortcomings have been improved. For example, to improve computational efficiency, computer hardware has been upgraded, and computing technologies such as adaptive refinement and multiscale methods are proposed [45, 197]. Furthermore, literature aiming at solving the boundary conditions and wave dispersion can be found in [443, 324].

# Chapter 3

## A finite element model for hydraulic fracturing in porous media

### 3.1 Introduction

Hydraulic fracturing involves a process by which fractures initiate and propagate in a formation due to the injection of fluid at high pressure and has received a great deal of attention, mainly due to its importance in engineering applications, including shale gas reservoir stimulation, compensation grouting, caving and fault reaction in mining [22, 123, 198]. In the oil and gas recovery industry, the induced fractures increase the permeability of the reservoir, thereby increasing the extraction of petroleum and natural gas. The economic benefits to the petroleum industry make it essential to predict fracture propagation and understand the physics involved in the evolution of fractures. Considerable numerical and experimental studies have been carried out to investigate the hydraulic fracturing process. Even though all the analytical solutions and most numerical results give smooth results, recently, it has been observed in field tests, laboratory experiments and a few numerical simulations that the propagation of fractures is not continuous but stepwise [318, 380]. However, until now, only a few authors reproduced the stepwise phenomenon in numerical simulation [67, 68, 279, 380, 283]. In addressing the stepwise fracture tip advancement, one would like to determine: (1) the existence of this phenomenon, especially in numerical simulations (whether the cause of the phenomenon is physical or a numerical artifact); (2) the factors influencing the stepwise phenomenon; (3) if the phenomenon exists, under which condition the phenomenon can be captured. In this chapter, we begin with a discussion of these problems and a survey of the literature. This is followed by a presentation of the numerical method developed to model this phenomenon, with the aim of providing more insight into the process.

The existence of the stepwise phenomenon is discussed in two aspects: in practice and numerical simulation. In practice, field tests and laboratory experiments have confirmed the presence of stepwise fracture advancement during the hydraulic fracturing process during the past decades. It was argued that fracturing could occur abruptly, and the fracture could extend at a rate greater than the velocity of entry of fluid and might approach one-fifth of the speed of sound in some cases [321]. Through the observation of the development of brecciated normal faults and breccia zones, it was implied in [316] that abrupt episodes of hydraulic fracturing were separated by longer periods. By analyzing test data related to lost circulation, it is also confirmed that the propagation of fractures is not continuous and during which the pressure is fluctuating [145, 269, 289]. A two-dimensional lattice model was presented in [427], and it was found that pressure inside the fracture dropped in time and had oscillations on short time scales, resulting in discontinuous fracture propagation, similar to what was measured in the field. An experiment was specially designed to verify this phenomenon in [318], where a single-edge-notch test was conducted on hydrogel (one of the most homogeneous materials). Evidence of fracture propagation jumps was observed in the experiment. By measuring the size of different physical parameters as well as analyzing the relationship between them, it was found that the stiffness of the hydrogel is related linearly with the spatial lengths of the steps and inversely with the time that each step needs to propagate and break [318].

On the other hand, in numerical simulations, only a few authors have successfully reproduced the stepwise phenomenon [67, 68, 279, 380, 283]. The complexity of the physical process of hydraulic fracturing has led to the development of a multitude of numerical methods, including but not limited to: the finite element method (FEM), the extended/generalized finite element method (XFEM/GFEM), the boundary element method (BEM), the phase field method (PFM), the discrete element method (DEM) and peridynamics (PD). Though these approaches have been successfully applied to the numerical simulation of hydraulic fracturing, not all of them have the ability to reproduce the stepwise phenomenon. Among all the approaches, the FEM has proven to be versatile and capable of reproducing the stepwise phenomenon numerically. A fully coupled pressure-induced cohesive fracture model in a porous medium was developed with FEM in [379, 377, 380]. The results show that the fracture tip advances stepwise in a pressure-induced fracture with pressure exchange and flow between the fracture and surrounding media. A dynamic model of cohesive fracture propagation in porous saturated media with FEM was presented in [213]. A comparison between the quasi-static and fully dynamic solutions was made. There is a sudden increase of fracture length and fracture mouth opening in the dynamic fracture propagation process, whereas in quasi-static analysis, the values of fracture mouth opening and fracture length increase gradually. In [279], a 2D quasi-static hydraulic fracture model in porous media was



developed using cohesive interface elements with FEM. It is concluded that the stepwise phenomenon can be observed with a small step, whereas monotonic growth is obtained with a large time step. However, whether the stepwise can still be observed with a smaller mesh size is not given. The stepwise phenomenon was also investigated in [68] with three different methods, namely the central force model, the standard Galerkin finite element method and the extended finite element method. The results show that the stepwise phenomenon can be observed even in dry materials. Later, the phenomenon was further explored in [67] with a dynamic fracturing model based on the standard Galerkin finite element method under two different loading cases: the mechanical and hydraulic loading conditions. It shows that the phenomenon holds in quasi-static and dynamic conditions. In terms of pressure oscillation and related frequencies, more information is given in the dynamic condition than in the quasi-static condition. A hybrid FEM and peridynamic model was employed in [283] to predict the dynamic solution of hydro-mechanical coupled problems. With this model, the forerunning fracture behaviour is observed both in dry and saturated conditions, which further proves the existence of the stepwise phenomenon.

Explanation of the stepwise behaviour remains a challenge. It was pointed out in [316] that the rate of fracture propagation could depend on the porosity and permeability consequently. Before the critical stress conditions are reached under the prevailing pore water pressure, a long period is needed for the pore fluid to flow into the fracture for restoration. Another explanation is that the fracture is enlarged, followed by a drop in pressure [420]. Therefore, if the pressure drops suddenly, the stresses at the fracture tips fall below their cohesion value, and the fracture cannot grow at the next time step. The fracture will not grow again until a ready supply of fluid is available. By analyzing the field data of Marcellus shale and Eagleford shale, it was pointed out in [408] that the difference between the major pressure changes could be observed when fractures intersect with natural faults and the minor fluctuations related to intermittent propulsion. It was proposed in [466] that the intersection of hydraulic fractures and natural fractures are the likely reasons for the stepwise phenomenon observed in the field. When hydraulic fractures interact with nature fractures, a time delay may occur for the natural fracture to build up fluid pressure and initiate failure, which can be seen in the injection pressure profile. The natural fracture slip can cause a lost circulation event, which results in multiple episodes of pressure drop and build up [466]. Based on the experimental data, a relationship between the pause time, the hydraulic permeability, Young's modulus and the spatial step length was derived, and a possible explanation for the stepwise phenomenon was given in [318]. It is concluded that a consolidation time (the time needed for all the fluid to flow out of that layer of materials) is required before the crack tip advancement to dissipate the over-pressure caused by the last crack tip advancement. By

invoking "self-organization of rupture", it was proposed in [314] that special requirements for self-organized criticality (SOC) need to be satisfied to reproduce the stepwise behaviour. The numerical and experimental results in [229, 260] show that the transition from continuous to staccato fracture tip advancements is related to fluid injection rate and fluid viscosity. However, the clear relationship between these factors is yet to be demonstrated. Though various explanation has been given, it is still hard to reach a consensus on the mechanism behind the stepwise phenomenon, since it is a sensitive process affected by many factors in the field and experiments.

The stepwise phenomenon is also sensitive in numerical simulations. It was concluded in [68] that the choice of the loading increment/fracture advancement/time-stepping algorithm might have a substantial influence on the predicted behaviour. In [128], it was found that a continuum model can hardly predict the stepwise phenomenon since the stepwise phenomenon observed disappears upon refinement of the discretisation and the time step. Later in [315], it was argued that the steps obtained in [128] are regular steps, which are caused by numerical reasons. Only the irregular steps caused by physical reasons don't disappear upon refinement of the discretisation and the time step. Since the observation of the stepwise phenomenon interferes with three velocities, namely crack tip velocity, fluid seepage velocity in the domain, and fluid velocity in the crack tip [68], the varying of physical influencing factors may contribute to the observation of the stepwise caused by physical reasons. Therefore, we postulate that only under specific conditions can the physical stepwise phenomenon (irregular steps) be captured. A series of simulations are conducted in an attempt to find the specific conditions by varying the influencing factors.

Following the explanation of stepwise behaviour above, the main factors which may affect fracture propagation can be grouped into two categories: (1) the formation variables, which include rock porosity and permeability, Young's modulus, Poisson's ratio, Biot coefficient, Biot modulus and fracture energy; (2) the fluid variables, which include viscosity and the injection rate. By considering the controlling factors influencing the observation of the stepwise phenomenon, a 2D dynamic model of hydraulic fracturing in porous media has been developed. The finite element method is used for spatial discretisation, and an implicit backward Euler time scheme is adopted. Cohesive elements are employed for fracture initiation and propagation. After verification of the model, the stepwise process is investigated. Since stepwise behaviour has only been observed in relatively recent studies [318, 380], there are few, if any, numerical studies on the impacts of these parameters on stepwise behaviour making the study presented here quite meaningful, filling a gap in the literature.

The chapter is organized as follows. The problem formulation and the governing equations are explained first in § 3.2. Then the corresponding weak forms and solution of the discrete equations are presented in § 3.3. § 3.4 gives benchmarks for verification, including dynamic verification, cohesive zone verification and KGD model [151, 215] verification. § 3.5 is devoted to a mesh independence study, which discusses whether the stepwise phenomenon observed with our model is mainly due to numerical or physical reasons. § 3.6 conducts various numerical simulations by varying the influencing factors to find under which conditions the stepwise phenomenon caused by physical reasons (irregular steps) can be reproduced. Then, conclusions are presented in § 3.7.

## 3.2 Governing equations

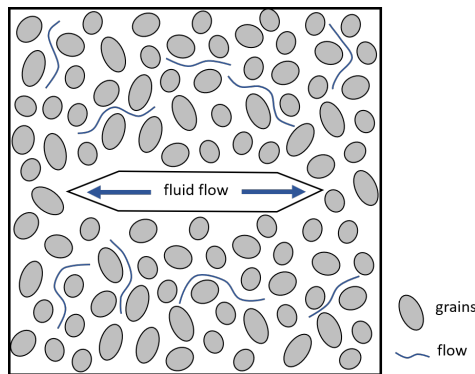


Fig. 3.1 Fracture propagation in porous media.

A schematic illustration of fracture propagation in porous media is shown in Fig. 3.1. To model dynamic fracture propagation in a porous formation, the following four physical processes are considered: (i) deformation of the porous formation, (ii) fluid flow in porous media, (iii) fluid flow in the fracture, and (iv) fracture propagation criteria. These processes reveal a strong coupling between the formation and the fluid. The corresponding governing equations adopted in the simulation are given in the following parts.

### 3.2.1 Deformation of porous formation

The deformation of a porous formation is typically modelled by the theory of poroelasticity. The basic theory of poroelasticity, Biot's theory, was first introduced by Biot [38] and then it was supplemented from a physics perspective in [361]. For a fully saturated porous medium

with single-phase fluid, the equilibrium equation is

$$\nabla \cdot \boldsymbol{\sigma} + \rho \mathbf{g} - \rho \ddot{\mathbf{u}} = 0 \quad (3.1)$$

where  $\boldsymbol{\sigma}$  is the Cauchy stress,  $\mathbf{g}$  the gravity acceleration,  $\ddot{\mathbf{u}}$  the acceleration of the solid phase, and  $\rho$  the density of the porous medium defined as:

$$\rho = (1 - n)\rho_s + n\rho_w \quad (3.2)$$

where  $n$  is the porosity,  $\rho_s$  and  $\rho_w$  are the intrinsic densities of the solid and the fluid, respectively.

The total stress tensor  $\boldsymbol{\sigma}$  can be expressed in terms of the effective stress tensor  $\boldsymbol{\sigma}'$ :

$$\sigma_{ij} = \sigma'_{ij} - I_{ij}\alpha p_w \quad (3.3)$$

where  $p_w$  is the pressure of pore fluid,  $I_{ij}$  the identity tensor, and  $\alpha = 1 - K_t/K_s$  the Biot coefficient, with  $K_t$  denoting the bulk modulus of the porous skeleton and  $K_s$  the bulk modulus of the solid. The Biot coefficient  $\alpha$  denotes the ratio of the fluid volume gained (or lost) in a material element to the volume change of that element, and it equals 1 for incompressible solids.

The effective stress  $\boldsymbol{\sigma}'$  can be determined as:

$$\boldsymbol{\sigma}' = \mathbf{C} : \boldsymbol{\varepsilon}' \quad (3.4)$$

where  $\mathbf{C}$  denotes the elasticity tensor and  $\boldsymbol{\varepsilon}'$  the strain tensor.

### 3.2.2 Fluid flow in porous media

The continuity equation for the fluid flow in porous media is

$$\frac{\partial \zeta}{\partial t} + \nabla \cdot \mathbf{q} = 0 \quad (3.5)$$

where  $\zeta$  is the variation of fluid volume per unit volume of the porous material, and  $\mathbf{q}$  denotes the flux. Described by Darcy's law, the flux  $\mathbf{q}$  can be expressed as:

$$\mathbf{q} = -\frac{\mathbf{k}_w}{\mu} \cdot \nabla p_w \quad (3.6)$$

where  $\mu$  is the fluid viscosity, and  $\mathbf{k}_w$  the permeability tensor.

The constitutive equation for the pore fluid is

$$p_w = Q(\zeta - \alpha \varepsilon_b) \quad (3.7)$$

where  $Q$  is the Biot modulus,  $\alpha$  the Biot coefficient, and  $\varepsilon_b$  the bulk volumetric strain.

The above equations can be combined by substitution and elimination as:

$$\alpha \nabla \cdot \dot{\mathbf{u}} + \frac{1}{Q} \dot{p}_w + \nabla \cdot \mathbf{q} = 0 \quad (3.8)$$

where  $\dot{\mathbf{u}}$  denotes the velocity of the solid phase and  $\frac{1}{Q}$  the compressibility coefficient. The first term can be seen as a source term driving pressure distribution and the flux. The compressibility coefficient  $\frac{1}{Q}$  is defined as:

$$\frac{1}{Q} = \frac{\alpha - n}{K_s} + \frac{n}{K_w} \quad (3.9)$$

where  $K_s$  and  $K_w$  are the bulk module of the solid and fluid phases, respectively.

### 3.2.3 Fluid flow in the fracture

The mass conservation equation for the fluid flow in the fracture is

$$\frac{\partial w}{\partial t} + \frac{\partial q}{\partial x} = 0 \quad (3.10)$$

where  $w$  is the fracture opening (width),  $q$  the flow rate, and  $x$  the local coordinate aligned with the tangential direction to the fracture path.

Assuming the fluid flow in the fracture is laminar, the cubic width law formulated for flow between parallel plates is adopted and stated as follows:

$$q = -\frac{w^3}{12\mu} \frac{\partial p_f}{\partial x} \quad (3.11)$$

where  $\mu$  is the viscosity of the fracturing fluid, and  $p_f$  the pressure of fluid within the fracture.

### 3.2.4 Fracture propagation criteria

The cohesive zone model is adopted for the fracture propagation criterion. First developed by Dugdale and Barenblatt [28, 122], the cohesive zone model assumes a process zone ahead of the real fracture tip and, by doing so, avoids the singularity at the fracture tip. In the process

zone a traction-separation law controls the variation of cohesive traction with the separation (width) of the crack. When the maximum principal stress reaches the cohesive strength of the material, the crack initiates. With the crack opening, the cohesive traction will decrease and once it has decreased to zero, the maximum crack width opening is obtained and complete separation is reached.

A close view of the process zone is shown in Fig. 3.2, where  $t_n$  denotes the cohesive traction on the fracture surface,  $p_f$  the fluid pressure within the fracture,  $\delta_n$  the fracture opening. Fluid pressure exerts on the broken cohesive element, and cohesive traction exerts on the unbroken cohesive element. In our study, the bilinear traction-separation law is adopted, as shown in Fig. 3.3. The traction and separation are quantified as follows:

$$t_n = \begin{cases} (1 - D)k_n \delta_n, & \delta_n \geq 0 \text{ (tension)} \\ k_n \delta_n, & \delta_n < 0 \text{ (compression)} \end{cases} \quad (3.12)$$

where subscripts  $n$  and  $s$  identify the normal direction and the shear direction, and  $t$ ,  $k$  and  $\delta$  are the traction, initial stiffness and relative displacement.

$D$  is the damage variable, which increases from 0 to 1 monotonically:

$$D = \begin{cases} 0 & (\delta_n^{max} < \delta_n^0) \\ \frac{\delta_n^f (\delta_n^{max} - \delta_n^0)}{\delta_n^{max} (\delta_n^f - \delta_n^0)} & (\delta_n^0 \leq \delta_n^{max} \leq \delta_n^f) \\ 1 & (\delta_n^{max} > \delta_n^f) \end{cases} \quad (3.13)$$

where superscripts 0,  $f$  and  $max$  are the parameters at damage initiation, complete failure and the maximum value. A high initial stiffness  $k_n$  is adopted to obtain realistic results and  $\delta_n^f$  is assumed to be far more than  $\delta_n^0$ . The area under the traction-separation curve equals the fracture energy  $G_c$ , representing the work needed to create a unit area of a fully developed crack. Thus, the displacement corresponding to the complete failure point can be determined by:

$$\delta_n^f = \frac{2G_c}{t_n^0} \quad (3.14)$$

### 3.3 Numerical implementation

In order to solve the system of equations described in section § 3.2, a piecewise linear Galerkin finite element method (FEM) is used for spatial discretisation and solved implicitly in time using backward Euler.

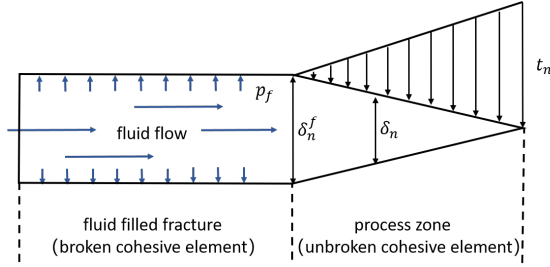


Fig. 3.2 Cohesive traction on the fracture surface.

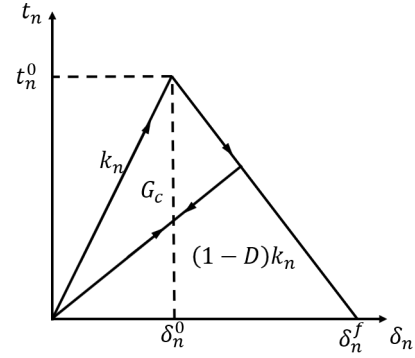


Fig. 3.3 The traction-separation law.

### 3.3.1 Discretisation for the governing equations

The equations are numerically solved by using the FEM for space discretisation. Let  $\delta \mathbf{u}$  denote the test function for the displacement, the weak form of Eq. (3.1) can be written as follows:

$$\begin{aligned} & \int_{\Omega} \delta \boldsymbol{\varepsilon} : \boldsymbol{\sigma}' d\Omega - \int_{\Omega} \delta \boldsymbol{\varepsilon} : \mathbf{I} \alpha p_w d\Omega - \int_{\Omega} (\delta \mathbf{u} \cdot \rho \mathbf{g} - \delta \mathbf{u} \cdot \rho \ddot{\mathbf{u}}) d\Omega \\ & = \int_{\Gamma_e} \delta \mathbf{u} \cdot \mathbf{t}_e d\Gamma_e - \int_{\Gamma_t} \delta \mathbf{u} \cdot \mathbf{t}_t d\Gamma_t + \int_{\Gamma_f} \delta \mathbf{u} \cdot \mathbf{n} \alpha p_f d\Gamma_f \end{aligned} \quad (3.15)$$

where  $\delta \boldsymbol{\varepsilon}$  is the strain corresponding to the displacement test function  $\delta \mathbf{u}$ ,  $\Omega$  the domain of the porous formation,  $\Gamma_e$  the external boundary of the domain  $\Omega$ ,  $\Gamma_t$  the cohesive zone surface,  $\Gamma_f$  the fracture surface,  $\mathbf{t}_e$  the external forces (often referred to as the confining stress),  $\mathbf{t}_t$  the cohesive traction, and  $\mathbf{n}$  the normal of the fracture surface.

The weak form of Eq. (3.8) is:

$$\int_{\Omega} \delta p_w \alpha \nabla \cdot \dot{\mathbf{u}} d\Omega + \int_{\Omega} \delta p_w \frac{1}{Q} \dot{p}_w d\Omega + \int_{\Omega} \frac{k_w}{\mu} \nabla \delta p_w \cdot \nabla p_w d\Omega = - \int_{\Gamma_q} \delta p_w \mathbf{n} \cdot \mathbf{q} d\Gamma_q \quad (3.16)$$

where  $\delta p_w$  is the test function for pore-fluid pressure,  $\Gamma_q$  the boundary of porous formation, and  $\mathbf{n}$  the normal of the boundary  $\Gamma_q$ .

The weak form of Eq. (3.10) is:

$$\int_{\Gamma_f} \delta p_f \frac{\partial w}{\partial t} d\Gamma + \int_{\Gamma_f} (\delta p_f)_{,x} \frac{w^3}{12\mu} p_{f,x} d\Gamma_f = \delta p_f(0) q(0) - \delta p_f(x_f) q(x_f) \quad (3.17)$$

where  $\delta p_f$  is the test function for fluid pressure within the fracture,  $p_f(0)$  and  $q(0)$  are the fluid pressure and the flow rate at the origin of the fracture,  $p_f(x_f)$  and  $q(x_f)$  are the fluid pressure and the flow rate at the fluid front.

Following the standard FEM discretisation, the above weak-form equations can be expressed in a compact matrix form as:

$$\mathbf{M}\ddot{\mathbf{u}} + (\mathbf{K} + \mathbf{K}_{coh})\mathbf{u} - (\mathbf{Q} + \mathbf{Q}_{int})\mathbf{p}_w = \mathbf{f}_1 \quad (3.18a)$$

$$\mathbf{Q}^T \dot{\mathbf{u}} + \mathbf{C}\dot{\mathbf{p}}_w + \mathbf{H}\mathbf{p}_w = \mathbf{f}_2 \quad (3.18b)$$

$$\mathbf{Q}_{int}^T \dot{\mathbf{u}} + \mathbf{C}_{int}\dot{\mathbf{p}}_f + (\mathbf{H}_{long} + \mathbf{H}_{trans})\mathbf{p}_f = \mathbf{f}_3 \quad (3.18c)$$

where  $\mathbf{u}$ ,  $\mathbf{p}_w$  and  $\mathbf{p}_f$  denote the nodal displacement, the nodal pore-fluid pressure and the nodal fluid pressure in the fracture, respectively. In this work, the fluid pressure is assumed to be continuous across the fracture surface for convenient calculation, i.e.  $\mathbf{p}_w = \mathbf{p}_f$  in  $\Gamma_f$ . Thus,  $\mathbf{H}_{trans}$  is omitted.

Eq. (3.18b) and Eq. (3.18c) can be assembled together and the following equations can be obtained:

$$\mathbf{M}\ddot{\mathbf{u}} + \bar{\mathbf{K}}\mathbf{u} - \bar{\mathbf{Q}}\mathbf{p} = \mathbf{f}_1 \quad (3.19a)$$

$$\bar{\mathbf{Q}}^T \dot{\mathbf{u}} + \bar{\mathbf{C}}\dot{\mathbf{p}} + \bar{\mathbf{H}}\mathbf{p} = \bar{\mathbf{f}} \quad (3.19b)$$

The matrix  $\bar{\mathbf{K}}$  is obtained by assembling matrices  $\mathbf{K}$  and  $\mathbf{K}^{coh}$ ;  $\bar{\mathbf{Q}}$  is obtained by assembling matrices  $\mathbf{Q}$  and  $\mathbf{Q}_{int}$ ;  $\bar{\mathbf{C}}$  is obtained by assembling matrices  $\mathbf{C}$  and  $\mathbf{C}_{int}$ ,  $\bar{\mathbf{H}}$  is obtained by assembling matrices  $\mathbf{H}$  and  $\mathbf{H}_{trans}$ ,  $\bar{\mathbf{f}}$  is obtained by assembling matrices  $\mathbf{f}_2$  and  $\mathbf{f}_3$ . The detailed definitions for the coefficient matrices/vectors  $\mathbf{M}$ ,  $\mathbf{K}$ ,  $\mathbf{K}_{coh}$ ,  $\mathbf{Q}$ ,  $\mathbf{Q}_{int}$ ,  $\mathbf{C}$ ,  $\mathbf{C}_{int}$ ,  $\mathbf{H}_{long}$ ,  $\mathbf{f}_1$ ,  $\mathbf{f}_2$ ,  $\mathbf{f}_3$  are given in following parts.

$$\mathbf{K} = \int_{\Omega} \mathbf{B}_u^T \mathbf{D} \mathbf{B}_u d\Omega \quad (3.20)$$

$$\mathbf{K}^{coh} = \int_{\Gamma_t} \mathbf{N}_{int}^T \mathbf{R}^T \mathbf{T} \mathbf{R} \mathbf{N}_{int}, \quad \mathbf{R} = \begin{bmatrix} \cos\theta & \sin\theta \\ -\sin\theta & \cos\theta \end{bmatrix} \quad (3.21)$$

$$\mathbf{M} = \int_{\Omega} \mathbf{N}_u^T \rho \mathbf{N}_u d\Omega \quad (3.22)$$

$$\mathbf{Q} = \int_{\Omega} \alpha \mathbf{B}_u^T \mathbf{m} \mathbf{N}_p d\Omega, \quad \mathbf{m} = \{1, 1, 0\}^T \quad (3.23)$$



$$\mathbf{Q}_{int} = \int_{\Gamma_f} \mathbf{N}_{int}^T \mathbf{R}^T \alpha_f \mathbf{m}_2 \mathbf{N}_f, \mathbf{m}_2 = \{0, 1\}^T \quad (3.24)$$

$$\mathbf{C} = \int_{\Omega} \frac{1}{Q} \mathbf{N}_p^T \mathbf{N}_p d\Omega \quad (3.25)$$

$$\mathbf{H} = \int_{\Omega} \mathbf{B}_p^T \frac{\mathbf{k}_w}{\mu} \mathbf{B}_p d\Omega \quad (3.26)$$

$$\mathbf{H}_{long} = \int_{\Gamma_d} \nabla \mathbf{N}_f^T \frac{w^3}{12\mu} \mathbf{N}_f d\Gamma_d, \mathbf{k}_w = \begin{bmatrix} k_x & 0 \\ 0 & k_y \end{bmatrix} \quad (3.27)$$

$$\mathbf{f}_1 = \int_{\Gamma_e} \mathbf{N}_u^T \mathbf{t}_e d\Gamma_e + \int_{\Gamma_t} \mathbf{N}_u^T \mathbf{t}_t d\Gamma_t \quad (3.28)$$

$$\mathbf{f}_2 = - \int_{\Gamma_q} \mathbf{N}_p^T q d\Gamma_q \quad (3.29)$$

$$\mathbf{f}_3 = [q(0), 0, \dots, 0, q(N+1)]^T \quad (3.30)$$

where  $N$  is the number of linear elements along the fracture length,  $\mathbf{N}_u$  the shape function matrix,  $\mathbf{B}_u$  the strain displacement matrix, and  $\mathbf{B}_p$  the first derivatives of  $\mathbf{N}_p$ .

### 3.3.2 Solution details

The Newmark method is used to solve the coupled dynamic nonlinear equation system. The variables  $\dot{\mathbf{u}}, \mathbf{u}, \mathbf{p}$  at time  $n+1$  can be represented as:

$$\mathbf{u}^{n+1} = \mathbf{u}^n + \Delta t \dot{\mathbf{u}}^n + \left(\frac{1}{2} - \beta\right) \Delta t^2 \ddot{\mathbf{u}}^n + \beta \Delta t^2 \ddot{\mathbf{u}}^{n+1} \quad (3.31a)$$

$$\dot{\mathbf{u}}^{n+1} = \dot{\mathbf{u}}^n + \Delta t \ddot{\mathbf{u}}^n - \gamma \Delta t \ddot{\mathbf{u}}^n + \gamma \Delta t \ddot{\mathbf{u}}^{n+1} \quad (3.31b)$$

$$\mathbf{p}^{n+1} = \mathbf{p}^n + \Delta t \dot{\mathbf{p}}^n - \theta \Delta t \dot{\mathbf{p}}^n + \theta \Delta t \dot{\mathbf{p}}^{n+1} \quad (3.31c)$$

After substituting Eq. (3.31) into Eq. (3.19), we can get the following equation system:

$$\begin{bmatrix} \mathbf{M} + \bar{\mathbf{K}}\beta\Delta t^2 & -\bar{\mathbf{Q}}\theta\Delta t \\ \bar{\mathbf{Q}}\gamma\Delta t & \mathbf{C} + \theta\Delta t\mathbf{H} \end{bmatrix} \begin{Bmatrix} \ddot{\mathbf{u}}^{n+1} \\ \dot{\mathbf{p}}^{n+1} \end{Bmatrix} = - \begin{Bmatrix} \mathbf{G}_s^{n+1} \\ \mathbf{G}_p^{n+1} \end{Bmatrix} \quad (3.32)$$

When  $\gamma \geq 1/2$ ,  $\beta \geq 1/4$ , and  $\theta \geq 1/2$ , the equation system is unconditionally stable. The nonlinear equation system is solved via the Newton-Raphson method.

To enforce the pressure continuous across the crack surface, the multi-points constraints master-slave method is employed [279], see Fig. 3.4. Nodes 4, 5, 6 are used for fluid flow inside the fracture and nodes 1, 2, 3, 7, 8, 9 are used for cohesive elements. Fluid pressure  $p_f$  at node 4 is equal to the pore pressure  $p_w$  at node 1 and 7. Similarly,  $p_f$  at node 5 is equal to  $p_w$  at node 2 and 8, and  $p_f$  at node 6 is equal to  $p_w$  at node 3 and 9. Take nodes 2, 5, 8 as an example. The pore pressure degree of freedom (dof) of node 2 is taken as the master dof, and pore pressure dofs of node 5 and 8 are taken as slave dofs. Therefore, the pressure at node 5 and 8 is forced to be the same with the pressure at node 2.

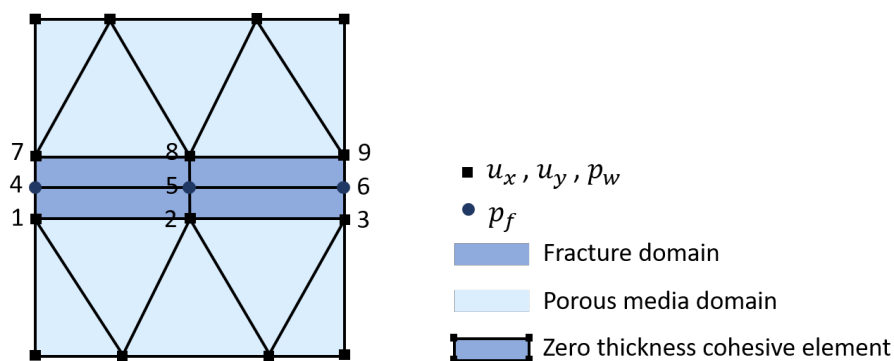


Fig. 3.4 A case to illustrate the FE mesh with cohesive elements.

### 3.4 Model Verification

The proposed hydraulic fracturing model and its implementation are based on our previous work [75, 78], where the functional modulus for formation deformation, fluid flow in the fracture and fracture propagation have been fully validated. The newly integrated functional modules include mainly the dynamic model, the poroelasticity model and the cohesive zone model. In order to verify the accuracy and robustness of the numerical framework presented, especially for the new functional modules, three benchmark problems are selected here. The dynamic verification, cohesive zone verification and 2D KGD plane strain model verification are given to prove the correctness of our model.

#### 3.4.1 Dynamic solution verification

The first example is a fully saturated poroelastic column with pressure applied on its top, which was used in [189] to verify the dynamic behaviour in porous media. The height of the column is 30 m. And its top surface is subjected to a step loading of  $1 \text{ kN/m}^2$  applied in 0.1 s, and the pressure on the top equals zero, which is fixed as time increases. The boundary

Table 3.1 Material properties for the poroelastic column.

Properties	Symbols	Values
Young's modulus	$E$	$3.0 \times 10^7 \text{ N/m}^2$
Poisson's ratio	$\nu$	0.2
Porosity	$n$	0.3
Bulk modulus(fluid)	$K_w$	$2.1 \times 10^9 \text{ N/m}^2$
Density(solid)	$\rho_s$	$1.0 \times 10^3 \text{ kg/m}^3$
Density(fluid)	$\rho_w$	$2.0 \times 10^3 \text{ kg/m}^3$
Permeability coefficient	$\frac{k}{\mu}$	$1.0 \times 10^{-8} \text{ m}^2/(\text{Pa}\cdot\text{s})$

condition for the problem is shown in Fig. 3.5, and the material properties are listed in Table 3.1. Node 1, node 11 are located at the bottom and middle of the column, respectively. Node 19 is located 3 meters from the top. As time increases, pressure increases at the bottom and decreases at the top of the column. Fig. 3.6 shows good agreement of our numerical solution with the solution obtained from [189].

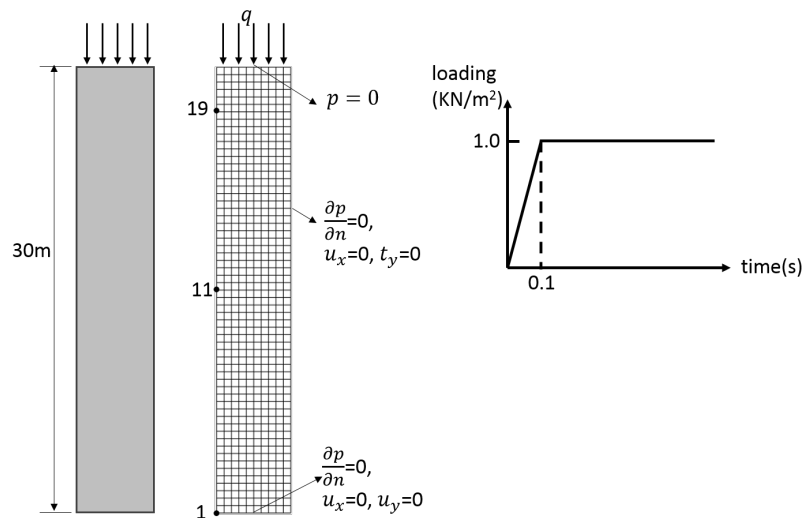


Fig. 3.5 The basic geometry of 1D column model.

### 3.4.2 Cohesive zone verification

The cohesive zone model is verified through a numerical example from [70] in the storage-toughness dominated regime. Compared with the parameters provided in Table 3.2, the permeability is assigned a value of  $k = 10^{-16} \text{ m}^2$  and  $k = 10^{-15} \text{ m}^2$ , respectively. The

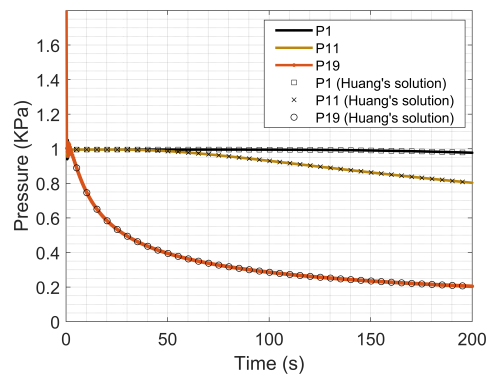
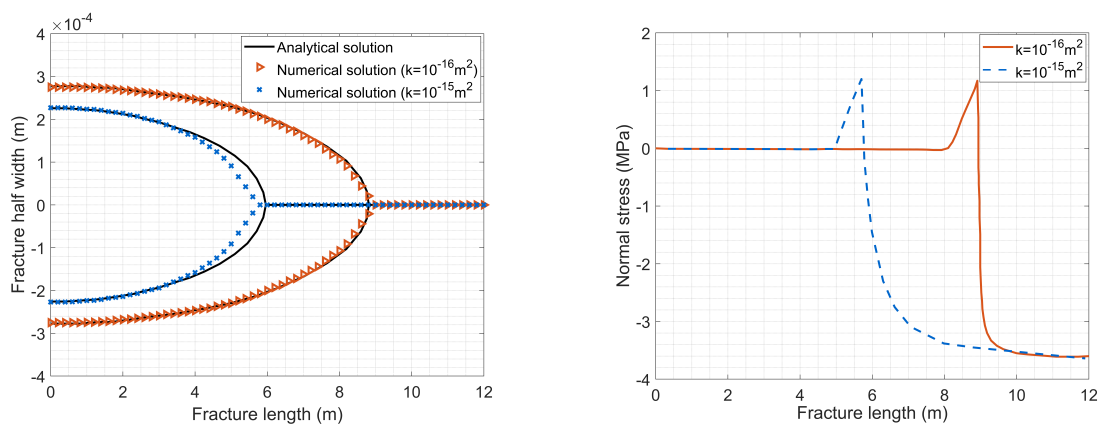


Fig. 3.6 The pressure history at different nodes.

viscosity is  $\mu = 10^{-4}$  Pa·s, the fracture energy  $G_c$  is 0.12 N/mm, the critical stress is 1.25 MPa, and the confining stress is 3.7 MPa. Fig. 3.7a presents the fracture shape at  $t = 10$  s, and the numerical solution shows good agreement with the analytical solution in the storage-toughness dominated regime [62]. On the right, Fig. 3.7b shows the normal effective stress across the fracture. As expected, the value of normal effective stress turns to zero when complete separation of the fracture is reached. In the process zone, the traction increases with decreasing fracture width (separation) and reaches its maximum critical stress 1.25 MPa at the fracture tip. Then, away from the fracture tip, it equals the far-field stress ahead of the fracture tip 3.7 MPa.



(a) The fracture shape in different permeability at  $t = 10$  s.

(b) The normal effective stress across the fracture at  $t = 10$  s.

Fig. 3.7 Cohesive zone verification.

### 3.4.3 KGD model

To test the numerical approaches, the two-dimensional plane strain KGD model is adopted, in which the borehole is treated as a point source in the plane because the radius is very small compared to the fracture length. The basic geometry of this model is shown in Fig. 3.8.

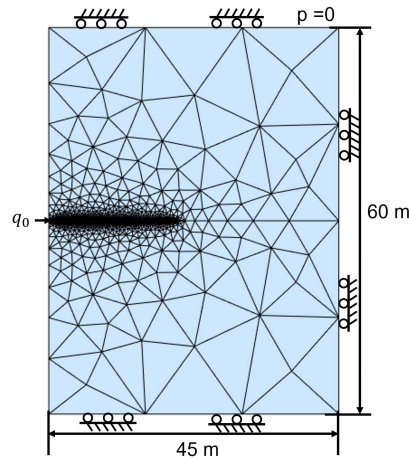


Fig. 3.8 The basic geometry of the KGD model.

The fracture is then restricted to grow symmetrically with respect to the borehole in the horizontal direction while remaining planar at all times. The fracture opening is assumed to be perpendicular to the minimum far-field confining stress. The intrinsic cohesive zone model is used, which saves the trouble of remeshing when crack shape changes with time. The cohesive elements are inserted along the central line of the model before simulation. The rock media is assumed to be homogeneous, with fully saturated media and small deformation. Incompressible fluid fills the fracture, and there is zero fluid lag. The initial conditions on the domain are  $p_w = p_0$ ,  $\mathbf{u} = \mathbf{u}_0$ ,  $\dot{\mathbf{u}} = \dot{\mathbf{u}}_0$ . For simplicity, the pressure is assumed to be continuous across the fracture, so fluid pressure  $p_f$  within the fracture is equal to pore pressure  $p_w$  along the fracture surface. In order to allow the fluid to penetrate the rock, the most left interface element is treated as a traction free crack. The boundary conditions here for the fluid in the fracture involve a constant flow rate at the mouth of the fracture and zero flow rate at the fracture tip (no lag assumption). The analytical solutions for the fracture length  $l$ , the

wellbore fracture aperture  $w$  and the wellbore pressure  $p_f$  are [152]:

$$l(t) = 0.68 \left[ \frac{Gq_0^3}{\mu(1-\nu)} \right]^{1/6} t^{2/3} \quad (3.33a)$$

$$w(0,t) = 1.87 \left[ \frac{\mu(1-\nu)q_0^3}{G} \right]^{1/6} t^{1/3} \quad (3.33b)$$

$$p_f(0,t) = 1.38 \left[ \frac{G^3 q_0 \mu}{(1-\nu)^3 l^2(t)} \right]^{1/4} + \sigma_0 \quad (3.33c)$$

where  $G$  describes the plane strain modulus,  $G = E/(1 + 2\nu)$ ,  $t$  the time,  $\sigma_0$  the confining stress,  $q_0$  the injection flow rate. All parameters, including the rock properties and fluid properties used in the numerical simulation, are listed in Table 3.2. We note that when plugging the parameters into KGD equations, they need to be converted into SI the international system of units. Good agreement between the numerical and analytical results is obtained as shown in Fig. 3.9, which demonstrates the reliability of the numerical method for approximation of the KGD model solution.

Table 3.2 Rock properties and fluid properties used in KGD simulation

Properties	Symbols	Values
Elasticity modulus	$E$	17 GPa
Poisson's ratio	$\nu$	0.2
Biot coefficient	$\alpha$	0.75
Biot modulus	$Q$	12.2 GPa
Viscosity	$\mu$	0.1 Pa · s
Material density	$\rho$	$1.81 \times 10^3$ kg/m <sup>3</sup>
Porosity	$n$	0.2
Permeability	$k$	$1.0 \times 10^{-13}$ m <sup>2</sup>
Critical energy release rate	$G_c$	0.05 N/mm
Initial stiffness	$k_n$	$17 \times 10^{14}$ N/m <sup>3</sup>
Tensile strength	$t_n^0$	0.9 MPa
Injection flow rate	$q_0$	$1 \times 10^{-3}$ m <sup>2</sup> /s

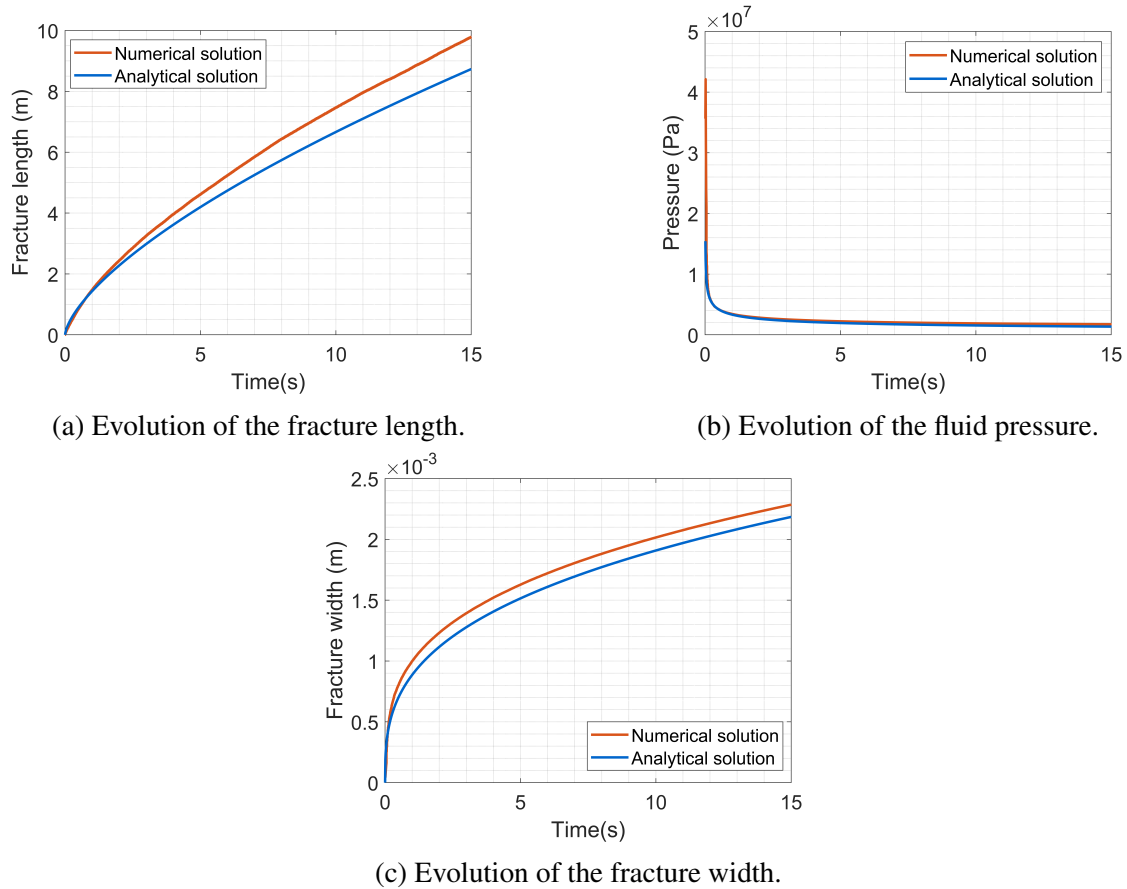


Fig. 3.9 The KGD model verification.

### 3.5 Discussions

After verification of the model, the stepwise process is investigated here with a discussion on whether the stepwise phenomenon observed with our model is mainly due to numerical or physical reasons.

**Time refinement** Using a mesh size  $\Delta x = 0.05$  m, consecutive simulations are performed with decreasing time step  $\Delta t$  chosen to be 0.01 s, 0.005 s, 0.001 s, respectively. Referring to the results shown in Fig. 3.10a, the stepwise phenomenon becomes increasingly noticeable with a smaller time step. The results are consistent with those in the literature [279] for a fixed spatial interval.

**Mesh refinement** To answer whether the stepwise phenomenon observed is mesh independent or not, consecutive simulations are performed with a constant time step  $\Delta t = 0.01$  s and different mesh size  $\Delta x$ . To avoid the singularity, the mesh needs to be refined along the

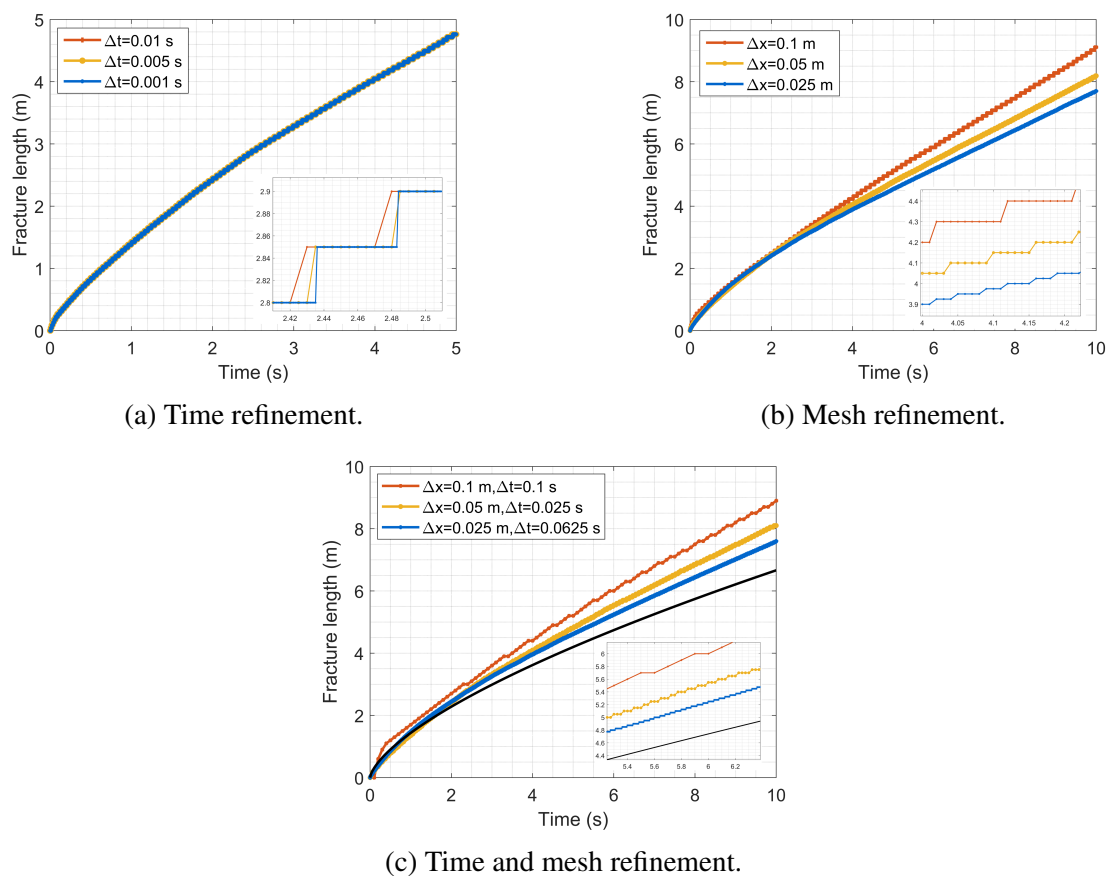


Fig. 3.10 Fracture length versus time.

fracture path, and an element threshold number needs to be satisfied over the cohesive zone [68]. Considering the computational cost, the mesh size  $\Delta x$  is chosen to be 0.1 m, 0.05 m and 0.025 m, respectively. Referring to the results shown in Fig. 3.10b, the stepwise phenomenon reduces with mesh refinement.

**Time and mesh refinement** It can be concluded from Fig. 3.10a and Fig. 3.10b that during simulation, the stepwise phenomenon increases with temporal refinement and reduces under mesh refinement. Since both temporal and spatial approximations are influential, time and mesh refinement are required to study the stepwise phenomenon. While the current approximations are essentially first order in time (Backward Euler) and second-order in space (standard Galerkin piecewise linear on triangles), in order to demonstrate numerical convergence behaviour, each refinement must be conducted such that the spatial and temporal errors are proportionately balanced, where for a given spatial interval  $\Delta x$ , the time step should be adopted following the equation below, where  $C$  is a coefficient, and parabolic diffusion



approximation errors provide a guide.

$$\Delta t = C\Delta x^2 \quad (3.34)$$

The results of Fig. 3.10c show that under spatial and temporal refinement, the overall trend in fracture length tends to the analytical solution and the stepwise phenomenon (regular steps) decreases. This implies that the stepwise phenomenon observed with our model is mesh dependent and mainly due to numerical origin. However, the stepwise phenomenon does exist since it has been documented both in field tests [145, 289, 316, 321], laboratory experiments [318, 427] and numerical simulations [380, 379, 67, 283]. We note that in most of the literature and our model, the irregular stepwise phenomenon caused by physical reasons is not captured. A likely reason is given in [315], which states that the improper time step/fracture advancement algorithm adopted may yield regular steps. Another likely reason is given in [68] that various physical influencing factors may contribute to the observation of the stepwise phenomenon since the phenomenon interferes with three velocities, namely crack tip velocity, fluid seepage velocity in the domain, and fluid velocity in the crack tip. Therefore, we postulate that only under specific conditions can the physical stepwise phenomenon (irregular steps) be captured. A series of simulations are conducted in an attempt to find the specific conditions by varying the influencing factors.

## 3.6 Investigation of stepwise fracture propagation

With the assumption that only under specific conditions can the physical stepwise phenomenon (irregular steps) be captured, the effects of different parameters, including Young's modulus, Poisson's ratio, Biot coefficient, Biot modulus, rock porosity and permeability, viscosity, injection rate and fracture energy, on the stepwise phenomenon have been investigated. According to the controlling equation and propagation criterion, the key variables can be divided into two categories: the formation variables and the fluid variables, which are given in Table 3.3.

### 3.6.1 Young's modulus and Poisson's ratio

Typical values of Young's modulus for rock formations range from a couple of 11.3 GPa to about 40 GPa [458]. In this study, Young's modulus is selected as: 8.5 GPa, 17 GPa and 34 GPa. The relationship between fracture length and time step under conditions for a range of Young's modulus for different formation rocks is investigated. Fig. 3.11 shows that the smaller Young's modulus is, the longer the time interval between each fracture propagation.

Table 3.3 Key variables influencing the stepwise phenomenon.

Formation variables	Fluid variables
Young's modulus $E$	Injection flow rate $q_0$
Poisson's ratio $\nu$	Viscosity $\mu$
Biot coefficient $\alpha$	
Biot modulus $Q$	
Porosity $n$	
Permeability $k$	
Fracture energy $G_c$	

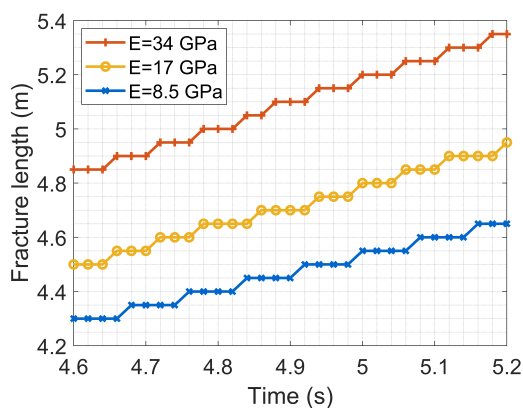


Fig. 3.11 Stepwise phenomenon with different Young's moduli.

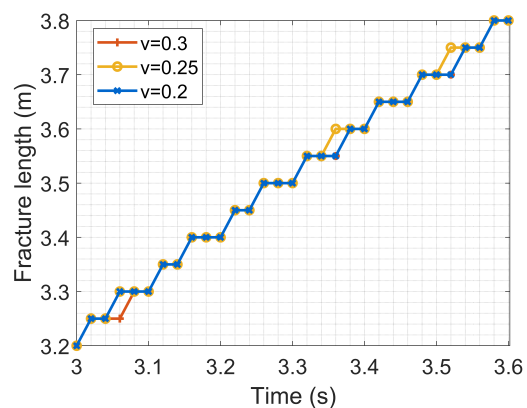


Fig. 3.12 The stepwise phenomenon with different Poisson's ratios.

A likely reason for this observation is that the smaller Young's modulus, the easier the rock deforms. The rock will not break until it deforms to a certain extent. Therefore, the fluid in the fracture needs more time to accumulate energy to deform the rock and then break the rock, which means the fracture propagation velocity will be slower. However, though the value of Young's modulus is changed, only the regular step can be observed. This reflects that compared with Young's modulus, mesh is the main reason for the stepwise advancement observed here.

The Poisson's ratio for the formation is set at three different levels: 0.2, 0.25 and 0.3. The relationship between fracture length and time under different conditions of Poisson's ratio is shown in Fig. 3.12. The jump and the pause time of the red line are nearly the same as that of the blue line. The fracture propagation velocity appears to be relatively insensitive to Poisson's ratio. It can be observed that though the Poisson's ratio is varying, the stepwise phenomenon is still dominated by numerical reason, and no irregular steps can be captured.

### 3.6.2 Biot coefficient and Biot modulus

The Biot coefficient is 1 for incompressible grain and is less than 1 for compressible grain. In this study, three values of Biot coefficient are considered: 0.5, 0.75 and 1. Fig. 3.13 shows that the fracture propagation velocity is insensitive to the factors. The Biot modulus is the inverse of a storage coefficient [38], defined as the increase of the amount of fluid (per unit volume of rock) as a result of a unit increase of pore pressure, under constant volumetric strain,  $\frac{1}{Q} = \frac{\partial \zeta}{\partial p} \Big|_{\epsilon}$ . The values we adopt here are 11 GPa, 12 GPa and 13 GPa. The pause time of the stepwise phenomenon is longer for the smallest Biot modulus  $Q$ , as indicated by the red line in Fig. 3.14. Since a smaller Biot modulus  $Q$  leads to a larger porosity  $n$ , more fluid will be stored in porous media, with less flow in the fracture. Consequently, it will take more time for the fracture to accumulate energy and propagate. In Fig. 3.13 and Fig. 3.14, both the steps observed are regular no matter how the Biot coefficient and Biot modulus are changed.

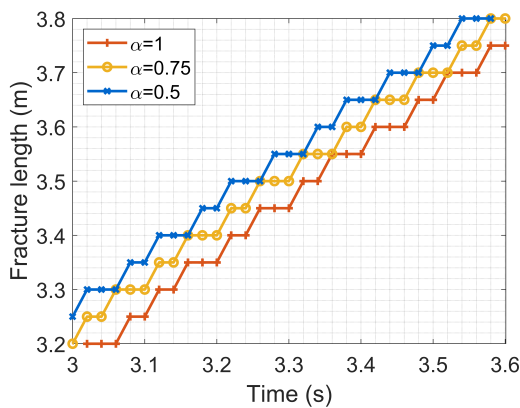


Fig. 3.13 Stepwise phenomenon with different Biot coefficients.

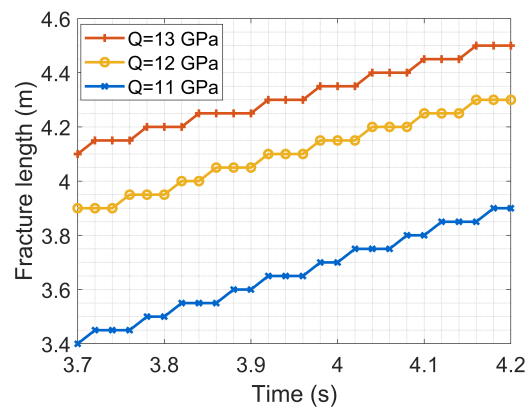


Fig. 3.14 Stepwise phenomenon with different Biot moduli.

### 3.6.3 Porosity and permeability

Fig. 3.15 shows that the permeability has an obvious effect on the fracture propagation velocity. As permeability increases, the propagation velocity of the fracture will decrease, and the pause time will increase. The result is consistent with what was found in the literature [131, 376]. A likely reason is that the fluid within the fracture can be divided into two parts: the fluid flowing into the porous medium and the fluid flowing into the fracture to overcome the propagation criterion. If the permeability is increased, more fluid will flow into the porous media and less fluid for propagation, which means it will take more time for the fracture to propagate. The influence of permeability on the physical stepwise is less obvious due to no

irregular steps can be obtained with varying permeability. Similar to permeability, porosity also has little effect on the observation of the physical stepwise, see Fig. 3.16.

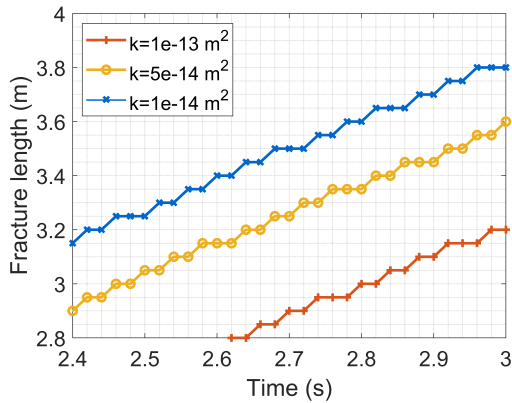


Fig. 3.15 Stepwise phenomenon with different permeability.

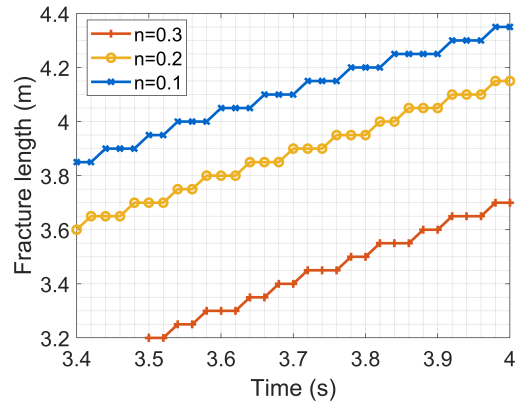


Fig. 3.16 Stepwise phenomenon with different porosity.

### 3.6.4 Fracture energy

The fracture energy  $G_c$  represents the energy required to create a new crack. Referring to the traction separation law (see Fig. 3.3), if  $\delta_n^f$  keeps constant, the value of the fracture energy is proportional to the tensile strength  $t_n^0$ . The fracture propagation velocity is sensitive to fracture energy. It is easier for the fracture to propagate in low fracture energy materials, while more time is needed for the fracture to accumulate energy for propagation in high fracture energy materials. Though different fracture energy is adopted, it is hard to see the irregular stepwise phenomenon caused by physical reasons, see Fig. 3.17.

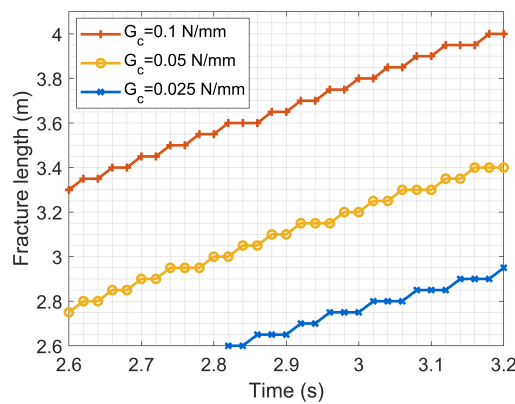


Fig. 3.17 Stepwise phenomenon with different fracture energy.

### 3.6.5 Viscosity and injection flow rate

The effect of variation in viscosity of the fluid is presented in Fig. 3.18. With high viscosity, the fluid within the fracture may flow more slowly, which means it needs more time for the fluid to catch up with the fracture tip and accumulate more pressure to break the propagation criterion. Regular steps are observed with different viscosity, which hints that though related to fluid velocity, the varying viscosity can not capture the physical stepwise phenomenon.

A high injection rate leads to faster fracture propagation velocity, as shown in Fig. 3.19. A high injection rate causes the fluid to flow faster, reducing the time for the high injection rate fluid to fill in fracture. Therefore, it is easier for the fluid within the fracture to accumulate energy for the fracture to break the “propagation criterion”. However, no irregular steps can be observed.

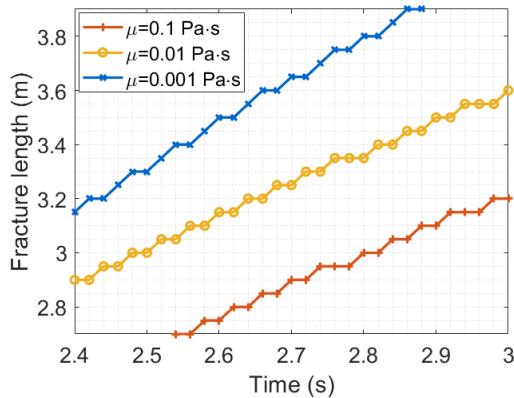


Fig. 3.18 Stepwise phenomenon with different viscosity.

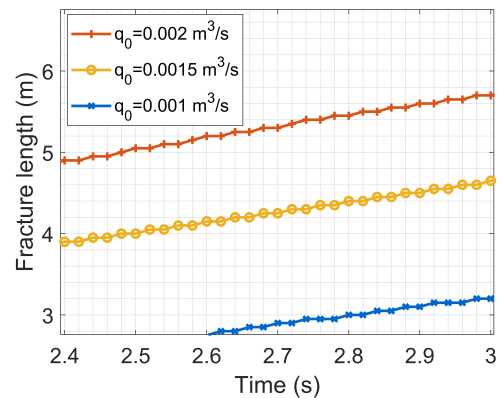


Fig. 3.19 Stepwise phenomenon with different injection rate.

## 3.7 Conclusions

A 2D plane strain dynamics fluid-driven fracture model in porous media is developed and employed to study the stepwise phenomenon. From a survey of the literature and a series of numerical tests, we arrive at the following conclusions. (1) The stepwise fracture advancement during the hydraulic fracturing process does exist in field tests and laboratory experiments. (2) It is important to distinguish whether the stepwise phenomenon observed in numerical simulation is due to physical or numerical reasons. Only a few studies have captured the physical stepwise phenomenon numerically. The stepwise phenomenon observed in our model is proved to be dependent on mesh size and time step even with poroelastic effect and dynamic rock deformation and fracture propagation considered. (3) The factors

influencing the stepwise phenomenon are summarised: the formation variables and the fluid variables, including Young's modulus, Poisson's ratio, Biot coefficient, Biot modulus, rock porosity and permeability, fracture energy, viscosity and injection rate. Under the assumption that only under specific conditions can the physical stepwise phenomenon (irregular steps) be captured, a series of simulations are conducted in an attempt to find the specific conditions for irregular stepwise. Although influencing factors are tested over a prescribed range, no irregular stepwise phenomenon is observed with our model, indicating that the stepwise fracture propagation may be induced by some other factors or physical processes not included in our model.

Work is in progress to develop a mesh-independent model to improve understanding of the stepwise phenomenon. In addition, the model in this study is confined to fully saturated homogeneous media, with a Newtonian fluid in two dimensions and mode I propagation for simplicity. However, in reality, the fracture propagates in a more complicated way. This suggests that further physical mechanisms might also contribute to this phenomenon and may need to be introduced in order to capture the stepwise phenomenon.

# Chapter 4

## A peridynamic approach for modelling hydraulic fracturing in porous media

### 4.1 Introduction

Hydraulic fracturing defines a process by which a fracture initiates and propagates due to the high-pressure fluid. It has abundant applications, including the magma-driven fractures, heat production from geothermal reservoirs, fault reactivation in mining operations and re-injection of drilling cuttings [1, 370]. The extraction of gas and oil underground is also an important application. In order to enhance the oil and gas recovery rate, a mixture of viscous fluid and proppant need to be pumped at high pressure through a borehole, and the increase of fluid pressure leads to rock break, thus forming an effective fracture network. The effective fracture network can increase the permeability of the reservoir and make the oil easily flow into the well through the fractures, which enhances the production and improve economic returns. Hence, the study of fluid-driven fracture process in rocks and the related fracture networks is of great significance in the engineering area.

In the past few decades, a series of laboratory experiments [125, 126, 164, 40, 470] and field studies [25, 21, 200, 249] have been conducted to investigate hydraulic fracturing in order to better understand fracture propagation mechanisms. Laboratory studies can range from a few cubic centimetres of small rock samples to one cubic centimetre or more of large rock samples [231]. The advantages of laboratory research lie in: (1) the experiment can be repeated many times; (2) the experimental parameters, such as stress conditions, are convenient to control; (3) the experimental results, such as the length and width of cracks, are more convenient for detection and observation. However, laboratory research has encountered experimental funding constraints. In addition, laboratory conditions make it

difficult to replicate complex geological conditions and stress conditions in the field, making results different from the actual field results. The field experiment is the primary data for the evaluation of hydraulic fracturing. Although the observation results of crack development on the site may not be as intuitive as those in the laboratory, there are still various technical means for evaluation. For example, radioactive tracer logs and temperature logs can be used to infer fracture geometry near the wellbore [24]; production data and production logging information can be used to analyse the fracture development process [319]; acoustic and resistivity logs can be used to evaluate the location where fractures develop [203]. In addition to laboratory experiments and field studies, theoretical mathematical models including the PKN model, KGD model and the radial model [313, 151, 288, 407, 159] and various analytical solutions [109, 370, 150] are also employed to investigate mechanisms involved in hydraulic fracturing. Further details of the theoretical mathematical models and analytical solutions can be found in § 2.1. Compared with laboratory, field experiments and theoretical models, numerical methods are more flexible with lower cost, making them become necessary tools to study the fluid-driven fracture behaviours.

In order to study the process of hydraulic fracturing and reveal the mechanisms involved, a variety of numerical methods have been developed. The numerical methods can be roughly divided into the continuum methods and the discontinuum methods. The commonly used continuum methods include the finite element method (FEM), the extended finite element method (XFEM), the boundary element method (BEM), and the phase-field method (PFM). A detailed procedure for numerical implementation with FEM for a 2D fully-coupled hydraulic fracturing model was given in [52]. Combined with cohesive process zone, 2D and 3D fully-coupled hydraulic fracturing models were presented and related hydraulic fracturing behaviour were studied in [70, 379, 278]. By circumventing the remeshing problem, XFEM is also applied to the simulation of hydraulic fracturing problem [359, 266]. As one of the earliest studies in modelling hydraulic fracture with XFEM, a hydraulic fracture driven by a uniform and constant fluid pressure at the bottom of a gravity dam was simulated in [359]. In [266], a fully coupled XFEM model was established with the nonlinear cohesive zone model and parameters influencing the hydraulic fracture propagation were studied. Compared with FEM, BEM overcomes the disadvantages of high computation cost due to mesh update in the whole domain [174]. Examples for modelling hydraulic fracturing in 2D and 3D with BEM can be found in [429, 71, 463]. Compared with the methods mentioned above, the PFM has advantages in coping with complex fracture patterns since it treats the fracture propagation process as an energy minimisation problem, avoiding the tracking of the fracture and additional criteria for fracture branching and intersection [79]. The first phase field model to simulate hydraulic fracturing in impermeable materials was developed by Bourdin



[59]. Later, in [257, 259], the model was extended to fluid-saturated poroelastic materials by adding poroelastic terms in the energy functional. The commonly used discontinuum method for hydraulic fracturing is DEM, which treats a material medium as an assembly of distinct particles and the motion of particles are governed by Newton's laws [98]. Applications of DEM in hydraulic fracturing are described in [101]. The influence of different parameters, including the rock properties, in-situ stress, injection flow rate, fluid viscosity on hydraulic fracturing, are also studied with the DEM model [274, 474, 119].

Though the methods mentioned above have been successfully applied in the study of hydraulic fracturing, most of them suffer from the limitations associated with simple fracture patterns/geometry. Since the controlling equations employed in these methods are partial differential equations where partial derivatives do not exist at discontinuities, complex crack patterns are hard to simulate. In order to overcome the limitation, Silling introduced peridynamics (PD) theory [394], using the spatial integrals equations instead of partial differential equations, which is very suitable for solving discontinuous problems. In addition, no complex criterion is required for crack propagation as the crack growth can be initialised spontaneously with only one bond-break criterion, which makes PD become a compromising tool to study hydraulic fracture behaviour. PD theory can be mainly classified into two types: the bond-based PD and the state-based PD. The difference between the bond-based PD and the state-based PD is that the bond-based PD is restricted with a constant Poisson ratio while the state-based PD overcomes the limitations of the fixed Poisson's ratio [394, 403]. However, when conducting fracture modelling and investigating the corresponding behaviour, the limitation of the bond-based PD can be ignored since it is easier to understand and implement compared with the state-based PD [284].

Due to the advantages of PD in modelling complex crack problems, it is widely applied in investigating the mechanisms of crack propagation and branching in brittle media [47, 49, 84, 169]. The influence of different parameters, including reflecting stress waves [169], horizon size [47], the micromodulus function [84], rock properties and loading conditions [49] on crack geometry and crack path/branch in brittle media, are studied. The first application of PD in hydraulic fracturing can be traced in [426], in which a new formulation for incorporating the effects of pore pressure was presented to simulate the deformation of porous media. Following the work, a new hydraulic fracturing model which couples a new PD formulation of porous flow and the existing PD solid formulation together was developed in [300] to simulate fluid-driven fractures in an arbitrary heterogeneous poroelastic medium. After verification by comparing its simulation results with the well-known KGD model, the model is used to simulate hydraulic fractures in more complex natural fracture networks and investigate the key parameters influencing the interactions between the hydraulic fracture and

natural fractures in [299]. A novel 3D simulation of the hydraulic fracturing initiation and propagation in a heterogeneous geological medium was presented by a linear viscoelastic PD model in [271], which is then used to investigate the interaction between induced fractures and a pre-existing fracture, as well as the influence of the angle of approach and differential horizontal stress on the fracture propagation behaviour. In [296], a new fully coupled poroelastic PD formulation was proposed using the analogy between poroelasticity and thermoelasticity. The formulation demonstrates the capability in analysis of more complex poroelastic problems, including fluid-filled rock fractures as in hydraulic fracturing, has been demonstrated. Combining both advantages of FEM and PD, a hybrid modelling approach for simulating hydraulic fracture in porous media with hybrid FEM and PD was proposed in [284], which demonstrates its ability in modelling complex crack patterns such as crack branching and crack interaction. Though the PD theory has been applied in investigating the crack propagation and branching in brittle media, to the best of the author's knowledge, little related work has been published about using the bond-based PD to analyse the following two crack behaviours: (1) the study of fracture branching in porous media on different loading conditions and (2) the study of the stepwise phenomenon. Stepwise means that the propagation of fractures is not continuous but intermittent. It has been recently observed in field tests and laboratory experiments, but only a few studies reproduced it numerically [318, 380].

In this chapter, an explicit peridynamic approach for modelling hydraulic fracture propagation in saturated porous media is presented to investigate cracking branching behaviours in porous media under different loading conditions and the stepwise phenomenon. In the framework of bond based PD, the rocks deformation equation system is solved for the displacement field, and the fluid flow equation in porous media is solved for the fluid pressure field. A staggered strategy and an explicit time integration scheme are used. The approach is verified via two benchmark examples. Subsequently, two crack propagation behaviours, including cracking branching in porous media under different loading conditions and the stepwise phenomenon, are investigated. By comparing our results with previous numerical results, the effect of the pore pressure on hydraulic fracturing branching is discussed and more evidence for stepwise phenomena is provided.

The chapter is organised as follows. The governing equations of the problem of hydraulic fractures in porous media are given in § 4.2, followed by § 4.3 which is devoted to the numerical implementation details. Benchmark examples are provided for verification in § 4.4. § 4.5 is devoted to the application of the model, which includes the study of the crack branching phenomenon and the stepwise phenomenon. Conclusions are presented in § 4.6.

## 4.2 Mathematical models for hydraulic fracturing

Hydraulic fracturing is a complex process that includes four physical processes: (1) deformation of porous media, (2) fluid flow in porous media, (3) fluid flow in the fracture, and (4) fracture propagation criteria. These processes reveal a strong coupling between deformation of rocks and the fluid flow. The governing equations involved in these processes are described as follows.

### 4.2.1 Governing equations for deformation of porous media

Introduced by Biot [38], the theory of poroelasticity is used for deformation of a porous formation. For a fully saturated porous medium with a single-phase fluid, the equilibrium equation is:

$$\nabla \cdot \boldsymbol{\sigma} + \rho \mathbf{g} - \rho \ddot{\mathbf{u}} = 0 \quad (4.1)$$

where  $\boldsymbol{\sigma}$  is the Cauchy stress,  $\mathbf{g}$  the gravity acceleration,  $\ddot{\mathbf{u}}$  the acceleration of the solid phase, and  $\rho$  the density of the porous medium defined as:

$$\rho = (1 - n)\rho_s + n\rho_w \quad (4.2)$$

where  $n$  is the porosity,  $\rho_s$  and  $\rho_w$  are the intrinsic densities of the solid and the fluid, respectively. The total stress tensor  $\boldsymbol{\sigma}$  can be expressed in terms of the effective stress tensor  $\boldsymbol{\sigma}'$  [420]:

$$\sigma_{ij} = \sigma'_{ij} - I_{ij}\alpha p \quad (4.3)$$

where  $p$  is the pressure of pore fluid,  $I_{ij}$  the identity tensor, and  $\alpha = 1 - K_t/K_s$  the Biot coefficient, which denotes the ratio of the fluid volume gained in a material element to the volume change of that element.  $K_t$  denotes the bulk modulus of the porous skeleton and  $K_s$  the bulk modulus of the solid.

Derived by Silling [394], PD is a new continuum mechanics formulation. It uses the spatial integrals equation instead of the partial differential equation, which makes it very attractive for solving discontinuous problems, e.g. crack propagation. In the PD theory, a continuum material is treated as a composition of material points  $\mathbf{x}$  that interact with other material points  $\mathbf{x}'$  inside a horizon  $H_{\mathbf{x}}$ , and the interactions vanish outside of the horizon, see Fig. 4.1. The set of points inside the horizon of point  $\mathbf{x}$  are denoted as

$$H_{\mathbf{x}} = \mathbf{x}' \in \Omega, |\mathbf{x}' - \mathbf{x}| < \delta \quad (4.4)$$

where  $\delta$  is the horizon size (radius of the horizon).

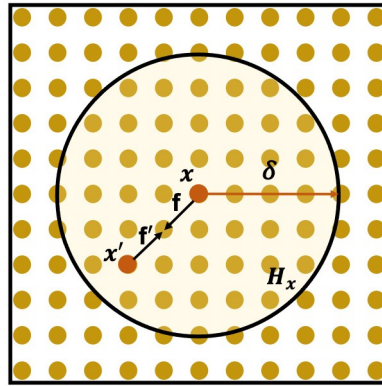


Fig. 4.1 Interaction of a material point with its neighbouring points.

At a reference position of  $\mathbf{x}$  and time  $t$ , the PD equation of motion is described by an integral formulation [394]:

$$\rho(\mathbf{x})\ddot{\mathbf{u}}(\mathbf{x},t) = \int_{H_x} \mathbf{f}(\mathbf{x}' - \mathbf{x}, \mathbf{u}' - \mathbf{u})dV_{\mathbf{x}'} + \mathbf{b}(\mathbf{x},t) \quad (4.5)$$

where  $\rho$  is the mass density,  $\mathbf{u}$  the displacement vector,  $\ddot{\mathbf{u}}$  the acceleration,  $\mathbf{b}$  a prescribed body-force density vector,  $dV_{\mathbf{x}'}$  the differential volume of  $\mathbf{x}'$ ,  $\mathbf{f}$  the force vector between two material points  $\mathbf{x}'$  and  $\mathbf{x}$ . The interaction  $\mathbf{f}$  between material points is related to the deformation, pressure and constitutive properties of the material and is called a bond.

Based on the PD theory, the governing equation for deformation Eq. (4.1) can be written in the PD form [296], which is defined as:

$$\rho(\mathbf{x})\ddot{\mathbf{u}}(\mathbf{x},t) = \int_{H_x} \lambda c(s - \alpha\gamma\bar{P}) \frac{\boldsymbol{\xi} + \boldsymbol{\eta}}{|\boldsymbol{\xi} + \boldsymbol{\eta}|} dV + \mathbf{b}(\mathbf{x},t) \quad (4.6)$$

in which  $\boldsymbol{\xi}$  and  $\boldsymbol{\eta}$  represent the initial relative position  $\mathbf{x}' - \mathbf{x}$  and the current relative displacement  $\mathbf{u}' - \mathbf{u}$ , respectively.  $\lambda$  is a scalar to describe the bond state: broken or not so as to judge whether the crack will propagate or not. Detailed explanation will be given in § 4.2.3.  $\alpha$  is the Biot coefficient.  $c$  is the PD material parameter, which can be interpreted as the bond stiffness. For an isotropic material, it can be expressed as:

$$c = \frac{2E}{A\delta^2} \quad (1D) \quad (4.7a)$$

$$c = \begin{cases} \frac{9E}{\pi h\delta^3} & (2D, \text{plane stress}) \\ \frac{48E}{5\pi h\delta^3} & (2D, \text{plane strain}) \end{cases} \quad (4.7b)$$

$$c = \frac{12E}{\pi\delta^4} \quad (3D) \quad (4.7c)$$

in which  $E$  is the Young's modulus of the solid skeleton,  $A$  the cross-sectional area, and  $h$  the thickness.

$\gamma$  is the coefficient of fluid pore pressure defined as:

$$\gamma = \frac{1}{E} \quad (1D) \quad (4.8a)$$

$$\gamma = \begin{cases} \frac{1-\nu}{E} & (2D, \text{plane stress}) \\ \frac{(1-2\nu)(1+\nu)}{E} & (2D, \text{plane strain}) \end{cases} \quad (4.8b)$$

$$\gamma = \frac{1-2\nu}{E} \quad (3D) \quad (4.8c)$$

with  $\nu$  representing the Poisson's ratio.  $\bar{P}$  is the average fluid pore pressure of points  $\mathbf{x}'$  and  $\mathbf{x}$  is defined as:

$$\bar{P} = \frac{P(\mathbf{x}', t) + P(\mathbf{x}, t)}{2} \quad (4.9)$$

$s$  is the stretch between the material points, which represents the relative elongation of the bond, which is defined as:

$$s = \frac{|\boldsymbol{\eta} + \boldsymbol{\xi}| - |\boldsymbol{\xi}|}{|\boldsymbol{\xi}|} \quad (4.10)$$

## 4.2.2 Governing equations for fluid flow in porous media and in the fracture

The continuity equation for the fluid flow in porous media is [38]:

$$\frac{\partial \zeta}{\partial t} + \nabla \cdot \mathbf{q} = 0 \quad (4.11)$$

where  $\zeta$  is the variation of fluid volume per unit volume of the porous material, and  $\mathbf{q}$  denotes the flux. Described by Darcy's law, the flux  $\mathbf{q}$  can be expressed as:

$$\mathbf{q} = -\frac{k_w}{\mu} \cdot \nabla p \quad (4.12)$$

where  $\mu$  is the fluid viscosity, and  $k_w$  the permeability. And  $p$  is the pore fluid pressure defined as:

$$p = Q(\zeta - \alpha \varepsilon_b) \quad (4.13)$$

where  $Q$  is the Biot modulus,  $\alpha$  the Biot coefficient, and  $\varepsilon_b$  the bulk volumetric strain. The compressibility coefficient  $\frac{1}{Q}$  is defined as:

$$\frac{1}{Q} = \frac{\alpha - n}{K_s} + \frac{n}{K_w} \quad (4.14)$$

where  $K_s$  and  $K_w$  are the bulk module of the solid and fluid phases, respectively.

By substituting Eq. (4.12) and Eq. (4.13) into Eq. (4.11), the governing equation for fluid flow in porous media can be obtained:

$$\alpha \nabla \cdot \dot{\mathbf{u}} + \frac{1}{Q} \dot{p} + \nabla \cdot \mathbf{q} = 0 \quad (4.15)$$

where  $\dot{\mathbf{u}}$  denotes the velocity of the solid phase and  $\frac{1}{Q}$  the compressibility coefficient. The first term can be seen as a source term driving pressure distribution and the flux.

Using analogy between poroelasticity and thermoelasticity [294, 296], Eq. (4.15) can be written in the PD form:

$$\frac{1}{Q} \dot{P}(\mathbf{x}, t) = \int_{H_x} (\kappa_P \frac{P(\mathbf{x}', t) - P(\mathbf{x}, t)}{|\mathbf{x}' - \mathbf{x}|} - \frac{c}{2} \alpha \gamma \dot{\varepsilon}) dV + \frac{q}{\rho} \quad (4.16)$$

where  $q$  is the mass of fluid per unit volume per unit time,  $\rho$  the fluid density,  $\kappa_P$  the PD parameter and can be expressed in terms of the permeability  $k_w$ .

$$\kappa_P = \frac{2k_w}{\mu A \delta^2} \quad (1D) \quad (4.17a)$$

$$\kappa_P = \frac{6k_w}{\pi \mu h \delta^3} \quad (2D) \quad (4.17b)$$

$$\kappa_P = \frac{6k_w}{\pi \mu \delta^4} \quad (3D) \quad (4.17c)$$

$\dot{\varepsilon}$  denotes the time rate of change of extension and can be described as:

$$\dot{\varepsilon} = \frac{\xi + \eta}{|\xi + \eta|} \cdot (\dot{\mathbf{u}}' - \dot{\mathbf{u}}) \quad (4.18)$$

The equation for fracture domain can be seen as a special form of Eq. (4.16) if the volumetric strain term is neglected [284] supposing that the fluid in the fracture is incompressible. And

in the fracture domain, the permeability  $k_w$  becomes  $k_f$ ;

$$k_f = \frac{1}{\eta} \frac{w^2}{12} \quad (4.19)$$

where  $w$  is the fracture width and  $\eta$  is a fracture parameter set equal to unity in this study.

### 4.2.3 Propagation criterion

In fracture mechanics, the fracture propagation criterion is used to control the propagation of a fracture. One of the commonly used criteria used in PD is called the critical bond stretch criterion [400]. When the stretch of the bond  $s$  is greater than the critical value  $s_c$ , the bond is assumed to be broken, and the pairwise force between the pair of nodes disappears.  $\lambda$  is a scalar to describe the bond state: broken or not.  $\lambda$  equals 1 when the bond is intact.  $\lambda$  equals 0 when the bond is broken.

$$\lambda(\mathbf{x}, t, \boldsymbol{\xi}) = \begin{cases} 0 & (s \geq s_c) \\ 1 & (s < s_c) \end{cases} \quad (4.20)$$

The critical stretch  $s_c$  can be determined by the critical energy release rate  $G_c$ . The relationship between  $s_c$  and  $G_c$  is defined as [247, 286, 471]:

$$s_c = \sqrt{\frac{4\pi G_c}{9E\delta}} \quad (2D, \text{plane stress}) \quad (4.21a)$$

$$s_c = \sqrt{\frac{5\pi G_c}{12E\delta}} \quad (2D, \text{plane strain}) \quad (4.21b)$$

$$s_c = \sqrt{\frac{5G_c}{6E\delta}} \quad (3D) \quad (4.21c)$$

The break of the bond is a process that cannot be recovered. The time taken by the bond break is completely determined by the material geometry and loading conditions. When a series of bonds break, the discontinuous space formed by these broken bonds becomes a macroscopic crack. Without the requirement of external criterion for crack propagation direction or crack branching angles, in the "critical bond stretch" criterion, the crack growth is a natural outcome of the calculation result.

To describe the crack path, a scalar  $\phi$  called damage parameter is used. It represents the local damage of point  $\mathbf{x}$ , which is defined as the ratio of the sum of the volumes bound to the family nodes connected by the broken bonds to the sum of the volumes of all the family

nodes in the original horizon:

$$\phi(\mathbf{x}, t) = 1 - \frac{\int_H \lambda(\mathbf{x}, \mathbf{x}', t) dV_{\mathbf{x}'}}{\int_H dV_{\mathbf{x}'}} \quad 0 \leq \phi \leq 1 \quad (4.22)$$

Thus, the value of the damage parameter is between 0 and 1, with 0 representing no failure at the point  $\mathbf{x}$  while 1 representing total failure because all the bonds connected to the point are broken. The crack path can be indicated by plotting the damage parameter.

## 4.3 Numerical implementation

### 4.3.1 Space discretisation

In the PD theory, a material can be seen as a composition of material points. Thus, the domain can be divided into nodes with a volume, and the whole body can be seen as a combination of the points.

The discretised form of solid deformation Eq. (4.6) for every node  $\mathbf{x}_i$  of the discretised domain is:

$$\rho \ddot{\mathbf{u}}_{(i)} = \sum_{j=1}^{N_{(j)}} \lambda c(s_{(i)(j)} - \alpha \gamma \bar{P}_{(i)(j)}) \frac{\boldsymbol{\xi}_{(i)(j)} + \boldsymbol{\eta}_{(i)(j)}}{|\boldsymbol{\xi}_{(i)(j)} + \boldsymbol{\eta}_{(i)(j)}|} V_{(j)} + \mathbf{b}_{(i)} \quad (4.23)$$

where  $i$  and  $j$  represent the material points,  $N_{(j)}$  the number of material points inside the horizon of point  $i$ , and  $V_{\mathbf{x}_j}$  the volume of material point  $\mathbf{x}_j$ .

Similarly, the discretised form of fluid flow Eq. (4.16) for every node  $\mathbf{x}_i$  of the discretised domain can be written as:

$$\frac{1}{Q} \dot{P}_{(i)} = \sum_{j=1}^{N_{(j)}} \left( \kappa_P \frac{P_{(j)} - P_{(i)}}{|\mathbf{x}_{(j)} - \mathbf{x}_{(i)}|} - \frac{c}{2} \alpha \gamma \dot{e}_{(i)(i)} \right) dV_{(j)} + \frac{q_{(i)}}{\rho_{(i)}} \quad (4.24)$$

### 4.3.2 Time integration

An explicit time integration scheme is used to solve the coupled equation system. Since the explicit method is conditionally stable, the critical time step can be estimated following the rules from [400, 247]. And the time step should satisfy both the equation for deformation of porous media and the equation for fluid flow. Eq. (4.23) and Eq. (4.24) can be written as:

$$\rho \ddot{\mathbf{u}}_{(i)}^n = \sum_{j=1}^{N_{(j)}} \lambda c(s_{(i)(j)}^n - \alpha \gamma \bar{P}_{(i)(j)}^n) \frac{\boldsymbol{\xi}_{(i)(j)}^n + \boldsymbol{\eta}_{(i)(j)}^n}{|\boldsymbol{\xi}_{(i)(j)}^n + \boldsymbol{\eta}_{(i)(j)}^n|} dV_{(j)} + \mathbf{b}_{(i)}^n \quad (4.25)$$



$$\frac{1}{Q} \dot{P}_{(i)}^n = \sum_{j=1}^{N(j)} \left( \kappa_P \frac{P_{(j)}^n - P_{(i)}^n}{|\mathbf{x}_{(j)}^n - \mathbf{x}_{(i)}^n|} - \frac{c}{2} \alpha \gamma e_{(i)(i)}^n \right) dV_{(j)} + \frac{q_{(i)}^n}{\rho_{(i)}} \quad (4.26)$$

A numerical implementation flowchart is shown in Fig. 4.2. The equation for deformation of porous media is solved for the displacement field, and the equation for fluid flow in porous media is solved for the fluid pressure field. After inputting the initial parameters and applying pressure boundary conditions, the time rate of pressure change  $\dot{p}^n$  is first calculated. According to Eq. (4.26) and the value of  $\dot{\mathbf{u}}^n$ ,  $p^n$ , we can get  $\dot{p}^n$ . Then we update the pressure field  $p^{n+1}$  by Eq. (4.27).

$$p^{n+1} = p^n + \Delta t \dot{p}^n \quad (4.27)$$

$p^{n+1}$  is then applied on the fracture surface as mechanical boundary conditions, which is related with the body force density in Eq. (4.25). According to Eq. (4.25), the PD force as well as the stretch of the bond are calculated. Then, the stretch of the bonds is checked, and if its stretch exceeds the critical stretch value, the interaction between the two nodes is terminated. Eq. (4.25) is then integrated in time numerically via the following sequence:

$$\dot{\mathbf{u}}^{n+1} = \dot{\mathbf{u}}^n + \Delta t \ddot{\mathbf{u}}^n \quad (4.28)$$

$$\mathbf{u}^{n+1} = \mathbf{u}^n + \Delta t \dot{\mathbf{u}}^{n+1} \quad (4.29)$$

which depends on the values of  $\dot{\mathbf{u}}^n$ ,  $p^n$  at time level  $n$ , leading to the values of  $\mathbf{u}^{n+1}$  at the new time level, and the process is repeated by updating  $\mathbf{u}^{n+1}$  and  $p^{n+1}$ .

## 4.4 Verification of the model

The accuracy of the current algorithm and formulae is demonstrated by two examples presented below. The first case involves a one-dimensional fully coupled consolidation problem, and the solution is compared with the analytical solution. The second case is an example of a two-dimensional fluid-filled fracture propagation problem in porous media.

### 4.4.1 1D porous media bar

The model describes a consolidation problem of a fully saturated 1D poroelastic bar. A pressure of  $10^4$  Pa is applied on its left edge, see Fig. 4.3. The length of the bar is  $L=15$  m with a cross-section area of  $1 \text{ m}^2$ . The left surface is allowed for fluid drainage, and the pore pressure at the left surface remains zero, while the right surface is not allowed for

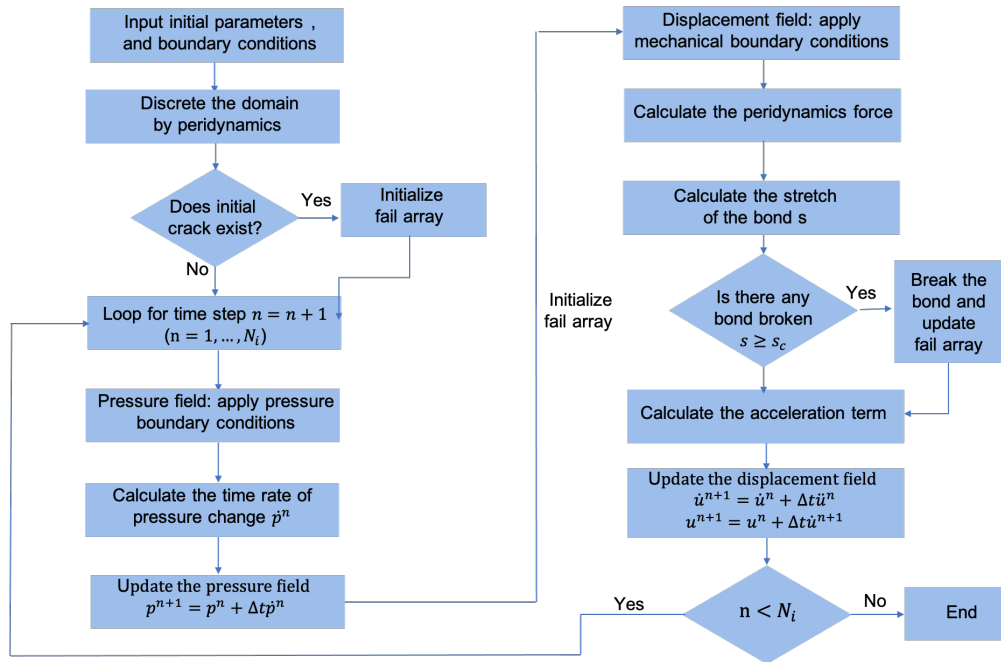


Fig. 4.2 The flow chart for the simulation process.

fluid drainage, and the flux is zero. The material properties are listed in Table 4.1. The grid spacing  $\Delta x = 0.0015$  m, and 1000 nodes are employed. The radius of horizon  $\delta$  is 0.0045 m. And the time step is  $\Delta t = 1 \times 10^{-6}$  s. For the 1D problem, the micro-modulus  $c = \frac{2E}{A\delta}$ , where  $A$  is the cross-section area.

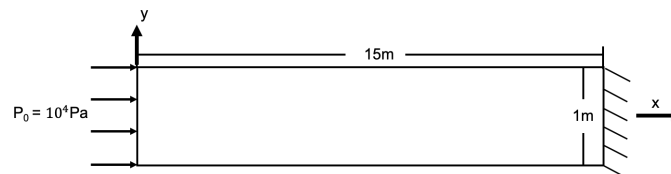


Fig. 4.3 The basic geometry of the poroelastic bar.

The initial condition is given as:

$$P(x, t = 0) = vP_0 \quad (4.30a)$$

$$u(x, t = 0) = a_i P_0 (L - x) \quad (4.30b)$$

where

$$v = \frac{a - a_i}{\alpha a}, \quad a_i = \frac{a}{1 + \alpha^2 a Q}, \quad a = 1.0 \times 10^{-8} \text{ N/m}^2 \quad (4.31)$$

Table 4.1 Material properties for the poroelastic column.

Properties	Symbols	Values
Young's modulus	$E$	$1.0 \times 10^8$ Pa
Biot coefficient	$\alpha$	0.5
Biot modulus	$Q$	$6.06 \times 10^9$ N/m <sup>2</sup>
Viscosity	$\mu$	$1.0 \times 10^{-3}$ (Pa·s)
Permeability	$k$	$1.0 \times 10^{-12}$ m <sup>2</sup>
Material density	$\rho$	$1.9 \times 10^3$ kg/m <sup>3</sup>

The analytical solution to this problem is given in [434]:

$$P(x,t) = \frac{4vP_0}{\pi} \sum_{m=0}^N \left\{ \frac{1}{2m+1} \exp\left(-\left(\frac{(2m+1)\pi}{2L}\right)^2 ct\right) \times \sin\left(\frac{(2m+1)\pi x}{2L}\right) \right\} \quad (4.32)$$

$$u(x,t) = c_m v P_0 \left\{ (L-x) - \frac{8L}{\pi^2} \sum_{m=0}^N \left\{ \frac{1}{(2m+1)^2} \right\} \right\} \times \exp\left(-\left(\frac{(2m+1)\pi}{2L}\right)^2 ct\right) \\ \times \cos\left(\frac{(2m+1)\pi x}{2L}\right) + a_i P_0 (L-x) \quad (4.33)$$

where

$$c = \frac{kQ}{(\alpha^2 a + Q)\mu}, \quad c_m = (a - a_i)/v \quad (4.34)$$

Fig. 4.4 shows the comparison between the analytical solution and numerical solution. Fig. 4.4a shows the pore pressure along the central axis at different times, while Fig. 4.4b shows the displacement along the central axis at different times. As time increases, the pore pressure decreases, and the displacement increases in the x-direction, which represents the water flows out from the top surface, and the soil consolidates.

#### 4.4.2 2D fluid-filled crack problem

The model describes a fluid-filled crack propagation problem. The propagation of the crack is driven by the pressure applied on its crack surfaces. The geometry and the boundary conditions of the model are shown in Fig. 4.5. The initial crack  $2a = 0.3$  m is set in the centre of a square of  $W = 6$  m long. All the surfaces of the square are impermeable. The top and bottom surfaces are constrained in the vertical direction, and the lateral surfaces are constrained in the horizontal direction.

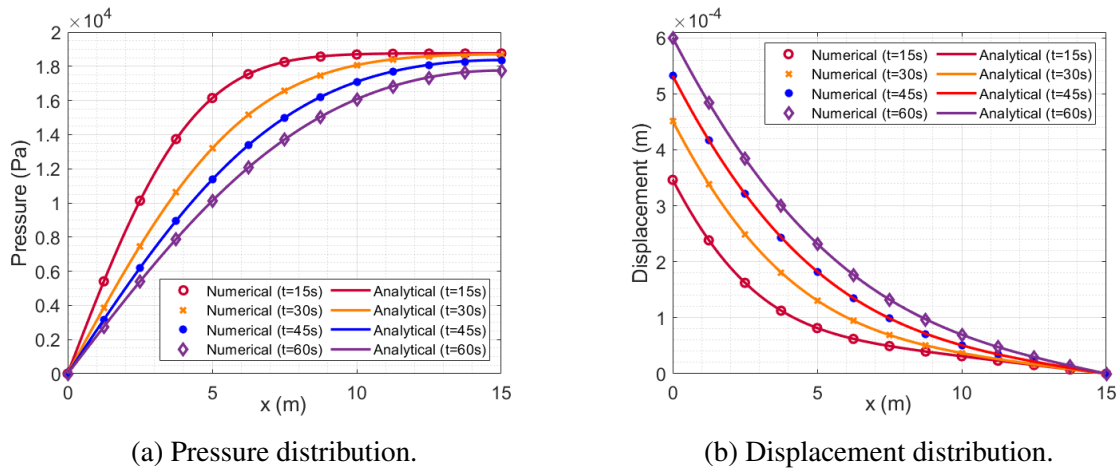


Fig. 4.4 The comparison of analytical and numerical solution along the bar.

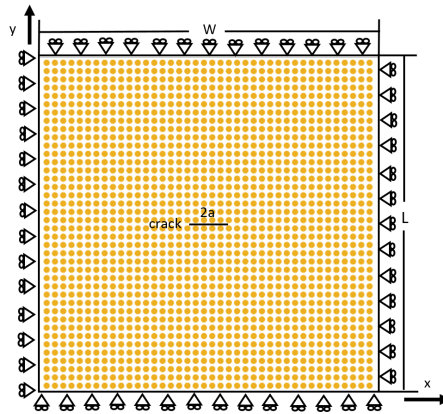


Fig. 4.5 The basic geometry of the fluid-filled crack problem model.

The pressure applied on crack surface is increased with time:

$$P_t(y = L/2, x) = P_0 \frac{t}{t_0} \quad (W/2 - a < x < W/2 + a) \quad (4.35a)$$

$$P_b(y = L/2, x) = -P_0 \frac{t}{t_0} \quad (W/2 - a < x < W/2 + a) \quad (4.35b)$$

where  $P_0 = 2000$  Pa and  $t_0 = 0.01$  s.  $P_t$  and  $P_b$  are the pressure applied on the crack top and bottom surfaces, respectively. The initial conditions are:

$$u_x(x, y, t = 0) = 0 \quad (4.36a)$$

$$u_y(x, y, t = 0) = 0 \quad (4.36b)$$

$$\dot{u}_x(x, y, t = 0) = 0 \quad (4.36c)$$

$$\dot{u}_y(x, y, t = 0) = 0 \quad (4.36d)$$

$$P(x, y, t = 0) = 0 \quad (4.36e)$$

The parameters of the model are listed in Table 4.2. The grid spacing is  $\Delta x = 0.015$  m and the time step is  $\Delta t = 1 \times 10^{-6}$  s.

Initially, the crack is not allowed to propagate, and the corresponding horizontal and vertical displacement are shown in Fig. 4.6a and Fig. 4.6b. The corresponding pressure distribution in the domain is shown in Fig. 4.7a. To verify the accuracy of the model, the numerical result obtained in [296] is given in Fig. 4.7b. The results obtained by the proposed PD model agree well with the results obtained in [296], which demonstrates the capability of the method for handling fluid-filled crack problems. As the pressure on crack surfaces increases with time, the crack becomes wider, and the pressure decreases gradually from the crack surface to the top and bottom surfaces of the model, which represents the fluid flow out from the crack to porous media. We note that the pressure is negative ahead of the crack tip. According to Biot theory, dilatation is positive in the regions ahead of the crack tips arising from the opening mode of deformation. There exists pressure pressure drop in the regions of positive dilatation, which causes large suction and negative pressure.

Table 4.2 Material properties for the 2D fluid filled crack problem.

Properties	Symbols	Values
Young's modulus	$E$	$1.0 \times 10^8$ Pa
Poisson's ratio	$\nu$	1/3
Biot coefficient	$\alpha$	0.1
Biot modulus	$Q$	$6.06 \times 10^9$ N/m <sup>2</sup>
Viscosity	$\mu$	$1.0 \times 10^{-3}$ (Pa·s)
Permeability	$k$	$1.0 \times 10^{-12}$ m <sup>2</sup>
Material density	$\rho$	$1.9 \times 10^3$ kg/m <sup>3</sup>

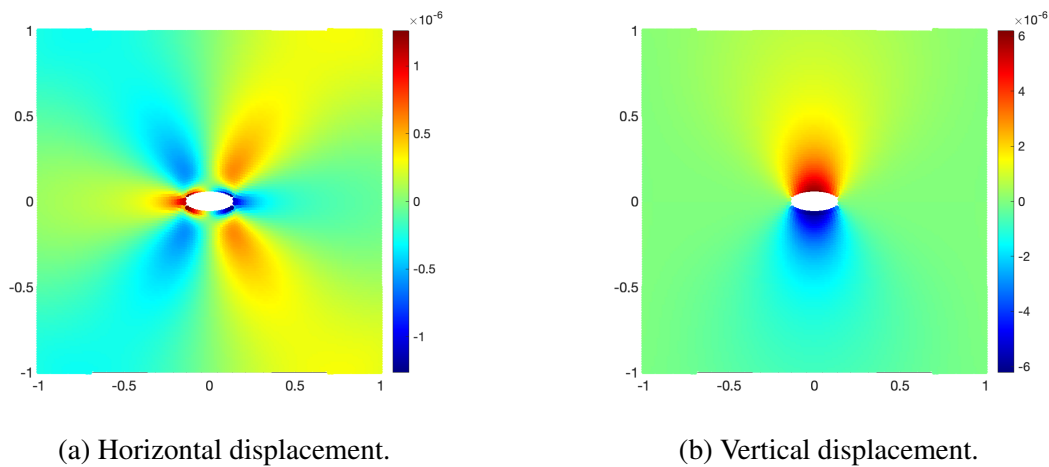


Fig. 4.6 Horizontal and vertical displacement at  $t = 0.01$  s (deformed configuration with a magnification of  $10^4$ ).

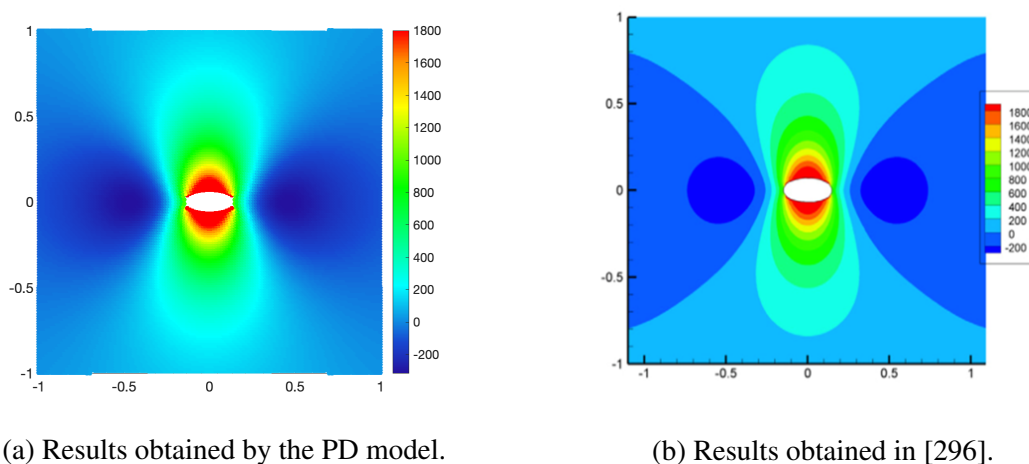


Fig. 4.7 Comparison of pressure distribution at  $t = 0.01$  s (deformed configuration with a magnification of  $10^4$  and pressure unit: Pa).

After verifying the model without failure, the crack is then allowed to propagate with a critical stretch  $s_c = 3 \times 10^{-6}$ . With crack length increasing, the crack surfaces on which the pressure applied are increasing. The pressure distribution with crack propagation at different times is shown in Fig.4.8. Negative pressure can be observed in the vicinity of the crack tip, and with time increasing, pore pressure increases on both sides of the crack surfaces and decreases towards the top and bottom surfaces of the model. The results agree well with the Ansys results in [296], which demonstrates the accuracy and the reliability of the numerical method for hydraulic fracturing problems.

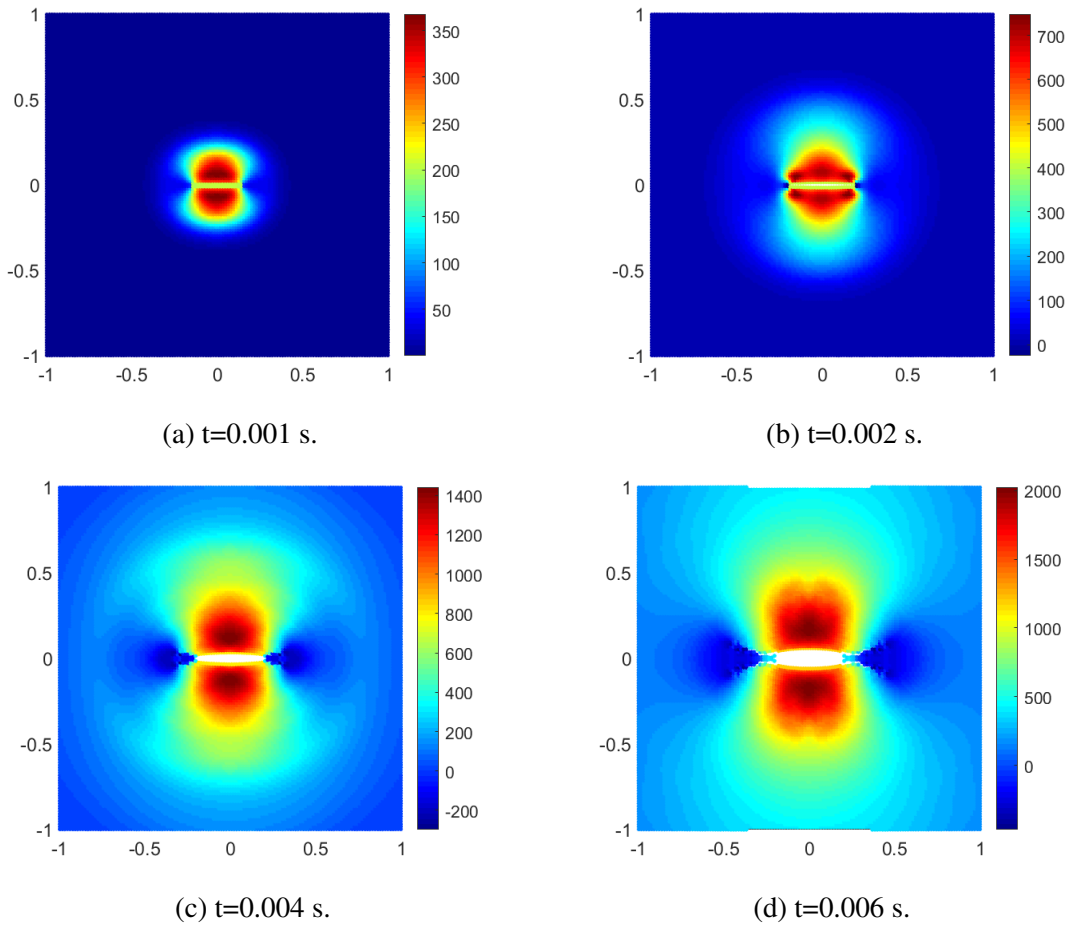


Fig. 4.8 Pressure distribution with crack prorogation at different times (deformed configuration with a magnification of  $10^4$  and pressure unit: Pa).

## 4.5 Application

After verifying the accuracy of the model, it is then applied to the investigation of two common kinds of phenomena observed in hydraulic fracturing: the crack branching phenomenon and the stepwise phenomenon. The crack branching phenomenon is often observed in dynamic crack propagation. However, since the crack patterns are complex, only a few new numerical methods have the capability of modelling the phenomenon [247], and the physical mechanism involved is unclear. With the advantages in modelling discontinuous problems, PD becomes a promising tool for crack branching problems. A bunch of studies have investigated the mechanics of crack branching in brittle media with PD, as described in the introduction part. However, to the author's best knowledge, crack branching in porous media with PD has not been investigated yet. Therefore, a crack branching model based on PD is designed and presented to the study of fracture branching in porous media on different

loading conditions. The stepwise phenomenon, standing for the intermittent propagation of hydraulic fractures, has been observed and investigated with the central force model, the standard Galerkin finite element method (SGFEM) and the extended finite element method (XFEM) [68, 67]. However, it has not been studied systematically under different loading conditions with PD. Therefore, models dealing both with hydraulic fracturing and mechanical loading conditions with PD are established to prove more evidence for the stepwise phenomenon in numerical aspects.

### 4.5.1 Study of crack branching

In order to obtain a more comprehensive understanding of crack branching mechanism in porous media in hydraulic fracturing, a comparison between crack branching in brittle media and crack branching in porous media is conducted. Two loading conditions, including the stress applied on boundaries and stress applied on crack surfaces, are designed. The grid spacing  $\Delta x$  is set to be the same as the benchmark examples in [49], which is small enough and matches the computing power of the computer. The horizon size is set to be  $\delta = 3\Delta x$  since it is demonstrated that with  $m=3$ , the crack branching behaviour can be captured, and the grid is independent of crack propagation [247]. The time step  $\Delta t$  is selected to satisfy the stability with the grid spacing and horizon size adopted in this simulation, which is  $0.05 \mu s$  in this subsection.

#### Study of crack branching in brittle media

The model describes a crack propagation and branching problem in brittle media. The model is established with a width of  $W = 0.1$  m and a height of  $H = 0.04$  m. Two boundary conditions are applied. The first boundary condition is added by applying the stress on the upper and lower surfaces of the model, see Fig. 4.9. The second boundary condition is added by applying the stress on the upper and lower surfaces of the crack, see Fig. 4.11. The initial crack is set along the central line of the model, and the crack length is 0.5 m. The total number of PD points is 400 in the x-direction and 160 in the y-direction. The grid spacing  $\Delta x = 2.5 \times 10^{-4}$  m and the horizon size  $\delta = 7.5 \times 10^{-4}$  m. The other parameters of the model are listed in Table 4.3.

Under the first loading condition, crack propagation is driven by the stress applied on the upper and lower surfaces of the model. By increasing the loading stress, different crack patterns can be observed, see Fig. 4.10. When the loading amplitude is  $\sigma = 2$  MPa, the crack propagates along the central line at first and then branches at  $t = 43 \mu s$ , see Fig. 4.10a. When the loading amplitude is  $\sigma = 4$  MPa, the crack propagates along the central line



Table 4.3 Material properties for the crack branching problem.

Properties	Symbols	Values
Young's modulus	$E$	$72.0 \times 10^9$ Pa
Poisson's ratio	$\nu$	0.22
Material density	$\rho$	$2.44 \times 10^3$ kg/m <sup>3</sup>
Critical energy release rate	$G_c$	3.8 N/m

at first and then at  $t = 33 \mu\text{s}$ , multiple branches can be observed, see Fig. 4.10b. If the energy-driven crack cannot be fully dissipated by the material after the first branching event, multiple branches happen and may lead to fragmentation [252]. Comparing Fig. 4.10a and Fig. 4.10b, it can be concluded that as applied load increases, multiple branching events develop, branching angles become smaller, branching time becomes earlier and the location of branching moves closer to the starting location.

Under the second loading condition, the driven energy for the crack propagation is from the stress applied on the upper and lower surfaces of the initial crack. When crack grows, the applied stress will not be extended to the newly developed crack surfaces. By increasing the loading stress from  $\sigma = 3$  MPa to  $\sigma = 6$  MPa, different crack patterns can be observed, see Fig. 4.12. The branching event happens at  $t = 35 \mu\text{s}$  when  $\sigma = 3$  MPa, and it happens earlier ( $t = 30 \mu\text{s}$ ) when  $\sigma$  increases to 6 MPa. The branching angles also become smaller, similar to the phenomenon obtained by the first loading condition. However, continued or cascading branching is not observed.

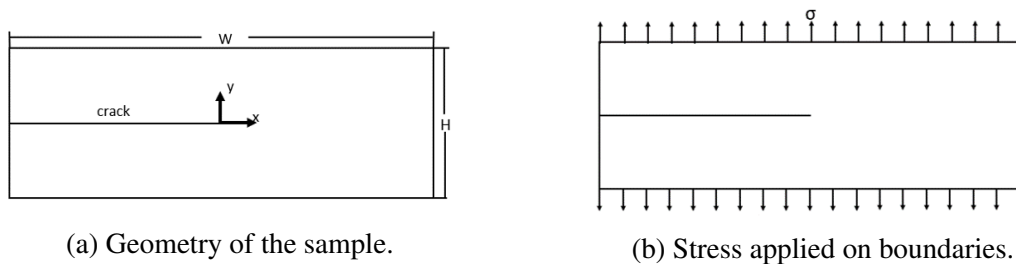


Fig. 4.9 Description of the crack propagation problem.

### Study of crack branching in porous media

The branching examples are then modified from brittle media to porous media. Since there exists a strong coupling between the rocks deformation and fluid flow in porous media, a

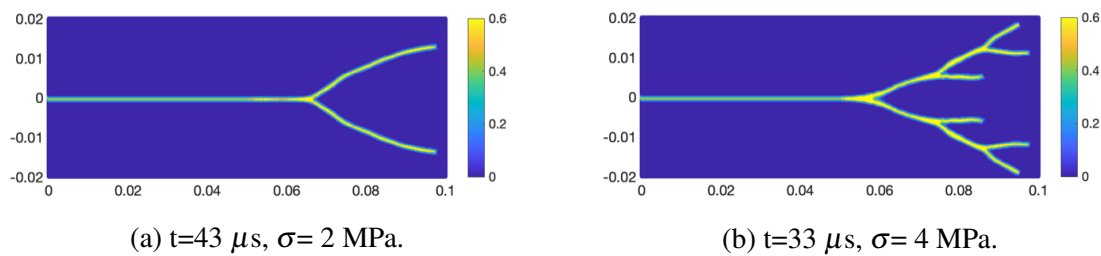


Fig. 4.10 Crack pattern under the condition that stress applied on boundaries.

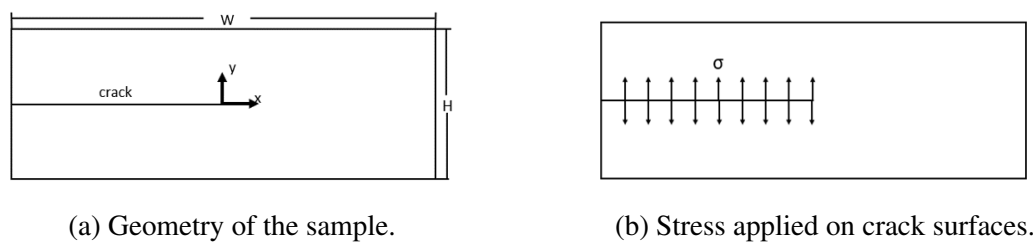


Fig. 4.11 Description of the crack propagation problem.

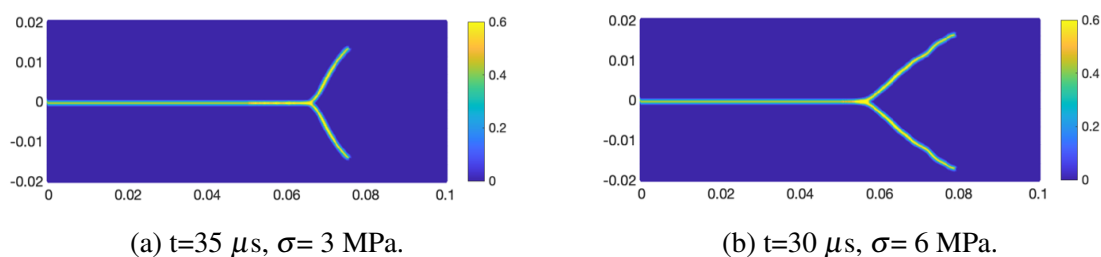


Fig. 4.12 Crack pattern under the condition that stress applied on crack surfaces.

second equation Eq.(4.24) is added to the simulation process to calculate the pore pressure field. The effect of pore pressure on crack branching is then investigated.

The geometry and two loading conditions remain the same, and the parameters used are listed in Table. 4.3. The initial pore pressure is set to be 3 MPa. Fig. 4.13 shows the comparison of crack branching between brittle media and porous media under two loading conditions: (1) stress applied on boundaries (left) and (2) stress applied on crack surfaces (right). According to Fig. 4.13a and Fig. 4.13c, under the first loading condition (stress applied on boundaries), with pore pressure increasing, the branching phenomenon remains the same. While according to Fig. 4.13b and Fig. 4.13d, under the second loading condition (stress applied on crack surfaces), the location of branching moves farther to the starting location, which indicates that the time needed for branching increases, and the length of crack branches decreases. The first loading condition stands for the mechanical loading, while the second loading condition is similar to hydraulic loading, under which the pressure

inside the crack drives the crack to grow. Thus, for fluid-driven fractures in porous media, the pore pressure in porous media plays an important role in crack branching. The higher the pore pressure, the harder crack branching event happens.

To sum up, in this subsection, a fully coupled hydraulic fracturing model fracture in porous media is presented and employed to capture the dynamic crack branching behaviour in both brittle and porous media to investigate the branching mechanisms. The results indicate that sufficient loading is required in order to initiate the crack branching process. With higher loading forces, multiple branches event can be observed. Compared with the stress applied on crack surfaces condition, crack branching is more easily induced with the stress applied on boundaries condition. In addition, for the fluid-driven crack (stress applied on crack surfaces), the existence of pore pressure will depress the growth and branching of the crack.

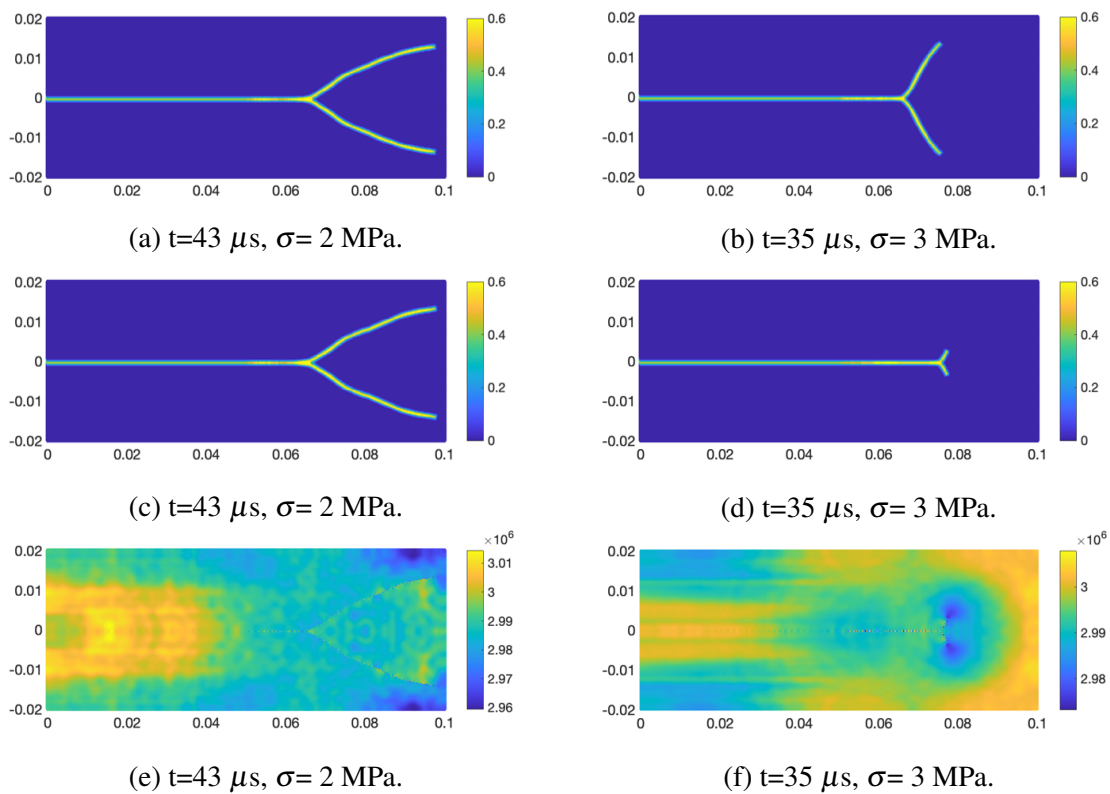


Fig. 4.13 The comparison of crack branching between brittle media and porous media under two loading conditions: (a) crack pattern in brittle media under the first loading condition; (b) crack pattern in brittle media under the second loading condition; (c) crack pattern in porous media under the first loading condition; (d) crack pattern in porous media under the second loading condition; (e) pore pressure distribution in porous media under the first loading condition; (f) pore pressure distribution in porous media under the second loading condition.

### 4.5.2 Study of the stepwise phenomenon

The stepwise phenomenon has been observed in field tests and laboratory experiments [318]. However, it is very hard to reproduce it numerically. Till now, only a few studies capture the stepwise phenomenon numerically [67, 68, 131, 379, 380]. It was pointed out in [68] that the observation of this phenomenon is influenced by many factors, including the choice of loading increment/fracture advancement/time stepping algorithm adopted. Unfortunately, in Chapter 3, we fail to reproduce the stepwise phenomenon with a FEM model. In this Chapter, we resort to PD to see if the physical irregular step can be observed. As a superior method to solve discontinuous problems, PD is rarely adopted to investigate the stepwise phenomenon. Recently, only one paper mentioned that the stepwise phenomenon can be reproduced successfully under hydraulic loading conditions with a hybrid FEM and PD approach [284]. The phenomenon has not been evidenced and investigated thoroughly. Therefore, in this subsection, the explicit PD model will be utilised to check whether the stepwise phenomenon could be reproduced with PD models.

Two test cases from [67], namely the mechanical loading and hydraulic loading cases, are employed here to investigate the fracture propagation process with our new explicit PD method. A comparison is made between our results and results obtained by FEM methods in [67], and the stepwise phenomenon is investigated.

#### Mechanical loading case

The model describes a plane strain problem of crack propagation driven by mechanical loading in saturated porous media. The model is established with a rectangle of  $2 \times 0.2$  m, see Fig. 4.14. The right surface is constrained in the horizontal and vertical direction, and all the surfaces are impermeable with no fluid flowing out. The mechanical loading condition is added by applying a vertical velocity boundary condition of  $u_y = 2.35 \times 10^2$  m/s on the upper and lower left surfaces of the rectangle. And time  $t_1$  equals 0.02 s. The initial crack set along the central line of the model on the left is 0.02 m. All material properties of the model are given in Table.4.4. In order to check the convergence of the results, three sets of parameters are used: (1)  $\Delta x = 0.001$  m, (2)  $\Delta x = 0.002$  m and (3)  $\Delta x = 0.004$  m, where  $\Delta x$  is the grid spacing. The horizon size  $\delta$  is equal to  $3\Delta x$ . A time step size of  $\Delta t = 1 \times 10^{-7}$  s is used to meet the stability condition for all grid spacing.

Fig. 4.15 shows that the crack length grows with time increasing and the irregular stepwise phenomenon, which evidences that the proposed PD model can reproduce the stepwise phenomenon observed in the experiment. With smaller grid spacing, the phenomenon can still be observed with the periods of quiescence, representing the behaviour is a truly stepwise

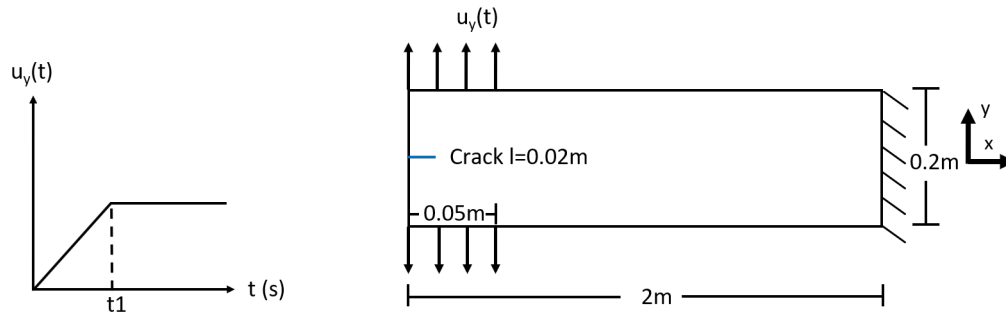


Fig. 4.14 Mechanical loading sample.

Table 4.4 Material properties for two loading cases.

Properties	Symbols	Values
Young's modulus	$E$	$25.85 \times 10^9$ Pa
Poisson's ratio	$\nu$	1/4
Biot coefficient	$\alpha$	1
Dynamic viscosity	$\mu$	$5.0 \times 10^{-4}$ (Pa·s)
Permeability	$k$	$1.0 \times 10^{-12}$ m <sup>2</sup>
Material density	$\rho$	$1.9 \times 10^3$ kg/m <sup>3</sup>
Porosity	$n$	0.2
Bulk modulus(solid)	$K_s$	$13.46 \times 10^9$ N/m <sup>2</sup>
Bulk modulus(fluid)	$K_w$	$0.2 \times 10^9$ N/m <sup>2</sup>
Density(solid)	$\rho_s$	$1.0 \times 10^3$ kg/m <sup>3</sup>
Density(fluid)	$\rho_w$	$2.0 \times 10^3$ kg/m <sup>3</sup>
Intrinsic permeability	$k$	$2.78 \times 10^{-21}$ m <sup>2</sup>

phenomenon, not numerical errors. A physical reason behind this phenomenon may be that when the crack is temporarily arrested, another sudden extension in the crack length occurs only after enough energy has been accumulated in the system [188]. Comparing the results obtained by the explicit PD model with the results obtained by the standard Galerkin finite element method (SGFEM) in [67], similar patterns can be found.

### Hydraulic loading case

The model describes a plane strain problem of crack propagation driven by hydraulic loading in saturated porous media. The model of 2m long and 0.2m wide is subjected to a rapid pressure increase of  $5 \times 10^5$  MPa/s at the crack mouth, reaching a maximum value of 100 MPa, see Fig. 4.17. The right surface is fixed, and all the surfaces are impervious. The initial

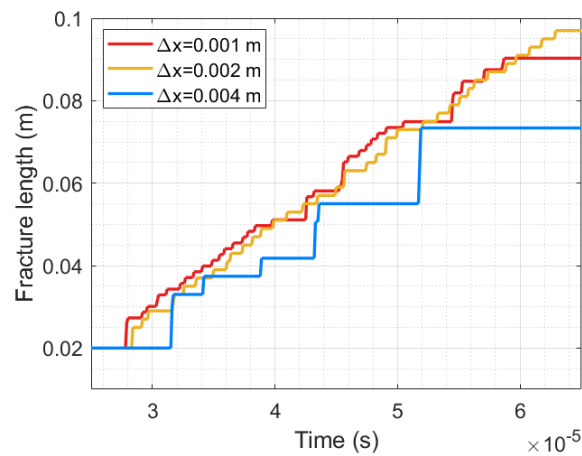
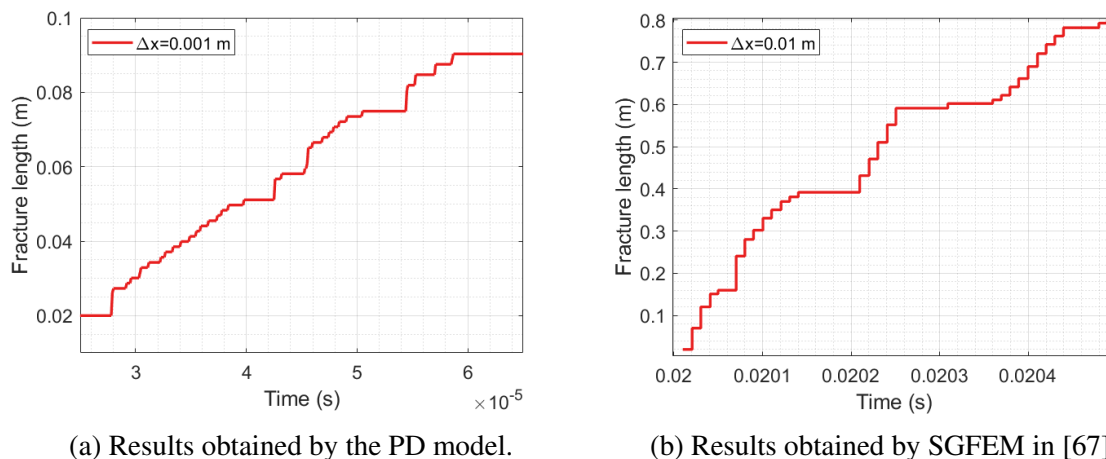


Fig. 4.15 Crack tip advancement under mechanical loading condition.



(a) Results obtained by the PD model.

(b) Results obtained by SGFEM in [67].

Fig. 4.16 Comparison of crack tip advancement under mechanical loading.

crack set along the central line of the model on the left is 0.02 m. As time increases, the crack propagates due to the injection of the fluid pressure. All material properties of the model are given in Table.4.4. And time  $t_1$  equals 0.02 s. The initial crack set along the central line of the model on the left is 0.02 m. Three sets of  $\Delta x$  are used: (1)  $\Delta x = 0.001$  m, (2)  $\Delta x = 0.002$  m and (3)  $\Delta x = 0.004$  m, and  $\Delta t = 1 \times 10^{-7}$  s.

Fig. 4.18 shows the crack tip advancement with different grid spacing under hydraulic loading. With the grid spacing decreasing, the stepwise phenomenon becomes less obvious, and no periods of quiescence can be observed, making it hard to tell whether the stepwise due to numerical errors or physical reasons. Similar patterns have also been obtained in [67], see Fig. 4.19. It is indicated in [67] that though in Fig. 4.19b the stepwise phenomenon under

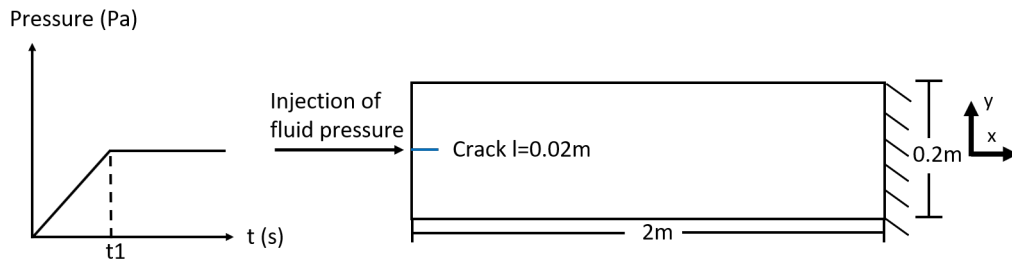


Fig. 4.17 Hydraulic loading sample.

hydraulic loading case is not as distinct as the case under mechanical loading, the horizontal water velocity contours will be beneficial for observing and evidencing the phenomenon.

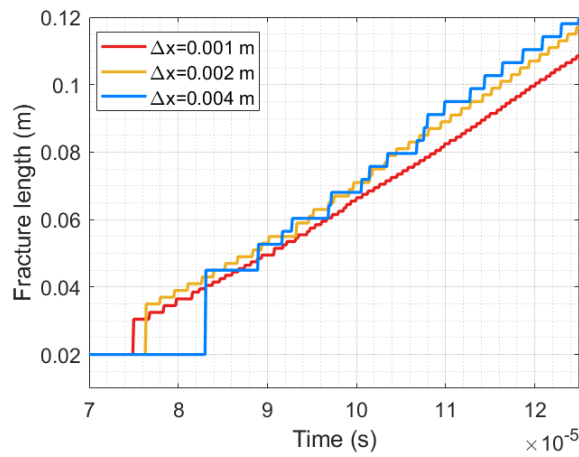
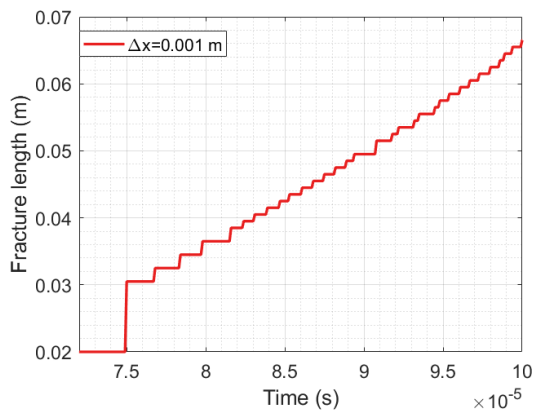
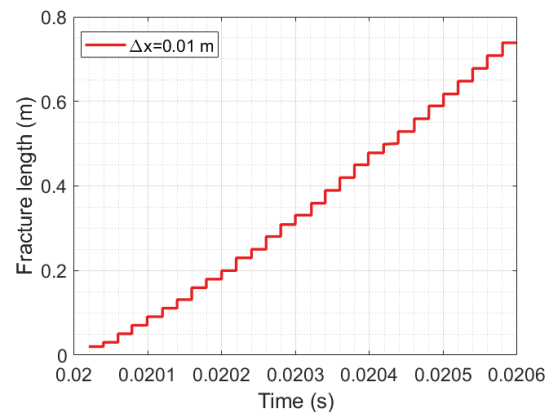


Fig. 4.18 Crack tip advancement under hydraulic loading condition.



(a) Results obtained by the PD model.



(b) Results obtained by SGFEM in [67].

Fig. 4.19 Comparison of crack tip advancement under hydraulic loading.

In this subsection, the PD model for fracture propagation under two different loading conditions is established and proves to be capable of reproducing the stepwise phenomenon. The results obtained by the PD approach are similar to results obtained by the SGFEM, indicating that the explicit PD modelling approach is a promising tool to study the stepwise phenomenon. The examples also indicate that under mechanical loading conditions, the stepwise phenomenon is more distinct due to the solid behaviour. Sudden jump or crack extension will happen when energy accumulated is enough in the hydraulic fracturing system.

## 4.6 Conclusions

This chapter focuses on the study of hydraulic fracturing problems with peridynamics. An explicit peridynamic modelling approach for simulating hydraulic fracture propagation in saturated porous media is presented. A staggered strategy and an explicit time integration scheme are used. The rocks deformation equation system is solved for the displacement field, and the fluid flow equation is solved for the pressure field with PD. The approach is validated via benchmark examples, including a one-dimensional consolidation problem and a two-dimensional fluid-filled crack propagation problems, which demonstrate the ability of the approach to simulate the hydraulic fracture process. We use the approach to perform a series of peridynamic computational tests in order to aid understanding of the physical mechanisms involved in hydraulic fracturing.

First, the results show that the approach is capable of capturing dynamic crack branching in brittle media and porous media. Crack branching requires a sufficiently high loading condition. Under higher loading conditions, multiple branching occurs. The pore pressure will depress the growth and branching of the crack under the fluid-driven condition. Second, the approach proves to be capable of reproducing the stepwise phenomenon in the fracture examples under the mechanical loading case as well as the hydraulic loading case, which is in agreement with experimental observations and numerical simulations obtained with SGFEM. Based on the above results, it can be concluded that the proposed peridynamic approach has the potential to analyse various phenomena in hydraulic fracturing and the mechanisms involved. With further development, the modelling approach could be used in the future to tackle problems with more complex hydraulic fracture patterns as observed in the field. Since the simulation scale in the practice and in the field is relatively large, the development of an implicit model without time step limitation is of great importance, which will be discussed in the next Chapter.



# Chapter 5

## A hybrid FEM and PD approach for modelling hydraulic fracturing in porous media

### 5.1 Introduction

Hydraulic fracturing describes the process of injecting fluid with proppant into the wellbore, creating pressure that causes cracks in the rock to develop and spread [1, 26]. It is widely used in the petroleum industry for the development of oil and gas reservoirs, especially low permeability tight formations. In the past few decades, extensive laboratory experiments [40, 125, 126, 164, 470] and field studies [21, 25, 200, 249] have been conducted to study hydraulic fracturing in order to obtain a better understanding of fracture propagation mechanism. In addition, numerical methods are necessary to reveal the fluid-driven fracture behaviors since they are usually more flexible, cheaper and faster to perform compared to laboratory and field experiments. The simulation of hydraulic fracturing in porous media includes three physical processes: (i) deformation of the porous formation, (ii) fluid flow in porous media and in the fracture, and (iii) fracture propagation [370]. These processes reveal a strong coupling between the solid formation and the fluid, making the associated numerical simulation a challenging task. Using a numerical approach, this study focuses on the branching of fluid-driven fractures in porous media, which often occurs during hydraulic fracturing and critically affects the productivity enhancement.

Complicated by the occurrence of complex fracture patterns and fluid networks, numerical studies of hydraulic fracturing and branching in porous media are limited. Guo et al. [163] studied hydraulic fracture branching with a phase-field model and concluded that the crack

branch occurs when the crack propagates towards stiff rock under certain conditions (e.g. Young's modulus ratio exceeding a critical value) and low in-situ stress difference promotes crack branching. Phase-field models were also developed by Zhou et al. [485], Ni et al. [282] to investigate hydraulic fracture propagation in porous media. It is found in [485] that the final crack branching pattern is not sensitive to the flux rate, and by increasing the flux rate branches will occur but secondary branches either will not occur or remain unchanged. The influence of energy release rate on hydraulic branching is also studied in [485], where smaller critical energy release rate is found to promote more complex crack branching patterns. The permeability is found to have a limited effect on crack propagation directions [282]. Using a finite element crack band model, Rahimi-Aghdam et al. [340] studied the branching of hydraulic fracture and found the porosity, seepage force (highly related with the permeability), and weak layers are essential for the crack branching phenomenon. Using a bonded-particle model, Zhang et al. [477] investigated fracture patterns in tight sandstone. Complex crack patterns are found more prone to develop under low differential in-situ stress, while the injection of high flow rate and low viscosity fluid are found to encourage dominant fracture development. Ni et al. [284] presented a hybrid finite element and peridynamics model to simulate hydraulic crack branching and found secondary crack branching can occur under higher flux rate. There appears to be a consensus from these limited studies that high injection flow rate leads to crack branching and more complex crack patterns [282, 284, 368, 485]. However, different researchers often come to different conclusions when using different methods, and the effect of various physical parameters on crack branching still needs further investigation.

Commonly used methods for the simulation of fluid-driven fractures include the finite element method (FEM), the extended finite element method (XFEM), the phase-field method (PFM), the discrete element method (DEM) and the peridynamics method (PD). Note that each numerical method has its advantages and disadvantages, and a good numerical method should have the ability to simulate complex fracture propagation processes with reasonable computational cost [224]. The aforementioned simulation methods can be roughly classified into two groups: continuum and discontinuum methods, which are briefly recapped below to put the present study in perspective.

The continuum methods for hydraulic fracturing simulation include FEM, XFEM and PFM. The FEM has been successfully applied in hydraulic fracturing simulation for several decades. Boone and Ingraffea [52] presented an early work to simulate hydraulic fracturing using a fully-coupled 2D FEM model. More recently, many other more advanced 2D and 3D FEM models [70, 76, 77, 278, 379] have been developed to simulate hydraulic fracturing in impermeable or porous media, including the use of cohesive zone models to overcome

the numerical difficulty caused by stress concentration at fracture tips. To date, the FEM is often used for simple crack geometries (most often horizontal cracks), while for complex crack patterns, e.g. crack branching and multiple branches with time-varying fluid flow network, it becomes almost impossible to achieve a stable and affordable FEM simulation due to the requirement of constant remeshing. Compared with FEM, XFEM avoids/reduces the need of constant mesh updating in the simulation of crack propagation and it has also been applied to hydraulic fracturing problems [359, 266]. However, the requirement of adaptive discontinuous displacement enrichment prevents such XFEM from being applicable to problems in which multiple cracks grow and intersect in complex patterns [247]. Compared with FEM and XFEM, the PFM has advantages in coping with complex fracture patterns since it treats fracture propagation and formation deformation simultaneously as an energy minimization problem, avoiding the tracking of individual fractures and the extra criteria for fracture branching and intersection [79]. The first phase field model to simulate hydraulic fracturing in impermeable materials is developed by Bourdin et al. [59]. Later, the model was expanded for fluid-saturated poroelastic materials by adding poroelastic terms in the energy functional [257, 259] or by utilizing minimization principles for coupling Darcy–Biot-type flow in poroelastic media [254]. However, extremely fine mesh are generally needed in phase field simulation of fracture propagation [79], which sharply increases the computational cost. The discontinuum methods include mainly DEM. In DEM [98], the material medium is treated as an assembly of distinct particles and the motion of particles are governed by Newton's laws, thus the discontinuities are the natural outcome of the deformation process. Application of DEM to simulation of hydraulic fracturing is described in [101]. The influence of different parameters including the rock properties, in-situ stress, injection flow rate, fluid viscosity on hydraulic fracturing are also studied with DEM models [274, 474, 120].

Introduced by Silling [394], the PD theory is a continuum theory based on integro-differential equations, which is a promising tool for studying fracture propagation problems. It uses spatial integrals equations instead of partial differential equations as the controlling equation so as to overcome the limitations of ill-posed partial derivatives at discontinuities, e.g. crack surfaces. In addition, crack growth can be initialised spontaneously with only one simple criterion so that no external criterion is required for complex crack patterns. With advantages in solving discontinuous problems, PD has been widely used for fracture branching analysis [10, 47, 49, 84, 169], which mostly focus on the branching phenomenon in impermeable media. The first application of PD in hydraulic fracturing was reported in [426], in which a new formulation for incorporating the effects of pore pressure is presented to simulate the deformation of porous media. Following this work, Ouchi et al. [300] proposed a hydraulic fracturing model which couples a new PD formulation of porous fluid flow with

the existing PD solid formulation together to simulate fluid driven fractures in an arbitrary heterogeneous poroelastic medium. Using a linear viscoelastic PD model, Nadimi et al. [271] simulated hydraulic fracturing initiation and propagation in a 3D heterogeneous geological medium. The simulation work is done by using the PDLAMMPS (peridynamic large-scale atomic/molecular massively parallel simulator) open source software; and the interaction between induced fractures and a pre-existing fracture, as well as the influence of the angle of approach and differential horizontal stress on the fracture propagation behaviour are investigated. Oterkus et al. [296] presented a new fully coupled poroelastic PD formulation by using the analogy between poroelasticity and thermo-elasticity. Combining both advantages of FEM and PD, a hybrid modelling approach for simulating hydraulic fracture in porous media with hybrid FEM and PD was proposed to study the hydraulic fracturing behaviour in [284, 283], where a staggered solver is employed. The fluid equation is solved by an implicit time integration iteration while the solid equation is solved by the adaptive dynamic relaxation algorithm, which makes the whole system unconditionally stable.

In this study, we focus on the influence of different parameters on hydraulic fracturing branching in porous media and to balance between efficiency and accuracy, a fully coupled hybrid FEM-PD modelling approach is adopted. Specifically, the solid deformation and fracture propagation are solved by FEM and PD, while the fluid flow equation is solved by FEM. For the solid simulation, the areas where cracks are likely to occur are discretised by PD, and the areas without cracks are discretised by FEM. After verification via benchmark examples including static and dynamic problems, a series of computational tests are performed to study the effects of different parameters on dynamic hydraulic fracture branching in porous media, providing some useful insights on crack branching mechanisms in porous media.

The rest of the chapter is organised as follows. First, § 5.2 describes the mathematical models and governing equations for hydraulic fracturing. Next, the corresponding numerical implementation including space discretisation, time discretisation, coupling strategy and solution strategy are explained in detail in § 5.3. Then, in § 5.4, benchmarks including static deformation problems without and with failure, dynamic deformation problems without and with failure, dynamic fluid and solid coupling problems without and with failure, are used for verification. Finally, § 5.5 is devoted to the study of dynamic branching phenomenon in porous media, after which conclusions are presented in § 5.6.

## 5.2 Mathematical models for hydraulic fracturing

Hydraulic fracturing is a physically complex procedure where underground rocks are fractured by injecting a viscous fluid [1]. The injected fluid increases the pressure on the surface

of the fracture, so as to reach the critical propagation conditions for the crack and split the rock at the crack tip. The fluid driven process includes a strong coupling between the fluid moving in porous media, the fluid moving in the fracture, and fracture propagation. In Chapter 3 and in Chapter 4, the mathematical models for hydraulic fracturing has already been discussed in detail. Here, we only give a brief introduction.

### 5.2.1 Deformation of a porous formation

In this work, the solid deformation equation is solved by FEM coupled with PD. The FEM is based on classical continuum mechanics, which assumes that a material point only interacts with its immediate neighbors (locality) and the local medium remains continuous as it deforms. The classical FEM formulation is established on spatial derivatives that are undefined at discontinuities. This leads to its limitation in solving discontinuous problems, such as crack propagation problems. PD is a non-local theory, employing spatial integral equations instead of partial differential equations, which makes it suitable for crack simulation. However, a limitation of the non-local PD theory is the difficulty to accurately represent boundary conditions, see § 5.3.3 for more details. Recognizing the strength and weakness of FEM and PD, we introduce a hybrid approach to describe continuum deformation.

#### Classical continuum mechanics description

The deformation of a porous formation is typically modelled by the theory of poroelasticity. The basic theory of poroelasticity was first introduced by Biot (1941) now known as Biot's theory, which was further developed from a physics perspective [361]. For a fully saturated porous medium with a single-phase fluid, the equilibrium equation is

$$\nabla \cdot \boldsymbol{\sigma} + \rho \mathbf{g} - \rho \ddot{\mathbf{u}} = 0 \quad (5.1)$$

where  $\boldsymbol{\sigma}$  is the Cauchy stress,  $\mathbf{g}$  the gravity acceleration,  $\ddot{\mathbf{u}}$  the acceleration of the solid phase, and  $\rho$  the density of the porous medium.

#### Peridynamics theory

At a reference position of  $\mathbf{x}$  and time  $t$ , the peridynamic equation of motion are described by an integral formulation [394]:

$$\rho(\mathbf{x}) \ddot{\mathbf{u}}(\mathbf{x}, t) = \int_{H_{\mathbf{x}}} \mathbf{f}(\mathbf{x}' - \mathbf{x}, \mathbf{u}' - \mathbf{u}) dV_{\mathbf{x}'} + \mathbf{b}(\mathbf{x}, t) \quad (5.2)$$

in which  $\rho$  is the mass density,  $\ddot{\mathbf{u}}$  the acceleration,  $H_{\mathbf{x}}$  the horizon,  $\mathbf{u}$  the displacement vector field,  $\mathbf{b}$  a prescribed body-force density field,  $dV_{\mathbf{x}'}$  the differential volume of  $\mathbf{x}'$ ,  $\mathbf{f}$  the force vector between two material points  $\mathbf{x}'$  and  $\mathbf{x}$ , and interaction  $\mathbf{f}$  between the material points is related to the deformation, pressure and constitutive properties of the material and is called a bond. There are two types of theoretical models for PD: the bond-based PD and the state-based PD. The bond-based PD assumes that any pair of particles interacts only through a central potential that is totally independent of all other local conditions [247]. This assumption results in that for an isotropic, linear, microelastic material, the Poisson's ratio is limited to 1/4 (plane strain) or 1/3 (plane stress). To remove the restrictions for Poisson's ratio, the state-based PD was proposed [402], where the interaction between two material points depends not only on the bond between the two points, but also on the deformation of all the other bonds in the horizon. Here, the bond-based PD are intentionally chosen for simplicity with lower computing times with respect to the state-based PD.

Based on the bond-based PD theory, the governing equation for solid deformation Eq. (5.1) is formulated as [296]:

$$\rho(\mathbf{x})\ddot{\mathbf{u}}(\mathbf{x},t) = \int_{H_{\mathbf{x}}} \lambda c(s - \alpha\gamma\bar{P}) \frac{\boldsymbol{\xi} + \boldsymbol{\eta}}{|\boldsymbol{\xi} + \boldsymbol{\eta}|} dV_{\mathbf{x}'} + \mathbf{b}(\mathbf{x},t) \quad (5.3)$$

where  $\boldsymbol{\xi} = \mathbf{x}' - \mathbf{x}$  denotes the initial relative position,  $\boldsymbol{\eta} = \mathbf{u}' - \mathbf{u}$  the current relative displacement,  $\lambda$  a scalar describing the bond state (i.e. broken or not),  $c$  the bond stiffness, and  $\gamma$  the coefficient of fluid pore pressure. Details of  $c$  and  $\gamma$  can be found in §4.2.1.  $\bar{P}$  is the average fluid pore pressure of points  $\mathbf{x}'$  and  $\mathbf{x}$  is defined as:

$$\bar{P} = \frac{P(\mathbf{x}',t) + P(\mathbf{x},t)}{2} \quad (5.4)$$

$s$  is the stretch between the material points, which represents the relative elongation of the bond:

$$s = \frac{|\boldsymbol{\eta} + \boldsymbol{\xi}| - |\boldsymbol{\xi}|}{|\boldsymbol{\xi}|} \quad (5.5)$$

The fracture propagation is determined by  $\lambda$  and associated failure criteria, for which further details are given in § 5.2.3.

## 5.2.2 Fluid flow in porous media and in the fracture

The continuity equation for the fluid flow in a porous medium can be written as:

$$\alpha \nabla \cdot \dot{\mathbf{u}} + \frac{1}{Q} \dot{p} + \nabla \cdot \mathbf{q} = 0 \quad (5.6)$$

where  $\mathbf{u}$  denotes the velocity of the solid phase,  $p$  the velocity of the fluid pressure, and  $\frac{1}{Q}$  the compressibility coefficient. The first term can be seen as a source term driving pressure distribution and the flux.  $\mathbf{q}$  is defined by Darcy's law. Darcy's law, a phenomenologically derived constitutive equation that describes the flow of a fluid through a porous medium, is used. The Darcy's law reads:

$$\mathbf{q} = -\frac{\mathbf{k}_w}{\mu} \cdot \nabla p \quad (5.7)$$

where  $\mu$  is the fluid viscosity, and  $\mathbf{k}_w$  the permeability tensor. In two dimensions,  $\mathbf{k}_w$  is written as:

$$\mathbf{k}_w = \begin{bmatrix} k_x & 0 \\ 0 & k_y \end{bmatrix} \quad (5.8)$$

where  $k_x$  and  $k_y$  are principle permeability coefficients in the x and y directions, respectively. Note here for a fracture domain, in Eq. (5.6), the first term of the equation can be neglected [284], and the permeability  $k_x$  and  $k_y$  becomes:

$$\begin{cases} k_x = k_f \sin \theta \\ k_y = k_f \cos \theta \end{cases} \quad (5.9)$$

where  $\theta$  is the direction angle of maximum principal strain and can be calculated by Eq. (5.10):

$$\theta = \frac{1}{2} \text{atan} \left( \frac{\gamma_{xy}}{\varepsilon_x - \varepsilon_y} \right) \quad (5.10)$$

where  $\varepsilon_x$ ,  $\varepsilon_y$  and  $\gamma_{xy}$  are the normal strain in the x-direction, normal strain in the y-direction and the shear strain.

$k_f$  is the fracture permeability, which is given in and Eq. (5.10). In Eq. (5.11),  $w$  is the fracture width and is calculated via the stretch of the bond [284] and  $\eta$  is a fracture parameter set equal to unity in this research.

$$k_f = \frac{1}{\eta} \frac{w^2}{12} \quad (5.11)$$

### 5.2.3 Failure criterion

In fracture mechanics, the fracture propagation criterion is used to control the propagation of a fracture. With FEM method, linear elastic fracture mechanics (LEFM) is normally adopted as the fracture propagation criterion. The LEFM includes the maximum tensile stress criterion and minimum strain energy density criterion, the maximum principal strain criterion and maximum strain energy release criterion [341]. When modeling crack branching phenomenon with FEM, an external branching criterion is required to determine the branching time and

branching angle. Compared with FEM, the criterion used for crack propagation in PD is relatively simple. Without the requirement of external criteria for crack propagation direction or crack branching angles, the crack growth is a natural outcome of the computation.

One of the most common criteria in PD is called the “critical bond stretch ” criterion [400]. When the stretch of the bond  $s$  is greater than the critical value  $s_c$ , the bond is assumed to be broken, and the pairwise force between the pair of nodes disappears.  $\lambda$  is a scalar to describe the bond state where  $\lambda$  equals 1 when the bond is not broken,  $\lambda$  equals 0 otherwise.

$$\lambda(\mathbf{x}, t, \boldsymbol{\xi}) = \begin{cases} 0 & (s \geq s_c) \\ 1 & (s < s_c) \end{cases} \quad (5.12)$$

The critical stretch  $s_c$  is determined by the critical energy release rate  $G_c$ . The relationship between  $s_c$  and  $G_c$  is defined as presented in:[247, 286, 471]:

$$s_c = \sqrt{\frac{4\pi G_c}{9E\delta}} \quad (2D, \text{plane stress}) \quad (5.13a)$$

$$s_c = \sqrt{\frac{5\pi G_c}{12E\delta}} \quad (2D, \text{plane strain}) \quad (5.13b)$$

$$s_c = \sqrt{\frac{5G_c}{6E\delta}} \quad (3D) \quad (5.13c)$$

When a series of bonds break, the discontinuous space formed by these broken bonds becomes a macroscopic crack. An example of broken bonds is given in Fig. 5.1, where a horizon size  $\delta = 2\Delta x$  is adopted.

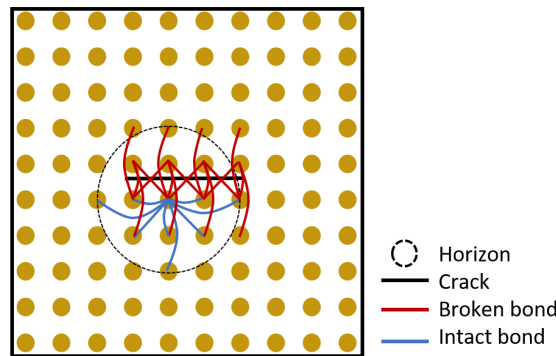


Fig. 5.1 Crack formed by broken bonds ( $\delta = 2\Delta x$ ).

To describe the crack path, a scalar  $\phi$  called the damage parameter is used. It represents the local damage of point  $\mathbf{x}$ , which is defined as the ratio of the number of broken bonds to



the total number of bonds connected to point  $\mathbf{x}$ :

$$\phi(\mathbf{x}, t) = 1 - \frac{\int_H \lambda(\mathbf{x}, \mathbf{x}', t) dV_{\mathbf{x}'}}{\int_H dV_{\mathbf{x}'}} \quad 0 \leq \phi \leq 1 \quad (5.14)$$

## 5.3 Numerical implementation

### 5.3.1 FEM spatial discretisation of the governing equations

A detailed explanation of the discretisation procedure for the poroelasticity problem with FEM can be found in [490]. The weak form of the governing equations (solid deformation equation Eq. (5.1) and fluid flow equation Eq. (5.6)) is first obtained and then the unknown field parameters (the displacement and pressure) are represented by nodal values and interpolation functions. Following the standard FEM discretisation, the discretised governing equations Eq. (5.1) and equation Eq. (5.6) can be expressed in a compact matrix as [52]:

$$\mathbf{M}_F \ddot{\mathbf{u}} + \mathbf{K}_F \mathbf{u} - \mathbf{Q}_F \mathbf{p} = \mathbf{f}_F \quad (5.15a)$$

$$\mathbf{Q}_F^T \dot{\mathbf{u}} + \mathbf{C}_F \dot{\mathbf{p}} + \mathbf{H}_F \mathbf{p} = \mathbf{q}_F \quad (5.15b)$$

where  $\mathbf{u}$  denotes the nodal displacement,  $\mathbf{p}$  the nodal fluid pressure,  $\mathbf{f}_F$  the nodal force,  $\mathbf{q}_F$  the nodal flow source. The coefficient matrices/vectors  $\mathbf{M}_F$ ,  $\mathbf{K}_F$ ,  $\mathbf{Q}_F$ ,  $\mathbf{C}_F$  and  $\mathbf{H}$  are given by the following expressions:

$$\begin{aligned} \mathbf{M}_F &= \int_{\Omega} \mathbf{N}_u^T \rho \mathbf{N}_u d\Omega, \quad \mathbf{K}_F = \int_{\Omega} \mathbf{B}_u^T \mathbf{D} \mathbf{B}_u d\Omega \\ \mathbf{Q}_F &= \int_{\Omega} \alpha \mathbf{B}_u^T \mathbf{m} \mathbf{N}_p d\Omega, \quad \mathbf{m} = \{1, 1, 0\}^T \\ \mathbf{C}_F &= \int_{\Omega} \frac{1}{Q} \mathbf{N}_p^T \mathbf{N}_p d\Omega, \quad \mathbf{H}_F = \int_{\Omega} \mathbf{B}_p^T \frac{\mathbf{k}_w}{\mu} \mathbf{B}_p d\Omega \end{aligned} \quad (5.16)$$

where  $\mathbf{N}_u$  denotes the shape function matrix for displacement,  $\mathbf{N}_p$  the shape function matrix for pressure,  $\mathbf{B}_u$  the strain-displacement matrix, and  $\mathbf{B}_p$  the matrix of first derivatives of the shape functions  $\mathbf{N}_p$ .

$$\begin{aligned}
 \mathbf{N}_u &= \begin{bmatrix} \mathbf{N}_1 & 0 & \mathbf{N}_2 & 0 & \cdots & \mathbf{N}_n & 0 \\ 0 & \mathbf{N}_1 & 0 & \mathbf{N}_2 & \cdots & 0 & \mathbf{N}_n \end{bmatrix} \\
 \mathbf{N}_p &= \begin{bmatrix} \mathbf{N}_1 & \mathbf{N}_2 & \cdots & \mathbf{N}_n \end{bmatrix} \\
 \mathbf{B}_u &= \begin{bmatrix} \mathbf{N}_{1,x} & 0 & \mathbf{N}_{2,x} & 0 & \cdots & \mathbf{N}_{n,x} & 0 \\ 0 & \mathbf{N}_{1,y} & 0 & \mathbf{N}_{2,y} & \cdots & 0 & \mathbf{N}_{n,y} \\ \mathbf{N}_{1,y} & \mathbf{N}_{1,x} & \mathbf{N}_{2,y} & \mathbf{N}_{2,x} & \cdots & \mathbf{N}_{n,y} & \mathbf{N}_{n,x} \end{bmatrix} \\
 \mathbf{B}_p &= \begin{bmatrix} \mathbf{N}_{1,x} & \mathbf{N}_{2,x} & \cdots & \mathbf{N}_{n,x} \\ \mathbf{N}_{1,y} & \mathbf{N}_{2,y} & \cdots & \mathbf{N}_{n,y} \end{bmatrix}
 \end{aligned} \tag{5.17}$$

### 5.3.2 PD spatial discretisation of the governing equations

Following the meshless PD discretisation [247], Eq. (5.3) can be written as:

$$\rho \ddot{\mathbf{u}}_{(i)} = \sum_{j=1}^{N_{(j)}} \lambda c(s_{(i)(j)} - \alpha \gamma \bar{P}_{(i)(j)}) \frac{\boldsymbol{\xi}_{(i)(j)} + \boldsymbol{\eta}_{(i)(j)}}{|\boldsymbol{\xi}_{(i)(j)} + \boldsymbol{\eta}_{(i)(j)}|} V_{(j)} + \mathbf{b}_{(i)} \tag{5.18}$$

where  $i$  and  $j$  represent the material points and  $N_{(j)}$  represents the number of material points inside the horizon of point  $i$ . Multiplying Eq. (5.18) by the volume of material point  $i$   $V_{(i)}$ , the following equation is obtained:

$$m \ddot{\mathbf{u}}_{(i)} = \sum_{j=1}^{N_{(j)}} \lambda c(s_{(i)(j)} - \alpha \gamma \bar{P}_{(i)(j)}) \frac{\boldsymbol{\xi}_{(i)(j)} + \boldsymbol{\eta}_{(i)(j)}}{|\boldsymbol{\xi}_{(i)(j)} + \boldsymbol{\eta}_{(i)(j)}|} V_{(j)} V_{(i)} + \mathbf{b}_{(i)} V_{(i)} \tag{5.19}$$

Under the assumption of small deformation, the PD space discretisation for the solid deformation Eq. (5.19) is expressed as:

$$\mathbf{M}_{PD} \ddot{\mathbf{u}} + \mathbf{K}_{PD} \mathbf{u} - \mathbf{Q}_{PD} \mathbf{p} = \mathbf{f}_{PD} \tag{5.20}$$

$$\begin{aligned}
 \mathbf{M}_{PD} &= \mathcal{A}_{i=1}^N \rho V_{(i)} \\
 \mathbf{f}_{PD} &= \mathcal{A}_{i=1}^N \mathbf{b}_{(i)} V_{(i)} \\
 \mathbf{K}_{PD} &= \mathcal{A}_{b=1}^{N_{bond}} \mathbf{K}_b \\
 \mathbf{Q}_{PD} &= \mathcal{A}_{b=1}^{N_{bond}} \mathbf{Q}_b
 \end{aligned} \tag{5.21}$$

where  $\mathcal{A}$  is the operator for assembling matrix,  $\mathbf{M}_{PD}$  the global mass matrix,  $\mathbf{K}_{PD}$  the global stiffness matrix, and  $\mathbf{f}_{PD}$  the external force,  $N$  the number of material points for the whole system,  $N_{bond}$  the number of bonds,  $\mathbf{K}_b$  the stiffness matrix of the bond between nodes  $\mathbf{x}_i$

and  $\mathbf{x}_j$ .

$$\mathbf{K}_b = \begin{bmatrix} k_{ij} \\ k_{ji} \end{bmatrix} \quad (5.22)$$

where  $k_{ij}$  and  $k_{ji}$  are the stiffness matrices of the bond for node  $\mathbf{x}_i$  and node  $\mathbf{x}_j$ , respectively. It is noted here  $k_{ij} = -k_{ji}$ .

Take the first term of the left side of Eq. (5.19) as an example, if the assumption “small displacement” is made ( $|\boldsymbol{\eta}| \ll |\boldsymbol{\xi}|$ ), it can be simplified as:

$$\mathbf{f}_{ij} = cs\lambda \frac{\boldsymbol{\eta} + \boldsymbol{\xi}}{|\boldsymbol{\eta} - \boldsymbol{\xi}|} \cong cs\lambda \frac{\boldsymbol{\xi}}{|\boldsymbol{\xi}|} \quad (5.23)$$

According to Eq. (5.23), the derivative of the pairwise force  $\mathbf{f}_{ij}$  with respect to  $\boldsymbol{\eta}$  is:

$$\frac{\partial f}{\partial \eta_1} = c\lambda \frac{\partial s}{\partial \eta_1} = c\lambda \frac{\partial(\frac{\sqrt{(\xi_1 + \eta_1)^2 + (\xi_2 + \eta_2)^2} - |\boldsymbol{\xi}|}{|\boldsymbol{\xi}|})}{\partial \eta_1} = \frac{c\lambda}{|\boldsymbol{\xi}|} \frac{\frac{1}{2} \cdot 2 \cdot (\xi_1 + \eta_1)}{\sqrt{(\xi_1 + \eta_1)^2 + (\xi_2 + \eta_2)^2}} \quad (5.24)$$

where  $f$  is the norm of the vector of  $\mathbf{f}_{ij}$ ,  $\boldsymbol{\xi} = (\xi_1, \xi_2)$  and  $\boldsymbol{\eta} = (\eta_1, \eta_2)$ . Due to the assumption “small displacement”, the following relation holds

$$\sqrt{(\xi_1 + \eta_1)^2 + (\xi_2 + \eta_2)^2} \cong |\boldsymbol{\xi}| \quad (5.25)$$

Substituting Eq. (5.25) into Eq. (5.24) yields:

$$\frac{\partial f}{\partial \eta_1} = \lambda \frac{c\xi_1}{|\boldsymbol{\xi}|^2} \quad (5.26)$$

Similarly,

$$\frac{\partial f}{\partial \eta_2} = \lambda \frac{c\xi_2}{|\boldsymbol{\xi}|^2} \quad (5.27)$$

Thus,

$$\mathbf{f}_{ij} = \begin{bmatrix} \frac{\partial f_1}{\partial \eta_1} & \frac{\partial f_1}{\partial \eta_2} \\ \frac{\partial f_2}{\partial \eta_1} & \frac{\partial f_2}{\partial \eta_2} \end{bmatrix} \begin{bmatrix} \eta_1 \\ \eta_2 \end{bmatrix} = \lambda \begin{bmatrix} \frac{c\xi_1}{|\boldsymbol{\xi}|^2} \cdot \frac{\xi_1}{|\boldsymbol{\xi}|} & \frac{c\xi_2}{|\boldsymbol{\xi}|^2} \cdot \frac{\xi_1}{|\boldsymbol{\xi}|} \\ \frac{c\xi_1}{|\boldsymbol{\xi}|^2} \cdot \frac{\xi_2}{|\boldsymbol{\xi}|} & \frac{c\xi_2}{|\boldsymbol{\xi}|^2} \cdot \frac{\xi_2}{|\boldsymbol{\xi}|} \end{bmatrix} \begin{bmatrix} -1 & 0 & 1 & 0 \\ 0 & -1 & 0 & 1 \end{bmatrix} \begin{bmatrix} u_{i1} \\ u_{i2} \\ u_{j1} \\ u_{j2} \end{bmatrix} \quad (5.28)$$

Therefore,  $k_{ij}$  can be written as:

$$k_{ij} = \frac{\lambda c V_i V_j}{|\boldsymbol{\xi}|^3} \begin{bmatrix} -\xi_1^2 & -\xi_1 \xi_2 & \xi_1^2 & \xi_1 \xi_2 \\ -\xi_1 \xi_2 & -\xi_2^2 & \xi_1 \xi_2 & \xi_1^2 \end{bmatrix} \quad (5.29)$$

Thus, according to Eq. (5.22), the stiffness matrix of the bond  $\mathbf{K}_b$  can be described as:

$$\mathbf{K}_b = \frac{\lambda c V_i V_j}{|\boldsymbol{\xi}|} \begin{bmatrix} -\cos^2 \theta & -\cos \theta \sin \theta & \cos^2 \theta & \cos \theta \sin \theta \\ -\cos \theta \sin \theta & -\sin^2 \theta & \cos \theta \sin \theta & \sin^2 \theta \\ \cos^2 \theta & \cos \theta \sin \theta & -\cos^2 \theta & -\cos \theta \sin \theta \\ \cos \theta \sin \theta & \sin^2 \theta & -\cos \theta \sin \theta & -\sin^2 \theta \end{bmatrix} \quad (5.30)$$

where  $\theta$  is the angle between the angle between the bond and the x axis at the current configuration. Similarly,  $\mathbf{Q}_b$  is the coefficient matrix for pressure, and can be expressed as:

$$\mathbf{Q}_b = -\frac{\lambda c \alpha_B \gamma V_i V_j}{2} \begin{bmatrix} \cos \theta & \cos \theta \\ \sin \theta & \sin \theta \\ -\cos \theta & -\cos \theta \\ -\sin \theta & -\sin \theta \end{bmatrix} \quad (5.31)$$

### 5.3.3 Coupling strategy

To solve the mathematical models described in § 5.2 using the hybrid FEM-PD approach, we need to effectively deal with two types of coupling: (1) the coupling between PD and FEM and (2) the coupling between the solid deformation and the fluid pressure. The former is reflected by the coupled FEM-PD spatial discretisation of porous media, while the latter is reflected by the coupled fluid and solid equations. In this section, we focus on the FEM-PD coupling, while the numerical treatment for fluid-solid coupling will be explained in § 5.3.4.

Both FEM and PD are used to solve the deformation of porous media. Due to the non-local feature of PD, the application of boundary conditions for peridynamics need to follow specific rules [247], see Table 4.1. In this research, FEM is adopted for the outer area, and PD is adopted for the inner area where cracks are likely to occur. As shown in Fig. 5.2, the porous media  $\Omega$  is discretised into FEM sub-domain  $\Omega_F$  and PD sub-domain  $\Omega_P$  such that

$$\Omega = \Omega_F + \Omega_P, \quad \Omega_F \cap \Omega_P = \phi \quad (5.32)$$

The nodes in PD sub-domain are called the PD nodes (red circles), while the nodes in FEM sub-domain are called the FEM nodes (blue and white diamonds). Since the FEM nodes shown as blue diamonds (in Fig. 5.2) are used to define the appropriate internal forces on the

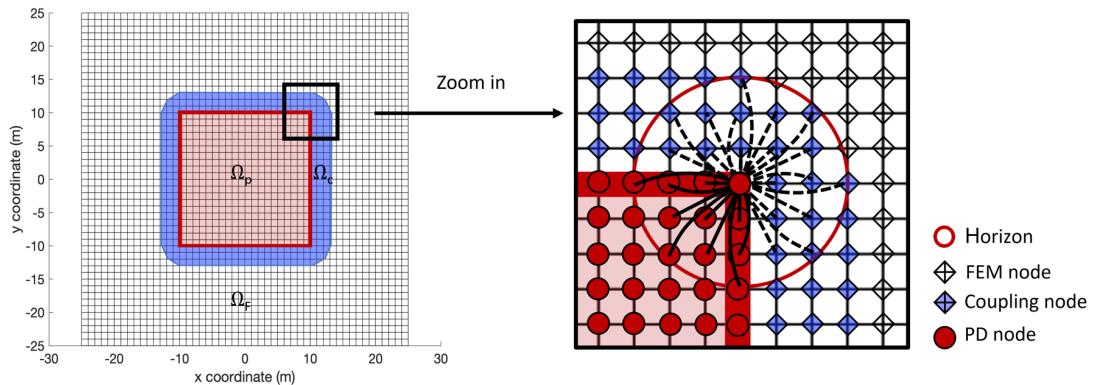


Fig. 5.2 Illustration of FEM and PD sub-domain.

Table 5.1 Rules for the application of boundary conditions for peridynamics.

Boundary condition	Traction boundary condition	Displacement or velocity boundary condition
Rules	can be applied as body force density in a “real material layer” along the boundary of a nonzero volume.	can be applied by prescribing constraints on displacement and velocity fields in a “fictitious material layer” along the boundary of a nonzero volume.

real PD nodes (red circles), we call these FEM nodes the coupling nodes. The dashed lines represent the bonds coupling PD nodes to the surrounding FEM elements. The continuous lines represent standard bonds between PD nodes. The bonds connecting PD nodes to coupling nodes only apply forces to PD nodes while the FEM elements having PD nodes only apply forces to FEM nodes. The coupling is realised by adopting in the global stiffness matrix the terms coming from the FEM theory, representing forces acting on FEM nodes, and the terms coming from the PD discretisation, representing forces acting on PD nodes. This coupling ensures not only the completeness of the integral of the non-local strain energy for all PD nodes, but also the smooth transition from the local model to the non-local model [285].

### 5.3.4 Solution strategy

#### Static approach

For the static situation, the first item of Eq. (5.20), the acceleration terms, can be neglected. Here the Backward Euler is used for time discretisation and the resulting system is given below:

$$\begin{cases} \dot{\mathbf{u}}^{n+1} = \frac{1}{\Delta t}(\mathbf{u}^{n+1} - \mathbf{u}^n) \\ \dot{\mathbf{p}}^{n+1} = \frac{1}{\Delta t}(\mathbf{p}^{n+1} - \mathbf{p}^n) \end{cases} \quad (5.33)$$

$$\bar{\mathbf{K}}\mathbf{u}^{n+1} - \bar{\mathbf{Q}}\mathbf{p}^{n+1} = \bar{\mathbf{f}}^{n+1} \quad (5.34a)$$

$$\mathbf{Q}_F^T \dot{\mathbf{u}}^{n+1} + \mathbf{C}_F \dot{\mathbf{p}}^{n+1} + \mathbf{H}_F \mathbf{p}^{n+1} = \mathbf{q}_F^{n+1} \quad (5.34b)$$

where  $\bar{\mathbf{K}}$  is obtained by assembling  $\mathbf{K}_{PD}$  and  $\mathbf{K}_F$ ,  $\bar{\mathbf{Q}}$  by assembling  $\mathbf{Q}_F$  and  $\mathbf{Q}_{PD}$ , and  $\bar{\mathbf{f}}$  by assembling  $\mathbf{f}_F$  and  $\mathbf{f}_{PD}$ .

After substituting Eq. (5.33) into Eq. (5.34), the following equation system is obtained:

$$\begin{Bmatrix} \mathbf{u} \\ \mathbf{p} \end{Bmatrix}^{(n+1)} = \begin{Bmatrix} \mathbf{u} \\ \mathbf{p} \end{Bmatrix}^{(n)} - \frac{\mathbf{R}}{\mathbf{J}} \quad (5.35)$$

$$\mathbf{J} = \begin{bmatrix} \bar{\mathbf{K}} & -\bar{\mathbf{Q}} \\ \mathbf{Q}_F^T & \frac{\mathbf{C}_F}{\Delta t} + \mathbf{H}_F \end{bmatrix} \quad (5.36)$$

$$\mathbf{R} = \begin{bmatrix} \bar{\mathbf{K}}\mathbf{u}^{n+1} - \bar{\mathbf{Q}}\mathbf{p}^{n+1} - \bar{\mathbf{f}}^{n+1} \\ \mathbf{Q}_F^T \dot{\mathbf{u}}^{n+1} + \mathbf{C}_F \dot{\mathbf{p}}^{n+1} + \mathbf{H}_F \mathbf{p}^{n+1} - \mathbf{q}_F^{n+1} \end{bmatrix} \quad (5.37)$$

The coupled equation system is solved via Newton-Raphson method.

#### Simulation flowchart of static problems with failure

If failure occurs, the simulation flow chart for solving the static failure problem with the FEM-PD approach is shown in Fig. 5.3. First, the initial and boundary conditions are given, Then, the domain is divided into the FEM sub-domain and PD sub-domain following the

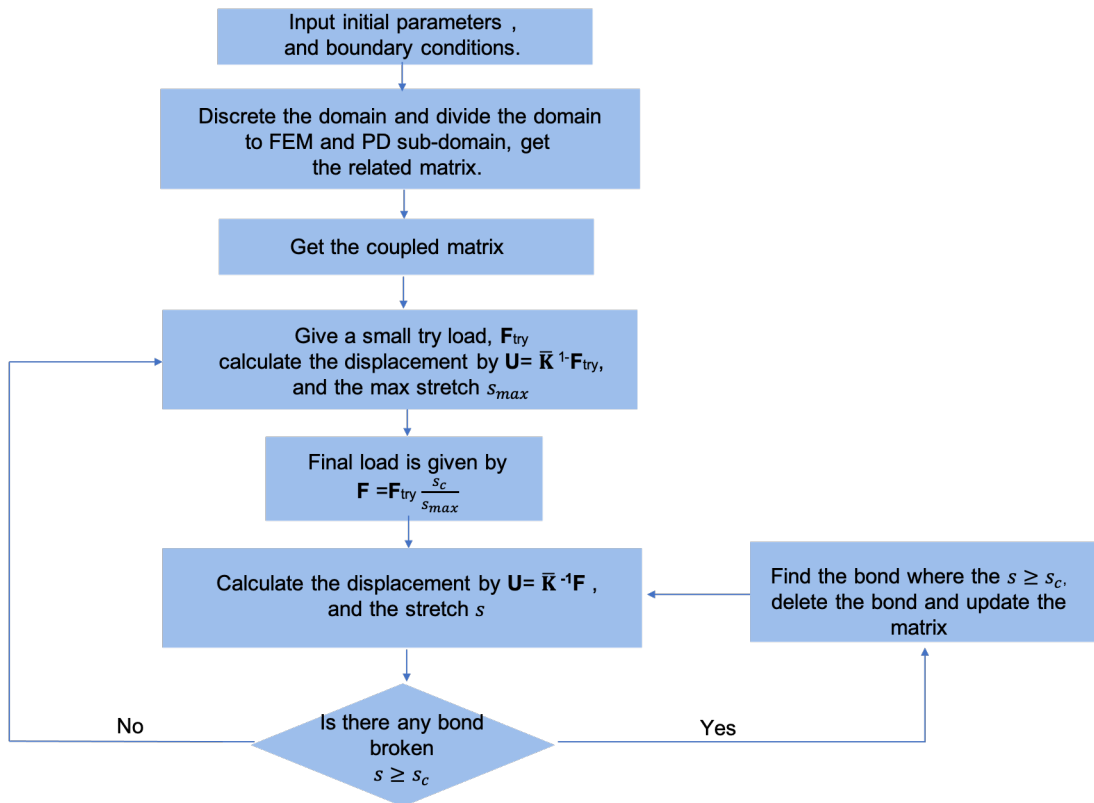


Fig. 5.3 Flowchart for solving the static failure problem with the FEM-PD approach.

rules that the crack is assumed to develop in the PD sub-domain. Then, the PD stiffness matrix and FEM matrix are coupled together as described in § 5.3.3. The coupling method follows the action and reaction principle at the transition between FEM and PD sub-domain. For static failure problem, one of the most important things is to find the equilibrium once the failure occurs. Here, a small try load is given first, which will not cause any failure. Then under the loading condition, the displacement  $u$  of each node and the max stretch  $s_{max}$  of the bond are calculated. The failure criterion  $s_c$  has already been given. With the proportion of  $\frac{s_c}{s_{max}}$ , the smallest load to cause failure (break the balance) can be calculated by  $F = F_{try} \frac{s_c}{s_{max}}$ . With the calculated load, the displacement  $u$  of each node and the max stretch  $s_{max}$  of the bond are calculated again. Check whether there is any bond broken (the bond of which the stretch is over the critical stretch  $s_c$ ), if yes, delete the broken bonds and update the matrix  $K_{PD}$  since the PD forces don't exist in broken bonds. By deleting the broken bond iteratively until there is no bond broken, the equilibrium is finally made. Then, a small try load is given again to find the next equilibrium state.

### Dynamic approach

The coupled fluid-solid equations for crack branching in porous media are dynamic and nonlinear. Here the Newmark method [276] is used for time discretisation taking into account the inertial force and the acceleration terms, and the resulting system is given below:

$$\begin{cases} \ddot{\mathbf{u}}^{n+1} = a_0(\mathbf{u}^{n+1} - \mathbf{u}^n) - a_2\dot{\mathbf{u}}^n - a_3\ddot{\mathbf{u}}^n \\ \dot{\mathbf{u}}^{n+1} = a_1(\mathbf{u}^{n+1} - \mathbf{u}^n) - a_4\dot{\mathbf{u}}^n - a_5\ddot{\mathbf{u}}^n \\ \mathbf{p}^{n+1} = \mathbf{p}^n + \Delta t(1 - \theta)\dot{\mathbf{p}}^n + \theta\Delta t\dot{\mathbf{p}}^{n+1} \end{cases} \quad (5.38)$$

with

$$\begin{aligned} a_0 &= \frac{1}{\beta\Delta t^2}, & a_1 &= \frac{\gamma_a}{\beta\Delta t}, & a_2 &= \frac{1}{\beta\Delta t} \\ a_3 &= \frac{1}{2\beta} - 1, & a_4 &= \frac{\gamma_a}{\beta} - 1, & a_5 &= \Delta t\left(\frac{\gamma_a}{2\beta} - 1\right) \end{aligned} \quad (5.39)$$

$$\bar{\mathbf{M}}\ddot{\mathbf{u}}^{n+1} + \bar{\mathbf{K}}\mathbf{u}^{n+1} - \bar{\mathbf{Q}}\mathbf{p}^{n+1} = \bar{\mathbf{f}}^{n+1} \quad (5.40a)$$

$$\mathbf{Q}_F^T\dot{\mathbf{u}}^{n+1} + \mathbf{C}_F\dot{\mathbf{p}}^{n+1} + \mathbf{H}_F\mathbf{p}^{n+1} = \mathbf{q}_F^{n+1} \quad (5.40b)$$

where  $\bar{\mathbf{M}}$  is obtained by assembling  $\mathbf{M}_{PD}$  and  $\mathbf{M}_F$ .

After substituting Eq. (5.38) into Eq. (5.40), we obtain the following equation system:

$$\begin{Bmatrix} \mathbf{u} \\ \mathbf{p} \end{Bmatrix}^{(n+1)} = \begin{Bmatrix} \mathbf{u} \\ \mathbf{p} \end{Bmatrix}^{(n)} - \frac{\mathbf{R}}{\mathbf{J}} \quad (5.41)$$

$$\mathbf{J} = \begin{bmatrix} a_0\bar{\mathbf{M}} + \bar{\mathbf{K}} & -\bar{\mathbf{Q}} \\ a_1\mathbf{Q}_F^T & \frac{\mathbf{C}_F}{\theta\Delta t} + \mathbf{H}_F \end{bmatrix} \quad (5.42)$$

$$\mathbf{R} = \begin{bmatrix} \bar{\mathbf{M}}(a_0(\mathbf{u}^{n+1} - \mathbf{u}^n) - a_2\dot{\mathbf{u}}^n - a_3\ddot{\mathbf{u}}^n) + \bar{\mathbf{K}}\mathbf{u}^{n+1} - \bar{\mathbf{Q}}\mathbf{p}^{n+1} - \bar{\mathbf{f}}^{n+1} \\ \mathbf{Q}_F^T(a_1(\mathbf{u}^{n+1} - \mathbf{u}^n) - a_4\dot{\mathbf{u}}^n - a_5\ddot{\mathbf{u}}^n) + \mathbf{C}_F \cdot \frac{\mathbf{p}^{n+1} - \mathbf{p}_w^n - \Delta t(1 - \theta)\dot{\mathbf{p}}_w^n}{\theta\Delta t} + \dots \\ \mathbf{H}_F\mathbf{p}^{n+1} - \mathbf{q}^{n+1} \end{bmatrix} \quad (5.43)$$



When  $\gamma_a \geq 1/2$ ,  $\beta \geq 1/4$ , and  $\theta \geq 1/2$ , the above equation system is unconditionally stable. The coupled nonlinear equation system is solved via a monolithic scheme with the Newton-Raphson method.

### Simulation flowchart of dynamic problems with failure

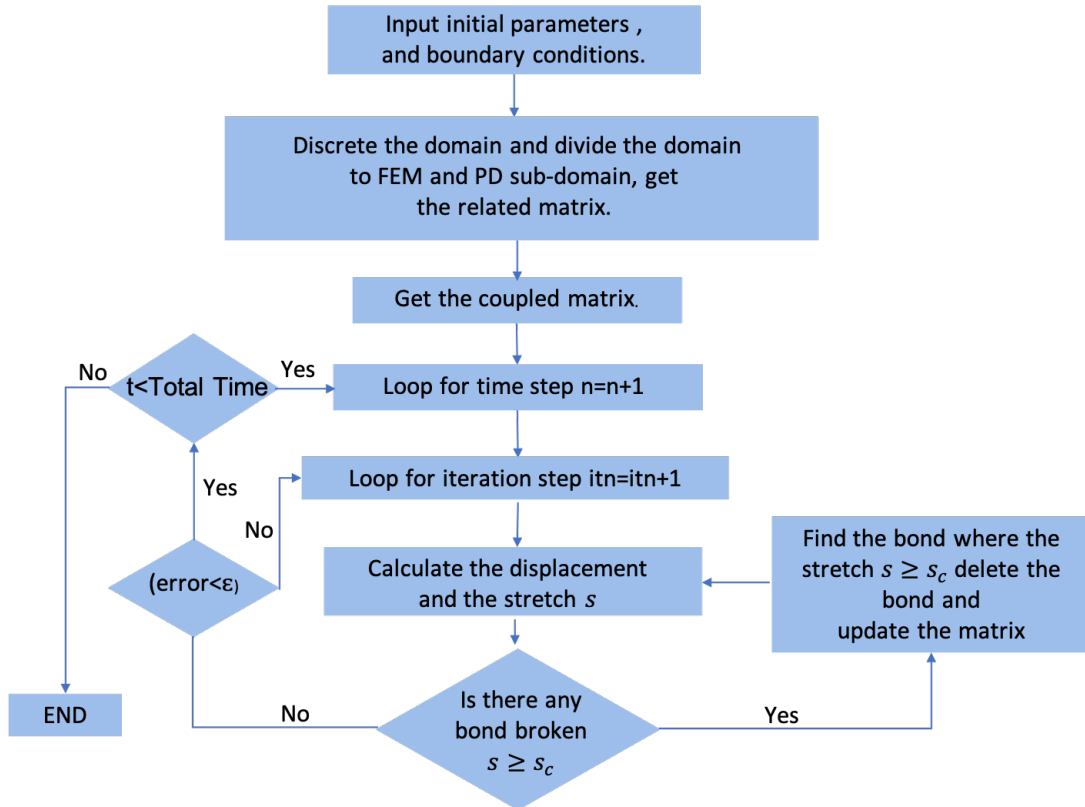


Fig. 5.4 Flowchart for solving the dynamic failure problem with the FEM-PD approach.

The simulation flow chart for solving the dynamic failure problem with the FEM-PD approach is illustrated in Fig. 5.4. After the initial and boundary conditions are given, the domain is divided into the FEM sub-domain and PD sub-domain following the rule that the crack is assumed to develop in the PD sub-domain. Then, the coupled matrix is assembled using the PD matrix and FEM matrix coupling strategy. The Newmark method is used for time discretisation. For each time step if local failure is detected ( $s \geq s_c$  in Eq. (5.12)), dynamic crack propagation develops and local bonds break accordingly, forming a nonlinear equation system. The stiffness matrix is updated according to the change in local connectivity whenever broken bonds are detected. Newton iteration is then used to solve the non-linear system. The loop continues until bond breaking has ceased and the result satisfies the convergent condition  $error < \varepsilon$ . Here,  $error = \left| \frac{x^{itn+1} - x^{itn}}{x^{itn+1}} \right|$ , where  $x$  represents the unknowns

(pressure or displacements in the 2D hydraulic fracturing problem) and  $itn$  represents the iteration step. Once the Newton iteration has converged, go to the next time step.

## 5.4 Model verification

### 5.4.1 Static problem without failure

#### 1D bar model under two different loading conditions

The 1D bar is composed of 31 nodes with a length of  $L = 30$  m. The PD sub-domain is composed of nodes 13-25, while the FEM sub-domain is composed of nodes 1-12 and 26-31. The parameters used in this model is shown in Table 5.2. Two different loading conditions are considered. (1) With the left end fixed, the right end of the bar is subjected to a tensile unit force, see Fig. 5.5. (2) With both ends fixed, the bar is subjected to uniformly distributed axial unit forces.

Table 5.2 Parameters for 1D bar model.

Grid spacing $\Delta x$ (m)	Young's modulus $E$ (Pa)	Bar cross section area $A$ (m)	Radius of horizon $\delta$ (m)	Micro-modulus $c$
1	1	1	3	2/9

Fig. 5.6 and Fig. 5.7 show the comparison of displacement between PD-FEM and analytical solution under the first and second loading conditions. The coupled PD-FEM numerical solution is in good agreement with the analytical solution. The relative error is calculated with the equation given below:

$$e_{rel,i} = \frac{u_i^* - u_i}{u_i} \quad (5.44)$$

where  $i$  is the node index,  $u$  the exact displacement value and  $u^*$  the numerically computed displacement value. Using the equation, the relative errors under two different loading conditions are calculated only with nodes in which no boundary conditions have been applied. The relative error for the first loading condition is  $2.6e-14$  while for the second loading condition is  $5.8e-15$ . It can be seen that the result of simulation by PD-FEM is accurate enough for 1D bar model.

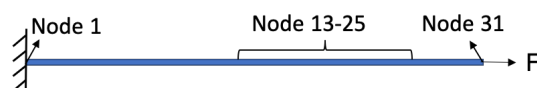


Fig. 5.5 Geometry and discretisation of 1D bar model.

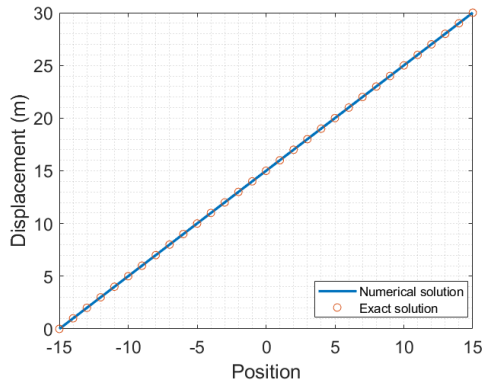


Fig. 5.6 The comparison of displacement under the first loading condition.

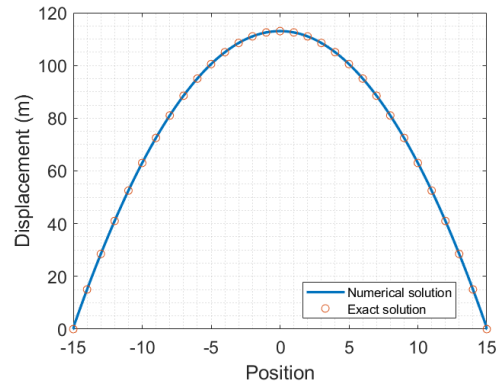


Fig. 5.7 The comparison of displacement under the second loading condition.

**2D plane stress model**

As shown in Fig. 5.8, a 2D plane stress square model with 50 m side length and 1 m thickness is established. The PD sub-domain is in red rectangular composed of 475 material points ( $\mathbf{x}_i(x_1, x_2) \in \Omega_P, -11 \text{ m} \leq x_1 \leq 7 \text{ m}$  and  $-8 \text{ m} \leq x_2 \leq 16 \text{ m}$ ) while the FEM sub-domain is the rest and composed of 1980 rectangular elements. The parameters used in this model are listed in Table 5.3.

Table 5.3 Parameters for 2D plane stress square model.

Grid spacing $\Delta x$ (m)	Young's modulus $E$ (Pa)	Poisson ratio $\nu$	Radius of horizon $\delta$ (m)	Micro-modulus $c$
1	1	1/3	3	2/9

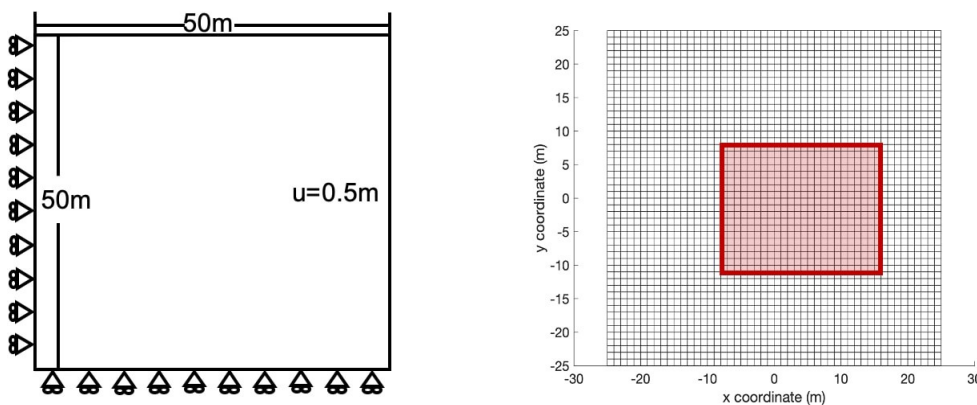


Fig. 5.8 Geometry and discretisation of 2D solid deformation model.

The vertical displacement on the left edge and the horizontal displacement on the bottom edge are constrained while the displacement on the top edge are free. By applying a uniform

horizontal displacement  $u = 0.5$  m on the right edge, the plate is stretched in the horizontal direction. According to the analytical solution, the exact solutions of displacements are evaluated with equations  $u^* = 0.5 \frac{x}{E}$   $v^* = -0.5v \frac{y}{E}$ . The relative errors distribution of the horizontal and vertical displacements are shown in Fig. 5.9 and Fig. 5.10. The relative error of  $u$  reaches  $2e-13$  while the relative error of  $v$  reaches  $3e-13$ . It can be seen that no spurious behaviour is observed at the interface between FEM and PD sub-domain and the result of simulation by PD-FEM is accurate enough for 2D model.

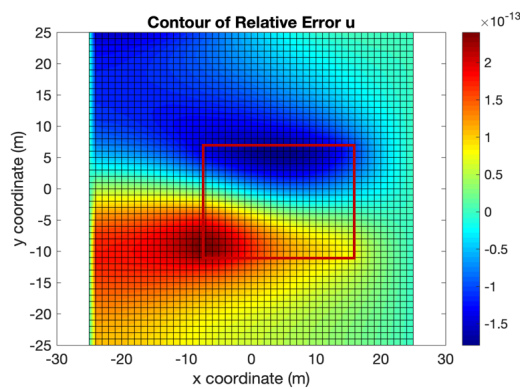


Fig. 5.9 The relative error of horizontal displacement  $u$ .

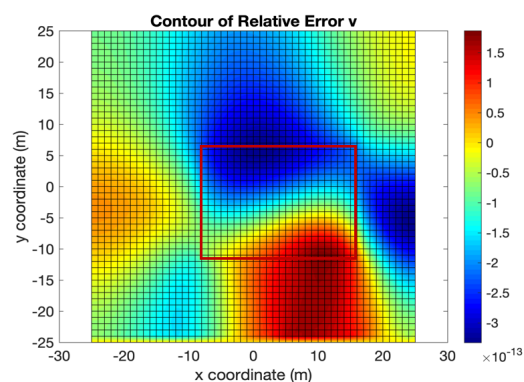


Fig. 5.10 The relative error of vertical displacement  $v$ .

### 5.4.2 Static problem with failure

#### A double cantilever beam crack model (crack caused by tension)

A double cantilever beam model is established with the length of 0.1 m and the width of 0.025 m, see Fig. 5.11. An initial crack of 0.05 m length is in the left middle of the model. The FEM sub-domain is composed of 5100 rectangular elements while the PD sub-domain, shown as the red rectangle, has 5226 material points  $(\mathbf{x}_i(x_1, x_2) \in \Omega_P, -0.05 \text{ m} \leq x_1 \leq 0.05 \text{ m}$  and  $-0.005 \text{ m} \leq x_2 \leq 0.005 \text{ m})$ . The parameters used in this model are listed in Table 5.4.

Table 5.4 Parameters for a double cantilever beam crack model.

Grid spacing $\Delta x$ (m)	Young's modulus $E$ (GPa)	Poisson ratio $\nu$	Radius of horizon $\delta$ (m)	Micro-modulus $c$ (N/m <sup>6</sup> )	Critical stretch $s_c$
5e-4	200	1/3	1.5e-3	1.68e+20	6.7e-3

The right edge is fixed and the loading conditions is applied by giving displacement on the two vertices of the left edge. With the applied displacements, the crack starts to propagate. Fig. 5.12 shows the crack development history with time varying. From (a) to (d), time increases and the crack develops, and when the crack tip reaches close to the right edge, the crack branches. The results shows the same with results in paper [285].

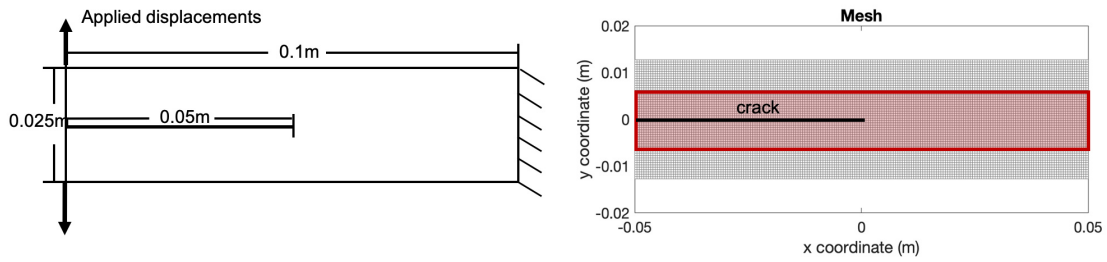


Fig. 5.11 Geometry and discretisation of a double cantilever beam crack model.

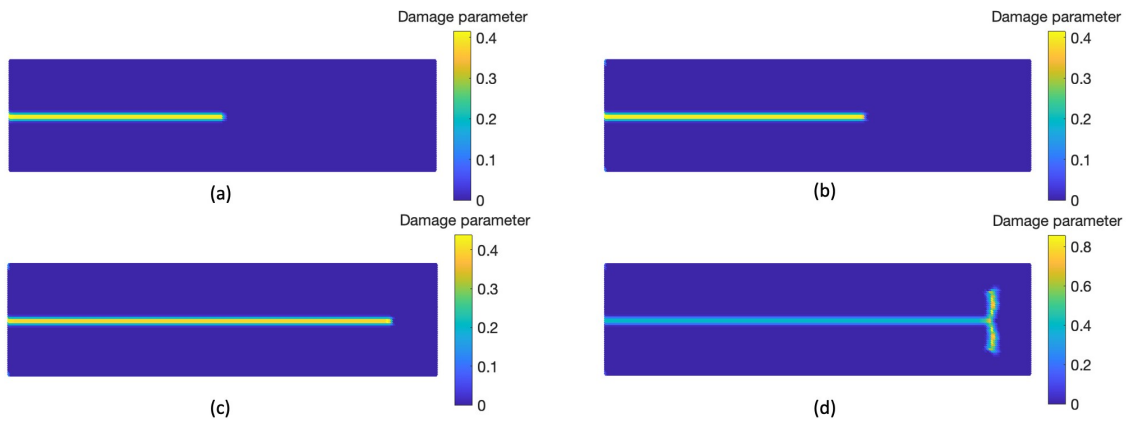


Fig. 5.12 Crack development history with time varying from (a) to (d).

#### A diagonally loaded square plate crack model (crack caused by shear force)

As shown in Fig. 5.13, a diagonally loaded square plate model with an initial crack in the center is established. The side length is 0.15 m. The length of the crack is 0.045 m and the angle between the crack and the horizontal direction is  $62.5^\circ$ . The PD sub-domain is in red rectangle. As a square, its side length is 0.016 m smaller than the whole domain. The rest is the FEM sub-domain, which is suitable for applying diagonally loading boundary conditions. The FEM sub-domain is composed of 1136 rectangular elements while the PD sub-domain, shown as the red rectangle, has 4624 material points. The parameters used in this model are listed in Table 5.5.

Table 5.5 Parameters for a diagonally loaded square plate crack model.

Grid spacing $\Delta x$ (m)	Young's modulus $E$ (GPa)	Poisson ratio $\nu$	Radius of horizon $\delta$ (m)	Micro-modulus $c$ (N/m <sup>6</sup> )	Critical stretch $s_c$
2e-3	2.94	0.38	6e-3	8.386e+18	8.9e-3

In the experiment [23], the load is given at the hole on the top and bottom corner and on a hole with a diameter of 0.004 m. Here, in order to get the results close to the experiment results, the velocity boundary conditions adopted are taken from [190]. The load is applied

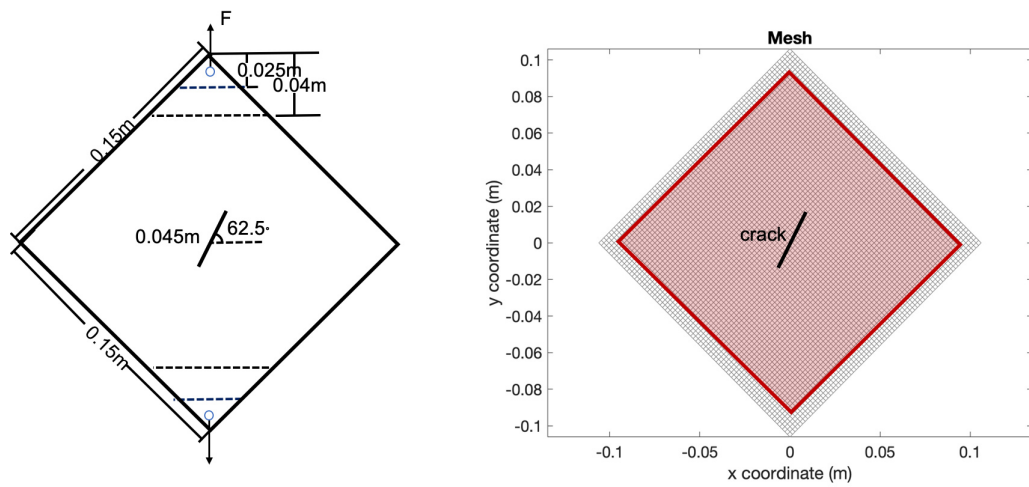


Fig. 5.13 Geometry and discretisation of a diagonally loaded square plate crack model.

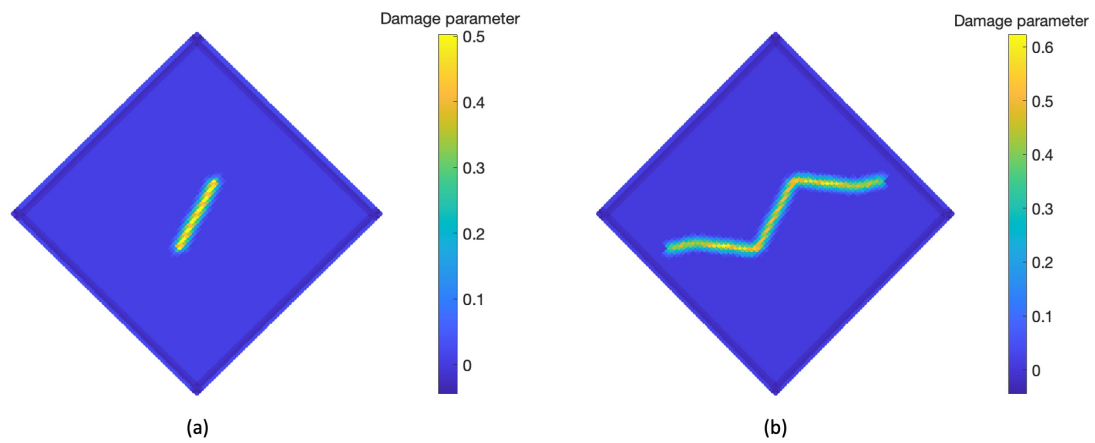


Fig. 5.14 Crack paths with time varying (a) initial crack and (b) final crack.



Fig. 5.15 Experimental result of a diagonally loaded square plate crack model.

through a constant velocity constraint of  $\dot{\mathbf{u}} = 1 \times 10^{-6}$  m/s within the region of 0.025 m from the top and bottom corner of the plate until damage is captured. Later, the damage analysis is performed with a constant velocity constraint of  $\dot{\mathbf{u}} = 1 \times 10^{-8}$  m/s to predict crack growth path.

In order to avoid spurious cracking near the region of loading, a no-fail region with a length of 0.04 m is introduced from the top and bottom corner of the plate. The deformation and damage progression of the plate are simulated through the PD-FEM model and the crack development history with time increasing from (a) to (b) are shown in Fig. 5.14. Compared with the experiment result in Fig. 5.15, the crack propagation path simulated by the PD-FEM approach agrees well with the experimental result, which demonstrates the accuracy and effectiveness of the hybrid PD-FEM approach.

### 5.4.3 Dynamic problem without failure

#### 2D plane stress model subjected to an external load

The 2D plane stress model with a side length of 8 m is subjected to an external load  $\mathbf{F}$ . The related parameters are listed in Table 5.6. And the time step  $\Delta t$  of the integration is chosen to be  $1 \times 10^{-3}$  s.

Table 5.6 Parameters for 2D plane stress crack model.

Grid spacing $\Delta x$ (m)	Young's modulus $E$ (GPa)	Poisson ratio $\nu$	Radius of horizon $\delta$ (m)	Micro-modulus $c$ (N/m <sup>6</sup> )	Density $\rho$ (kg·m <sup>-3</sup> )
0.1	0.05	0.25	0.3	5.6e+9	2647

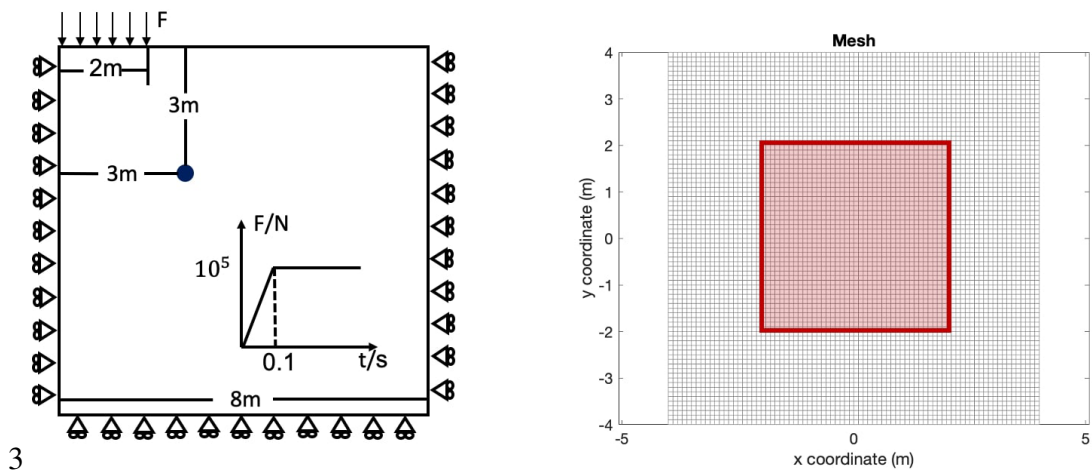


Fig. 5.16 Geometry and discretisation of a 2D plane stress model subjected to an external load.

As shown in Fig. 5.16, the PD sub-domain, shown as the red rectangle, has 1681 material points while the FEM sub-domain is the rest, composed of 4800 rectangular elements. The boundary conditions are also shown in Fig. 5.16. Both the left and right sides are fixed in the horizontal direction and the bottom edge is fixed in the vertical direction. The top left corner is imposed by an external load  $F$ . Fig. 5.17 and Fig. 5.18 show the horizontal and vertical displacement histories at point A obtained by the hybrid approach FEM-PD and FEM. Taking FEM results as a reference, it can be seen that the numerical results of the hybrid FEM-PD approach agrees well with the FEM results.

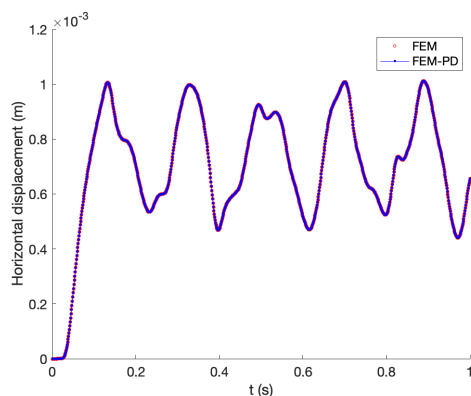


Fig. 5.17 The comparison of horizontal displacement at point A with FEM and PD-FEM.

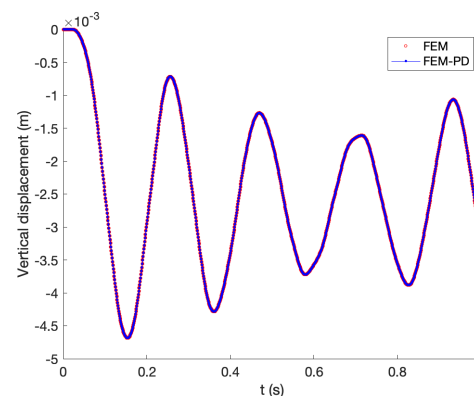


Fig. 5.18 The comparison of vertical displacement at point A with FEM and PD-FEM.

## 5.4.4 Dynamic problem with failure

### Three-point bending problem

As shown in Fig. 5.19, a notched three-point bending beam with an initial crack at the bottom has been established. The length of the beam is 1.01 m and the width of the beam is 0.4 m. The length of the initial crack is 0.2 m. The beam is divided into FEM-subdomain and PD-subdomain. The size of the PD sub-domain is  $0.4 \text{ m} \times 0.4 \text{ m}$ , which is the area of the red rectangle. The PD sub-domain has 6480 material points while the FEM sub-domain is composed of 8040 rectangular elements. The related parameters are listed in Table 5.7. And the density of the material is  $8 \times 10^3 \text{ kg} \cdot \text{m}^{-3}$ . the time step  $\Delta t$  of the integration is chosen to be  $1 \times 10^{-3} \text{ s}$ .

For the boundary conditions, the left end of the bottom is fixed, while the right end of the bottom edge is fixed in the vertical direction. In the middle of the top edge, a velocity boundary condition is applied with  $\dot{u} = 10 \text{ m/s}$  within a length of 0.21 m. Under this velocity



Table 5.7 Parameters for a three-point bending model.

Grid spacing $\Delta x$ (m)	Young's modulus $E$ (GPa)	Poisson ratio $\nu$	Radius of horizon $\delta$ (m)	Micro-modulus $c$ (N/m <sup>6</sup> )	Critical stretch $s_c$
5e-3	192	0.33	1.5e-2	1.61e17	1.41e-2

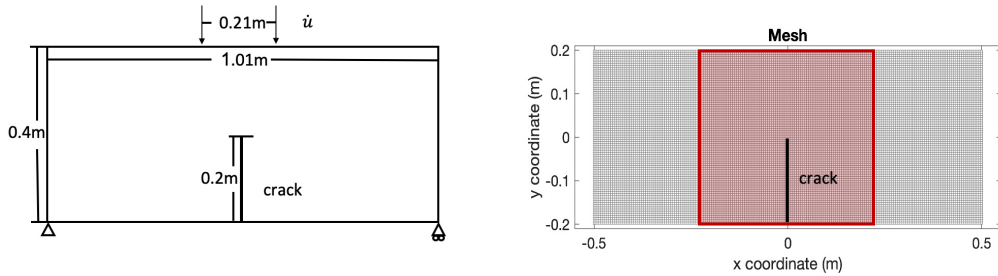
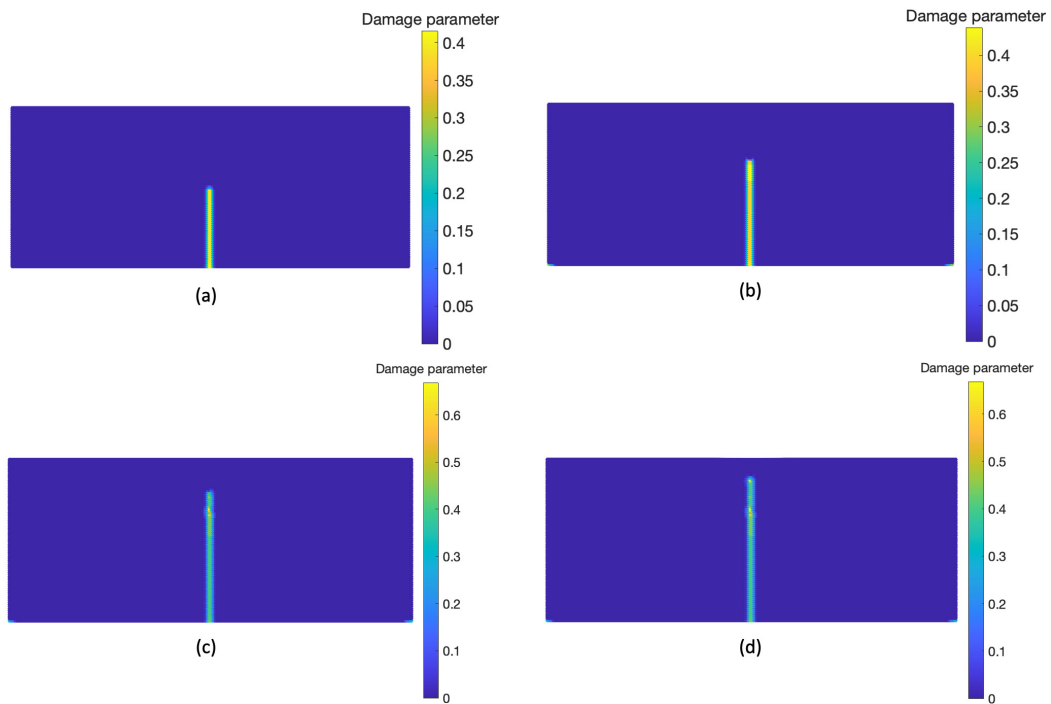


Fig. 5.19 Geometry and discretisation of a three-point bending model.

Fig. 5.20 crack development history with time varying (a)  $t = 400 \mu s$ , (b)  $t = 500 \mu s$ , (c)  $t = 650 \mu s$  and (d)  $t = 850 \mu s$ .

boundary condition, the crack development history is recorded with time increasing, see Fig. 5.19. From (a) to (d), time increases and the crack develops. The results shows the same with results in paper [230].

### 5.4.5 Dynamic problem with failure and pressure field

#### 1D porous media bar

The model describes a fully saturated 1D poroelastic column bar with a pressure applied at the top of the bar, see Fig. 5.21. The height of the column is 15 m. The top surface is subjected to a constant pressure of  $10^4$  Pa. The top surface is used for fluid drainage and the pore pressure at the top surface remains zero, while the bottom surface acts as a solid wall and the fluid flux is zero. The PD is used to describe the deformation of the porous media and the FEM is used to describe the fluid flow in the porous media. Referring to [284], the material properties are listed in Table 5.8. To check the convergence, three different grid spacings are considered: (1)  $\Delta x = 0.2$  m; (2)  $\Delta x = 0.1$  m and (3)  $\Delta x = 0.05$  m, where  $\Delta x$  is the grid spacing. The horizon size  $\delta$  is equal to  $3\Delta x$ .

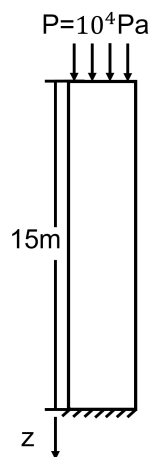


Fig. 5.21 The basic geometry of 1D porous media bar model.

The analytical solution to this problem is given in [434]:

$$P(z,t) = \frac{4\nu P_0}{\pi} \sum_{m=0}^N \left\{ \frac{1}{2m+1} \exp\left(-\left(\frac{(2m+1)\pi}{2L}\right)^2 ct\right) \times \sin\left(\frac{(2m+1)\pi z}{2L}\right) \right\} \quad (5.45)$$

$$u(z,t) = c_m \nu P_0 \left\{ (L-z) - \frac{8L}{\pi^2} \sum_{m=0}^N \left\{ \frac{1}{(2m+1)^2} \right\} \right\} \times \exp\left(-\left(\frac{(2m+1)\pi}{2L}\right)^2 ct\right) \\ \times \cos\left(\frac{(2m+1)\pi z}{2L}\right) + a_i P_0 (h-z) \quad (5.46)$$

where

$$v = \frac{a - a_i}{\alpha a}, \quad a_i = \frac{a}{1 + \alpha^2 a Q}, \quad c = \frac{kQ}{(\alpha^2 a + Q)\mu}, \quad c_m = (a - a_i)/v \quad (5.47)$$

with  $a = 1.0 \times 10^{-8} \text{ N/m}^2$ .

Fig. 5.22 shows the distributions of pore pressure and displacement along the central axis at different times with different grid sizes. The numerical solutions show good agreement with the analytical solutions and with smaller grid size, the numerical results indicate convergence towards the analytical results. As time increases, the pore pressure decreases and the displacement increases in  $z$  direction, indicating water out flow from the top surface together with soil consolidation.

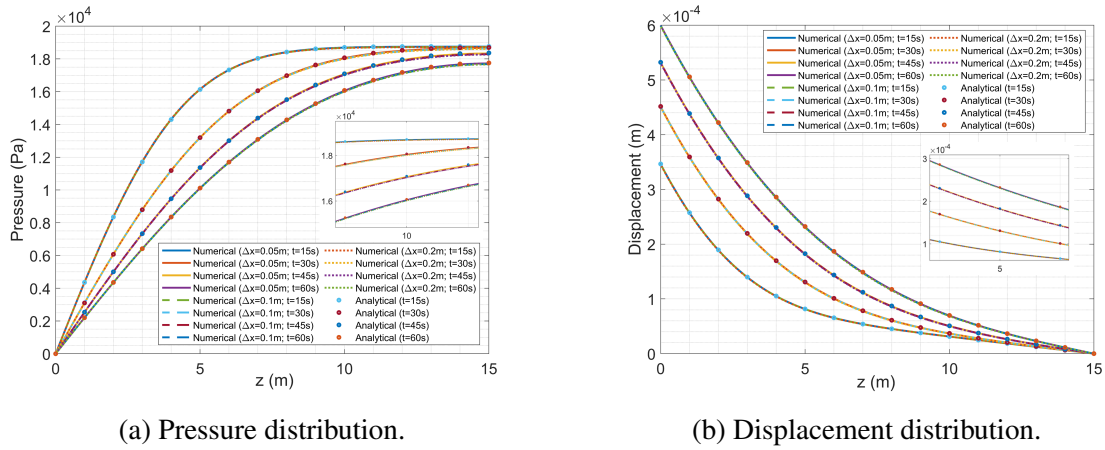


Fig. 5.22 The comparison of analytical and numerical solution along the bar.

Table 5.8 Material properties for the proelastic column.

Properties	Symbols	Values
Elasticity modulus	$E$	$1.0 \times 10^8 \text{ Pa}$
Biot constant	$\alpha$	0.5
Biot modulus	$Q$	$6.06 \times 10^9 \text{ N/m}^2$
Viscosity	$\mu$	$1.0 \times 10^{-3} \text{ Pa}\cdot\text{s}$
Permeability	$k$	$1.0 \times 10^{-12} \text{ m}^2$
Material density	$\rho$	$1.9 \times 10^3 \text{ kg/m}^3$

### KGD problem

As shown in Fig. 5.23, a plane strain KGD problem [76] is employed to examine the hybrid numerical scheme in two-dimensions. The borehole is treated as a point source in the plane because the radius is very small compared to the fracture length. Due to symmetry, Fig. 5.23 only shows half of the model, which is 16 m in height and 8 m in width. The domain is divided into a FEM-subdomain and a PD-subdomain, where the PD-subdomain is the area where the crack can potentially occur. The PD sub-domain is  $8\text{ m} \times 8\text{ m}$ , as indicated by the red rectangle in Fig. 2.4.

For boundary conditions, the top and bottom sides are fixed in the vertical direction, the right edge is fixed in the horizontal direction, and the pressure on the boundaries is set as zero. The initial crack length is 0.1 m and a flux  $q = 0.0001\text{ m}^3/\text{s}$  is injected in the left borehole. For the introduced fractures, the fluid pressure exerts on the fracture surfaces and no friction is considered. The rock media is assumed homogeneous and fully saturated, and it undergoes small deformation. All parameters including the rock properties, fluid properties and other conditions used in the numerical simulation are listed in Table 4.3. When plugging the parameters into KGD equations, they need to be converted into SI the international system of units. Note that for the element inside the fracture domain, the porosity is 1 and the permeability is calculated using Eq. (5.9) and Eq. (5.11).

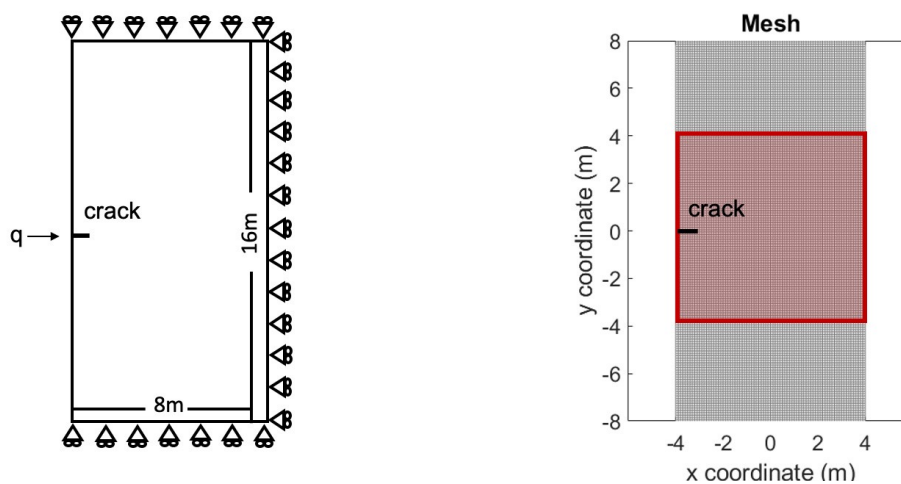


Fig. 5.23 Geometry and discretisation of a KGD model.

In order to check for convergence of the results, three different grid spacings and time steps are used: (1)  $\Delta x = 0.2\text{ m}$ ,  $\Delta t = 0.2\text{ s}$ ; (2)  $\Delta x = 0.1\text{ m}$ ,  $\Delta t = 0.1\text{ s}$  and (3)  $\Delta x = 0.05\text{ m}$ ,  $\Delta t = 0.05\text{ s}$ . The horizon size  $\delta$  is equal to  $3\Delta x$ . The comparison between the analytical solutions [151, 411] and numerical results in terms of evolution of the fracture length, pressure and width are shown in Fig. 5.24. Using  $\Delta x = 0.05\text{ m}$  and  $\Delta t = 0.05\text{ s}$ , the growth

Table 5.9 Rock properties, fluid properties and loading conditions used in KGD simulation.

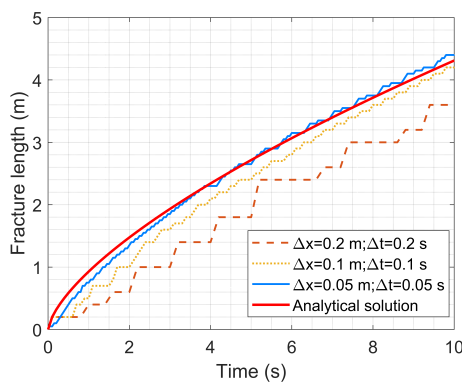
Properties	Symbols	Values
Elasticity modulus	$E$	$15.96 \times 10^9$ Pa
Poisson's ratio	$\nu$	0.25
Biot constant	$\alpha$	1
Bulk modulus(Solid)	$K_s$	$36 \times 10^9$ Pa
Bulk modulus(Fluid)	$K_f$	$3 \times 10^9$ Pa
Viscosity	$\mu$	$1.0 \times 10^{-3}$ Pa·s
Material density	$\rho$	$1.81 \times 10^3$ kg/m <sup>3</sup>
Porosity	$n$	0.19
Permeability	$k$	$1.0 \times 10^{-14}$ m <sup>2</sup>
Critical energy release rate	$G_c$	100 N/m

of crack and the distribution of pressure in porous media and in the fracture are shown in Fig. 5.25. We note that the pressure is negative ahead of the crack tip. According to Biot theory, dilatation is positive in the regions ahead of the crack tips arising from the opening mode of deformation. There exists pressure pressure drop in the regions of positive dilatation, which causes large suction and negative pressure.

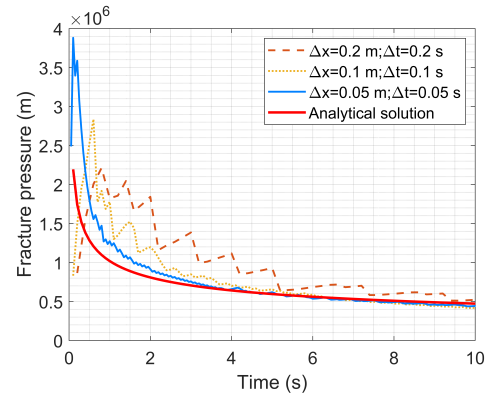
All three parameters show convergence with accuracy increasing with the decrease of time step and mesh size, which demonstrates the reliability of the numerical method for hydraulic fracturing problems. However, we note that while errors are decreasing the largest errors are in the evolution of the fluid pressure and fracture width at the borehole. There are two potential causes for this difference. First, the analytical solution is based on the local theory while the numerical solution is established on non-local theory (peridynamics). Secondly, the medium in the analytical solution is linearly elastic and there is no leak-off at the fracture surface, while in our model, the medium is poroelastic and the fracture surface is permeable since the leak-off is automatically captured by the model.

### Fluid-driven fracture interaction with natural cracks

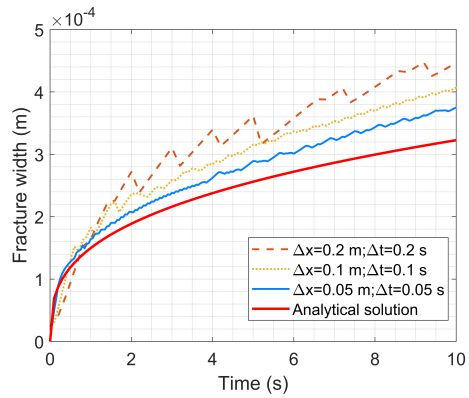
To test the method capability of describing multiple cracks and evaluating fluid pressure in and out of the fracture area, a problem involving a fluid-driven fracture interacting with natural cracks [484] is considered. With the exception of an additional natural crack, the geometry of the model is similar to that of the KGD model. The natural crack is 4 m long and 3.8 m away from the original crack that is 0.2 m in length. The domain is divided into an



(a) Fracture length evolution.

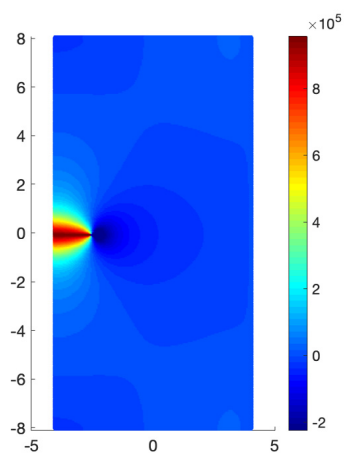


(b) Fracture pressure evolution.

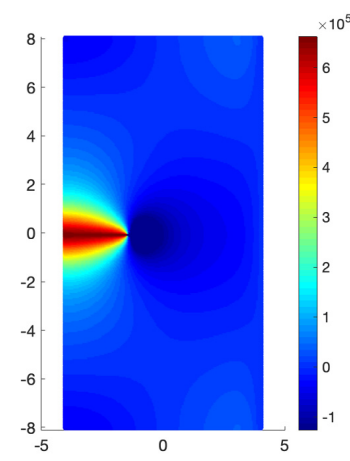


(c) Fracture width evolution.

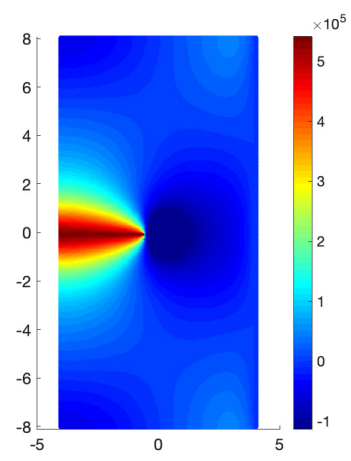
Fig. 5.24 Verification of the KGD model.



(a) t=2.5s.



(b) t=5s.



(c) t=7.5s.

Fig. 5.25 Pore pressure and fracture pressure distribution with time varying (unit: Pa).

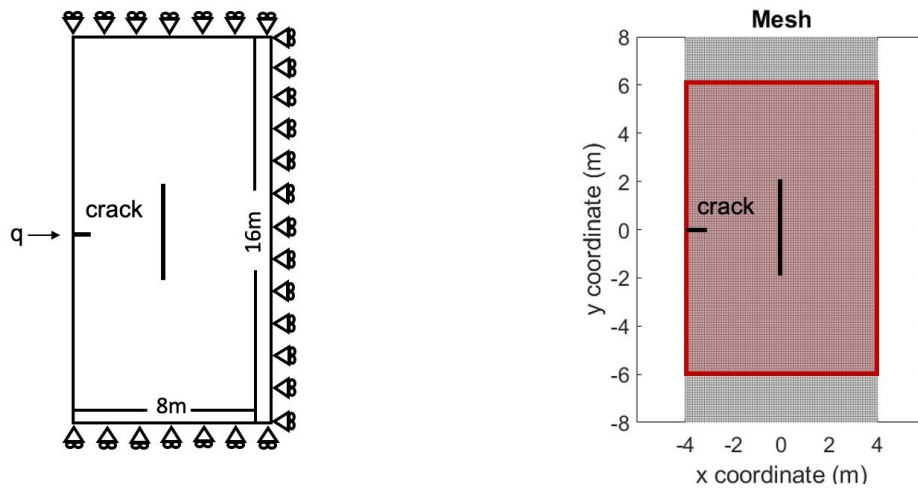


Fig. 5.26 Geometry and discretisation of fracture interaction model.

FEM-subdomain and a PD-subdomain, where the PD-subdomain is  $8\text{ m} \times 12\text{ m}$ , as indicated by the red rectangle in Fig. 5.26.

The boundary conditions and material properties are listed in Table 5.9, together with a flux of  $q = 0.0001\text{ m}^3/\text{s}$  applied. The time step  $\Delta t$  is set to  $0.1\text{ s}$ . The fracture path evolution with time  $t$  is shown in Fig. 5.27. The time varying pressure distribution in and out of the fracture is shown in Fig. 5.28.

Both the fracture path and the pressure results are in good agreement with the literature [284, 484]. Initially, the fracture propagates in the horizontal direction. Fluid is injected in the borehole as time evolves and the fracture starts to interact with the natural crack (the vertical crack in Fig. 5.26), and the fluid starts to flow along the vertical direction. Due to the interaction between the cracks, the crack propagation direction changes. Model verification demonstrates that the proposed method can describe hydraulic fracturing propagation in porous media in a relatively straight forward way.

## 5.5 Dynamic branching study

The simulation results of hydraulic fracture branching are influenced by many factors, which can essentially be divided into two types: physical and non-physical factors. Physical factors refer to properties of porous media and operational conditions, and non-physical factors refer to assumptions made in the mathematical model or method itself. As discussed in § 5.1, the physical factors mainly include Young's modulus, in-situ stress condition, injection rate, viscosity, porosity and permeability, energy release rate and heterogeneity. Until now, how they affect hydraulic fracture branching has not been systematically investigated, while the

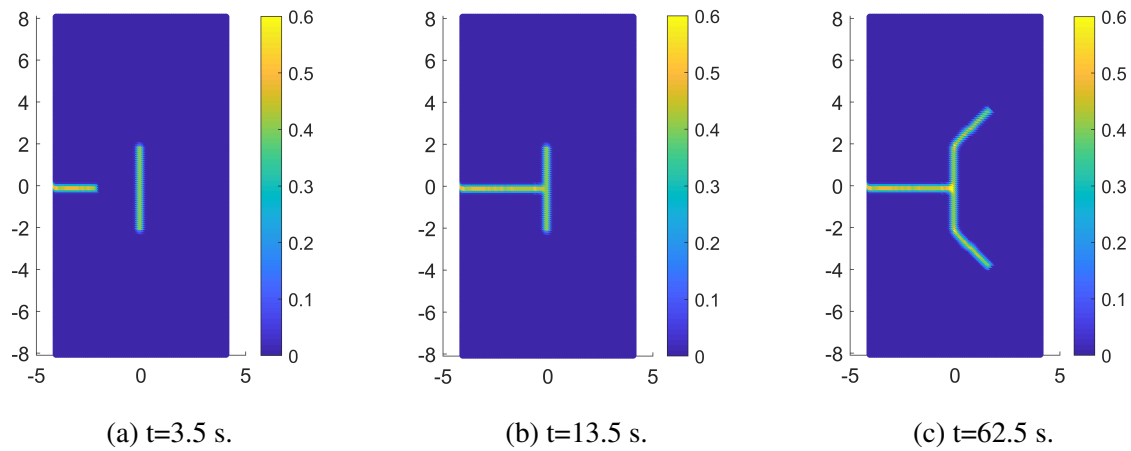


Fig. 5.27 Fracture path evolution with time varying.

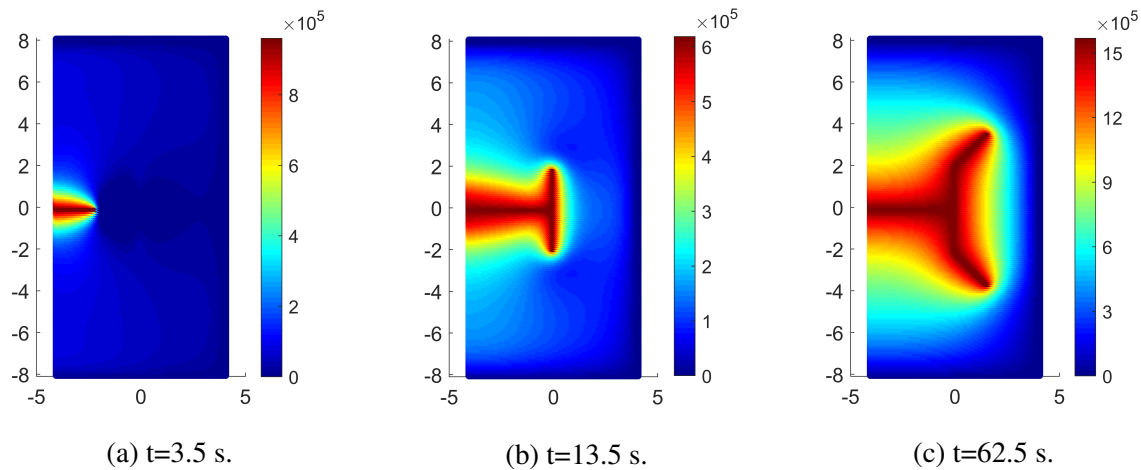


Fig. 5.28 Pore pressure and fracture pressure distribution with time varying (unit: Pa).

conclusions from related studies by different authors are not always consistent, see Table 5.10. In the effort to bridge this gap, we use the proposed hybrid FEM-PD model to study the sensitivity of different physical parameters to the branching phenomenon.

Specifically, six parameters are selected in this study: the flux rate, Young’s modulus, porosity, permeability, viscosity, and energy release rate. The influence of in-situ stress and heterogeneity is not included here because all models and field and experimental results reach a consensus on this point, namely, low in-situ stress difference and heterogeneity is beneficial for crack branching. In addition, to reduce the complexity and ensure the uniqueness of variables, the influence of non-physical factors is eliminated in this study. In peridynamics, the grid size, the horizon size and micro-modulus function model all have an influence on the crack geometry and crack branch [47, 84]. In order to reduce the dependence of crack paths on grid and capture the crack branching behavior accurately [113], an  $m$  ratio of  $m = 3$ ,



Table 5.10 Comparison between the previous conclusions and our conclusions.

Physical Factors	Existing conclusions	Our conclusions
Flux rate	Faster flux rate leads to branching phenomenon. (1) Secondary branching is observed with increasing flux (fem hybrid peridynamics model) [284] (2) No secondary branching is observed with increasing flux and flux rate has little effect on final crack patterns (phase field model) [485]	Faster flux rate leads to branching phenomenon, no secondary branching is observed and branching angles increases with increasing flux rate
Young's modulus	Branching occur when the crack propagates into rock with high Young's modulus (phase field model) [163]	Multiple branches are observed with higher Young's modulus
Porosity	No porosity, no branching phenomenon (finite element crack band model) [340]	Porosity has a limited effect on branching phenomenon, with higher porosity, the branching angles slightly decrease
Permeability	(1) No permeability, no branching phenomenon (finite element crack band model) [340] (2) The permeability has limited effect on crack propagation direction (phase field model) [282]	Lower permeability is beneficial to crack branching
Viscosity	(1) Lower viscosity is beneficial to crack branching [284] (2) In homogeneous rock, low viscosity fluids result exerts little influence on fracture complexity (lattice Boltzmann method (LBM) - discrete element method (DEM) coupled model) [83]	Effects of viscosity to branching phenomenon is multifacet.
Energy release rate	Lower energy release rate leads to branching phenomenon (phase field model) [485]	Lower energy release rate leads to branching phenomenon, secondary branching is observed with decreasing energy release rate

namely the ratio between the horizon and the grid spacing, is adopted. The grid size and micro modulus function keeps constant and the horizon size is set to be  $\delta = 3\Delta x$ . The results from this work and various literatures are compared in Table 4.4, which shows both agreement and differences and are discussed in the following subsections.

### 5.5.1 Effect of flux rate

The effect of flux rate on crack branching is investigated and discussed in this subsection. The geometry and the boundary conditions are the same as that used in the KGD model. Three different cases are studied with three different flux rates, namely, case 1-1 ( $q = 0.001 \text{ m}^3/\text{s}$ ), case 1-2 ( $q = 0.005 \text{ m}^3/\text{s}$ ), case 1-3 ( $q = 0.01 \text{ m}^3/\text{s}$ ). The other parameters are unchanged, see Table 5.9. The crack patterns under different flux rate are shown in Fig. 5.29. As expected, as the flux rate increases, the crack starts to branch. With the flux rate increasing, the fluid velocity increases together with the energy that drives the fracture. When the energy is much higher than what the porous media can dissipate, the crack starts to branch. A secondary crack branching phenomenon with increase in flux rate is not observed in our model. However, with increasing flux rate, the crack angle increases, which is also observed in [484]. Fig. 5.30 shows the fluid pressure under different flux rate at the injection point. As observed, a higher flux rate will cause a larger fluid pressure. The pressure oscillation occurs because it is influenced by the mesh size (see Fig. 3.9b) and the interacting velocities: the

velocity of the crack advancement, the velocity of the fluid in the fracture and the seepage velocity of the fluid in the domain and from the crack [68].

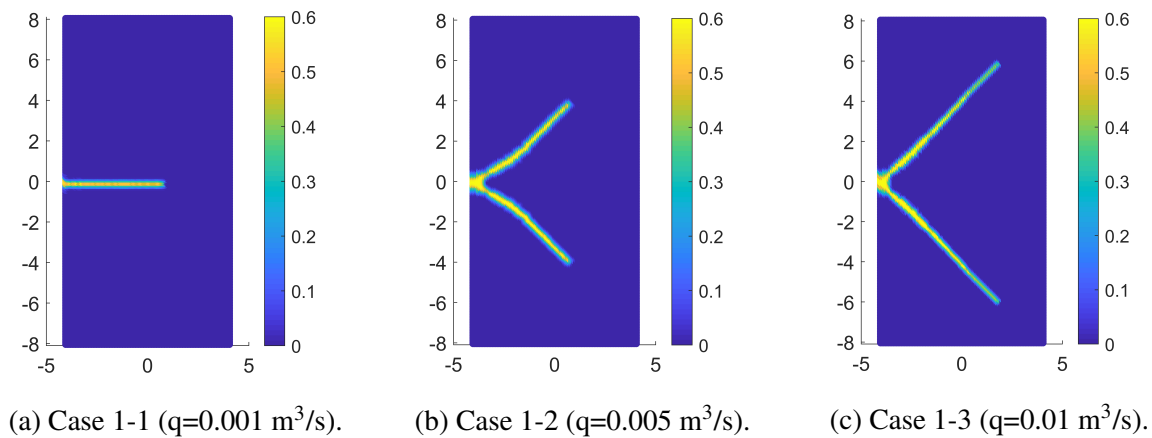


Fig. 5.29 Crack patterns under different flux rate.

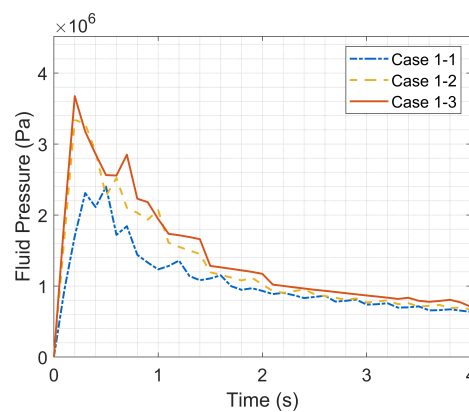


Fig. 5.30 The variation of pressure under different flux rate.

### 5.5.2 Effect of Young's modulus

With a fixed high flux rate  $q = 0.01 \text{ m}^3/\text{s}$ , the influence of Young's modulus on crack branching is investigated. Typical values of Young's modulus for rock formations range from 20 GPa to about 40 GPa [458]. Thus, three different cases are investigated here, which are marked as: case 2-1 ( $E = 15.96 \text{ GPa}$ ), case 2-2 ( $E = 23.94 \text{ GPa}$ ), case 2-3 ( $E = 31.92 \text{ GPa}$ ). The other parameters are unchanged. Fig. 5.31 shows the crack patterns resulting from different Young's modulus. With the increase in Young's modulus, the crack angle becomes smaller and the crack patterns become complex, even secondary crack branching can be

observed. There are two possible reasons behind this phenomenon. First, since the Young's modulus describes the ability of the material to resist deformation, rocks with low Young's modulus tend to be ductile and rocks with high Young's modulus tend to be brittle [246]. Cracks with sharp tips propagate easier than cracks having blunt tips [65]. Secondly, the value of critical stretch  $s_c$ , marked as the crack propagation (bond-break) criterion, is calculated from the value of Young's modulus, see Eq. (5.13c). Therefore, if the Young's modulus is increased, the criterion for crack development decreases, which results in more branches. The variation of pressure value at injection point under different Young's modulus is presented in Fig. 5.32. For a smaller Young's modulus, the fluid pressure will be smaller.

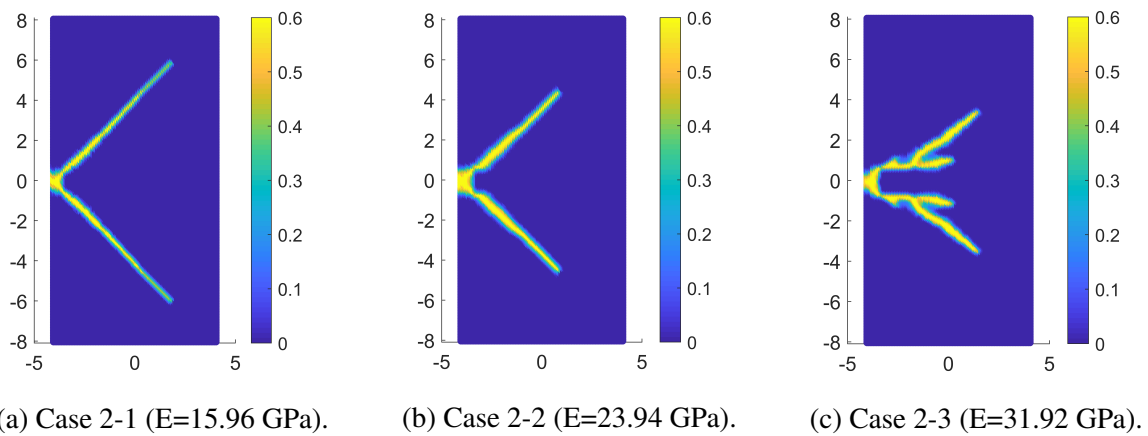


Fig. 5.31 Crack patterns under different Young's modulus.

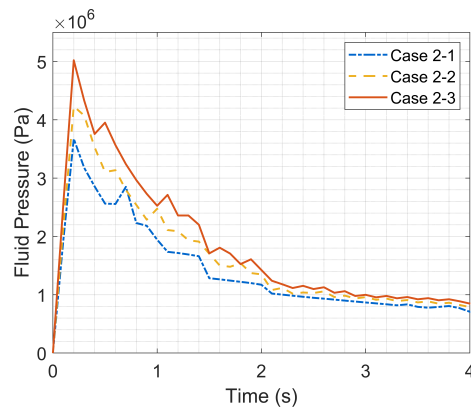


Fig. 5.32 The variation of pressure under different Young's modulus.

### 5.5.3 Effect of porosity and permeability

In geology, the porosity is the fraction of bulk volume of the reservoir that is not occupied by the solid framework of the reservoir and the permeability describes reservoir rock's ability to allow the fluids to flow through its interconnected pores [422]. They are closely related to each other [94]. So we study these two factors together.

The porosity values for sedimentary rocks reservoirs range from 0.1 to 0.4 in sandstones and from 0.05 to 0.5 in carbonates [97]. Thus, with a flux rate  $q = 0.01 \text{ m}^3/\text{s}$ , three cases are selected: case 3-1 ( $n = 0.2$ ), case 3-2 ( $n = 0.3$ ), case 3-3 ( $n = 0.4$ ). For permeability, since ( $k = 1.0 \times 10^{-14} \text{ m}^2$ ) is already very small, an increasing permeability scheme is selected. Three cases including case 4-1 ( $k = 1.0 \times 10^{-14} \text{ m}^2$ ), case 4-2 ( $k = 1.0 \times 10^{-13} \text{ m}^2$ ), case 4-3 ( $k = 1.0 \times 10^{-12} \text{ m}^2$ ) are tested with the porosity  $n = 0.2$  and the flux rate  $q = 0.01 \text{ m}^3/\text{s}$ . The effect of different porosity and permeability on crack branching is studied. Fig. 5.33 and Fig. 5.34 show the crack patterns under different porosity and permeability, separately.

From Fig. 5.33 and Fig. 5.34, it can be observed that compared with porosity, the branching phenomenon is much more sensitive to permeability. With higher porosity, the crack branching angle slightly decreases. However, with higher permeability, the crack patterns change significantly, the crack develops a much smaller branching angle, and propagates along a straight line instead of branching. The reason is most likely due to the permeability increase, which results in more fluid flow into the porous media, and consequently in less fluid flowing into the fracture, so that the energy driven by the fluid in the fracture becomes smaller and the crack propagation velocity decreases. Fig. 5.35 and Fig. 5.36 show fluid pressure at the injection point for different porosity and permeability. It can be observed that the porosity has little effect on fluid pressure at the injection point while the fluid pressure decreases with the increase of permeability.

### 5.5.4 Effect of viscosity

To study the effect of different viscosity on hydraulic crack branching, parameters in Table 5.9 are modified here to make the propagation scheme belong to viscosity dominated regime [373]. The energy release rate is modified to  $G = 1 \text{ N/m}$  and the flux rate is set as  $q = 0.001 \text{ m}^3/\text{s}$ . The other parameters remain unchanged. Three different viscosity, namely, case 5-1 ( $\mu = 0.1 \text{ Pa}\cdot\text{s}$ ), case 5-2 ( $\mu = 0.01 \text{ Pa}\cdot\text{s}$ ), case 5-3 ( $\mu = 0.001 \text{ Pa}\cdot\text{s}$ ) are examined. The crack patterns under different viscosity are shown in Fig. 5.37. By decreasing the fluid viscosity from  $\mu = 0.1 \text{ Pa}\cdot\text{s}$  to  $\mu = 0.01 \text{ Pa}\cdot\text{s}$ , the branching angle grows. This phenomenon is also observed by increasing the flux rate, which indicates that increasing the flux rate or decreasing the viscosity may cause a similar effect. This is consistent with what has

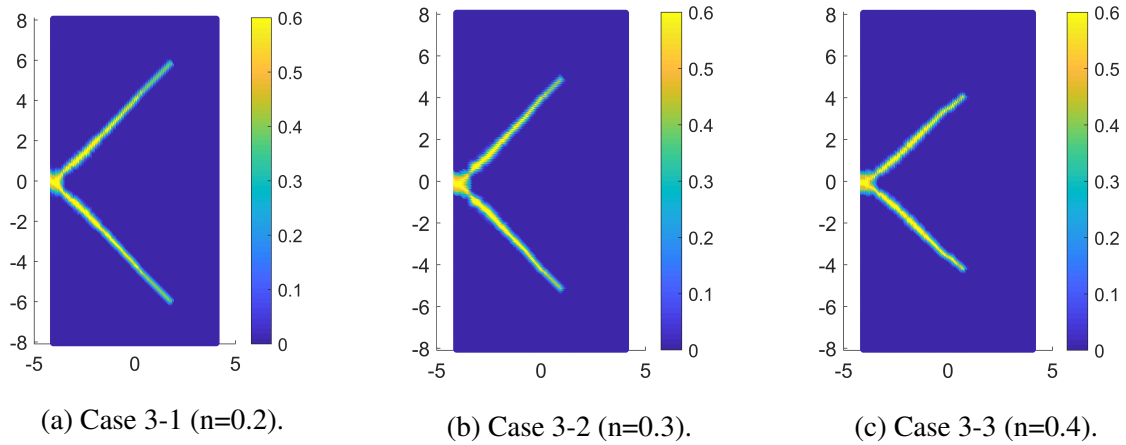


Fig. 5.33 Crack patterns under different porosity.

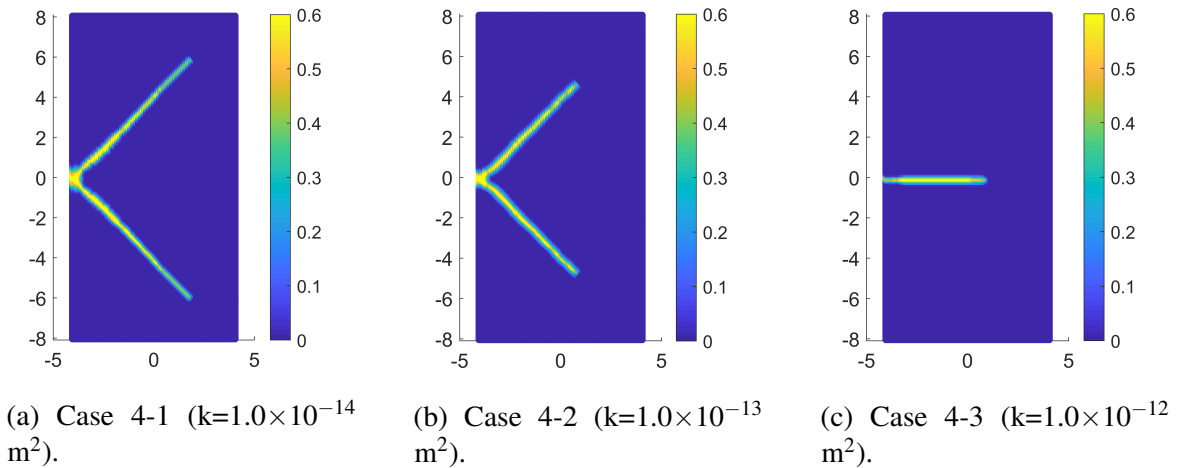


Fig. 5.34 Crack patterns under different permeability.

been observed in numerical and experimental results: complex fracture patterns are prone to form with lower viscosity and high flux rate [284, 388, 473]. However, when the viscosity varies from  $\mu = 0.01$  Pa·s to  $\mu = 0.001$  Pa·s, the increasing angles phenomenon becomes less obvious. A likely reason is that: due to the propagation of the fracture is a complex interaction process between the solid formation and the fluid, the effect of viscosity on hydraulic fracturing is multifaceted. Reducing viscosity will increase the velocity of the fluid, thereby enhancing the hydraulic driving force. Increasing the intrinsic permeability of the porous media causes more fluid to flow into the porous media, so the hydraulic driving force is reduced. The variation of pressure value at injection point under different viscosity is plotted in Fig. 5.38, from which it can be observed that higher viscosity will cause higher fluid pressure at the injection point.

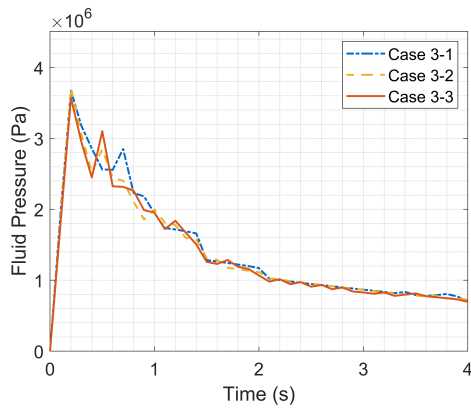


Fig. 5.35 The variation of pressure under different porosity.

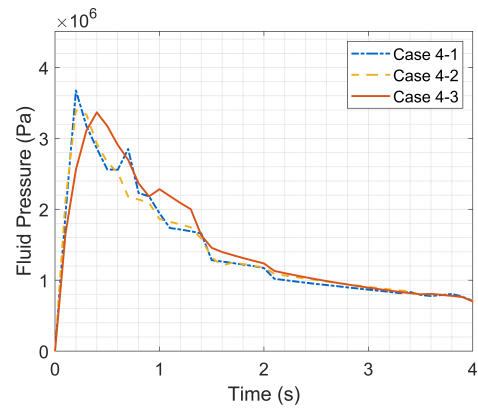
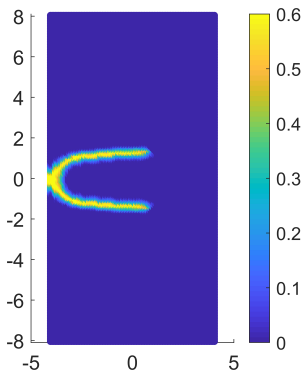
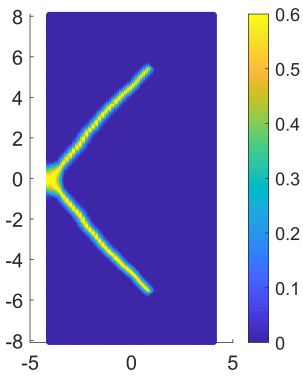


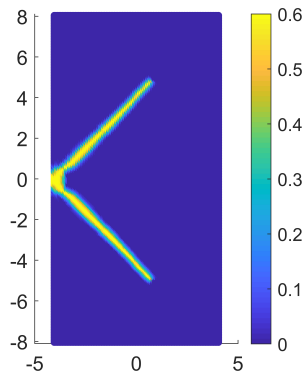
Fig. 5.36 The variation of pressure under different permeability.



(a) Case 5-1 ( $\mu=0.1$  Pa.s).



(b) Case 5-2 ( $\mu=0.01$  Pa.s).



(c) Case 5-3 ( $\mu=0.001$  Pa.s).

Fig. 5.37 Crack patterns under different viscosity.

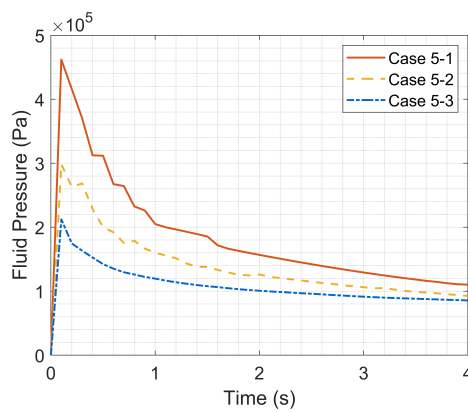


Fig. 5.38 The variation of pressure under different viscosity.

### 5.5.5 Effect of energy release rate

With the viscosity  $\mu = 0.001$  Pa·s, the flux rate  $q = 0.0001$  m<sup>3</sup>/s and the other parameters fixed, the effect of energy release rate is investigated with three different cases: case 6-1 ( $G = 1$  N/m), case 6-2 ( $G = 0.01$  N/m), case 6-3 ( $G = 0.001$  N/m). The crack patterns under different energy release rates are shown in Fig. 5.39. As expected, by decreasing the energy release rate, the crack branching phenomenon can be observed. When the energy release rate is sufficiently low, the complex crack patterns, e.g. secondary crack branching, are prone to form. We note that the thicknesses of some parts of the crack patterns are abnormally large, which may be caused by the widening damage process-zone before crack branching due to the increasing fracture roughness [351, 352] and the simultaneous breaking of a series of bonds due to the change of the physical parameters (e.g. energy release rate) during dynamic simulation. The fluid pressure from the injection point under different energy release rate is compared in Fig. 5.40, from which it can be concluded that a larger energy release rate causes larger fluid pressure, which is also observed in [484].

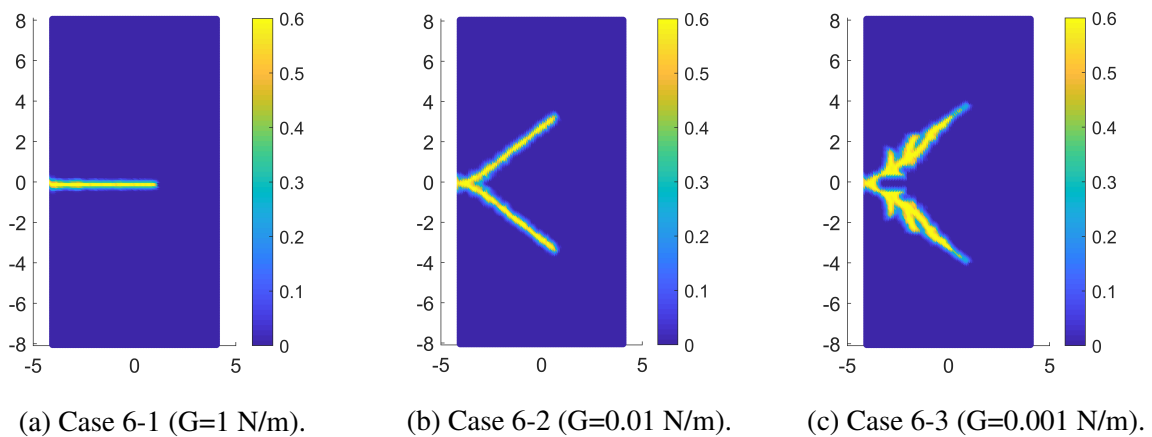


Fig. 5.39 Crack patterns under different energy release rate.

## 5.6 Conclusions

In this chapter, a fully coupled hydraulic fracture propagation simulation approach with a hybrid finite element method (FEM) - peridynamics (PD) scheme is presented. The approach has been verified with three benchmark examples and proved to be effective for simulating complex dynamic crack propagation process. The effects of different factors on branching phenomenon are investigated using the presented approach. From the conducted analysis, we

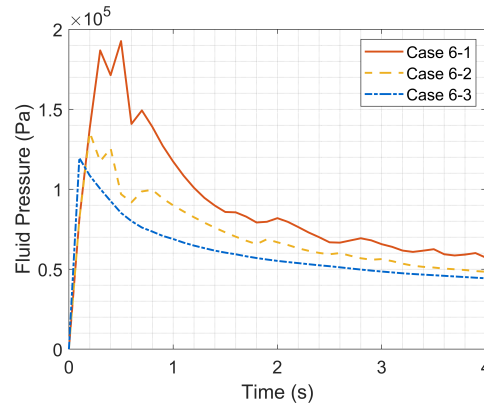


Fig. 5.40 The variation of pressure under different energy release rate.

found that complex crack patterns are prone to form with faster loading rate, more brittle and impermeable media, and with lower energy release rate.

Compared with a staggered solver, the monolithic solver used here solves the displacements and pressure simultaneously. Not only the strong coupling between the porous media and growing fractures can be captured accurately, but also the time step limitation is removed, which makes this approach very competitive and stable in solve hydraulic fracture problems in geological scale. Moreover, no external criterion is required for branching, making branching a natural outcome of the simulation, which solves mesh dependency problem and reduces calculation costs. The limitation of the method lies in that the bond-based peridynamics is only applicable in elastic materials with a fixed Poisson's ratio of  $1/4$  or  $1/3$ . The bond-based peridynamics are intentionally chosen here for simplicity. The method can be extended to an advanced version "state-based peridynamics" to remove the limitations of constraints on fixed Poisson's ratios and to be applied to the modelling of non-linear elastic materials, plastic materials, viscous elastic materials.



# Chapter 6

## Conclusions and outlook

### 6.1 Conclusions

In this thesis, a comprehensive overview of the numerical simulation of fracture propagation is provided and three sets of fracture propagation models, which are based on FEM, peridynamics and hybrid FEM and peridynamics, are developed. With the fracture propagation model based on FEM, the stepwise phenomenon is investigated. With the fracture propagation model based on peridynamics, both the stepwise phenomenon and the branching phenomenon are investigated. With the fracture propagation model based on a hybrid FEM and peridynamic approach, the branching phenomenon is further investigated. The contributions in this thesis are summarised as follows.

First, comprehensive reviews of fracture propagation, crack branching and peridynamics theory are presented. The fracture propagation review includes a review of the hydraulic fracture process, fracture propagation models and various numerical methods for predicting fracture propagation. In terms of the hydraulic fracture process, three basic processes are included: (1) the mechanical deformation; (2) the fluid flow within the fracture; and (3) the fracture propagation. In addition to the three basic processes, the poroelastic effect is also considered. The historical development of several classic hydraulic fracturing models, including the PKN model, the KGD model, the Radial model, the Pseudo 3D model and the Planar 3D model, are introduced. Compared with 2D models and the P3D model, both the flexibility and accuracy of the PL3D model have improved. More importantly, various numerical methods applied in fracture propagation are reviewed, and their advantages and limitations are summarised. The finite element method (FEM) has flexibility and universal applicability in dealing with fracture propagation problems under various conditions but encounters challenges with remeshing, crack tip singularity and calculation cost for multiple fractures. The extended finite element method (XFEM) is independent of the mesh, but

special enrichment needs to be developed to account for the discontinuous at junctions when dealing with multiple fractures or fracture intersections. The boundary element method (BEM) has an advantage in terms of computational efficiency for modelling fracture propagation processes from a macro point of view due to its relatively easy implementation of mesh updating, while it is not suitable for modelling heterogeneous formation properties and complex constitutive model (e.g. elasto-plasticity). For the phase field method (PFM), formation heterogeneities are relatively easy to implement, and remeshing is not essential when dealing with the complex intersection of fractures, even in 3D space. However, the PFM has a high computational cost when an extremely fine mesh and small-time steps are required. The DEM does not need a specific propagation criterion for modelling, and remeshing is not required with fracture propagation, and it is suitable to study fracture propagation in heterogeneous materials or in fracture networks. However, a drawback of DEM is the computational cost, which is influenced by many factors, such as particle numbers, particle shapes and contact force models, resulting in difficulty in the determination of reasonable particle size and parameters.

A state-of-the-art review of crack branching is provided, including experimental observations, physics, and fracture models and associated numerical methods. In terms of experimental observations, high-speed photography is the most commonly used technique to be combined with photoelasticity, caustics, digital image correlation, digital gradient sensing to study the crack branching. The current focus is on (1) how to combine and improve upon existing shortcomings with the combination of technology development; (2) how to simplify the operations and reduce operating costs while ensuring high temporal and spatial resolution. Supported by experimental research, the physics of branching, including the causes of crack branching and branching criteria, have been investigated and summarised. One explanation suggests that branching occurs once the crack velocity exceeds a critical value (related to the wave speed). Another explanation assumes branching is a natural outcome of the growth of microcracks near the crack tip and energy absorbed by the crack is related to the limiting velocity. Dynamic instabilities, which are related to critical velocity, fracture roughness and micro-branches, are also shown to be a strong mechanism for crack branching and are investigated. In addition, the crack front waves and the tilting and twisting of the stress vector at the crack front are responsible for the crack branching. Corresponding to these potential causes of crack branching, different branching criteria have been proposed, including external and internal criteria. The crack models and numerical methods for crack branching have been developed and continuously improved according to various crack branching criteria, which are further applied to simulate crack branching, to shed light on the mechanisms behind branching.

The review of peridynamics gives an overall picture of peridynamics theory, including the basic concepts, classification of peridynamics (bond-based and state-based peridynamics), damage prediction and numerical implementation. Peridynamics has been successfully applied to the following problems, including, but not limited to, material failure problems, impact problems, multifield problems, multiscale problems, wave dispersion problems. Peridynamics has various advantages: (1) it combines continuous and discontinuous descriptions together by replacing the partial differential equation with the integral equation as the approximated equation; (2) the crack development (crack nucleation, growth and branching) and crack intersection phenomena are naturally captured by allowing bonds to break when the bond stretch is greater than the critical criterion without excessive judgment conditions; (3) it is applicable in multiscale problems: by both employing peridynamics alone and by combining the peridynamics model with other models, such as finite element model and molecular dynamics model, large deformation and impact/failure problems on the macro scale and kinetics of phase transformations and damage/failure problems on the micro-scale can be studied; (4) it is applicable in multifield problems. The coupling formulations involving peridynamics have been developed for the analysis of thermal, chemical, diffusion, and electrical problems as well as porous media flow; (5) it is straightforwardly implemented in any dimension. However, peridynamics has some shortcomings, such as the high computational cost, the difficult implementation of the boundary conditions and wave dispersion problems. Despite these shortcomings, peridynamics is still a competitive tool for fracture and damage analysis due to its unique characteristics of dealing with discontinuities in a straightforward way.

The second contribution of the thesis is to develop a fully implicit, FEM-based fracture propagation model using zero thickness cohesive interface elements and investigate the stepwise phenomenon with the model. The rock formation is considered as a fully saturated porous medium. The fracture surface is deemed to be permeable, the fracturing fluid is treated as an incompressible Newtonian fluid, and the cohesive zone model is employed for the fracture propagation criterion. A fully implicit numerical solution scheme is formulated, where the solid and the fluid are solved together in a monolithic finite element scheme. A recent explanation of the stepwise phenomenon is summarised, and the factors that are most likely to affect the phenomenon are investigated. From the survey of the literature and a series of numerical tests, we arrive at the following conclusions. (1) The stepwise fracture advancement during the fracture propagation process does exist in field tests and laboratory experiments. (2) It is important to distinguish whether the stepwise phenomenon observed in numerical simulation is due to physical or numerical reasons. Only a few studies have captured the physical stepwise phenomenon numerically. The stepwise phenomenon observed

in our model is shown to be dependent on mesh size and time step even with poroelastic effect and dynamic rock deformation and fracture propagation considered. (3) Although influencing factors are tested over a prescribed range, no irregular stepwise phenomenon is observed with our model, indicating that the stepwise fracture propagation may be induced by some other factors or physical processes not included in our model.

The third contribution of the thesis is to develop an explicit peridynamic approach for simulating fracture propagation in saturated porous media, which proved to have the ability to reproduce the physical stepwise phenomenon. A staggered method is adopted to solve the coupled system. The solid deformation equation is solved for the displacement field, and the fluid flow equation is solved for the pressure field with peridynamics. After verification via benchmark examples, including a 1D consolidation problem and 2D fluid-filled crack propagation problems, a series of tests are conducted to study the fracture propagation phenomenon in porous media, including the crack branching phenomenon and the stepwise phenomenon. First, the approach proved to be capable of capturing the dynamic crack branching in brittle media and porous media. The crack branching needs a sufficiently high loading condition. Under higher loading conditions, multiple branches event occurs. And the pore pressure depresses the growth and branching of the crack under the fluid-driven condition. Second, the approach proved to be capable of reproducing the stepwise phenomenon in the fracture examples under the mechanical loading case as well as the hydraulic loading case, which is in agreement with experimental observations and numerical simulations obtained with the adaptive FEM. Based on the above results, the proposed peridynamic approach has the potential to analyse various phenomena in fracture propagation and the mechanisms behind it. With further development, the approach could be used in the future to tackle problems with more complex fracture propagation patterns as observed in the field.

Finally, a hybrid FEM and peridynamics approach for modelling fracture propagation in porous media is proposed, which combines the advantages of both the FEM and the peridynamics. Considering the ability of peridynamics in solving discontinuous problems, the area where cracks can potentially occur is discretised by peridynamics and the crack-free area is discretised by FEM. The solid deformation and fracture propagation are captured by peridynamics and FEM, while the fluid flow in both the reservoir and fracture is simulated with FEM. The whole process is solved in a monolithic way with an implicit scheme. The approach demonstrates the capability of modelling complex dynamic crack propagation occurring in benchmark examples, including a 1D consolidation problem, a 2D KGD problem and a fracture interaction problem. The effects of different factors on the branching phenomenon were investigated using the approach. From the conducted analysis, we find

that complex crack patterns are prone to form with faster loading rate, more brittle and impermeable media with a lower energy release rate.

## 6.2 Outlook

In this thesis, we have reviewed the existing models and numerical methods for predicting fracture propagation. Three approaches are developed. On the basis of the work in this thesis, the following work can be further carried out: (1) The mechanical analysis of the fracture propagation model in this thesis is based on linear elastic fracture mechanics. However, in practical problems, the mechanical deformation processes involve plastic deformation. Therefore, the introduction of complex elastoplastic constitutive laws are of great significance in understanding the mechanical deformation mechanism behind fracture propagation in engineering applications. (2) Extension of the proposed methods to a solid-liquid-gas multiphase flow simulation is a natural next step. (3) A 3D model can be developed to further explore the mechanism for fracture propagation, especially fracture branching. In addition, more complex geological conditions, such as heterogeneity and natural fracture networks, can be considered to simulate more “realistic” fracture propagation processes. (4) The bond break in this model now is a process that cannot be recovered over time. The closure of the fracture and the reversal of flow direction need further study. (5) For large-scale geological problems, multiscale methods can be considered for prediction of complex fracture propagation patterns with reduced computational cost.



# References

- [1] Adachi, J., Siebrits, E., Peirce, A., and Desroches, J. (2007). Computer simulation of hydraulic fractures. *International Journal of Rock Mechanics and Mining Sciences*, 44(5):739–757.
- [2] Adachi, J. I., Detournay, E., and Peirce, A. P. (2010). Analysis of the classical pseudo-3d model for hydraulic fracture with equilibrium height growth across stress barriers. *International Journal of Rock Mechanics and Mining Sciences*, 47(4):625–639.
- [3] Adda-Bedia, M. (2004). Brittle fracture dynamics with arbitrary paths. ii. dynamic crack branching under general antiplane loading. *Journal of the Mechanics and Physics of Solids*, 52(6):1407–1420.
- [4] Adda-Bedia, M. (2005). Brittle fracture dynamics with arbitrary paths iii. the branching instability under general loading. *Journal of the Mechanics and Physics of Solids*, 53(1):227–248.
- [5] Adda-Bedia, M. and Arias, R. (2003). Brittle fracture dynamics with arbitrary paths i. kinking of a dynamic crack in general antiplane loading. *Journal of the Mechanics and Physics of Solids*, 51(7):1287–1304.
- [6] Adda-Bedia, M., Arias, R. E., Bouchbinder, E., and Katzav, E. (2013). Dynamic stability of crack fronts: out-of-plane corrugations. *Physical review letters*, 110(1):014302.
- [7] ADVANI, S., LEE, T., and LEE, J. (1990). Three-dimensional modeling of hydraulic fractures in layered media. i, finite element formulations. *Journal of energy resources technology*, 112(1):1–9.
- [8] Advani, S., Torok, J., Lee, J., and Choudhry, S. (1987). Explicit time-dependent solutions and numerical evaluations for penny-shaped hydraulic fracture models. *Journal of Geophysical Research: Solid Earth*, 92(B8):8049–8055.
- [9] Advani, S. H., Lee, T. S., and Lee, J. K. (1990). Three-dimensional modeling of hydraulic fractures in layered media: Part i—finite element formulations. *Journal of Energy Resources Technology*, 112(1):1–9.
- [10] Agwai, A., Guven, I., and Madenci, E. (2011). Predicting crack propagation with peridynamics: a comparative study. *International Journal of Fracture*, 171(1):65.
- [11] Agwai, A. G. (2011). *A peridynamic approach for coupled fields*. PhD thesis, The University of Arizona.

- [12] Al-Busaidi, A., Hazzard, J. F., and Young, R. P. (2005). Distinct element modeling of hydraulically fractured lac du bonnet granite. *Journal of Geophysical Research*, 110(B6).
- [13] Alali, B. and Lipton, R. (2012). Multiscale dynamics of heterogeneous media in the peridynamic formulation. *Journal of Elasticity*, 106(1):71–103.
- [14] Aliabadi, M. H. (2016). *Boundary Element Methods in Linear Elastic Fracture Mechanics*. Elsevier.
- [15] Alpay, S. and Madenci, E. (2013). Crack growth prediction in fully-coupled thermal and deformation fields using peridynamic theory. In *54th AIAA/ASME/ASCE/AHS/ASC structures, structural dynamics, and materials conference*, page 1477.
- [16] Anderson, T. L. (2017). *Fracture mechanics: fundamentals and applications*. CRC press.
- [17] Arias, I., Knap, J., Chalivendra, V. B., Hong, S., Ortiz, M., and Rosakis, A. J. (2007). Numerical modelling and experimental validation of dynamic fracture events along weak planes. *Computer Methods in Applied Mechanics and Engineering*, 196(37-40):3833–3840.
- [18] Armero, F. and Linder, C. (2009). Numerical simulation of dynamic fracture using finite elements with embedded discontinuities. *International Journal of Fracture*, 160(2):119.
- [19] Askari, E., Bobaru, F., Silling, S., Lehoucq, R., Parks, M., and Weckner, O. (2008). Peridynamics for multiscale materials modeling. In *Journal of Physics. Conference Series*, volume 125.
- [20] Askari, E., Xu, J., and Silling, S. (2006). Peridynamic analysis of damage and failure in composites. In *44th AIAA aerospace sciences meeting and exhibit*, page 88.
- [21] Atkinson, G. M., Eaton, D. W., Ghofrani, H., Walker, D., Cheadle, B., Schultz, R., Shcherbakov, R., Tiampo, K., Gu, J., Harrington, R. M., et al. (2016). Hydraulic fracturing and seismicity in the western canada sedimentary basin. *Seismological research letters*, 87(3):631–647.
- [22] Au, S., Soga, K., Jafari, M., Bolton, M., and Komiya, K. (2003). Factors affecting long-term efficiency of compensation grouting in clays. *Journal of Geotechnical and Geoenvironmental Engineering*, 129(3):254–262.
- [23] Ayatollahi, M. and Aliha, M. (2009). Analysis of a new specimen for mixed mode fracture tests on brittle materials. *Engineering Fracture Mechanics*, 76(11):1563–1573.
- [24] Ayoub, J., Jardine, S., and Fitzgerald, P. (2006). Means and method for assessing the geometry of a subterranean fracture during or after a hydraulic fracturing treatment. US Patent 7,082,993.
- [25] Bao, X. and Eaton, D. W. (2016). Fault activation by hydraulic fracturing in western canada. *Science*, 354(6318):1406–1409.
- [26] Barboza, B. R., Chen, B., and Li, C. (2021). A review on proppant transport modelling. *Journal of Petroleum Science and Engineering*, page 108753.



- [27] Barenblatt, G. I. (1962a). *The mathematical theory of equilibrium cracks in brittle fracture*, volume 7. Elsevier.
- [28] Barenblatt, G. I. (1962b). *The mathematical theory of equilibrium cracks in brittle fracture*, volume 7, pages 55–129. Elsevier.
- [29] Barree, R. et al. (1983). A practical numerical simulator for three-dimensional fracture propagation in heterogeneous media. In *SPE reservoir simulation symposium*. Society of Petroleum Engineers.
- [30] Batchelor, C. K. and Batchelor, G. (2000). *An introduction to fluid dynamics*. Cambridge university press.
- [31] Bažant, Z. P. and Jirásek, M. (2002). Nonlocal integral formulations of plasticity and damage: survey of progress. *Journal of engineering mechanics*, 128(11):1119–1149.
- [32] Bazant, Z. P. and Planas, J. (1997). *Fracture and size effect in concrete and other quasibrittle materials*, volume 16. CRC press.
- [33] Becker, G. and Noels, L. (2013). A full-discontinuous galerkin formulation of nonlinear kirchhoff–love shells: elasto-plastic finite deformations, parallel computation, and fracture applications. *International Journal for Numerical Methods in Engineering*, 93(1):80–117.
- [34] Belytschko, T. and Black, T. (1999). Elastic crack growth in finite elements with minimal remeshing. *International journal for numerical methods in engineering*, 45(5):601–620.
- [35] Belytschko, T., Chen, H., Xu, J., and Zi, G. (2003). Dynamic crack propagation based on loss of hyperbolicity and a new discontinuous enrichment. *International journal for numerical methods in engineering*, 58(12):1873–1905.
- [36] Belytschko, T., Lu, Y. Y., and Gu, L. (1994). Element-free galerkin methods. *International journal for numerical methods in engineering*, 37(2):229–256.
- [37] Beyer, H. R., Aksoylu, B., and Celiker, F. (2016). On a class of nonlocal wave equations from applications. *Journal of Mathematical Physics*, 57(6):062902.
- [38] Biot, M. A. (1941). General theory of three-dimensional consolidation. *Journal of applied physics*, 12(2):155–164.
- [39] Biot, M. A. (1956). Theory of propagation of elastic waves in a fluid-saturated porous solid. ii. higher frequency range. *The Journal of the acoustical Society of america*, 28(2):179–191.
- [40] Blanton, T. L. et al. (1982). An experimental study of interaction between hydraulically induced and pre-existing fractures. In *SPE unconventional gas recovery symposium*. Society of Petroleum Engineers.
- [41] Bleyer, J. and Molinari, J.-F. (2017). Microbranching instability in phase-field modelling of dynamic brittle fracture. *Applied Physics Letters*, 110(15):151903.

- [42] Bleyer, J., Roux-Langlois, C., and Molinari, J.-F. (2017). Dynamic crack propagation with a variational phase-field model: limiting speed, crack branching and velocity-toughening mechanisms. *International Journal of Fracture*, 204(1):79–100.
- [43] Bobaru, F. and Duangpanya, M. (2010). The peridynamic formulation for transient heat conduction. *International Journal of Heat and Mass Transfer*, 53(19-20):4047–4059.
- [44] Bobaru, F., Foster, J. T., Geubelle, P. H., and Silling, S. A. (2016). *Handbook of peridynamic modeling*. CRC press.
- [45] Bobaru, F. and Ha, Y. D. (2011). Adaptive refinement and multiscale modeling in 2d peridynamics. *International Journal for Multiscale Computational Engineering*, 9(6).
- [46] Bobaru, F., Ha, Y. D., and Hu, W. (2012). Damage progression from impact in layered glass modeled with peridynamics. *Central European Journal of Engineering*, 2(4):551–561.
- [47] Bobaru, F. and Hu, W. (2012). The meaning, selection, and use of the peridynamic horizon and its relation to crack branching in brittle materials. *International journal of fracture*, 176(2):215–222.
- [48] Bobaru, F., Yang, M., Alves, L. F., Silling, S. A., Askari, E., and Xu, J. (2009). Convergence, adaptive refinement, and scaling in 1d peridynamics. *International Journal for Numerical Methods in Engineering*, 77(6):852–877.
- [49] Bobaru, F. and Zhang, G. (2015). Why do cracks branch? a peridynamic investigation of dynamic brittle fracture. *International Journal of Fracture*, 196(1-2):59–98.
- [50] Bonamy, D. and Ravi-Chandar, K. (2005). Dynamic crack response to a localized shear pulse perturbation in brittle amorphous materials: on crack surface roughening. *International Journal of Fracture*, 134(1):1–22.
- [51] Boone, T. J. and Ingraffea, A. R. (1990a). A numerical procedure for simulation of hydraulically-driven fracture propagation in poroelastic media. *International Journal for Numerical and Analytical Methods in Geomechanics*, 14(1):27–47.
- [52] Boone, T. J. and Ingraffea, A. R. (1990b). A numerical procedure for simulation of hydraulically-driven fracture propagation in poroelastic media. *International Journal for Numerical and Analytical Methods in Geomechanics*, 14(1):27–47.
- [53] Bordas, S., Rabczuk, T., and Zi, G. (2008). Three-dimensional crack initiation, propagation, branching and junction in non-linear materials by an extended meshfree method without asymptotic enrichment. *Engineering Fracture Mechanics*, 75(5):943–960.
- [54] Borden, M. J., Verhoosel, C. V., Scott, M. A., Hughes, T. J., and Landis, C. M. (2012). A phase-field description of dynamic brittle fracture. *Computer Methods in Applied Mechanics and Engineering*, 217:77–95.
- [55] Bouchbinder, E., Goldman, T., and Fineberg, J. (2014). The dynamics of rapid fracture: instabilities, nonlinearities and length scales. *Reports on Progress in Physics*, 77(4):046501.

- [56] Bouchbinder, E., Livne, A., and Fineberg, J. (2008). Weakly nonlinear theory of dynamic fracture. *Physical Review Letters*, 101(26):264302.
- [57] Bouchbinder, E., Livne, A., and Fineberg, J. (2010). Weakly nonlinear fracture mechanics: experiments and theory. *International journal of fracture*, 162(1-2):3–20.
- [58] Bourdin, B., Chukwudozie, C. P., Yoshioka, K., et al. (2012a). A variational approach to the numerical simulation of hydraulic fracturing. In *SPE Annual Technical Conference and Exhibition*. Society of Petroleum Engineers.
- [59] Bourdin, B., Chukwudozie, C. P., Yoshioka, K., et al. (2012b). A variational approach to the numerical simulation of hydraulic fracturing. In *SPE Annual Technical Conference and Exhibition*. Society of Petroleum Engineers.
- [60] Bourdin, B., Francfort, G. A., and Marigo, J.-J. (2000). Numerical experiments in revisited brittle fracture. *Journal of the Mechanics and Physics of Solids*, 48(4):797–826.
- [61] Broberg, K. B. (1960). The propagation of a brittle crack. *Arkiv for Fysik*, 18:159–192.
- [62] Bungier, A. P., Detournay, E., and Garagash, D. I. (2005). Toughness-dominated hydraulic fracture with leak-off. *International journal of fracture*, 134(2):175–190.
- [63] Butt, S. N. and Meschke, G. (2021). Peridynamic analysis of dynamic fracture: influence of peridynamic horizon, dimensionality and specimen size. *Computational Mechanics*, 67(6):1719–1745.
- [64] Butt, S. N., Timothy, J. J., and Meschke, G. (2017). Wave dispersion and propagation in state-based peridynamics. *Computational Mechanics*, 60(5):725–738.
- [65] Callister, W. D. (2007). *Materials science and engineering an introduction*. John Wiley.
- [66] Camacho, G. T. and Ortiz, M. (1996). Computational modelling of impact damage in brittle materials. *International Journal of Solids and Structures*, 33(20-22):2899–2938.
- [67] Cao, T. D., Hussain, F., and Schrefler, B. A. (2018). Porous media fracturing dynamics: stepwise crack advancement and fluid pressure oscillations. *Journal of the Mechanics and Physics of Solids*, 111:113–133.
- [68] Cao, T. D., Milanese, E., Remij, E. W., Rizzato, P., Remmers, J. J., Simoni, L., Huyghe, J. M., Hussain, F., and Schrefler, B. A. (2017). Interaction between crack tip advancement and fluid flow in fracturing saturated porous media. *Mechanics Research Communications*, 80:24–37.
- [69] Carbonell, R., Desroches, J., and Detournay, E. (1999). A comparison between a semi-analytical and a numerical solution of a two-dimensional hydraulic fracture. *International Journal of Solids and Structures*, 36(31–32):4869–4888.
- [70] Carrier, B. and Granet, S. (2012). Numerical modeling of hydraulic fracture problem in permeable medium using cohesive zone model. *Engineering fracture mechanics*, 79:312–328.
- [71] Carter, B., Desroches, J., Ingraffea, A., and Wawrzynek, P. (2000a). Simulating fully 3d hydraulic fracturing. *Modeling in geomechanics*, 200:525–557.

- [72] Carter, B. J., Desroches, J., Ingraffea, A. R., and Wawrzynek, P. (2000b). *Simulating fully 3D hydraulic fracturing*, pages 525–557. John Wiley and Sons, New York.
- [73] Castonguay, S. T., Mear, M. E., Dean, R. H., Schmidt, J. H., et al. (2013). Predictions of the growth of multiple interacting hydraulic fractures in three dimensions. In *SPE annual technical conference and exhibition*. Society of Petroleum Engineers.
- [74] Chakraborty, S. and Shaw, A. (2013). A pseudo-spring based fracture model for sph simulation of impact dynamics. *International Journal of Impact Engineering*, 58:84–95.
- [75] Chen, B., Barron, A. R., Owen, D., and Li, C.-F. (2018a). Propagation of a plane strain hydraulic fracture with a fluid lag in permeable rock. *Journal of Applied Mechanics*, 85(9):091003.
- [76] Chen, B., Barron, A. R., Owen, D., and Li, C.-F. (2018b). Propagation of a plane strain hydraulic fracture with a fluid lag in permeable rock. *Journal of Applied Mechanics*, 85(9).
- [77] Chen, B., Cen, S., Barron, A. R., Owen, D., and Li, C. (2018c). Numerical investigation of the fluid lag during hydraulic fracturing. *Engineering Computations*, 35(5):2050–2077.
- [78] Chen, B., Cen, S., Barron, A. R., Owen, D., and Li, C. (2018d). Numerical investigation of the fluid lag during hydraulic fracturing. *Engineering Computations*, 35(5):2050–2077.
- [79] Chen, B., Sun, Y., Barboza, B. R., Barron, A. R., and Li, C. (2020a). Phase-field simulation of hydraulic fracturing with a revised fluid model and hybrid solver. *Engineering Fracture Mechanics*, 229:106928.
- [80] Chen, J.-W. and Zhou, X.-P. (2019). The enhanced extended finite element method for the propagation of complex branched cracks. *Engineering Analysis with Boundary Elements*, 104:46–62.
- [81] Chen, X. and Gunzburger, M. (2011). Continuous and discontinuous finite element methods for a peridynamics model of mechanics. *Computer Methods in Applied Mechanics and Engineering*, 200(9-12):1237–1250.
- [82] Chen, Z., Bungler, A., Zhang, X., and Jeffrey, R. G. (2009). Cohesive zone finite element-based modeling of hydraulic fractures. *Acta Mechanica Solida Sinica*, 22(5):443–452.
- [83] Chen, Z., Elsworth, D., and Wang, M. (2020b). Does low-viscosity fracturing fluid always create complex fractures? *Journal of Geophysical Research: Solid Earth*, 125(9):e2020JB020332.
- [84] Chen, Z., Ju, J. W., Su, G., Huang, X., Li, S., and Zhai, L. (2019). Influence of micro-modulus functions on peridynamics simulation of crack propagation and branching in brittle materials. *Engineering Fracture Mechanics*, 216:106498.
- [85] Choi, H. and Park, K. (2019). Removing mesh bias in mixed-mode cohesive fracture simulation with stress recovery and domain integral. *International Journal for Numerical Methods in Engineering*, 120(9):1047–1070.

- [86] Chukwudozie, C. (2016). Application of the variational fracture model to hydraulic fracturing in poroelastic media. *Journal of Petroleum Technology*.
- [87] Chung, Y., Yang, Z., and Lin, C. (2017). Modelling micro-crack initiation and propagation of crystal structures with microscopic defects under uni-axial tension by discrete element method. *Powder Technology*, 315:445–476.
- [88] Ciarlet, P. G. (1988). *Mathematical Elasticity: Volume I: three-dimensional elasticity*. North-Holland.
- [89] Clark, A. and Irwin, G. (1966). Crack-propagation behaviors. *Experimental Mechanics*, 6(6):321–330.
- [90] Cleary, M. P., Kavvadas, M., Lam, K. Y., et al. (1983). Development of a fully three-dimensional simulator for analysis and design of hydraulic fracturing. In *SPE/DOE Low Permeability Gas Reservoirs Symposium*. Society of Petroleum Engineers.
- [91] Clifton, R. and Abou-Sayed, A. (1979). On the computation of the three-dimensional geometry of hydraulic fractures. In *Symposium on Low Permeability Gas Reservoirs*. OnePetro.
- [92] Clifton, R., Wang, J., et al. (1988). Multiple fluids, proppant transport, and thermal effects in three-dimensional simulation of hydraulic fracturing. In *SPE annual technical conference and exhibition*. Society of Petroleum Engineers.
- [93] Clifton, R., Wang, J., et al. (1991). Modeling of poroelastic effects in hydraulic fracturing. In *Low Permeability Reservoirs Symposium*. Society of Petroleum Engineers.
- [94] Costa, A. (2006). Permeability-porosity relationship: A reexamination of the kozeny-carman equation based on a fractal pore-space geometry assumption. *Geophysical research letters*, 33(2).
- [95] Cottis, R. et al. (2010). *Shreir's corrosion*. Elsevier Amsterdam, The Netherlands:.
- [96] Courant, R., Friedrichs, K., and Lewy, H. (1928). Über die partiellen differenzgleichungen der mathematischen physik. *Mathematische annalen*, 100(1):32–74.
- [97] Coussy, O. (1995). *Mechanics of porous continua*. Wiley.
- [98] Cundall, P. A. and Strack, O. D. (1979). A discrete numerical model for granular assemblies. *geotechnique*, 29(1):47–65.
- [99] Dahi-Taleghani, A. and Olson, J. E. (2011). Numerical modeling of multistranded-hydraulic-fracture propagation: Accounting for the interaction between induced and natural fractures. *SPE Journal*, 16(3):575–581.
- [100] Dally, J. W. (1979). Dynamic photoelastic studies of fracture. *Experimental Mechanics*, 19(10):349–361.
- [101] Damjanac, B. and Cundall, P. (2016). Application of distinct element methods to simulation of hydraulic fracturing in naturally fractured reservoirs. *Computers and Geotechnics*, 71:283–294.

- [102] Daneshy, A. A. et al. (1973). On the design of vertical hydraulic fractures. *Journal of Petroleum Technology*, 25(01):83–97.
- [103] Daux, C., Moës, N., Dolbow, J., Sukumar, N., and Belytschko, T. (2000). Arbitrary branched and intersecting cracks with the extended finite element method. *International Journal for Numerical Methods in Engineering*, 48(12):1741–1760.
- [104] De Borst, R. (2003). Numerical aspects of cohesive-zone models. *Engineering fracture mechanics*, 70(14):1743–1757.
- [105] de Borst, R., Remmers, J. J., and Needleman, A. (2006). Mesh-independent discrete numerical representations of cohesive-zone models. *Engineering fracture mechanics*, 73(2):160–177.
- [106] De Meo, D., Diyaroglu, C., Zhu, N., Oterkus, E., and Siddiq, M. A. (2016). Modelling of stress-corrosion cracking by using peridynamics. *International Journal of Hydrogen Energy*, 41(15):6593–6609.
- [107] Dehghan, A. N., Goshtasbi, K., Ahangari, K., Jin, Y., and Bahmani, A. (2017). 3d numerical modeling of the propagation of hydraulic fracture at its intersection with natural (pre-existing) fracture. *Rock Mechanics and Rock Engineering*, 50(2):367–386.
- [108] Dempsey, J. P. (1989). Dynamic crack division in brittle solids. In *Twelfth Canadian Congress of Applied Mechanics*, pages 200–201.
- [109] Detournay, E. (2004). Propagation regimes of fluid-driven fractures in impermeable rocks. *International Journal of Geomechanics*, 4(1):35–45.
- [110] Detournay, E., Cheng, A., and McLennan, J. (1990). A poroelastic pkn hydraulic fracture model based on an explicit moving mesh algorithm. *Journal of Energy Resources Technology, Transactions of the ASME*, 112(4):224–230.
- [111] Diehl, P., Franzelin, F., Pflüger, D., and Ganzenmüller, G. C. (2016). Bond-based peridynamics: a quantitative study of mode I crack opening. *International Journal of Fracture*, 201(2):157–170.
- [112] Dinachandra, M. and Alankar, A. (2020). A phase-field study of crack propagation and branching in functionally graded materials using explicit dynamics. *Theoretical and Applied Fracture Mechanics*, 109:102681.
- [113] Dipasquale, D., Sarego, G., Zaccariotto, M., and Galvanetto, U. (2016). Dependence of crack paths on the orientation of regular 2d peridynamic grids. *Engineering Fracture Mechanics*, 160:248–263.
- [114] Dipasquale, D., Sarego, G., Zaccariotto, M., and Galvanetto, U. (2017). A discussion on failure criteria for ordinary state-based peridynamics. *Engineering Fracture Mechanics*, 186:378–398.
- [115] Dipasquale, D., Zaccariotto, M., and Galvanetto, U. (2014). Crack propagation with adaptive grid refinement in 2d peridynamics. *International Journal of Fracture*, 190(1-2):1–22.

- [116] Dong, C. and De Pater, C. (2001). Numerical implementation of displacement discontinuity method and its application in hydraulic fracturing. *Computer methods in applied mechanics and engineering*, 191(8-10):745–760.
- [117] Dong, C. Y. and de Pater, C. J. (2002). Numerical modeling of crack reorientation and link-up. *Advances in Engineering Software*, 33(7–10):577–587.
- [118] Dontsov, E. (2016). An approximate solution for a penny-shaped hydraulic fracture that accounts for fracture toughness, fluid viscosity and leak-off. *Royal Society open science*, 3(12):160737.
- [119] Duan, K., Kwok, C. Y., Wu, W., and Jing, L. (2018a). Dem modeling of hydraulic fracturing in permeable rock: influence of viscosity, injection rate and in situ states. *Acta Geotechnica*, 13(5):1187–1202.
- [120] Duan, K., Kwok, C. Y., Wu, W., and Jing, L. (2018b). Dem modelling of hydraulic fracturing in permeable rock: influence of viscosity, injection rate and in situ states. *Acta Geotechnica*, 13(5):1187–1202.
- [121] Dugdale, D. S. (1960a). Yielding of steel sheets containing slits. *Journal of the Mechanics and Physics of Solids*, 8(2):100–104.
- [122] Dugdale, D. S. (1960b). Yielding of steel sheets containing slits. *Journal of the Mechanics and Physics of Solids*, 8(2):100–104.
- [123] Economides MJ, N. K. (2000). *Reservoir stimulation*. John Wiley Sons, UK.
- [124] Eshelby, J. (1970). Inelastic behavior of solids. *Ed Kanninen*, pages 77–115.
- [125] Fallahzadeh, S., Rasouli, V., and Sarmadivaleh, M. (2015). An investigation of hydraulic fracturing initiation and near-wellbore propagation from perforated boreholes in tight formations. *Rock Mechanics and Rock Engineering*, 48(2):573–584.
- [126] Fallahzadeh, S. H., Hossain, M. M., James Cornwell, A., and Rasouli, V. (2017). Near wellbore hydraulic fracture propagation from perforations in tight rocks: the roles of fracturing fluid viscosity and injection rate. *Energies*, 10(3):359.
- [127] Fan, Z., Liao, H., Jiang, H., Wang, H., and Li, B. (2021). A dynamic adaptive eigenfracture method for failure in brittle materials. *Engineering Fracture Mechanics*, 244:107540.
- [128] Fathima, K. P. and de Borst (2019). Implications of single or multiple pressure degrees of freedom at fractures in fluid-saturated porous media. *Engineering Fracture Mechanics*, 213:1–20.
- [129] Fayyad, T. M. and Lees, J. M. (2017). Experimental investigation of crack propagation and crack branching in lightly reinforced concrete beams using digital image correlation. *Engineering Fracture Mechanics*, 182:487–505.
- [130] Fedelinski, P. (2017). Dynamically loaded branched and intersecting cracks. *Czasopismo Inżynierii Lądowej, Środowiska i Architektury*.

- [131] Feng, Y. and Gray, K. (2017). Parameters controlling pressure and fracture behaviors in field injectivity tests: a numerical investigation using coupled flow and geomechanics model. *Computers and Geotechnics*, 87:49–61.
- [132] Fineberg, J. and Bouchbinder, E. (2015). Recent developments in dynamic fracture: some perspectives. *International Journal of Fracture*, 196(1-2):33–57.
- [133] Fineberg, J., Gross, S. P., Marder, M., and Swinney, H. L. (1991). Instability in dynamic fracture. *Physical Review Letters*, 67(4):457.
- [134] Fineberg, J., Gross, S. P., Marder, M., and Swinney, H. L. (1992). Instability in the propagation of fast cracks. *Physical Review B*, 45(10):5146.
- [135] Fineberg, J. and Marder, M. (1999). Instability in dynamic fracture. *Physics Reports*, 313(1-2):1–108.
- [136] Foster, J. T., Silling, S. A., and Chen, W. (2011). An energy based failure criterion for use with peridynamic states. *International Journal for Multiscale Computational Engineering*, 9(6).
- [137] Foster, J. T., Silling, S. A., and Chen, W. W. (2010). Viscoplasticity using peridynamics. *International journal for numerical methods in engineering*, 81(10):1242–1258.
- [138] Francfort, G. A. and Marigo, J.-J. (1998). Revisiting brittle fracture as an energy minimization problem. *Journal of the Mechanics and Physics of Solids*, 46(8):1319–1342.
- [139] Freund, L. (1972a). Crack propagation in an elastic solid subjected to general loading—i. constant rate of extension. *Journal of the Mechanics and Physics of Solids*, 20(3):129–140.
- [140] Freund, L. (1972b). Crack propagation in an elastic solid subjected to general loading—ii. non-uniform rate of extension. *Journal of the Mechanics and Physics of Solids*, 20(3):141–152.
- [141] Freund, L. (1973). Crack propagation in an elastic solid subjected to general loading—iii. stress wave loading. *Journal of the Mechanics and Physics of Solids*, 21(2):47–61.
- [142] Freund, L. (1998). *Dynamic Fracture Mechanics*. Cambridge Monographs on Mechanics. Cambridge University Press.
- [143] Friedman, J. and Popescu, B. E. (2003). Gradient directed regularization for linear regression and classification. Technical report, Technical Report, Statistics Department, Stanford University.
- [144] Fries, T.-P. and Belytschko, T. (2010). The extended/generalized finite element method: an overview of the method and its applications. *International journal for numerical methods in engineering*, 84(3):253–304.
- [145] Fuh, G.-F., Morita, N., Boyd, P., McGoffin, S., et al. (1992). A new approach to preventing lost circulation while drilling. In *SPE annual technical conference and exhibition*. Society of Petroleum Engineers.



- [146] Fung, R., Vilayakumar, S., Cormack, D. E., et al. (1987). Calculation of vertical fracture containment in layered formations. *SPE formation evaluation*, 2(04):518–522.
- [147] Gao, H. (1993). Surface roughening and branching instabilities in dynamic fracture. *Journal of the Mechanics and Physics of Solids*, 41(3):457–486.
- [148] Garagash, D. I. (2006a). Plane-strain propagation of a fluid-driven fracture during injection and shut-in: Asymptotics of large toughness. *Engineering Fracture Mechanics*, 73(4):456–481.
- [149] Garagash, D. I. (2006b). Propagation of a plane-strain hydraulic fracture with a fluid lag: Early-time solution. *International journal of solids and structures*, 43(18-19):5811–5835.
- [150] Garagash, D. I. and Detournay, E. (2005). Plane-strain propagation of a fluid-driven fracture: Small toughness solution. *Journal of Applied Mechanics, Transactions ASME*, 72(6):916–928.
- [151] Geertsma, J., De Klerk, F., et al. (1969). A rapid method of predicting width and extent of hydraulically induced fractures. *Journal of petroleum technology*, 21(12):1–571.
- [152] Geertsma, J. and Haafkens, R. (1979). A comparison of the theories for predicting width and extent of vertical hydraulically induced fractures. *Journal of Energy Resources Technology*, 101(1):8–19.
- [153] Gerstle, W., Sau, N., and Silling, S. (2007). Peridynamic modeling of concrete structures. *Nuclear engineering and design*, 237(12-13):1250–1258.
- [154] Gerstle, W., Silling, S., Read, D., Tewary, V., and Lehoucq, R. (2008). Peridynamic simulation of electromigration. *Comput Mater Continua*, 8(2):75–92.
- [155] Geubelle, P. H. and Baylor, J. S. (1998). Impact-induced delamination of composites: a 2d simulation. *Composites Part B: Engineering*, 29(5):589–602.
- [156] Ghajari, M., Iannucci, L., and Curtis, P. (2014). A peridynamic material model for the analysis of dynamic crack propagation in orthotropic media. *Computer Methods in Applied Mechanics and Engineering*, 276:431–452.
- [157] Gordeliy, E. and Peirce, A. (2013a). Coupling schemes for modeling hydraulic fracture propagation using the xfem. *Computer Methods in Applied Mechanics and Engineering*, 253:305–322.
- [158] Gordeliy, E. and Peirce, A. (2013b). Implicit level set schemes for modeling hydraulic fractures using the xfem. *Computer Methods in Applied Mechanics and Engineering*, 266:125–143.
- [159] Green, A. and Sneddon, I. (1950). The distribution of stress in the neighbourhood of a flat elliptical crack in an elastic solid. In *Mathematical Proceedings of the Cambridge Philosophical Society*, pages 159–163. Cambridge University Press.
- [160] Gross, S. P., Fineberg, J., Marder, M., McCormick, W., and Swinney, H. L. (1993). Acoustic emissions from rapidly moving cracks. *Physical review letters*, 71(19):3162.

- [161] Guan, P.-C., Chi, S., Chen, J., Slawson, T., and Roth, M. (2011). Semi-lagrangian reproducing kernel particle method for fragment-impact problems. *International Journal of Impact Engineering*, 38(12):1033–1047.
- [162] Guiducci, C., Collin, F., Radu, J.-P., Pellegrino, A., Charlier, R., et al. (2003). Numerical modeling of hydro-mechanical fracture behavior. In *10th ISRM Congress*. International Society for Rock Mechanics and Rock Engineering.
- [163] Guo, J., Lu, Q., Chen, H., Wang, Z., Tang, X., and Chen, L. (2018). Quantitative phase field modeling of hydraulic fracture branching in heterogeneous formation under anisotropic in-situ stress. *Journal of Natural Gas Science and Engineering*, 56:455–471.
- [164] Guo, T., Zhang, S., Qu, Z., Zhou, T., Xiao, Y., and Gao, J. (2014). Experimental study of hydraulic fracturing for shale by stimulated reservoir volume. *Fuel*, 128:373–380.
- [165] Guozden, T. M., Jagla, E. A., and Marder, M. (2010). Supersonic cracks in lattice models. *International journal of fracture*, 162(1-2):107–125.
- [166] Gupta, V., Duarte, C., Babuška, I., and Banerjee, U. (2015). Stable gfem (sgfem): Improved conditioning and accuracy of gfem/xfem for three-dimensional fracture mechanics. *Computer methods in applied mechanics and engineering*, 289:355–386.
- [167] Gupta, V., Duarte, C. A., Babuška, I., and Banerjee, U. (2013). A stable and optimally convergent generalized fem (sgfem) for linear elastic fracture mechanics. *Computer methods in applied mechanics and engineering*, 266:23–39.
- [168] Ha, Y. D. (2020). An extended ghost interlayer model in peridynamic theory for high-velocity impact fracture of laminated glass structures. *Computers & Mathematics with Applications*, 80(5):744–761.
- [169] Ha, Y. D. and Bobaru, F. (2010). Studies of dynamic crack propagation and crack branching with peridynamics. *International Journal of Fracture*, 162(1-2):229–244.
- [170] Ha, Y. D. and Bobaru, F. (2011). Characteristics of dynamic brittle fracture captured with peridynamics. *Engineering Fracture Mechanics*, 78(6):1156–1168.
- [171] Ha, Y. D., Lee, J., and Hong, J.-W. (2015). Fracturing patterns of rock-like materials in compression captured with peridynamics. *Engineering Fracture Mechanics*, 144:176–193.
- [172] Hamidi, F. and Mortazavi, A. (2014). A new three dimensional approach to numerically model hydraulic fracturing process. *Journal of Petroleum Science and Engineering*, 124:451–467.
- [173] Han, F., Lubineau, G., Azdoud, Y., and Askari, A. (2016). A morphing approach to couple state-based peridynamics with classical continuum mechanics. *Computer methods in applied mechanics and engineering*, 301:336–358.
- [174] Hattori, G., Trevelyan, J., Augarde, C. E., Coombs, W. M., and Aplin, A. C. (2017). Numerical simulation of fracking in shale rocks: current state and future approaches. *Archives of Computational Methods in Engineering*, 24(2):281–317.

- [175] Hattori, G., Trevelyan, J., and Coombs, W. M. (2018). A non-ordinary state-based peridynamics framework for anisotropic materials. *Computer Methods in Applied Mechanics and Engineering*, 339:416–442.
- [176] Hauch, J. and Marder, M. (1998). Energy balance in dynamic fracture, investigated by a potential drop technique. *International Journal of Fracture*, 90(1-2):133–151.
- [177] Hawong, J., Kobayashi, A., Dadkhah, M., Kang, B.-J., and Ramulu, M. (1987). Dynamic crack curving and branching under biaxial loading. *Experimental Mechanics*, 27(2):146–153.
- [178] Hedjazi, L., Martin, C., Guessasma, S., Della Valle, G., and Dendievel, R. (2012). Application of the discrete element method to crack propagation and crack branching in a vitreous dense biopolymer material. *International Journal of Solids and Structures*, 49(13):1893–1899.
- [179] Henry, H. (2008). Study of the branching instability using a phase field model of inplane crack propagation. *EPL (Europhysics Letters)*, 83(1):16004.
- [180] Hofacker, M. and Miehe, C. (2012). Continuum phase field modeling of dynamic fracture: variational principles and staggered fe implementation. *International Journal of Fracture*, 178(1-2):113–129.
- [181] Hofacker, M. and Miehe, C. (2013). A phase field model of dynamic fracture: Robust field updates for the analysis of complex crack patterns. *International Journal for Numerical Methods in Engineering*, 93(3):276–301.
- [182] Hofmann, H., Babadagli, T., and Zimmermann, G. (2015). A grain based modelling study of fracture branching during compression tests in granites. *International Journal of Rock Mechanics and Mining Sciences*, 77:152–162.
- [183] Hossain, M. M. and Rahman, M. K. (2008). Numerical simulation of complex fracture growth during tight reservoir stimulation by hydraulic fracturing. *Journal of Petroleum Science and Engineering*, 60(2):86–104.
- [184] Hu, W., Ha, Y. D., and Bobaru, F. (2011). Modeling dynamic fracture and damage in a fiber-reinforced composite lamina with peridynamics. *International Journal for Multiscale Computational Engineering*, 9(6).
- [185] Hu, W., Ha, Y. D., and Bobaru, F. (2012). Peridynamic model for dynamic fracture in unidirectional fiber-reinforced composites. *Computer Methods in Applied Mechanics and Engineering*, 217:247–261.
- [186] Hu, Y., De Carvalho, N., and Madenci, E. (2015). Peridynamic modeling of delamination growth in composite laminates. *Composite Structures*, 132:610–620.
- [187] Hu, Y. and Madenci, E. (2017). Peridynamics for fatigue life and residual strength prediction of composite laminates. *Composite Structures*, 160:169–184.
- [188] Huang, H. and Detournay, E. (2013). Discrete element modeling of tool-rock interaction ii: rock indentation. *International Journal for Numerical and Analytical Methods in Geomechanics*, 37(13):1930–1947.

- [189] Huang, M. and Zienkiewicz, O. (1998). New unconditionally stable staggered solution procedures for coupled soil-pore fluid dynamic problems. *International Journal for Numerical Methods in Engineering*, 43(6):1029–1052.
- [190] Huang, X., Bie, Z., Wang, L., Jin, Y., Liu, X., Su, G., and He, X. (2019). Finite element method of bond-based peridynamics and its abaqus implementation. *Engineering Fracture Mechanics*, 206:408–426.
- [191] Huerta, A., Belytschko, T., Fernández-Méndez, S., Rabczuk, T., Zhuang, X., and Arroyo, M. (2018). Meshfree methods. *Encyclopedia of Computational Mechanics Second Edition*, pages 1–38.
- [192] Hull, D. (1999). *Fractography: observing, measuring and interpreting fracture surface topography*. Cambridge University Press.
- [193] Hunsweck, M. J., Shen, Y., and Lew, A. J. (2013). A finite element approach to the simulation of hydraulic fractures with lag. *International Journal for Numerical and Analytical Methods in Geomechanics*, 37(9):993–1015.
- [194] Islam, M. R. I. and Shaw, A. (2020). Numerical modelling of crack initiation, propagation and branching under dynamic loading. *Engineering Fracture Mechanics*, 224:106760.
- [195] Ivankovic, A., Pandya, K., and Williams, J. (2004). Crack growth predictions in polyethylene using measured traction–separation curves. *Engineering Fracture Mechanics*, 71(4-6):657–668.
- [196] Jabakhanji, R. and Mohtar, R. H. (2015). A peridynamic model of flow in porous media. *Advances in water resources*, 78:22–35.
- [197] Javili, A., Morasata, R., Oterkus, E., and Oterkus, S. (2019). Peridynamics review. *Mathematics and Mechanics of Solids*, 24(11):3714–3739.
- [198] Jeffrey, R., Mills, K., et al. (2000). Hydraulic fracturing applied to inducing longwall coal mine goaf falls. In *4th North American rock mechanics symposium*. American Rock Mechanics Association.
- [199] Jeffrey, R., Zhang, X., and Chen, Z. (2017). Hydraulic fracture growth in naturally fractured rock. In *Porous rock fracture mechanics*, pages 93–116. Elsevier.
- [200] Jeffrey, R. G., Bungler, A., Lecampion, B., Zhang, X., Chen, Z., van As, A., Allison, D. P., De Beer, W., Dudley, J. W., Siebrits, E., et al. (2009). Measuring hydraulic fracture growth in naturally fractured rock. In *SPE annual technical conference and exhibition*. Society of Petroleum Engineers.
- [201] Jing, L. and Stephansson, O. (2007). *Fundamentals of discrete element methods for rock engineering: theory and applications*. Elsevier.
- [202] Jirasek, M. (1998). Nonlocal models for damage and fracture: comparison of approaches. *International Journal of Solids and Structures*, 35(31-32):4133–4145.

- [203] Johnson, R., Glassborow, B., Meyer, J., Scott, M., Datey, A., and Pallikathekathil, Z. (2010). Utilising current technologies to understand permeability, stress azimuths and magnitudes and their impact on hydraulic fracturing success. *The APPEA Journal*, 50(2):736–736.
- [204] Jung, J. and Seok, J. (2016). Fatigue crack growth analysis in layered heterogeneous material systems using peridynamic approach. *Composite Structures*, 152:403–407.
- [205] Jung, J. and Yang, Q. (2017). A two-dimensional augmented finite element for dynamic crack initiation and propagation. *International Journal of Fracture*, 203(1-2):41–61.
- [206] Kalthoff, J. (1973). On the propagation direction of bifurcated cracks. In *Proceedings of an international conference on Dynamic Crack Propagation*, pages 449–458. Springer.
- [207] Kamensky, D., Moutsanidis, G., and Bazilevs, Y. (2018). Hyperbolic phase field modeling of brittle fracture: part i—theory and simulations. *Journal of the Mechanics and Physics of Solids*, 121:81–98.
- [208] Karihaloo, B. (2003). Failure of concrete. In Milne, I., Ritchie, R., and Karihaloo, B., editors, *Comprehensive Structural Integrity*, pages 477–548. Pergamon, Oxford.
- [209] Katiyar, A., Foster, J. T., Ouchi, H., and Sharma, M. M. (2014). A peridynamic formulation of pressure driven convective fluid transport in porous media. *Journal of Computational Physics*, 261:209–229.
- [210] Katzav, E., Adda-Bedia, M., and Arias, R. (2007). Theory of dynamic crack branching in brittle materials. *International Journal of Fracture*, 143(3):245–271.
- [211] Kerkhof, F. (1973). General lecture wave fractographic investigations of brittle fracture dynamics. In *Proceedings of an international conference on Dynamic Crack Propagation*, pages 3–35. Springer.
- [212] Khoei, A. (2015). *Extended Finite Element Method: Theory and Applications*. Wiley Series in Computational Mechanics. Wiley.
- [213] Khoei, A., Barani, O., and Mofid, M. (2011). Modeling of dynamic cohesive fracture propagation in porous saturated media. *International Journal for Numerical and Analytical Methods in Geomechanics*, 35(10):1160–1184.
- [214] Khoei, A. R., Vahab, M., Haghghat, E., and Moallemi, S. (2014). A mesh-independent finite element formulation for modeling crack growth in saturated porous media based on an enriched-fem technique. *International Journal of Fracture*, 188(1):79–108.
- [215] Khristianovic, S. and Zheltov, Y. (1955). Formation of vertical fractures by means of highly viscous fluids. In *Proc. 4th world petroleum congress, Rome*, volume 2, pages 579–586.
- [216] Kilic, B. (2008). *Peridynamic theory for progressive failure prediction in homogeneous and heterogeneous materials*. PhD thesis, The University of Arizona.
- [217] Kishen, J. C. and Singh, K. D. (2001). Stress intensity factors based fracture criteria for kinking and branching of interface crack: application to dams. *Engineering Fracture Mechanics*, 68(2):201–219.

- [218] Klein, P., Foulk, J., Chen, E., Wimmer, S., and Gao, H. (2001). Physics-based modelling of brittle fracture: cohesive formulations and the application of meshfree methods. *Theoretical and Applied Fracture Mechanics*, 37(1-3):99–166.
- [219] Kobayashi, A. (1987). Handbook on experimental mechanics. *Englewood Cliffs, NJ, Prentice-Hall, Inc., 1987, 1020*.
- [220] Kobayashi, A. and Mall, S. (1978). Dynamic fracture toughness of homalite-100. *Experimental Mechanics*, 18(1):11–18.
- [221] Kobayashi, A. and Ramulu, M. (1985). A dynamic fracture analysis of crack curving and branching. *Le Journal de Physique Colloques*, 46(C5):C5–197.
- [222] Lam, K. Y. and Cleary, M. P. (1987). Three-dimensional analysis of hydraulic fracturing. *Computers and Geotechnics*, 3(4):213–228.
- [223] Lecampion, B. (2009). An extended finite element method for hydraulic fracture problems. *Communications in Numerical Methods in Engineering*, 25(2):121–133.
- [224] Lecampion, B., Bungler, A., and Zhang, X. (2018). Numerical methods for hydraulic fracture propagation: a review of recent trends. *Journal of natural gas science and engineering*, 49:66–83.
- [225] Leclerc, W., Haddad, H., and Guessasma, M. (2017). On the suitability of a discrete element method to simulate cracks initiation and propagation in heterogeneous media. *International Journal of Solids and Structures*, 108:98–114.
- [226] Lee, S., Mikelić, A., Wheeler, M. F., and Wick, T. (2016). Phase-field modeling of proppant-filled fractures in a poroelastic medium. *Computer Methods in Applied Mechanics and Engineering*, 312:509–541.
- [227] Leon, S., Spring, D., and Paulino, G. (2014). Reduction in mesh bias for dynamic fracture using adaptive splitting of polygonal finite elements. *International Journal for Numerical Methods in Engineering*, 100(8):555–576.
- [228] LeVeque, R. J. (2007). *Finite difference methods for ordinary and partial differential equations: steady-state and time-dependent problems*. SIAM.
- [229] Lhomme, T., De Pater, C., Helfferich, P., et al. (2002). Experimental study of hydraulic fracture initiation in colton sandstone. In *SPE/ISRM Rock Mechanics Conference*. Society of Petroleum Engineers.
- [230] Li, H., Zhang, H., Zheng, Y., Ye, H., and Lu, M. (2018). An implicit coupling finite element and peridynamic method for dynamic problems of solid mechanics with crack propagation. *International Journal of Applied Mechanics*, 10(04):1850037.
- [231] Li, Q., Xing, H., Liu, J., and Liu, X. (2015). A review on hydraulic fracturing of unconventional reservoir. *Petroleum*, 1(1):8–15.
- [232] Libersky, L. D., Petschek, A. G., Carney, T. C., Hipp, J. R., and Allahdadi, F. A. (1993). High strain lagrangian hydrodynamics: a three-dimensional sph code for dynamic material response. *Journal of computational physics*, 109(1):67–75.

- [233] Libersky, L. D., Randles, P. W., Carney, T. C., and Dickinson, D. L. (1997). Recent improvements in sph modeling of hypervelocity impact. *International Journal of Impact Engineering*, 20(6-10):525–532.
- [234] Liew, M., Danyaro, K. U., and Zawawi, N. A. W. A. (2020). A comprehensive guide to different fracturing technologies: A review. *Energies*, 13(13):3326.
- [235] Linder, C. and Armero, F. (2009). Finite elements with embedded branching. *Finite Elements in Analysis and Design*, 45(4):280–293.
- [236] Lisjak, A. and Grasselli, G. (2014). A review of discrete modelling techniques for fracturing processes in discontinuous rock masses. *Journal of Rock Mechanics and Geotechnical Engineering*, 6(4):301–314.
- [237] Littlewood, D. J. (2015). Roadmap for peridynamic software implementation. *SAND Report, Sandia National Laboratories, Albuquerque, NM and Livermore, CA*.
- [238] Liu, G., Li, Q., Msekh, M. A., and Zuo, Z. (2016). Abaqus implementation of monolithic and staggered schemes for quasi-static and dynamic fracture phase-field model. *Computational Materials Science*, 121:35–47.
- [239] Liu, G.-R. and Gu, Y.-T. (2005). *An introduction to meshfree methods and their programming*. Springer Science & Business Media.
- [240] Liu, S., Ma, F., Zhao, H., Guo, J., Lu, R., and Feng, X. (2020). Numerical analysis on the mechanism of hydraulic fracture behavior in heterogeneous reservoir under the stress perturbation. *Journal of Natural Gas Science and Engineering*, 78:103277.
- [241] Liu, W. K., Jun, S., and Zhang, Y. F. (1995). Reproducing kernel particle methods. *International journal for numerical methods in fluids*, 20(8-9):1081–1106.
- [242] Liu, Y., Liang, L., Irving, S., and Luk, T. (2008). 3d modeling of electromigration combined with thermal–mechanical effect for ic device and package. *Microelectronics Reliability*, 48(6):811–824.
- [243] Liu, Y., Mukherjee, S., Nishimura, N., Schanz, M., Ye, W., Sutradhar, A., Pan, E., Dumont, N. A., Frangi, A., and Saez, A. (2011). Recent advances and emerging applications of the boundary element method. *Applied Mechanics Reviews*, 64(3).
- [244] Livne, A., Ben-David, O., and Fineberg, J. (2007). Oscillations in rapid fracture. *Physical review letters*, 98(12):124301.
- [245] Livne, A., Cohen, G., and Fineberg, J. (2005). Universality and hysteretic dynamics in rapid fracture. *Physical review letters*, 94(22):224301.
- [246] Ma, Y. Z., Sobernheim, D., and Garzon, J. R. (2016). Glossary for unconventional oil and gas resource evaluation and development. In *Unconventional Oil and Gas Resources Handbook*, pages 513–526. Elsevier.
- [247] Madenci, E. and Oterkus, E. (2014). Peridynamic theory. In *Peridynamic Theory and Its Applications*, pages 19–43. Springer.

- [248] Madenci, E. and Oterkus, S. (2016). Ordinary state-based peridynamics for plastic deformation according to von mises yield criteria with isotropic hardening. *Journal of the Mechanics and Physics of Solids*, 86:192–219.
- [249] Mahrer, K. D. (1999). A review and perspective on far-field hydraulic fracture geometry studies. *Journal of Petroleum Science and Engineering*, 24(1):13–28.
- [250] Mandal, T. K., Nguyen, V. P., and Wu, J.-Y. (2020). Evaluation of variational phase-field models for dynamic brittle fracture. *Engineering Fracture Mechanics*, 235:107169.
- [251] Marji, M. F. (2014). Numerical analysis of quasi-static crack branching in brittle solids by a modified displacement discontinuity method. *International Journal of Solids and Structures*, 51(9):1716–1736.
- [252] Meyers, M. A. (1994). *Dynamic behavior of materials*. John wiley & sons.
- [253] Miehe, C. and Mauthe, S. (2016a). Phase field modeling of fracture in multi-physics problems. part iii. crack driving forces in hydro-poro-elasticity and hydraulic fracturing of fluid-saturated porous media. *Computer Methods in Applied Mechanics and Engineering*, 304:619–655.
- [254] Miehe, C. and Mauthe, S. (2016b). Phase field modeling of fracture in multi-physics problems. part iii. crack driving forces in hydro-poro-elasticity and hydraulic fracturing of fluid-saturated porous media. *Computer Methods in Applied Mechanics and Engineering*, 304:619–655.
- [255] Miehe, C., Mauthe, S., and Teichtmeister, S. (2015). Minimization principles for the coupled problem of darcy–biot-type fluid transport in porous media linked to phase field modeling of fracture. *Journal of the Mechanics and Physics of Solids*, 82:186–217.
- [256] Mikelic, A., Wheeler, M. F., and Wick, T. (2015a). A phase-field method for propagating fluid-filled fractures coupled to a surrounding porous medium. *Multiscale Modeling & Simulation*, 13(1):367–398.
- [257] Mikelic, A., Wheeler, M. F., and Wick, T. (2015b). A phase-field method for propagating fluid-filled fractures coupled to a surrounding porous medium. *Multiscale Modeling & Simulation*, 13(1):367–398.
- [258] Mikelić, A., Wheeler, M. F., and Wick, T. (2015a). Phase-field modeling of a fluid-driven fracture in a poroelastic medium. *Computational Geosciences*, 19(6):1171–1195.
- [259] Mikelić, A., Wheeler, M. F., and Wick, T. (2015b). A quasi-static phase-field approach to pressurized fractures. *Nonlinearity*, 28(5):1371.
- [260] Milanese, E., Yılmaz, O., Molinari, J.-F., and Schrefler, B. (2016). Avalanches in dry and saturated disordered media at fracture. *Physical Review E*, 93(4):043002.
- [261] Miller, O., Freund, L., and Needleman, A. (1999). Energy dissipation in dynamic fracture of brittle materials. *Modelling and Simulation in Materials Science and Engineering*, 7(4):573.



- [262] Mitchell, J. A. (2011a). A non-local, ordinary-state-based viscoelasticity model for peridynamics. *Sandia National Lab Report*, 8064:1–28.
- [263] Mitchell, J. A. (2011b). A nonlocal ordinary state-based plasticity model for peridynamics. Technical report, Sandia National Lab.(SNL-NM), Albuquerque, NM (United States).
- [264] Moës, N., Dolbow, J., and Belytschko, T. (1999). A finite element method for crack growth without remeshing. *International journal for numerical methods in engineering*, 46(1):131–150.
- [265] Mohammadnejad, M., Liu, H., Chan, A., Dehkoda, S., and Fukuda, D. (2018). An overview on advances in computational fracture mechanics of rock. *Geosystem Engineering*, pages 1–24.
- [266] Mohammadnejad, T. and Khoei, A. (2013a). An extended finite element method for hydraulic fracture propagation in deformable porous media with the cohesive crack model. *Finite Elements in Analysis and Design*, 73:77–95.
- [267] Mohammadnejad, T. and Khoei, A. R. (2013b). An extended finite element method for hydraulic fracture propagation in deformable porous media with the cohesive crack model. *Finite Elements in Analysis and Design*, 73:77–95.
- [268] Monaghan, J. J. and Gingold, R. A. (1983). Shock simulation by the particle method sph. *Journal of computational physics*, 52(2):374–389.
- [269] Morita, N., Black, A., Guh, G., et al. (1990). Theory of lost circulation pressure. In *SPE annual technical conference and exhibition*. Society of Petroleum Engineers.
- [270] Murphy, N., Ali, M., and Ivankovic, A. (2006). Dynamic crack bifurcation in pmma. *Engineering Fracture Mechanics*, 73(16):2569–2587.
- [271] Nadimi, S., Miscovic, I., and McLennan, J. (2016). A 3d peridynamic simulation of hydraulic fracture process in a heterogeneous medium. *Journal of Petroleum Science and Engineering*, 145:444–452.
- [272] Nagel, N. B., Sanchez-Nagel, M. A., Zhang, F., Garcia, X., and Lee, B. (2013). Coupled numerical evaluations of the geomechanical interactions between a hydraulic fracture stimulation and a natural fracture system in shale formations. *Rock Mechanics and Rock Engineering*, 46(3):581–609.
- [273] Nasehi, M. J. and Mortazavi, A. (2013a). Effects of in-situ stress regime and intact rock strength parameters on the hydraulic fracturing. *Journal of Petroleum Science and Engineering*, 108:211–221.
- [274] Nasehi, M. J. and Mortazavi, A. (2013b). Effects of in-situ stress regime and intact rock strength parameters on the hydraulic fracturing. *Journal of Petroleum Science and Engineering*, 108:211–221.
- [275] Needleman, A. (1987). A continuum model for void nucleation by inclusion debonding. *Journal of Applied Mechanics*, 54(3):525–531.

- [276] Newmark, N. M. (1959). A method of computation for structural dynamics. *Journal of the Engineering Mechanics Division*, 85(3):67–94.
- [277] Nguyen, V. P. (2014). Discontinuous galerkin/extrinsic cohesive zone modeling: Implementation caveats and applications in computational fracture mechanics. *Engineering fracture mechanics*, 128:37–68.
- [278] Nguyen, V. P., Lian, H., Rabczuk, T., and Bordas, S. (2017a). Modelling hydraulic fractures in porous media using flow cohesive interface elements. *Engineering Geology*, 225:68–82.
- [279] Nguyen, V. P., Lian, H., Rabczuk, T., and Bordas, S. (2017b). Modelling hydraulic fractures in porous media using flow cohesive interface elements. *Engineering Geology*, 225:68–82.
- [280] Nguyen, V. P., Rabczuk, T., Bordas, S., and Duflo, M. (2008). Meshless methods: a review and computer implementation aspects. *Mathematics and computers in simulation*, 79(3):763–813.
- [281] Nguyen, V. P. and Wu, J.-Y. (2018). Modeling dynamic fracture of solids with a phase-field regularized cohesive zone model. *Computer Methods in Applied Mechanics and Engineering*, 340:1000–1022.
- [282] Ni, L., Zhang, X., Zou, L., and Huang, J. (2020a). Phase-field modeling of hydraulic fracture network propagation in poroelastic rocks. *Computational Geosciences*, pages 1–16.
- [283] Ni, T., Pesavento, F., Zaccariotto, M., Galvanetto, U., and Schrefler, B. A. (2021). Numerical simulation of forerunning fracture in saturated porous solids with hybrid fem/peridynamic model. *Computers and Geotechnics*, 133:104024.
- [284] Ni, T., Pesavento, F., Zaccariotto, M., Galvanetto, U., Zhu, Q.-Z., and Schrefler, B. A. (2020b). Hybrid fem and peridynamic simulation of hydraulic fracture propagation in saturated porous media. *Computer Methods in Applied Mechanics and Engineering*, 366:113101.
- [285] Ni, T., Zaccariotto, M., Zhu, Q.-Z., and Galvanetto, U. (2019). Static solution of crack propagation problems in peridynamics. *Computer Methods in Applied Mechanics and Engineering*, 346:126–151.
- [286] Ni, T., Zhu, Q.-z., Zhao, L.-Y., and Li, P.-F. (2018). Peridynamic simulation of fracture in quasi brittle solids using irregular finite element mesh. *Engineering Fracture Mechanics*, 188:320–343.
- [287] Nishioka, T., Furutuka, J., Tchouikov, S., and Fujimoto, T. (2002). Generation-phase simulation of dynamic crack bifurcation phenomenon using moving finite element method based on delaunay automatic triangulation. *Computer modelling in Engineering and Sciences*, 3(1):129–145.
- [288] Nordgren, R. et al. (1972). Propagation of a vertical hydraulic fracture. *Society of Petroleum Engineers Journal*, 12(04):306–314.

- [289] Okland, D., Gabrielsen, G. K., Gjerde, J., Koen, S., Williams, E. L., et al. (2002). The importance of extended leak-off test data for combatting lost circulation. In *SPE/ISRM Rock Mechanics Conference*. Society of Petroleum Engineers.
- [290] Olson, J. et al. (2008). Multi-fracture propagation modeling: Applications to hydraulic fracturing in shales and tight gas sands. In *The 42nd US rock mechanics symposium (USRMS)*. American Rock Mechanics Association.
- [291] Olson, J. E., Taleghani, A. D., et al. (2009). Modeling simultaneous growth of multiple hydraulic fractures and their interaction with natural fractures. In *SPE hydraulic fracturing technology conference*. Society of Petroleum Engineers.
- [292] Oterkus, E., Guven, I., and Madenci, E. (2010). Fatigue failure model with peridynamic theory. In *2010 12th IEEE Intersociety Conference on Thermal and Thermomechanical Phenomena in Electronic Systems*, pages 1–6. IEEE.
- [293] Oterkus, S., Fox, J., and Madenci, E. (2013). Simulation of electro-migration through peridynamics. In *2013 IEEE 63rd Electronic Components and Technology Conference*, pages 1488–1493. IEEE.
- [294] Oterkus, S., Madenci, E., and Agwai, A. (2014a). Fully coupled peridynamic thermo-mechanics. *Journal of the Mechanics and Physics of Solids*, 64:1–23.
- [295] Oterkus, S., Madenci, E., and Agwai, A. (2014b). Peridynamic thermal diffusion. *Journal of Computational Physics*, 265:71–96.
- [296] Oterkus, S., Madenci, E., and Oterkus, E. (2017). Fully coupled poroelastic peridynamic formulation for fluid-filled fractures. *Engineering geology*, 225:19–28.
- [297] Oterkus, S., Madenci, E., Oterkus, E., Hwang, Y., Bae, J., and Han, S. (2014c). Hygro-thermo-mechanical analysis and failure prediction in electronic packages by using peridynamics. In *2014 IEEE 64th Electronic Components and Technology Conference (ECTC)*, pages 973–982. IEEE.
- [298] Ouchi, H. et al. (2016). *Development of peridynamics-based hydraulic fracturing model for fracture growth in heterogeneous reservoirs*. PhD thesis, The University of Texas at Austin.
- [299] Ouchi, H., Katiyar, A., Foster, J. T., Sharma, M. M., et al. (2017). A peridynamics model for the propagation of hydraulic fractures in naturally fractured reservoirs. *SPE Journal*, 22(04):1–082.
- [300] Ouchi, H., Katiyar, A., York, J., Foster, J. T., and Sharma, M. M. (2015). A fully coupled porous flow and geomechanics model for fluid driven cracks: a peridynamics approach. *Computational Mechanics*, 55(3):561–576.
- [301] Ouyang, S., Carey, G. F., and Yew, C. H. (1997). An adaptive finite element scheme for hydraulic fracturing with proppant transport. *International Journal for Numerical Methods in Fluids*, 24(7):645–670.

- [302] Palmer, I. D. and Carroll, H. B., J. (1983). Three-dimensional hydraulic fracture propagation in the presence of stress variations. *Society of Petroleum Engineers Journal*, 23(06):870–878.
- [303] Pandolfi, A. and Ortiz, M. (2002). An efficient adaptive procedure for three-dimensional fragmentation simulations. *Engineering with Computers*, 18(2):148–159.
- [304] Pandolfi, A. and Ortiz, M. (2012). An eigenerosion approach to brittle fracture. *International Journal for Numerical Methods in Engineering*, 92(8):694–714.
- [305] Papanastasiou, P. (1997). The influence of plasticity in hydraulic fracturing. *International Journal of Fracture*, 84(1):61–79.
- [306] Papanastasiou, P. (2000). Hydraulic fracture closure in a pressure-sensitive elastoplastic medium. *International journal of fracture*, 103(2):149–161.
- [307] Papoulia, K. D., Sam, C.-H., and Vavasis, S. A. (2003). Time continuity in cohesive finite element modelling. *International Journal for Numerical Methods in Engineering*, 58(5):679–701.
- [308] Park, K. and Paulino, G. H. (2011). Cohesive zone models: a critical review of traction-separation relationships across fracture surfaces. *Applied Mechanics Reviews*, 64(6):060802.
- [309] Park, K., Paulino, G. H., Celes, W., and Espinha, R. (2012). Adaptive mesh refinement and coarsening for cohesive zone modelling of dynamic fracture. *International Journal for Numerical Methods in Engineering*, 92(1):1–35.
- [310] Park, S.-J. and Seo, M.-K. (2011). *Interface science and composites*, volume 18. Academic Press.
- [311] Paul, B., Faivre, M., Massin, P., Giot, R., Colombo, D., Golfier, F., and Martin, A. (2018). 3d coupled hm–xfem modeling with cohesive zone model and applications to non planar hydraulic fracture propagation and multiple hydraulic fractures interference. *Computer Methods in Applied Mechanics and Engineering*, 342:321–353.
- [312] Paulino, G. H., Park, K., Celes, W., and Espinha, R. (2010). Adaptive dynamic cohesive fracture simulation using nodal perturbation and edge-swap operators. *International Journal for Numerical Methods in Engineering*, 84(11):1303–1343.
- [313] Perkins, T., Kern, L. R., et al. (1961). Widths of hydraulic fractures. *Journal of Petroleum Technology*, 13(09):937–949.
- [314] Peruzzo, C., Cao, D., Milanese, E., Favia, P., Pesavento, F., Hussain, F., and Schrefler, B. (2019a). Dynamics of fracturing saturated porous media and self-organization of rupture. *European Journal of Mechanics-A/Solids*, 74:471–484.
- [315] Peruzzo, C., Simoni, L., and Schrefler, B. (2019b). On stepwise advancement of fractures and pressure oscillations in saturated porous media. *Engineering Fracture Mechanics*, 215:246–250.

- [316] Phillips, W. J. et al. (1972). Hydraulic fracturing and mineralization. *Journal of the Geological Society*, 128(4):337–359.
- [317] Pine, R. and Cundall, P. (1985). Applications of the fluid-rock interaction program (frip) to the modelling of hot dry rock geothermal energy systems. In *International symposium on fundamentals of rock joints*, pages 293–302.
- [318] Pizzocolo, F., Huyghe, J., and Ito, K. (2013). Mode I crack propagation in hydrogels is step wise. *Engineering Fracture Mechanics*, 97:72–79.
- [319] Poe, B. (2006). Evaluation of reservoir and hydraulic fracture properties in multi-layer commingled reservoirs using commingled reservoir production data and production logging information. US Patent 7,089,167.
- [320] Pradhan, K. K. and Chakraverty, S. (2019). Chapter four - finite element method. In Pradhan, K. K. and Chakraverty, S., editors, *Computational Structural Mechanics*, pages 25–28. Academic Press.
- [321] Price, N. (1968). A dynamic mechanism for the development of second order faults. In *Proceedings of the Conference on Research in Tectonics*. Geological Survey of Canada, pages 52–68.
- [322] Profit, M., Dutko, M., Yu, J., Armstrong, J., Parfitt, D., and Mutlu, U. (2016a). Application of state of the art hydraulic fracture modelling techniques for safe-optimized design and for enhanced production. In *50th US Rock Mechanics/Geomechanics Symposium*. OnePetro.
- [323] Profit, M., Dutko, M., Yu, J., Cole, S., Angus, D., and Baird, A. (2016b). Complementary hydro-mechanical coupled finite/discrete element and microseismic modelling to predict hydraulic fracture propagation in tight shale reservoirs. *Computational Particle Mechanics*, 3(2):229–248.
- [324] Prudhomme, S. and Diehl, P. (2020). On the treatment of boundary conditions for bond-based peridynamic models. *Computer Methods in Applied Mechanics and Engineering*, 372:113391.
- [325] Rabczuk, T. (2013). Computational methods for fracture in brittle and quasi-brittle solids: state-of-the-art review and future perspectives. *ISRN Applied Mathematics*, 2013.
- [326] Rabczuk, T. and Areias, P. (2006). A meshfree thin shell for arbitrary evolving cracks based on an extrinsic basis. *Computer mechanics*.
- [327] Rabczuk, T. and Belytschko, T. (2004). Cracking particles: a simplified meshfree method for arbitrary evolving cracks. *International Journal for Numerical Methods in Engineering*, 61(13):2316–2343.
- [328] Rabczuk, T. and Belytschko, T. (2007). A three-dimensional large deformation meshfree method for arbitrary evolving cracks. *Computer methods in applied mechanics and engineering*, 196(29-30):2777–2799.

- [329] Rabczuk, T., Belytschko, T., and Xiao, S. (2004). Stable particle methods based on lagrangian kernels. *Computer methods in applied mechanics and engineering*, 193(12-14):1035–1063.
- [330] Rabczuk, T. and Eibl, J. (2003). Simulation of high velocity concrete fragmentation using sph/mlsph. *International Journal for Numerical Methods in Engineering*, 56(10):1421–1444.
- [331] Rabczuk, T. and Eibl, J. (2006). Modelling dynamic failure of concrete with meshfree methods. *International Journal of Impact Engineering*, 32(11):1878–1897.
- [332] Rabczuk, T. and Ren, H. (2017). A peridynamics formulation for quasi-static fracture and contact in rock. *Engineering Geology*, 225:42–48.
- [333] Rabczuk, T., Song, J.-H., and Belytschko, T. (2009). Simulations of instability in dynamic fracture by the cracking particles method. *Engineering Fracture Mechanics*, 76(6):730–741.
- [334] Rabczuk, T., Song, J.-H., Zhuang, X., and Anitescu, C. (2019). *Extended finite element and meshfree methods*. Academic Press.
- [335] Rabczuk, T. and Zi, G. (2007). A meshfree method based on the local partition of unity for cohesive cracks. *Computational Mechanics*, 39(6):743–760.
- [336] Rabczuk, T., Zi, G., Bordas, S., and Nguyen-Xuan, H. (2010). A simple and robust three-dimensional cracking-particle method without enrichment. *Computer Methods in Applied Mechanics and Engineering*, 199(37-40):2437–2455.
- [337] Radovitzky, R., Seagraves, A., Tupek, M., and Noels, L. (2011). A scalable 3d fracture and fragmentation algorithm based on a hybrid, discontinuous galerkin, cohesive element method. *Computer Methods in Applied Mechanics and Engineering*, 200(1-4):326–344.
- [338] Rafiee, S., Seelig, T., and Gross, D. (2003). Simulation of dynamic crack curving and branching under biaxial loading by a time domain boundary integral equation method. *International Journal of Fracture*, 120(3):545–561.
- [339] Rahim, Z. and Holditch, S. (1992). The effects of mechanical properties and selection of completion interval upon the created and propped fracture dimensions in layered reservoirs. In *SPE Rocky Mountain Regional Meeting*. OnePetro.
- [340] Rahimi-Aghdam, S., Chau, V.-T., Lee, H., Nguyen, H., Li, W., Karra, S., Rougier, E., Viswanathan, H., Srinivasan, G., and Bažant, Z. P. (2019). Branching of hydraulic cracks enabling permeability of gas or oil shale with closed natural fractures. *Proceedings of the National Academy of Sciences*, 116(5):1532–1537.
- [341] Rahman, M., Hossain, M., and Rahman, S. (2000). An analytical method for mixed-mode propagation of pressurized fractures in remotely compressed rocks. *International journal of fracture*, 103(3):243–258.
- [342] Rahman, M. M., Hossain, M. M., Crosby, D. G., Rahman, M. K., and Rahman, S. S. (2002). Analytical, numerical and experimental investigations of transverse fracture propagation from horizontal wells. *Journal of Petroleum Science and Engineering*, 35(3-4):127–150.

- [343] Rahman, M. M. and Rahman, M. K. (2010). A review of hydraulic fracture models and development of an improved pseudo-3d model for stimulating tight oil/gas sand. *Energy Sources, Part A: Recovery, Utilization, and Environmental Effects*, 32(15):1416–1436.
- [344] Rahman, R., Foster, J. T., and Haque, A. (2014). A multiscale modeling scheme based on peridynamic theory. *International Journal for Multiscale Computational Engineering*, 12(3).
- [345] Rajagopal, S. and Gupta, N. (2011). Meshfree modelling of fracture—a comparative study of different methods. *Meccanica*, 46(5):1145–1158.
- [346] Rajapakse, R. and Xu, X.-L. (2001). Boundary element modelling of cracks in piezoelectric solids. *Engineering Analysis with Boundary Elements*, 25(9):771–781.
- [347] Ramulu, M. and Kobayashi, A. (1985). Mechanics of crack curving and branching—a dynamic fracture analysis. *Dynamic fracture*, pages 61–75.
- [348] Randles, P. and Libersky, L. D. (1996). Smoothed particle hydrodynamics: some recent improvements and applications. *Computer methods in applied mechanics and engineering*, 139(1-4):375–408.
- [349] Ravi-Chandar, K. (2004). *Dynamic Fracture*. Elsevier Science.
- [350] Ravi-Chandar, K. and Knauss, W. (1984a). An experimental investigation into dynamic fracture: I. crack initiation and arrest. *International Journal of Fracture*, 25(4):247–262.
- [351] Ravi-Chandar, K. and Knauss, W. (1984b). An experimental investigation into dynamic fracture: II. microstructural aspects. *International Journal of Fracture*, 26(1):65–80.
- [352] Ravi-Chandar, K. and Knauss, W. (1984c). An experimental investigation into dynamic fracture: III. on steady-state crack propagation and crack branching. *International Journal of Fracture*, 26(2):141–154.
- [353] Ravi-Chandar, K. and Knauss, W. (1984d). An experimental investigation into dynamic fracture: IV. on the interaction of stress waves with propagating cracks. *International Journal of Fracture*, 26(3):189–200.
- [354] Ren, B., Wu, C., and Askari, E. (2017a). A 3d discontinuous galerkin finite element method with the bond-based peridynamics model for dynamic brittle failure analysis. *International Journal of Impact Engineering*, 99:14–25.
- [355] Ren, H., Zhuang, X., Anitescu, C., and Rabczuk, T. (2019). An explicit phase field method for brittle dynamic fracture. *Computers & Structures*, 217:45–56.
- [356] Ren, H., Zhuang, X., Cai, Y., and Rabczuk, T. (2016). Dual-horizon peridynamics. *International Journal for Numerical Methods in Engineering*, 108(12):1451–1476.
- [357] Ren, H., Zhuang, X., and Rabczuk, T. (2017b). Dual-horizon peridynamics: A stable solution to varying horizons. *Computer Methods in Applied Mechanics and Engineering*, 318:762–782.

- [358] Ren, Q., Dong, Y., and Yu, T. (2009a). Numerical modeling of concrete hydraulic fracturing with extended finite element method. *Science in China Series E: Technological Sciences*, 52(3):559–565.
- [359] Ren, Q., Dong, Y., and Yu, T. (2009b). Numerical modeling of concrete hydraulic fracturing with extended finite element method. *Science in China Series E: Technological Sciences*, 52(3):559–565.
- [360] Ribeiro, T., Beer, G., and Dünser, C. (2008). Efficient elastoplastic analysis with the boundary element method. *Computational Mechanics*, 41(5):715–732.
- [361] Rice, J. R. and Cleary, M. P. (1976). Some basic stress diffusion solutions for fluid-saturated elastic porous media with compressible constituents. *Reviews of Geophysics*, 14(2):227–241.
- [362] Rockfield Software Ltd. (2014). Elfen tgr manual.
- [363] Rokkam, S., Gunzburger, M., Brothers, M., Phan, N., and Goel, K. (2019). A nonlocal peridynamics modeling approach for corrosion damage and crack propagation. *Theoretical and Applied Fracture Mechanics*, 101:373–387.
- [364] Roy, P., Behera, D., and Madenci, E. (2020). Peridynamic simulation of finite elastic deformation and rupture in polymers. *Engineering Fracture Mechanics*, 236:107226.
- [365] Rungamornrat, J., Wheeler, M. F., Mear, M. E., et al. (2005). Coupling of fracture/non-newtonian flow for simulating nonplanar evolution of hydraulic fractures. In *SPE annual technical conference and exhibition*. Society of Petroleum Engineers.
- [366] Sam, C.-H., Papoulia, K. D., and Vavasis, S. A. (2005). Obtaining initially rigid cohesive finite element models that are temporally convergent. *Engineering Fracture Mechanics*, 72(14):2247–2267.
- [367] Santana, E. and Portela, A. (2016). Dual boundary element analysis of fatigue crack growth, interaction and linkup. *Engineering Analysis with Boundary Elements*, 64:176–195.
- [368] Santillán, D., Juanes, R., and Cueto-Felgueroso, L. (2018). Phase field model of hydraulic fracturing in poroelastic media: Fracture propagation, arrest, and branching under fluid injection and extraction. *Journal of Geophysical Research: Solid Earth*, 123(3):2127–2155.
- [369] Sarego, G., Le, Q. V., Bobaru, F., Zaccariotto, M., and Galvanetto, U. (2016). Linearized state-based peridynamics for 2-d problems. *International Journal for Numerical Methods in Engineering*, 108(10):1174–1197.
- [370] Sarris, E. and Papanastasiou, P. (2011). The influence of the cohesive process zone in hydraulic fracturing modelling. *International Journal of Fracture*, 167(1):33–45.
- [371] Sarris, E. and Papanastasiou, P. (2012). Modeling of hydraulic fracturing in a poroelastic cohesive formation. *International Journal of Geomechanics*, 12(2):160–167.



- [372] Sarris, E. and Papanastasiou, P. (2013). Numerical modeling of fluid-driven fractures in cohesive poroelastoplastic continuum. *International Journal for Numerical and Analytical Methods in Geomechanics*, 37(12):1822–1846.
- [373] Savitski, A. and Detournay, E. (2002). Propagation of a penny-shaped fluid-driven fracture in an impermeable rock: asymptotic solutions. *International journal of solids and structures*, 39(26):6311–6337.
- [374] Schardin, H. (1959). Velocity effects in fracture. In *ICF0, Swampscott-MA (USA) 1959*, pages 297–330.
- [375] Schmidt, B., Fraternali, F., and Ortiz, M. (2009). Eigenfracture: an eigendeformation approach to variational fracture. *Multiscale Modeling & Simulation*, 7(3):1237–1266.
- [376] Schrefler, B. A. and Sanavia, L. (2015). *Coupled and multiphysics phenomena*. ALERT Geomaterials.
- [377] Schrefler, B. A., Secchi, S., and Simoni, L. (2006). On adaptive refinement techniques in multi-field problems including cohesive fracture. *Computer methods in applied mechanics and engineering*, 195(4-6):444–461.
- [378] Seagraves, A. and Radovitzky, R. (2009). Advances in cohesive zone modeling of dynamic fracture. In *Dynamic failure of materials and structures*, pages 349–405. Springer.
- [379] Secchi, S. and Schrefler, B. (2012). A method for 3-d hydraulic fracturing simulation. *International journal of fracture*, 178(1-2):245–258.
- [380] Secchi, S. and Schrefler, B. A. (2014). Hydraulic fracturing and its peculiarities. *Asia Pacific Journal on Computational Engineering*, 1(1):1–21.
- [381] Secchi, S., Simoni, L., and A. Schrefler, B. (2007). Mesh adaptation and transfer schemes for discrete fracture propagation in porous materials. *International journal for numerical and analytical methods in geomechanics*, 31(2):331–345.
- [382] Seelig, T. and Gross, D. (1999). On the interaction and branching of fast running cracks—a numerical investigation. *Journal of the Mechanics and Physics of Solids*, 47(4):935–952.
- [383] Segura, J. M. and Carol, I. (2008). Coupled hm analysis using zero-thickness interface elements with double nodes. part i: Theoretical model. *International journal for numerical and analytical methods in geomechanics*, 32(18):2083–2101.
- [384] Sharon, E., Cohen, G., and Fineberg, J. (2002). Crack front waves and the dynamics of a rapidly moving crack. *Physical Review Letters*, 88(8):085503.
- [385] Sharon, E. and Fineberg, J. (1996). Microbranching instability and the dynamic fracture of brittle materials. *Physical Review B*, 54(10):7128.
- [386] Sharon, E., Gross, S. P., and Fineberg, J. (1995). Local crack branching as a mechanism for instability in dynamic fracture. *Physical Review Letters*, 74(25):5096.

- [387] Sharon, E., Gross, S. P., and Fineberg, J. (1996). Energy dissipation in dynamic fracture. *Physical review letters*, 76(12):2117.
- [388] Shimizu, H., Murata, S., and Ishida, T. (2011). The distinct element analysis for hydraulic fracturing in hard rock considering fluid viscosity and particle size distribution. *International Journal of Rock Mechanics and Mining Sciences*, 48(5):712–727.
- [389] Shojaei, A., Mudric, T., Zaccariotto, M., and Galvanetto, U. (2016). A coupled meshless finite point/peridynamic method for 2d dynamic fracture analysis. *International Journal of Mechanical Sciences*, 119:419–431.
- [390] Shojaei, A. and Shao, J. (2017). *Porous Rock Fracture Mechanics: With Application to Hydraulic Fracturing, Drilling and Structural Engineering*. Woodhead Publishing.
- [391] Shojaei, A., Taleghani, A. D., and Li, G. (2014). A continuum damage failure model for hydraulic fracturing of porous rocks. *International Journal of Plasticity*, 59:199–212.
- [392] Shrivastava, K., Sharma, M. M., et al. (2018). *Mechanisms for the formation of complex fracture networks in naturally fractured rocks*.
- [393] Siebrits, E. and Peirce, A. P. (2002). An efficient multi-layer planar 3d fracture growth algorithm using a fixed mesh approach. *International journal for numerical methods in engineering*, 53(3):691–717.
- [394] Silling, S. A. (2000). Reformulation of elasticity theory for discontinuities and long-range forces. *Journal of the Mechanics and Physics of Solids*, 48(1):175–209.
- [395] Silling, S. A. (2010). Linearized theory of peridynamic states. *Journal of Elasticity*, 99(1):85–111.
- [396] Silling, S. A. (2011). A coarsening method for linear peridynamics. *International Journal for Multiscale Computational Engineering*, 9(6).
- [397] Silling, S. A. (2016). Solitary waves in a peridynamic elastic solid. *Journal of the Mechanics and Physics of Solids*, 96:121–132.
- [398] Silling, S. A. and Askari, A. (2014). Peridynamic model for fatigue cracking. SAND2014-18590. Albuquerque: Sandia National Laboratories.
- [399] Silling, S. A. and Askari, E. (2004). Peridynamic modeling of impact damage. In *ASME Pressure Vessels and Piping Conference*, volume 46849, pages 197–205.
- [400] Silling, S. A. and Askari, E. (2005). A meshfree method based on the peridynamic model of solid mechanics. *Computers & structures*, 83(17-18):1526–1535.
- [401] Silling, S. A. and Bobaru, F. (2005). Peridynamic modeling of membranes and fibers. *International Journal of Non-Linear Mechanics*, 40(2-3):395–409.
- [402] Silling, S. A., Epton, M., Weckner, O., Xu, J., and Askari, E. (2007). Peridynamic states and constitutive modeling. *Journal of Elasticity*, 88(2):151–184.
- [403] Silling, S. A. and Lehoucq, R. B. (2010). Peridynamic theory of solid mechanics. In *Advances in applied mechanics*, volume 44, pages 73–168. Elsevier.

- [404] Simonson, E., Abou-Sayed, A., Clifton, R., et al. (1978). Containment of massive hydraulic fractures. *Society of Petroleum Engineers Journal*, 18(01):27–32.
- [405] Skarżyński, Ł. and Tejchman, J. (2013). Experimental investigations of fracture process using dic in plain and reinforced concrete beams under bending. *Strain*, 49(6):521–543.
- [406] Smith, M., Bale, A., Britt, L., Klein, H., Siebrits, E., and Dang, X. (2001). Layered modulus effects on fracture propagation, proppant placement, and fracture modeling. paper spe 71654 presented at the spe annual technical conference and exhibition, new orleans, 30 september–3 october.
- [407] Sneddon, I. N. (1946). The distribution of stress in the neighbourhood of a crack in an elastic solid. *Proceedings of the Royal Society of London. Series A. Mathematical and Physical Sciences*, 187(1009):229–260.
- [408] Soliman, M., Wigwe, M., Alzahabi, A., Pirayesh, E., and Stegent, N. (2014). Analysis of fracturing pressure data in heterogeneous shale formations. *Hydraulic Fracturing J*, 1(2):8–12.
- [409] Song, J.-H., Areias, P. M., and Belytschko, T. (2006). A method for dynamic crack and shear band propagation with phantom nodes. *International Journal for Numerical Methods in Engineering*, 67(6):868–893.
- [410] Song, J.-H., Wang, H., and Belytschko, T. (2008). A comparative study on finite element methods for dynamic fracture. *Computational Mechanics*, 42(2):239–250.
- [411] Spence, D. and Sharp, P. (1985). Self-similar solutions for elastohydrodynamic cavity flow. *Proceedings of the Royal Society of London. A. Mathematical and Physical Sciences*, 400(1819):289–313.
- [412] Spring, D. W., Leon, S. E., and Paulino, G. H. (2014). Unstructured polygonal meshes with adaptive refinement for the numerical simulation of dynamic cohesive fracture. *International Journal of Fracture*, 189(1):33–57.
- [413] Steinke, C., Özenç, K., Chinaryan, G., and Kaliske, M. (2016). A comparative study of the r-adaptive material force approach and the phase-field method in dynamic fracture. *International Journal of Fracture*, 201(1):97–118.
- [414] Stochino, F., Qinami, A., and Kaliske, M. (2017). Eigenerosion for static and dynamic brittle fracture. *Engineering Fracture Mechanics*, 182:537–551.
- [415] Sun, C. and Huang, Z. (2016). Peridynamic simulation to impacting damage in composite laminate. *Composite Structures*, 138:335–341.
- [416] Sundaram, B. M. and Tippur, H. V. (2018). Dynamic fracture of soda-lime glass: A full-field optical investigation of crack initiation, propagation and branching. *Journal of the Mechanics and Physics of Solids*, 120:132–153.
- [417] Suzuki, S. and Sakaue, K. (2004). Measurement of crack opening displacement and energy release rate of rapidly bifurcating cracks in pmma by high-speed holographic microscopy. *JSME International Journal Series A Solid Mechanics and Material Engineering*, 47(3):264–273.

- [418] Suzuki, S., Sakaue, K., and Iwanaga, K. (2007). Measurement of energy release rate and energy flux of rapidly bifurcating crack in homalite 100 and araldite b by high-speed holographic microscopy. *Journal of the Mechanics and Physics of Solids*, 55(7):1487–1512.
- [419] Tchouikov, S., Nishioka, T., and Fujimoto, T. (2004). Numerical prediction of dynamically propagating and branching cracks using moving finite element method. *CMC: Computers, Materials & Continua*, 1(2):191–204.
- [420] Terzaghi, K. (1943). *Theoretical Soil Mechanics*. John Wiley Sons.
- [421] Terzaghi, K., Peck, R. B., and Mesri, G. (1996). *Soil mechanics*. New York: John Wiley & Sons.
- [422] Tiab, D. and Donaldson, E. C. (2015). *Petrophysics: theory and practice of measuring reservoir rock and fluid transport properties*. Gulf professional publishing.
- [423] Tian, F., Tang, X., Xu, T., Yang, J., and Li, L. (2020). Bifurcation criterion and the origin of limit crack velocity in dynamic brittle fracture. *International Journal of Fracture*, 224:117–131.
- [424] Tian, X. and Du, Q. (2015). Nonconforming discontinuous galerkin methods for nonlocal variational problems. *SIAM Journal on Numerical Analysis*, 53(2):762–781.
- [425] Tong, Q. and Li, S. (2016). Multiscale coupling of molecular dynamics and peridynamics. *Journal of the Mechanics and Physics of Solids*, 95:169–187.
- [426] Turner, D. Z. (2013). A non-local model for fluid-structure interaction with applications in hydraulic fracturing. *International Journal for Computational Methods in Engineering Science and Mechanics*, 14(5):391–400.
- [427] Tzschichholz, F. and Herrmann, H. (1995). Simulations of pressure fluctuations and acoustic emission in hydraulic fracturing. *Physical Review E*, 51(3):1961.
- [428] Valkó, P. and Economides, M. J. (1995). *Hydraulic fracture mechanics*, volume 28. Wiley Chichester.
- [429] Vandamme, L. and Curran, J. (1989a). A three-dimensional hydraulic fracturing simulator. *International Journal for Numerical Methods in Engineering*, 28(4):909–927.
- [430] Vandamme, L. and Curran, J. H. (1989b). A three-dimensional hydraulic fracturing simulator. *International Journal for Numerical Methods in Engineering*, 28(4):909–927.
- [431] Vignjevic, R., Reveles, J. R., and Campbell, J. (2006). Sph in a total lagrangian formalism. *CMC-Tech Science Press*, 4(3):181.
- [432] Wang, H. (2015). Numerical modeling of non-planar hydraulic fracture propagation in brittle and ductile rocks using xfem with cohesive zone method. *Journal of Petroleum Science and Engineering*, 135:127–140.
- [433] Wang, H. and Qin, Q.-H. (2019). *Methods of fundamental solutions in solid mechanics*. Elsevier.

- [434] Wang, H. F. (2000). *Theory of linear poroelasticity with applications to geomechanics and hydrogeology*, volume 2. Princeton University Press.
- [435] Wang, T., Liu, Z., Zeng, Q., Gao, Y., and Zhuang, Z. (2017). Xfem modeling of hydraulic fracture in porous rocks with natural fractures. *Science China Physics, Mechanics Astronomy*, 60(8).
- [436] Wang, T., Zhou, W., Chen, J., Xiao, X., Li, Y., and Zhao, X. (2014). Simulation of hydraulic fracturing using particle flow method and application in a coal mine. *International Journal of Coal Geology*, 121:1–13.
- [437] Wang, Y., Zhou, X., and Kou, M. (2018). Peridynamic investigation on thermal fracturing behavior of ceramic nuclear fuel pellets under power cycles. *Ceramics International*, 44(10):11512–11542.
- [438] Wang, Y., Zhou, X., and Xu, X. (2016). Numerical simulation of propagation and coalescence of flaws in rock materials under compressive loads using the extended non-ordinary state-based peridynamics. *Engineering Fracture Mechanics*, 163:248–273.
- [439] Wang, Z., Shedbale, A. S., Kumar, S., and Poh, L. H. (2019). Localizing gradient damage model with micro inertia effect for dynamic fracture. *Computer Methods in Applied Mechanics and Engineering*, 355:492–512.
- [440] Watanabe, N., Wang, W., Taron, J., Görke, U., and Kolditz, O. (2012). Lower-dimensional interface elements with local enrichment: application to coupled hydro-mechanical problems in discretely fractured porous media. *International Journal for Numerical Methods in Engineering*, 90(8):1010–1034.
- [441] Weckner, O. and Abeyaratne, R. (2005). The effect of long-range forces on the dynamics of a bar. *Journal of the Mechanics and Physics of Solids*, 53(3):705–728.
- [442] Wildman, R. A. (2019). Discrete micromodulus functions for reducing wave dispersion in linearized peridynamics. *Journal of Peridynamics and Nonlocal Modeling*, 1(1):56–73.
- [443] Wildman, R. A. and Gazonas, G. A. (2014). A finite difference-augmented peridynamics method for reducing wave dispersion. *International Journal of Fracture*, 190(1-2):39–52.
- [444] Wildman, R. A., O’Grady, J. T., and Gazonas, G. A. (2017). A hybrid multiscale finite element/peridynamics method. *International Journal of Fracture*, 207(1):41–53.
- [445] Williams, B. (1970). Fluid loss from hydraulically induced fractures. *Journal of Petroleum Technology*, 22(07):882–888.
- [446] Wolff, C., Richart, N., and Molinari, J.-F. (2015). A non-local continuum damage approach to model dynamic crack branching. *International Journal for Numerical Methods in Engineering*, 101(12):933–949.
- [447] Wu, C. and Ren, B. (2015). A stabilized non-ordinary state-based peridynamics for the nonlocal ductile material failure analysis in metal machining process. *Computer Methods in Applied Mechanics and Engineering*, 291:197–215.

- [448] Wu, J.-Y. (2017). A unified phase-field theory for the mechanics of damage and quasi-brittle failure. *Journal of the Mechanics and Physics of Solids*, 103:72–99.
- [449] Wu, J.-Y. and Li, F.-B. (2015). An improved stable xfem (is-xfem) with a novel enrichment function for the computational modeling of cohesive cracks. *Computer Methods in Applied Mechanics and Engineering*, 295:77–107.
- [450] Wu, J.-Y. and Nguyen, V. P. (2018). A length scale insensitive phase-field damage model for brittle fracture. *Journal of the Mechanics and Physics of Solids*, 119:20–42.
- [451] Wu, J.-Y., Nguyen, V. P., Nguyen, C. T., Sutula, D., Bordas, S., and Sinaie, S. (2018). Phase field modeling of fracture. *Advances in applied mechanics: multi-scale theory and computation*, 52.
- [452] Wu, K. and Olson, J. E. (2015). Simultaneous multifracture treatments: Fully coupled fluid flow and fracture mechanics for horizontal wells. *SPE Journal*, 20(02):337–346.
- [453] Wu, K. and Olson, J. E. (2016). Numerical investigation of complex hydraulic-fracture development in naturally fractured reservoirs. *SPE Production and Operations*, 31(04):1–10.
- [454] Wu, L., Huang, D., Xu, Y., and Wang, L. (2020). A rate-dependent dynamic damage model in peridynamics for concrete under impact loading. *International Journal of Damage Mechanics*, 29(7):1035–1058.
- [455] Xie, Y., Hu, X., Wang, X., Chen, J., and Lee, K. (2011). A theoretical note on mode-I crack branching and kinking. *Engineering Fracture Mechanics*, 78(6):919–929.
- [456] Xu, D., Liu, Z., Liu, X., Zeng, Q., and Zhuang, Z. (2014). modelling of dynamic crack branching by enhanced extended finite element method. *Computational Mechanics*, 54(2):489–502.
- [457] Xu, F., Gunzburger, M., Burkardt, J., and Du, Q. (2016a). A multiscale implementation based on adaptive mesh refinement for the nonlocal peridynamics model in one dimension. *Multiscale Modeling & Simulation*, 14(1):398–429.
- [458] Xu, H., Zhou, W., Xie, R., Da, L., Xiao, C., Shan, Y., and Zhang, H. (2016b). Characterization of rock mechanical properties using lab tests and numerical interpretation model of well logs. *Mathematical Problems in Engineering*, 2016.
- [459] Xu, J., Askari, A., Weckner, O., and Silling, S. (2008). Peridynamic analysis of impact damage in composite laminates. *Journal of Aerospace Engineering*, 21(3):187–194.
- [460] Xu, S. (2014). Stable cracking particles method based on stabilized nodal integration and updated lagrangian kernel. *Mathematical Problems in Engineering*, 2014.
- [461] Xu, X.-P. and Needleman, A. (1994). Numerical simulations of fast crack growth in brittle solids. *Journal of the Mechanics and Physics of Solids*, 42(9):1397–1434.
- [462] Yamamoto, K., Shimamoto, T., and Sukemura, S. (2004a). Multiple fracture propagation model for a three-dimensional hydraulic fracturing simulator. *International Journal of Geomechanics*, 4(1):46–57.

- [463] Yamamoto, K., Shimamoto, T., and Sukemura, S. (2004b). Multiple fracture propagation model for a three-dimensional hydraulic fracturing simulator. *International Journal of Geomechanics*, 4(1):46–57.
- [464] Yan, X. (2006). Numerical analysis of a few complex crack problems with a boundary element method. *Engineering Failure Analysis*, 13(5):805–825.
- [465] Yang, D., Zhou, Y., Xia, X., Gu, S., Xiong, Q., and Chen, W. (2019). Extended finite element modeling nonlinear hydro-mechanical process in saturated porous media containing crossing fractures. *Computers and Geotechnics*, 111:209–221.
- [466] Ye, Z. and Ghassemi, A. (2018). Injection-induced shear slip and permeability enhancement in granite fractures. *Journal of Geophysical Research: Solid Earth*, 123(10):9009–9032.
- [467] Yoffe, E. H. (1951). Lxxv. the moving griffith crack. *The London, Edinburgh, and Dublin Philosophical Magazine and Journal of Science*, 42(330):739–750.
- [468] Yoshioka, K. and Bourdin, B. (2016). A variational hydraulic fracturing model coupled to a reservoir simulator. *International Journal of Rock Mechanics and Mining Sciences*, 88:137–150.
- [469] Yu, Y., Wang, H., et al. (2014). Peridynamic analytical method for progressive damage in notched composite laminates. *Composite Structures*, 108:801–810.
- [470] Yushi, Z., Shicheng, Z., Tong, Z., Xiang, Z., and Tiankui, G. (2016). Experimental investigation into hydraulic fracture network propagation in gas shales using ct scanning technology. *Rock Mechanics and Rock Engineering*, 49(1):33–45.
- [471] Zaccariotto, M., Mudric, T., Tomasi, D., Shojaei, A., and Galvanetto, U. (2018). Coupling of fem meshes with peridynamic grids. *Computer Methods in Applied Mechanics and Engineering*, 330:471–497.
- [472] Zehnder, A. (2012). *Fracture Mechanics*. Lecture Notes in Applied and Computational Mechanics. Springer Netherlands.
- [473] Zhang, B., Li, X., Zhang, Z., Wu, Y., Wu, Y., and Wang, Y. (2016a). Numerical investigation of influence of in-situ stress ratio, injection rate and fluid viscosity on hydraulic fracture propagation using a distinct element approach. *Energies*, 9(3):140.
- [474] Zhang, F., Dontsov, E., and Mack, M. (2017). Fully coupled simulation of a hydraulic fracture interacting with natural fractures with a hybrid discrete-continuum method. *International Journal for Numerical and Analytical Methods in Geomechanics*, 41(13):1430–1452.
- [475] Zhang, G., Le, Q., Loghin, A., Subramaniyan, A., and Bobaru, F. (2016b). Validation of a peridynamic model for fatigue cracking. *Engineering Fracture Mechanics*, 162:76–94.
- [476] Zhang, L., Zhou, J., Braun, A., and Han, Z. (2018). Sensitivity analysis on the interaction between hydraulic and natural fractures based on an explicitly coupled hydro-geomechanical model in pfc2d. *Journal of Petroleum Science and Engineering*, 167:638–653.

- [477] Zhang, Q., Zhang, X.-P., and Sun, W. (2020). Hydraulic fracturing in transversely isotropic tight sandstone reservoirs: A numerical study based on bonded-particle model approach. *Journal of Structural Geology*, page 104068.
- [478] Zhang, X., Jeffrey, R. G., and Thiercelin, M. (2007a). Deflection and propagation of fluid-driven fractures at frictional bedding interfaces: a numerical investigation. *Journal of Structural Geology*, 29(3):396–410.
- [479] Zhang, X., Jeffrey, R. G., and Thiercelin, M. (2009). Mechanics of fluid-driven fracture growth in naturally fractured reservoirs with simple network geometries. *Journal of Geophysical Research: Solid Earth*, 114(B12).
- [480] Zhang, X., Last, N., Powrie, W., and Harkness, R. (1999). Numerical modelling of wellbore behaviour in fractured rock masses. *Journal of Petroleum Science and Engineering*, 23(2):95–115.
- [481] Zhang, Z., Paulino, G. H., and Celes, W. (2007b). Extrinsic cohesive modelling of dynamic fracture and microbranching instability in brittle materials. *International Journal for Numerical Methods in Engineering*, 72(8):893–923.
- [482] Zhao, X. and Young, R. P. (2011). Numerical modeling of seismicity induced by fluid injection in naturally fractured reservoirs. *Geophysics*, 76(6):WC167–WC180.
- [483] Zhou, S., Rabczuk, T., and Zhuang, X. (2018a). Phase field modeling of quasi-static and dynamic crack propagation: Comsol implementation and case studies. *Advances in Engineering Software*, 122:31–49.
- [484] Zhou, S., Zhuang, X., and Rabczuk, T. (2019). Phase-field modelling of fluid-driven dynamic cracking in porous media. *Computer Methods in Applied Mechanics and Engineering*.
- [485] Zhou, S., Zhuang, X., Zhu, H., and Rabczuk, T. (2018b). Phase field modelling of crack propagation, branching and coalescence in rocks. *Theoretical and Applied Fracture Mechanics*, 96:174–192.
- [486] Zhou, X., Wang, Y., and Qian, Q. (2016). Numerical simulation of crack curving and branching in brittle materials under dynamic loads using the extended non-ordinary state-based peridynamics. *European Journal of Mechanics-A/Solids*, 60:277–299.
- [487] Zhuang, X., Augarde, C., and Mathisen, K. (2012). Fracture modeling using meshless methods and level sets in 3d: framework and modeling. *International Journal for Numerical Methods in Engineering*, 92(11):969–998.
- [488] Zhuang, Z., Liu, Z., Cheng, B., and Liao, J. (2014). *Extended Finite Element Method: Tsinghua University Press Computational Mechanics Series*. Tsinghua University Press Computational Mechanics. Elsevier Science.
- [489] Zi, G., Rabczuk, T., and Wall, W. (2007). Extended meshfree methods without branch enrichment for cohesive cracks. *Computational Mechanics*, 40(2):367–382.
- [490] Zienkiewicz, O. and Chan, A. (1989). Coupled problems and their numerical solution. In *Advances in Computational Nonlinear Mechanics*, pages 139–176. Springer.



- 
- [491] Zingales, M., Di Paola, M., and Inzerillo, G. (2011). The finite element method for the mechanically based model of non-local continuum. *International journal for numerical methods in engineering*, 86(13):1558–1576.